Feeding Black Holes: Gas Dynamics from the Outer Disk to the Very Nucleus in AGN Galaxies

Sebastian Haan

Max-Planck-Institut für Astronomie

Heidelberg 2008

DISSERTATION
submitted to the
Combined Faculties for the Natural Sciences and for Mathematics
of the Ruperto-Carola University of Heidelberg, Germany
for the degree of
Doctor of Natural Sciences

presented by
Dipl.-Phys. Sebastian Haan
born in Leipzig, Germany

Oral examination: 12 September 2008

Feeding Black Holes: Gas Dynamics from the Outer Disk to the Very Nucleus in AGN Galaxies

Referees:	Prof. Dr. Hans-Walter Rix Dr. Eva Schinnerer

Zusammenfassung

Wesentlich für das Verständnis der Galaxienentwicklung und der Aktivität von galaktischen Kernen ist ein genaues Bild der zugrunde liegenden Prozesse, die für die Umverteilung von interstellarem Material verantwortlich sind. Um den Gastransport aus den äußeren Bereichen (mehrere kpc Abstand) bis in das Zentrum (einige 10 pc) von Galaxien zu untersuchen, sind Beobachtungen des molekularen Gases (CO, mit dem IRAM PdBI) aus dem NUGA Projekt mit Beobachtungen des atomaren Gases (HI, mit dem VLA) für 16 aktive Galaxien kombiniert worden. Ein Ergebnis ist, dass die Gasverteilung sowie die Häufigkeit von dynamisch gestörten äußeren Galaxienscheiben davon abzuhängen scheint, welche Art von nuklearer Aktivität vorliegt (Seyfert oder LINER). Dies wiederum weist auf eine gemeinsame Entwicklung von nuklearer Aktivität und der Umverteilung des neutralen Gases hin. Eine genaue Untersuchung zweidimensionaler Abbildungen der Gasbewegung, basierend auf gravitativen Drehmomenten in den Galaxienscheiben, hat ergeben, dass Spiralgalaxien in der Tat sehr dynamische Systeme sind und ständigen Gasumverteilungen mit Zeitskalen von wenigen Rotationsperioden unterliegen. Aufgrund dieser gravitativen Drehmomente ist es Galaxien möglich, Gas aus der äußeren Scheibe bis zu ∼100 pc an das Zentrum zu transportieren. Interessanterweise können somit sogar Korotationsresonanzen von Galaxienbalken überwunden werden, von denen urspünglicherweise angenommen wurde, dass sie eine definitive Barriere für den Gastransport darstellen.

Abstract

Studying the process of fueling the centers of active galaxies with neutral gas is paramount for understanding the origin of nuclear activity and galaxy evolution. To trace the gas flow from the outer galactic disk at several kpc distance to a few 10 pc in the very center, the NUGA key project on molecular gas (CO, using the IRAM PdBI) is complemented with high quality spectroscopic observations of the atomic gas (HI, using the VLA) for a sample of 16 nearby active spiral galaxies (low luminosity AGN and starburst galaxies). The analysis of the outer disk properties revealed that the morphology of the atomic gas and the frequency of dynamically disturbed disks seems to correlate with the AGN type present (Seyfert, LINER), suggesting a time evolution of the AGN activity together with the redistribution of the neutral gas. To evaluate the efficiency and timescales of fueling mechanisms, twodimensional maps of the gas flow were calculated on the basis of NIR images combined with CO and HI data. This study shows that spiral disks are very dynamic systems that undergo strong secular evolution on timescales of a few rotation periods, due to the effectiveness of gravitational torques in redistributing cold galactic gas. Thus, gas can be transported from the outer disk all the way into the galaxy center at ∼100 pc, even overcoming previously assumed dynamical barriers to gas transport such as the corotation resonances of stellar bars.

Contents

1 Introduction

Yet science is still struggling to explain some of the most fundamental phenomena observed in our universe. How did galaxies form, how did they evolve from the dawn of the universe to the various types of galaxies observed today, and what will become of them in the distant future? In our quest to answer these questions, strong advancements in observational techniques and simulation methods have lead to new insight into galaxy formation and evolution processes, but also raised further important questions. One of these open problems is related to the center of galaxies, which appear for some galaxies more than 100 times brighter than the stars in the galaxy itself, and for some other galaxy they show no radiation at all. To explain this incredible discrepancy one has to understand the mechanisms that feed this central engine, nowadays associated with accretion of material onto a supermassive black hole sitting at the center of most galaxies. This thesis investigates possible fueling mechanisms and related galaxy evolution scenarios via studying in detail the gaseous dynamics and properties of a sample of nearby active galaxies on all spatial scales.

The outline of this thesis is as follows: Here, the theoretical framework for connecting our spectroscopic gas observations with the dynamical evolution of AGN host galaxies is given. The NUclei of GAlaxy (NUGA) project and its goal to find mechanisms for the fueling of low-luminosity AGN is described in Chapter II. The results of the distribution and kinematics of atomic hydrogen (HI) are presented for 16 nearby spiral galaxies in Chapter III and possible relationships between the evolution of the host galaxy and the AGN type are investigated. In Chapter IV gas flow maps are derived for seven representive galaxies using the combined spectroscopic CO and HI data. To determine gas in/out-flow rates as a function of location within the galactic disks, gravity torques are calculated on the basis of NIR images and compared to kinematical evidence for radial gas flow using the observed gaseous velocity fields. In Chapter V the results are discussed in the context of AGN fueling and an outlook on future progress in this area of research is given.

1.1 Scenarios for Galaxy Evolution

At early times, the evolution of galaxies were marked by hierarchical clustering and violent merging processes, while internal secular processes became increasingly dominant with time.

As both processes are very important for galaxy evolution, this section will give a brief introduction about early formation and secular evolution processes of galaxies with an emphasis on angular momentum transport in galaxies.

1.1.1 Early Formation and Evolution of Galaxies

The Formation of Galaxies

A fundamental assumption of cosmology is that the early universe was almost perfectly homogeneous as can be observed in the Cosmic Microwave Background (CMB; for a review see Hu & Dodelson, 2002), and that stars, galaxies, galaxy clusters, and other large-scale structures developed by the growth of gravitationally unstable density fluctuation (e.g. quantum fluctuations). The statistical nature of these fluctuations depend on how they were generated. Two classes of early universe models are widely considered to provide plausible mechanisms: inflation (Guth, 1981) and topological defects (Vilenkin & Shellard, 1994). Inflation predicts Gaussian fluctuations, while most defect models are non-Gaussian. However, the baryonic matter was tightly coupled to the photons of the CMB until the epoch of decoupling at redshift $z \backsimeq 1000$. Shortly after, Cold Dark Matter (CDM) or a similar effective gravitational potential (of yet unknown nature) began to drive baryons towards local density enhancements. Within the context of CDM, the dark halo of a galaxy assembled first, and it is likely that its growth continues to the present time. In general, the early stages of the evolution of galaxies were marked by violent gas dynamics and accretion events, leading to the high internal densities of the first globular clusters. Through the collapse of primordial molecular gas clouds, the first stars formed and started to re-ionize the surrounding gas at a redshift of $z \backsimeq 20$ (Loeb & Barkana, 2001). In some galaxies, this first episode of gas accretion may have established the stellar bulge, the central black hole, the first halo stars and the globular clusters.

The Origin of Angular Momentum and the Central Black Hole of Galaxies

As long as the cold ISM forms a quiescent disk, conservation of angular momentum keeps it on circular orbits and away from the center of a galaxy. But during the process of merging, the gravitational field is disturbed and far from axisymmetric, so that some amount of gas loses all its angular momentum and can fall into the center and feed the black hole. Thus, the black hole is expected to grow rapidly at times of bulge formation which may explain the observed correlation between black-hole mass and bulge luminosity and velocity dispersion (see §1.1.3). At least two other mechanisms are capable of forming bulges. First, buckling instabilities can fatten a barred disk into a peanut-shaped bulge (Kormendy & Kennicutt, 2004), and second, bulges can form out of disks when a satellite galaxy plunges deep into its host galaxy (Binney & Tremaine, 2008). It is likely that a combination of these processes may have formed the bulges presently observed.

Gas accretion has not stopped after this violent phase of the galaxy evolution in the early universe. Spiral galaxies are likely continually accreting gas, from the hot intergalactic medium or via merging with other galaxies. As gas can lose angular momentum through radiation, the incoming gas clouds will settle onto closed orbits on the galaxy's disk. In a few cases, gas is observed to orbit in a plane perpendicular to the disk of the host galaxy or the accreted gas disk lies in the same plane but rotates in an opposite sense (e.g. NGC 4550, NGC 4826).

One of the goals of studying galaxy formation and evolution is to establish the existence of global relations involving physically quantities such as the total mass M, total energy E_{tot}, or total angular momentum J_{tot} of a galaxy. The initial angular momentum of a galaxy is assumed to be generated by tidal torques between neighboring protogalaxies during hierarchical formation which predict the value of a spin parameter λ, defined as

$$\lambda = \frac{J_{tot}|E_{tot}|^{1/2}}{GM^{5/2}}, \tag{1.1}$$

close to 0.04. A distribution of λ-values for halos formed in a simulation of the standard ΛCDM cosmology is show in Fig. 1.1.

However, large amounts of angular momentum may be hidden in the outer parts of elliptical galaxies in which the kinematic profiles are less known and automatically implies a failure in making such measurements. Hence the principal limitation of λ is that the values J_{tot} and M are both sensitive to the location of the halo's boundary. Further, no strong correlation is found between the direction of the angular-momentum vectors of material near the center and on the periphery of a typical halo using cosmological hydrodynamic simulations (Bailin et al., 2005). These findings can be explained by linear theory that the direction of angular momentum that is being accreted by a halo varies dramatically over cosmic time (Quinn & Binney, 1992). Through collisionless relaxation processes within a halo, the angular-momentum vectors of different mass shells can align. As these processes act faster in the inner region where the crossing time is relatively short, the spin axis of the inner region may constantly slew under the influence of torques produced by the less coherent outer region (Ostriker & Binney, 1989) and may lead to the manifestation of disk warps (Binney & Tremaine, 2008).

Besides, other physical processes than pure gravitational forces during formation and evolution may act to enforce some scaling laws. Thus, empirically established global laws are more suitable, although the final translation into the desired physical variables generally depends on the model. The main empirical global laws between global physical properties of a galaxy are:

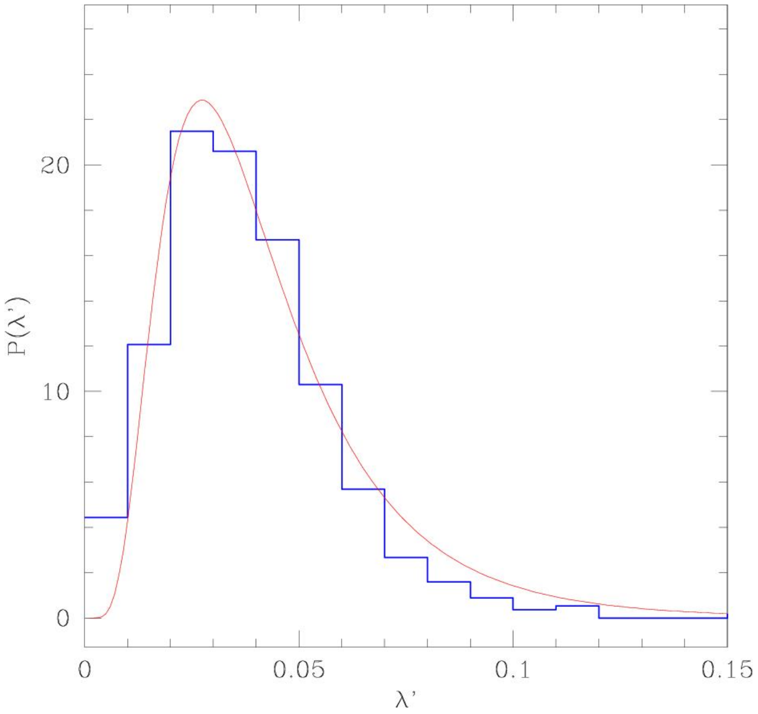

Figure 1.1: Distribution of halo spin parameter λ' (histogram), compared to a log-normal distribution about$\lambda'_0 = 0.035 \pm 0.005$ with a width $\sigma = 0.50 \pm 0.03$. (Adapted from Bullock et al., 2001).

- **Luminosity-velocity relation for spiral galaxies**: For spiral galaxies, a relation between total luminosity L and rotation velocity V has been found as $L \propto V^p$ with the wave-band parameter p (Tully & Fisher, 1977; Sakai et al., 2000).
- **The fundamental plane of elliptical galaxies**: A similar relation between central velocity dispersion σ and luminosity as $L \propto \sigma^4$. A better correlation, know as the fundamental plane, is often given in the form $R_e \propto \sigma^{1.35}\ I_e^{-0.84}$ with R_e the effective radius and I_e the surface brightness at the effective radius (e.g. Faber et al., 1989; Bender et al., 1992).

1.1.2 Secular Evolution Processes

At early times, galactic evolution was dominated by a combination of dissipative collapse (Sandage, 1990) and merging processes between galaxies. The evolution timescale was short, $t_{dyn} \simeq (1/G\rho)^{1/2}$, where ρ is the mean density and G the gravitational constant. After this violent phase, internal secular processes became increasingly dominant and are very important for processes in galaxies at present time and in the distant future. These processes are defined to be slow and operate at timescales presumably much longer than t_{dyn}. Some secular processes, such as disk heating via stellar encounters with molecular clouds, are likely important, whereas star-star relaxation is too slow to be important in most galaxy (Kormendy & Kennicutt, 2004). Therefore, relevant secular processes generally involve the interactions of individual stars or gas clouds with collective phenomena such as bars, oval distortions, spiral structure, and triaxial dark matter halos.

Although secular evolution is suggested to play a major role in barred and oval galaxies, it is not confined to galaxies with these features alone. Bars can self-destruct by building up the central mass concentration through infall of gas (Combes, 2001). Hence secular evolution may have happened even if no bar is seen at present. Also global spiral structure contribute to the evolution of galaxies, although more slowly than bars. These processes are manifestations of very general dynamical principles. In particular, bars and spiral arms are suggested to effectively redistribute angular momentum within a galaxy's disk and they will be discussed in the following.

Angular Momentum Transport in Disks

To minimize its total energy, a galaxy tends to concentrate its mass towards the center, and to transfer its angular momentum outwards (Lynden-Bell & Kalnajs, 1972). One important driver for angular momentum transfer are spiral density waves. The spiral structure produces a spiral gravitational field, which exerts torques and transfer angular momentum from one part of the disk to another. In the case of trailing arms (the most frequent form in spiral galaxies), the spirals exert a positive gravitational torque on the outer parts of the disk, and thereby transport angular momentum from the inner to the outer disk, while leading arms transport angular momentum inward. This is an example for secular evolution in galaxies which is generally characterized by slow changes due to internal dynamical processes. Other possible examples of secular evolution include gas inflow resulting from dissipation in the interstellar gas, the excitation of random velocities of disk stars by the gravitational fields from molecular clouds or spiral arms, the conversion of the inner parts of disks into bulge-like structures, and the slowing of bar pattern speeds due to dynamical friction from the dark halo (for an overview see Binney & Tremaine, 2008). Also bars grow by transferring angular momentum to the outer disk, thereby driving spiral structure (Lynden-Bell, 1979; Sellwood & Wilkinson, 1993; Athanassoula, 2003). Several simulation studies have explored the response of gas to a bar (e.g. Athanassoula, 1992). The important consequence of these works is that shocks generate gas flows toward the center.

The Importance of Dynamical Resonances

To explain bar- or spiral driven evolution processes, it is necessary to understand orbital resonances as described briefly in the following. An in-depth review is provided by Sellwood & Wilkinson (1993) and a detailed description can be found in Binney & Tremaine (2008). Seen from an inertial-frame, an orbit in a galactic disk is an unclosed rosette with a non-integral number of radial oscillations for every orbital period around the center. In a reference frame that rotates at the average angular velocity of the star Ω_0, the mean position of the star is fixed, and due to its radial oscillation the star moves in a small ellipse around that mean position. Any global density pattern such as a bar that rotates at the angular velocity Ω_P will constantly exert a gravitational attraction on the star in essentially the same way and will perturb its orbit. Corotation occurs at locations where the density pattern velocity Ω_P is equal to the angular velocity Ω_0. The corotation resonance is the strongest of a series of resonances in which the pattern repeatedly sees the star in the same way. For example, another rotating frame in which the star executes two radial oscillations for each circuit around the center is called the Inner Lindblad resonance (ILR, named after the pioneering footsteps by Lindblad, 1959). It occurs when the pattern speed of the bar is $\Omega_P = \Omega_0 - \kappa/2$, where κ is the frequency of radial oscillation. The limit of small radial oscillations is called the epicyclic approximation. Then κ can be expressed as $\kappa^2 = (2V/r)(V/r + dV/dr)$, where $V(r)$ is the circular-orbit rotation curve. Similar to the ILR is the Outer Lindblad resonance (OLR), except that the star drifts here backward with respect to the rotating frame while it executes two radial oscillations for each orbital period: $\Omega_P = \Omega_0 + \kappa/2$.

Resonances and periodic orbits are important for several reasons, such as to understand how a self-consistent bar is constructed. Periodic orbits in the bar rotating frame are orbits that close on themselves after one or more turns. These orbits define families of trapped orbits, which are non-periodic, but oscillate about one periodic orbit, with a similar shape. The various families are (Contopoulos & Grosbol, 1989):

- The x_1 family of periodic orbits is the main family that supports the bar. Orbits are elongated parallel to the bar, within corotation. This orbits can be similar to simple ellipses, and with energy increasing, they can form a cusp, and even two loops at the extremities.
- The x_2 family exists only between the two inner ILRs, if present. They are more round, and elongated perpendicular to the bar. Even when two ILRs are present, the existence of the x_2 family is not certain. In case the bar is strong enough, the x_2 orbits disappear, which also depends on the bar's pattern speed.
- Outside corotation, the orbits (which close after one turn and two epicycles) do run in the retrograde sense in the rotating frame; they are perpendicular to the bar inside the outer OLR, and parallel to the bar slightly outside the OLR.

Bars consist largely of x_1 orbits and similar, nonperiodic orbits that are trapped around them by the bar's self-gravity. Between corotation and OLR, the principal orbits are elongated perpendicular to the bar, and outside OLR, they are again oriented parallel to the bar. Near corotation is the Ultra-Harmonic resonance (UHR) in which a star executes 4 radial oscillations for every revolution: $\Omega_P = \Omega_0 - \kappa/4$. An important consequence is that gas clouds moving on such orbits must collide near resonances and gas density increases. Consequently, gas tends to build up in rings and to form stars at these resonances. Simulations (e.g. Athanassoula, 1992) have shown that the gas flow of bars is intimately linked to the properties of the periodic orbits and that shocks may form which force the gas towards the center (see Fig. 1.2).

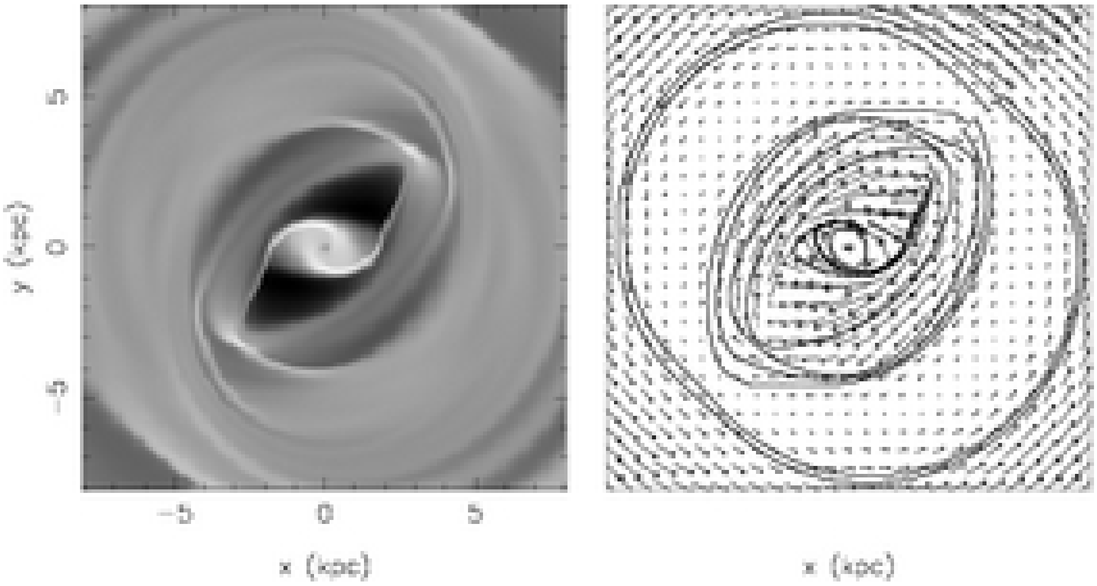

Figure 1.2: Simulation of the gas response to a bar model. The left panel shows the gas desnity and the right panel the gas flow lines and the velocity vectors in a frame of reference in which the bar is at rest. (Adapted from Athanassoula, 2000).

Bar-Driven Evolution

Several theoretical calculations (Lynden-Bell, 1979; Sellwood & Wilkinson, 1993; Binney & Tremaine, 2008) and simulations (e.g. Sparke & Sellwood, 1987; Athanassoula, 2003) have shown that bars grow by transferring angular momentum to the outer disk, thereby driving spiral structure. As a result, stellar orbits in the bar become more elongated, the bar grows in amplitude, and its pattern speed slows down. The response of the gas to a bar is that outside corotation, gas is driven outward by the angular momentum transfer from bar to disk that makes the bar grow and gas accumulates at an outer ring near OLR. Inside corotation, gas falls toward the center and accumulates at an inner ring near the ILR and/or UHR. Thus, bars are in general expected to rearrange disk gas to make outer rings, inner rings, and central mass concentrations. In general, gas accelerates where it approaches and decelerates where it leaves the potential minimum of the bar. Hence it tends to pile up near the major axis of the bar. As incoming gas overshoots a little before it plows into the departing gas, the shocks are nearly radial but offset from the major axis of the bar in the forward (rotation) direction. Hence the gas loses energy as it shocks and sinks toward the center (for a review secular evolution and bars see Kormendy & Kennicutt, 2004).

Bars can also destroy themselves if they drive gas inward and build up too large a central mass concentration (Berentzen et al., 1998; Shen & Sellwood, 2004). In these simulations orbits become chaotic and cease to support the bar. A possible explanation is that inward gas transport increases the circular-orbit velocity and the associated epicyclic frequency κ of radial oscillations near the center. As a result, $\Omega_0 - \kappa/2$ increases more rapidly toward small radii and it is less nearly constant. Thus, it is more difficult for self-gravity to pursue x_1 orbits. Furthermore, while $\Omega_0 - \kappa/2$ increases, the bar slows down because it transfers angular momentum to the outer disk. As the radius of the ILR grows, the radial range of the x_2 orbits that are perpendicular to the bar also grows. The amount of central mass concentration varies in different studies and the critical value is still under debate. In some simulations, a central mass of 2% of the disk already weakens the bar (Berentzen et al., 1998). Further, supermassive black holes are suggested to destroy bars even more easily than diffuse masses with radii of several hundred parsec like stellar bulges or dense molecular clouds (Shen & Sellwood, 2004).

Spiral-Driven Evolution

Nowadays, spiral structure is described as a density wave, a periodic compression and rarefaction of the disk surface density that propagates through the disk. Further, spiral structure seems to be long-lasting, so that the spiral pattern remains stationary over many orbital periods. These concepts led to the Lin-Shu hypothesis suggesting that spiral structure is a stationary density wave (Lin & Shu, 1966). In general, stars and gas orbit faster around the center than the spiral arms, so they catch up to the arms from behind and pass through them. Thus, young and bright stars are concentrated in the arms, because star formation is triggered when gas passes through the arms and gets compressed. Similar to bars, the gas accelerates as it approaches the arms and decelerates as it leaves them. Shocks form where the gas piles up. Also in this case gas loses energy at the shocks and sinks toward the center. The effect is weaker than in barred galaxies, because the pitch angles of spiral arms are much smaller than 60°.

Possible Effects of Magnetism on Disk Evolution

Another physical effect which was suggested to drive secular evolution processes, in particular spiral structure, is the interaction between the interstellar gas and the magnetic field. Typical magnetic fields in galaxies have a strength of ∼0.5 nT and are not strong enough to play a role in large-scale spirals (Binney & Tremaine, 2008). However, magnetic fields may facilitate the formation of smaller features such as spurs or nuclear rings (Beck et al., 1999).

1.1.3 Relations between Central Black Holes and their Host Galaxies

Dynamical studies of the centers of galaxies reveal that they often contain within a few pc the central mass concentration of $10^6 - 10^9$ $M_\odot$ which are generally associated with Super Massive Black Hole (SMBH). One of the best studied SMBH is the mass concentration at the center of our Galaxy with a mass of $(3.7 \pm 0.2) \cdot 10^6$ $M_\odot$ constrained to be within a radius less than 0.001 pc (Genzel et al., 2000; Ghez et al., 2005). Nowadays, it is generally accepted that most galaxies contain a SMBH at their centers. The main reasons to believe that these massive objects are SMBHs are 1) that no long-lived system or object other than a black hole can be so massive and highly concentrated, and 2) that no other physical mechanism as accretion onto a black hole is known to generate the high luminosities of quasars (10^{13} $L_\odot$).

The mass of the central black holes are typically between 0.001-0.002 of the total mass of the stars in the bulge of the host galaxy (Häring & Rix, 2004). A similar correlation exists between the black hole mass $M_\bullet$ and the stellar velocity dispersion σ_b of the bulge stars with $M_\bullet = 1.2(\pm 0.2) \cdot 10^8\ \mathrm{M}_\odot (\sigma_b / 200\ \mathrm{km\ s}^{-1})^{3.75(\pm 0.3)}$ over almost 3 orders of magnitude in $M_\bullet$ (e.g. Gebhardt et al., 2000). These two findings imply that the central black hole mass is constrained by and closely related to properties of the host galaxy's bulge which suggest a co-evolution of the central black hole and the galaxy itself. The massive black holes are very likely formed at the centers of galaxies and grow by subsequent gas accretion and merging with central BHs of other galaxies. Semi-analytic models, based on the Press-Schechter formalism, and a CDM hierarchical scenario of galaxy formation (Kauffmann & Haehnelt, 2000), can reproduce partially the essential observations: the proportionality relation between the bulge and black hole mass in every galaxy, the amount of energy radiated over the Hubble time due to accretion onto massive black holes, the past evolution of AGN activity. The assumptions are that the black holes grow through galaxy merging, both because of the merger of the pre-existing black holes, and due to infall of gas to the center during the merger event, that can fuel the merged BH. It is also assumed that the amount of cold gas in galaxies decrease with time. This implies that the fueling will also be less efficient with time which may contribute to the observed decline of AGN activity. Besides that, the gas accretion time-scale is proportional to the dynamical time-scale, which is shorter at high redshift. The quasars convert mass to energy at a fixed efficiency, and radiate close to the

Eddington limit (see § 1.2.2).

1.2 Active Galactic Nuclei (AGN)

In general the term Active Galactic Nucleus (AGN) refers to the existence of an high energetic phenomenon in the nucleus, or central region of a galaxy. Several classes of AGN exist ranging from low-luminosity AGN (LLAGN) to the most luminous ones, namely Quasars. While for a typical LLAGN, e.g. a Seyfert galaxy, the total energy emitted by the nuclear source at visible wavelengths is comparable to the energy emitted by all of the stars in the galaxy (i.e., $\sim 10^{11}$ $L_\odot$), the nuclear source of a typical Quasar can be more than 100 times brighter than the stars in the host galaxy.

1.2.1 The Origin of Nuclear Activity

AGN produce enormous luminosities (up to 10^{13} $L_\odot$) in extremely compact volumes and their luminosity can have large variations on time scales from years to hours. The combination of high luminosity and short variability time scale implies that the power source of AGN is more efficient in terms of energy release per unit mass than ordinary stellar processes (Fabian, 1979). Thus, the most plausible power source for AGN is accretion onto a massive black hole (SMBH). In fact, the accretion of matter onto a black hole can yield high radiative efficiencies (for a review see Rees, 1984). Nowadays, the basic AGN consists of a central SMBH, surrounded by an accretion disk, or more generally optically thick plasma (for a review see Ho, 2008). In this accretion disk, the material can lose its angular momentum through friction and fall onto the SMBH, releasing the gravitational energy in the form of radiation or jets. Clouds of line-emitting gas move at high velocity around this complex core and are in turn surrounded by an obscuring torus or warped disk of gas and dust. Yet a direct evidence of the SMBH surrounded by an accretion disk is still not possible with the current observational facilities, but many observational properties of the central regions of AGN support this presumed mechanism.

1.2.2 Eddington Luminosity and Mass

The Eddington luminosity (or Eddington limit) is defined as the point where the gravitational force inwards is equal the continuum radiation force outwards. The hydrostastatic equilibrum is given for a spherical distribution as

$$\frac{\mathrm{d}P}{\mathrm{d}r} = -\frac{GM\rho}{r^2} \tag{1.2}$$

where M is the mass of the central object and ρ the density. As the outward force of radiation pressure P is defined as

$$\frac{\mathrm{d}P}{\mathrm{d}r} = -\frac{\kappa\rho}{c} = -\frac{\sigma_T \rho L}{m_p c 4\pi r^2}, \tag{1.3}$$

the Eddington luminosity is given as

$$L_{Edd} = \frac{4\pi G M m_p c}{\sigma_T} \tag{1.4}$$

with the mass of the proton m_p and the Thomson cross-section σ_T for the electron. Similarly one can define the Eddington mass flow rate

$$\dot{M}_{Edd} \approx \frac{L_{Edd}}{\epsilon c^2} \tag{1.5}$$

with a mass-to-energy conversion efficiency ϵ for a thin disk (Shakura & Syunyaev, 1973) of ~10%.

For some AGN an accretion at super-Eddington rates has been observed (see Collin et al., 2002). A possible explanation might be that the BH masses, which are usually derived using the Reverberation method, are strongly underestimated. Reverberation mapping is a major tool for determining the mass of central black holes (BHs) of distant AGN and is based on correlated variations of the lines and continuum fluxes giving the size of the BLR (see § 1.2.4), while the measure of their Full Widths at Half Maximum (FWHM) provides the bulk velocity (for a review see Peterson, 2001). Other possible explanations for super-Eddington rates in these objects are that accretion discs are completely non-standard, or that the optical luminosity is not produced directly by the gravitational release of energy, but by another mechanism, so that super-Eddington rates are not required (for an overview see Collin et al., 2002).

1.2.3 Characteristic Radii of Black Holes

To answer on what scales the central engine of an AGN is acting and how they might be related to possible fueling mechanisms, one has to consider the following dynamical scales. For all calculations a BH mass of $1 \cdot 10^8$ $\mathrm{M}_\odot$ is used.

- The **accretion radius** R_a is the radius out to which the black hole with the mass $M_\bullet$ dominates the dynamics,

$$R_a = \frac{GM_\bullet}{\sigma^2} \sim 10 \text{ pc } (\frac{200\text{km/s}}{\sigma})^2 \, (\frac{10^8 \, M_\odot}{M_\bullet}) \tag{1.6}$$

  with the velocity dispersion σ of the stellar component and G the gravitational constant. That implies that other mechanisms than the gravitational force of the central

BH must be responsible for the transportation of the gas to the central 10 pc. Note that the typical BH masses for late-type galaxies can be an order below of 10^8 M$_\odot$, so that the radius above can likely decrease to 1 pc.

- The **tidal radius** R_t is the radius out to which a star can be disrupted by the tidal forces of the BH, $R_t \sim R_{star}(M_\bullet/M_{star})^{1/3} \sim 2 \cdot 10^{-5}$ pc $\rho_{star}^{-1/3}$ where ρ_{star} is the average density of a solar mass star.
- The **horizon radius** R_h of the black hole under which matter cannot escape, $R_h \sim 2GM_\bullet/c^2 \sim 10^{-5}$ pc.

As the black hole horizon grows faster with $M_\bullet$ than the tidal radius, the star disruption occurs inside the BH for BH masses $\gtrsim 3 \cdot 10^8$ M$_\odot$, and thus, no release of gas or AGN activity due to star disruption can occur above this limit (Hills, 1975), but the black hole grows even more rapidly. The required time to reach this critical mass is limited by the the Eddington luminosity (above which the radiation pressure of the AGN prevents the material to fall in). Given the critical mass of $3 \cdot 10^8$ M$_\odot$ the maximum AGN luminosity due to star dsirution is 10^{13}L$_\odot$ which is close to the peak luminosity of Quasars. Note that the AGN can still be very luminous above this peak luminosity through accretion of surrounding gas and dust instead of star disruption.

1.2.4 Emission Lines

The properties of the AGN emission lines provide valuable information about the physical condition of the ionized gas in different regions of the AGN, such as the temperature, density and degree of ionization. AGN emission lines can be separated in two types.

Broad Line Region

Luminous, unobscured AGNs distinguish themselves unambiguously by their characteristic broad permitted lines. LINERs, like Seyferts and quasars have detectable broad emission lines and can be divided into "type 1" and "type 2" sources according to the presence or absence of broad-line emission, respectively. The typical velocity with for Broad Line Regions (BLR) range from a few 1000 km s^{-1} up to 10000 km s^{-1} at full width at half maximum (FWHM). The most important broad lines are the hydrogen lines (e.g. Lyα, Hβ, Hα), the helium lines (e.g. HeII) and the carbon lines (e.g. CIV). The broad lines are assumed to be emitted by high velocity clouds in regions close to the SMBH and are generally spatially unresolved. Thus, the broad widths of these lines can be explained by the Doppler effect due to the motions of each line-emitting clouds. The strength of the broad emission lines varies with time which can be correlated with the fluctuations of the AGN continuum. The time delay between the continuum and broad line variations can be related to the size of the BLR, which typically extends from 0.01-0.1 pc from the BH.

Narrow Line Region

Narrow lines are emitted in spatially extended regions called the narrow line regions (NLR) and have typically a FWHM less than 1000 km s^{-1}. Narrow lines are not only permitted emission lines (as listed for the Broad lines above), but also [OII], [OIII], [NII], or [OI] can be detected. The relative strength of narrow emission lines are used to differentiate high and low ionisation processes using empirical diagnostic diagrams (see next section). NLR can be generally observed as elongated shapes, known as ionisation cones which can extend from 0.5 pc up to a few kpc. Inside the cone, emission line ratios are characteristic of highly ionised gas, while outside the cone, the gas is likely ionised by stars.

1.2.5 Low-Luminosity AGN

Most AGNs spend their lives in a low state, such that the bulk of the population has relatively modest luminosities. Over the past several decades, this attribute has led to considerable controversy regarding the physical origin of low-luminosity AGNs (LLAGNs). Emission-line AGNs can be divided into Seyferts and low-ionization narrow emission-line regions (LINERs). The majority of AGN are LINERs with nuclear optical spectra that are dominated by emission lines of low-ionization species such as [OI] λ6300, [OII] λ3726,9 and [SII] λ6717 (Ho et al., 1997). Up to approximately one-third of all galaxies have nuclear spectra typical of LINERs (Ho et al., 1997). The main difference between Seyferts and LINERs is thought to be the accretion rate, which explains why LINERs have lower AGN luminosities than Seyfert galaxies. Although Seyferts and LINERs are basically powered by the same mechanism, i.e. accretion onto a SMBH, the Seyfert/LINER distribution is bimodal (Groves et al., 2006), implying different accretion mechanisms (for a general review see Ulrich et al., 1997; Combes, 2001; Netzer & Shields, 2007).

Bolometric Luminosity

To gain further insight into the physical nature of nearby AGNs, it is also important to examine the bolometric luminosities of the AGNs. As AGNs emit a very broad spectrum, their bolometric luminosities should be ideally measured directly from their full spectral energy distributions (SEDs). In practice, however, complete SEDs are not readily available for most AGNs, and one commonly estimates the bolometric luminosity by applying bolometric corrections derived from a set of well-observed calibrators. What is available, by selection, are nuclear emission-line fluxes, and their upper limits. Whereas LINERs have a median $L_{bol} \sim 2 \cdot 10^{41}$ erg s^{-1}, Seyfert nuclei are typically an order of magnitude more luminous ($L_{bol} \sim 2 \cdot 10^{42}$ erg s^{-1}). Also in relation to their Eddington luminosity L_{bol}/L_{Edd}, LINERs have smaller relative luminosities (median L_{bol}/L_{Edd} $3 \cdot 10^{-5}$) than Seyferts (median L_{bol}/L_{Edd} $4 \cdot 10^{-4}$). An overview about the luminosities of LLAGN is presented in Fig. 1.3

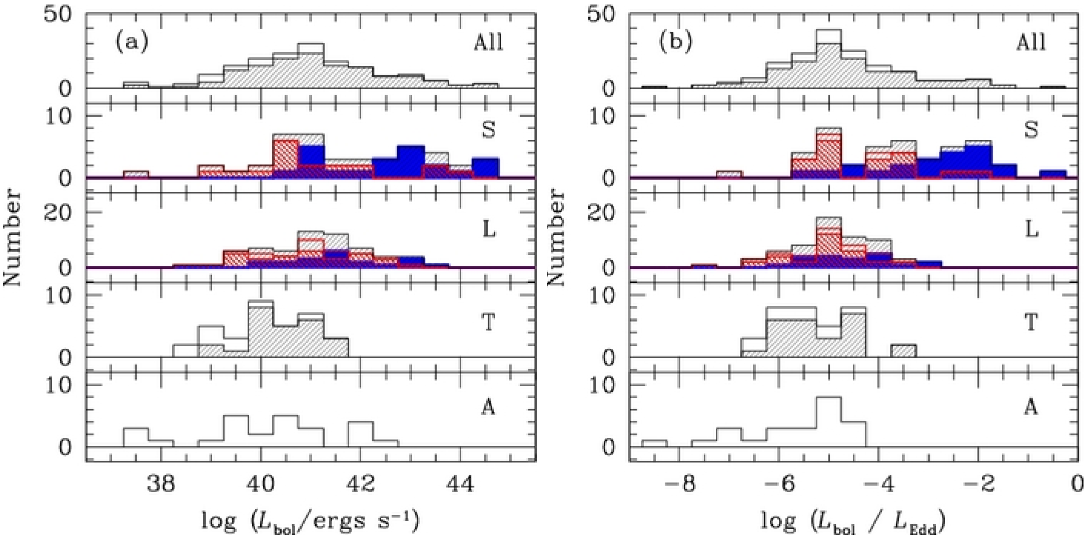

Figure 1.3: Distribution of (a) bolometric luminosity, L_{bol}, and (b) ratio of bolometric luminosity to the Eddington luminosity. L_{bol} is based on the X-ray (2-10 keV) luminosity. The shaded and open histograms denote detections and upper limits, respectively; type 1 objects are plotted in blue, type 2 objects in red. (Adapted from Ho, 2008).

Spectral Classification

LLAGNs can be identified by a variety of methods. Most LLAGN surveys rely on some aspects of the distinctive LLAGN spectrum, such as the presence of strong or broad emission lines, an unusually blue continuum, or strong radio or X-ray emission (Ho, 2008). The most widely used system of spectral classification of emission-line nuclei is based on the Baldwin, Phillips & Terlevich (1981, hereafter BPT) empirical diagnostic diagrams to classify the dominant energy source in emission-line galaxies. These diagrams are based on the four optical line ratios of [OI]/Hα, [SII]/Hα, [NII]/Hα, and [OIII]/Hβ. Kewley et al. (2001) used a combination of stellar population synthesis models and detailed self-consistent photoionization models to create a theoretical ”maximum starburst line” on the the BPT diagrams. Galaxies lying above this line are likely to be dominated by an AGN. Further, a modification of this scheme by Kauffmann et al. (2003) includes an empirical line dividing pure star-forming galaxies from Seyfert-HII composite objects whose spectra contain significant contributions from both AGN and star formation. A study by Kewley et al. (2006) based on a large SDSS sample of mission-line galaxies confirmed that LINERs form clearly separated branches on the standard optical diagnostic diagrams. Fig. 1.4 shows the empirical classification scheme proposed by Kewley et al. (2006) (red solid line) which separates star-forming galaxies, composite AGN-H II galaxies, Seyferts and LINERs.

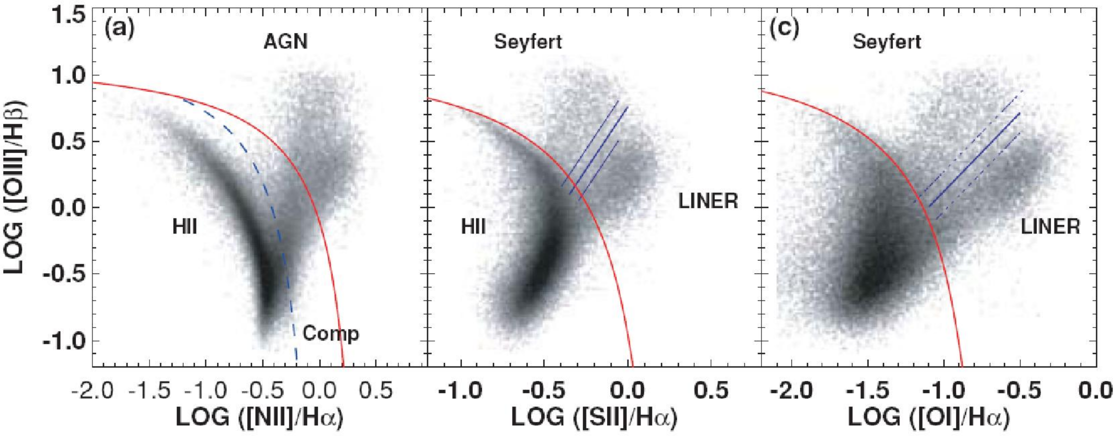

Figure 1.4: The three BPT diagrams show the empirical classification scheme proposed by Kewley et al. (2006) based on a large SDSS sample of mission-line galaxies . The Kewley et al. (2001) extreme starburst classification line (red solid line), Kauffmann et al. (2003) pure star formation line (blue dashed line), and the Kewley et al. (2006) Seyfert-LINER line (blue solid line) separate galaxies into HII-region like, composite AGN-HII galaxies, Seyferts and LINERs. (Adapted from Kewley et al., 2006).

Relations between Nuclear Activity and Host Galaxy Properties

The host galaxies of Seyferts, LINERs, and transition objects show a remarkable degree of homogeneity in their large-scale properties. All three classes seem to have identical total luminosities, bulge luminosities, sizes, and neutral gas content (Ho, 2008). However, a study of type-2 AGN based on SDSS data revealed that LINERs seem in general to be hosted by older, more massive, less dusty galaxies with higher stellar velocity dispersions and lower nuclear [OIII] luminosities than Seyfert galaxies (Kewley et al., 2006). Besides, first results of a detailed study of HI gas properties for active and non-active disk galaxies indicate possible relationships between Seyfert activity and HI properties (Mundell et al., 2007). But also for the central kiloparsec of galaxies, recent spectroscopic studies of the ionized gas show evidence for kinematic perturbations linked with Seyfert galaxies at small radii (Dumas et al., 2007). However, despite numerous studies in this field of research, the origin of their differences (e.g. different stages in evolution) is still under debate.

1.2.6 AGN Fueling Scenarios

At first we should consider why is there a problem in fueling AGNs? To estimate quantitatively the fueling problem, one has to consider the typical luminosity and power of an active nucleus that can be of the order of 10^{46} erg s^{-1} (typical quasar). Assuming a mass-to-energy conversion efficiency ϵ for a thin disk (Shakura & Syunyaev, 1973) of $\sim$10% ($L = dM/dt \cdot c^2 \cdot \epsilon$), the mass accretion rate dM/dt is $\sim$1.7 M$_\odot$ yr^{-1}. If the duty cycle of the AGN is of the order of 10^7 yr, then a total mass of up to $2 \cdot 10^7$ M$_\odot$ has to be transported to the BH. The mass accretion rate is commonly parametrized in terms of the Eddington rate as the dimensionless accretion rate $\dot{m} \equiv \dot{M}/\dot{M}_{Edd}$, similarly the bolometric luminosity can be expressed as Eddington ratio $l \equiv L_{bol}/L_{Edd}$.

With regard to LLAGN, the most luminous low-luminosity AGN, Seyfert 1s, appear to have central SMBH with $M_\bullet \approx 10^7$ M$_\odot$ (Ferrarese et al., 2001) and $l = 0.1$, which corresponds to accretion at $\dot{m} = 0.1$ or $\dot{M} = 0.02$ M$_\odot$ yr^{-1}. More typical Seyferts ($\sim$ 10% of the luminous galaxy population; Ho, 2008) likely accrete with $\dot{m} = 0.01$, while LINERs (30% of the luminous galaxy population) have accretion rates of $\dot{m} = 10^{-2}$ - 10^{-4} based on estimates of l (Ho, 1999; Martini, 2004). For example that all luminous galaxies go through periodic episodes as AGN, then over a time period of 10^8 yr, a 10^7 M$_\odot$ BH will appear as a Seyfert galaxy for a total of $\sim 10^7$ yr and accrete on order of $\sim 10^3$ M$_\odot$, then appear as a LINER for $3 \cdot 10^7$ yr and accrete $\sim 10^3$ M$_\odot$, and be inactive for another $6 \cdot 10^7$ yr.

As the fueling material (e.g. gas and dust) is distributed in a rotating disk and extends out to kpc scales, the problem of gas transport to the center is basically a problem of angular momentum removal from the gas. One possibility to lose angular momentum can be viscous forces. However, normal viscosity is not efficient, due to the very low density of the gas. Even with macroturbulent viscosity, the time-scales are longer than the Hubble time at large radii, and could be effective only inside the central 1 kpc (Lynden-Bell & Kalnajs, 1972). Another possibility might be that stars themselves provide gas to the nucleus. This can occur through their loss of mass in case a local stellar cluster is present which is dense and compact enough. However, the mass loss rate derived from normal stellar evolution is orders of magnitude below the required rate of a few percent of M$_\odot$ yr^{-1}. Only if a massive stellar cluster has just formed in a starburst, the contribution might be significant (Norman & Scoville, 1988). But still the angular momentum problem has to be solved for the large scale which can only happen through large-scale dynamical processes.

It is well established that asymmetries in galactic potentials, such as large-scale bars, transport gas very efficiently inward (e.g., Combes , 2003; Jogee , 2004), and that bars can fuel powerful starbursts (e.g., Jogee et al., 2005). Gravitational torques due to a bar can transport the gas only to the ILR where it is stalled in a nuclear ring. Through subsequent cloud collision the gas could lose energy and would stream in elliptical trajectories at lower radii. The problem is, that searches for mechanisms of low-luminosity AGN fueling have not found any strong correlation between the presence of morphological features, e.g. bars, and AGN activity (see for an overview Martini, 2004). One explanation might be that smaller-scale phenomena are responsible for AGN fueling. Thus, only observations with very high spatial resolution provide the possibility to find correlations between AGN fueling and dynamical perturbations. Martini & Pogge (1999) suggested that nuclear spiral dust lanes may be the channels by which gas from the host galaxy disks is being fed into the central engines. But also a high spatial resolution study with the Hubble Space Telescope (HST) of the circumnuclear region (on 100 pc scales) has still not found a significant differences between AGN and control samples for late-type galaxies, while early-type AGN galaxies show significant dust lanes compared to those without an AGN (Martini et al., 2003; Simões Lopes et al., 2007). However, it is also possible that multiple fueling mechanisms act together. In this case more than one mechanism is important (e.g. bars and interactions), and thus, the significance of a correlation between any one mechanism and AGN presence will be diluted by AGN fueled by other mechanisms.

Further, also the current classifications for fueling mechanisms might be too broad: Observational work has already shown that there is a wide dispersion in the detailed properties of mechanisms proposed for fueling, such as the fact that not all barred galaxies possess offset shocks that connect to grand-design nuclear spiral structure (Martini, 2004). In case only certain subclasses of a candidate fueling mechanism actually remove angular momentum (e.g. only certain types of bars), then the correlation between this broader class and AGN will be diluted. Another possibility is that a hierarchy of mechanisms combine to transport the gas from the outer disk (kpc scales) down to the center (pc scales). As these various mechanisms are working at different spatial scales, also the mass accretion involves different time scales (Shlosman et al., 1990; Combes , 2003; Wada & Koda, 2004; Martini, 2004). A scenario of a possible AGN time-evolution is shown in Fig. 1.5. This time-scale conspiracy could explain the lack of any correlation between the presence of non-axisymmetric perturbations and the onset of activity (Wada & Koda, 2004; García-Burillo et al., 2005).

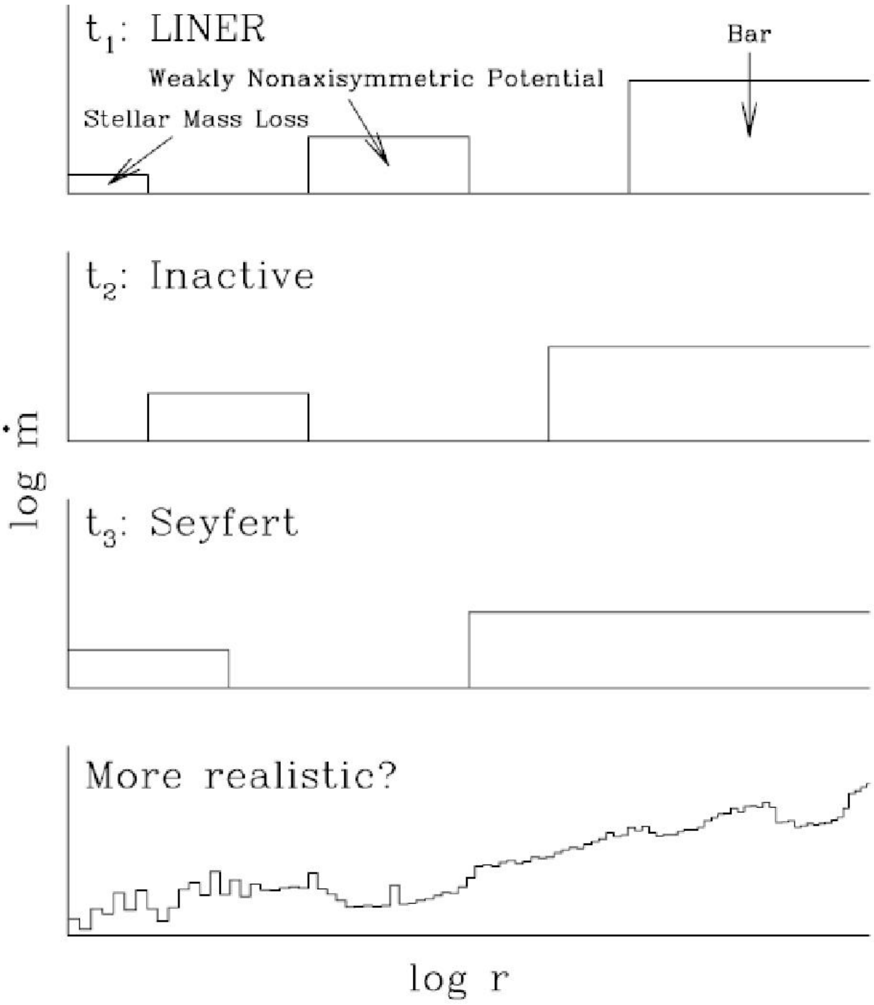

Figure 1.5: Illustration of the possible importance of time evolution in AGN fueling. The top three panels present snapshots of the mass accretion rate as a function of radius at three separate times. The presence of fueling mechanisms on larger spatial scales might be decoupled from the presence of an AGN if the AGN phase is comparable to or shorter than the inflow timescale due to the relevant fueling mechanism. In practice, the inflow rate for an actual galaxy is likely more complex as it is illustrated in the bottom panel. (Adapted from Martini, 2004).

1.3 Gas Observations with Radio Interferometry

Determining the neutral gas distribution and kinematics is necessary to establish if characteristics of the nuclear dynamics, and hence the nuclear activity, depend on overall host galaxy properties. To probe the neutral gas distribution and kinematics, high spatial and spectral resolution observations are required. Radio interferometric observations are ideally suited to trace the gas component on all spatial and kinematical scales as it is based on 3D spectroscopy. An excellent overview about the technique and underlying concept of radio interferometry can be found in, e.g., Thompson et al. (2001).

1.3.1 Studying the Kinematics of Galaxies

Kinematic measurements are the major tool for determining the distribution of the mass in galaxies. They provide fundamental information for understanding the dynamics, evolution, and formation of spiral galaxies. In particular, rotation curves have been widely used to estimate the dynamical mass and the dark matter component of galaxies (e.g. Rubin et al., 1985). The reconstruction of kinematic properties of galaxies relies on a suitable interpretation of observed line shifts and linewidths induced by the Doppler effect.

In this study we use in particular CO and HI interferometric observations. Besides, several observing techniques are also available for determining rotation curves and velocity fields for the ionized gas and stars (e.g. Hα). Traditional long slit spectra are still valuable for deducing the rotation curve of a galaxy from emission lines, but methods that return the entire velocity field, such as Fabry-Perot spectrographs or integral field instruments can provide more velocity information but are more complex. Single-dish observations in the millimeter (e.g. CO line) and centimeter (HI line) range have angular resolutions limited from hundreds to tens of arcseconds due to the aperture diffraction limit. However, interferometric observations have achieved angular resolutions of a few arcsec (HI) and even sub-arcsecond resolution for millimeter lines (e.g. Schinnerer et al., 2000), comparable to current optical measurements. Another advantage of CO and HI spectroscopy is their high velocity resolution of a few km s^{-1}.

1.3.2 The HI Line

An important tracer for the gaseous distribution and kinematics of galaxies is atomic hydrogen with its 21 cm line emission. This line corresponds to 1420 MHz and originates from the transition between the two levels of the hydrogen ground state (also known as hyperfine structure) which is split by the interaction between the electron spin and the nuclear spin.

Since the atomic gas extends in most disk galaxies much further than the optical disk, it provides an ideal tool to identify interactions and tidal features (e.g., Simkin et al., 1987; Mundell et al., 1995). The spatial distribution of atomic hydrogen is clumpy, being associated with clouds with sizes up to 100 pc, and characterized by random velocities of a few km/s with respect to streaming motions. Cloud-cloud inelastic collisions are rather frequent and make the cold medium a dissipative component. The fraction of atomic hydrogen to total mass of a galaxy is typically ∼10% for spiral galaxies (Bettoni et al., 2003).

The measurement of the HI line is also a powerful tool to obtain kinematics of spiral galaxies, in part because radial extent of the atomic gas disk is often greater (up to 3 or 4 times) than that of the visible disk. Because of its dissipative nature the atomic gas is also very sensible to small deviations from axial symmetry, and thus, a valuable tracer of barred or weak oval potentials (Mundell et al., 1999). As the gas is very sensitive to dynamical disturbances, one could expect, for example, to find a prevalence of Seyfert activity with asymmetries in the gas distribution and kinematics. Further, the HI line is ideal for the determination of rotation curves of spiral galaxies, because of the fact that atomic gas is cold, so that the mean flow motion provides an accurate direct measurement of the gradient of the mean gravitational potential. Some galaxies show signs of non-axisymmetric structure and warps, but for many galaxies the atomic gas disk is very flat, smooth, and axisymmetric. A rotation curve can be decomposed in various components of the underlying gravitational potential, mainly bulge, disk, and halo. In fact, the relevant mass-to-light ratios are not known a priori and one has to make assumptions about the possible amount of unseen matter (for an review on rotation curves see Sofue & Rubin, 2001).

1.3.3 CO Lines

The ISM in spiral galaxies is also very rich in molecules. Probably the most important source of radiation from molecular gas is that of carbon monoxide (CO), in particular, the 2.6-mm emission line of ^{12}CO, which is generally used as a tracer of the much more abundant molecule, of molecular hydrogen (H_2). The observed CO emission is usually converted into H_2 column density using a simple proportionality factor. For example, the conversion factor from CO to H_2 typical for galaxy nuclei is $X = N(H_2)/I(CO) = 2.2 \cdot 10^{20}$ cm^{-2} K^{-1} km^{-1} s (Solomon & Barrett, 1991). In general, molecular gas is more abundant at locations in galaxies with high gas densities (e.g. in the center of galaxies), while atomic hydrogen is often deficient in the inner part of the galaxy disk. This is in general explained by the phase transition from atomic to molecular gas in the neutral ISM with increasing gas density towards the center of galaxies (for an overview see Young & Scoville, 1991).

As the central few kiloparsecs of the disk are dominated by molecular gas, the molecular fraction, the ratio of the molecular-gas mass density to that of total molecular and HI masses, usually exceeds 90% (Sofue et al., 1995). The rotational transition lines of CO in the millimeter range [e.g., 115.27 GHz for ^{12}CO (J=1-0) line, 230.5 GHz for J=2-1] are valuable in studying kinematics of the inner disk and central regions of spiral galaxies. The extinction in the central dusty disks is negligible at CO wavelengths (Sofue & Rubin, 2001). CO lines are emitted from molecular clouds. The Hα, CO, and HI rotation curves agree well with each other in the intermediate region of disks of spiral galaxies (Sofue & Rubin, 2001). Small displacements between Hα and CO rotation curves can arise in the inner regions due to the extinction of the optical lines and the contamination of the star light from central bulges. Nowadays, high angular ($< 1''$) resolution observations of the molecular gas have become feasible using existing mm-interferometers such as the IRAM Plateau de Bure interferometer (PdBI) and the Combined Array for Research in Millimeter-wave Astronomy (CARMA).

2 The NUGA Project

In most Active Galactic Nuclei (AGN) the activity of the nucleus is powered by accretion of matter onto a super-massive black hole. The NUclei of GAlaxies project (NUGA) tests models for nuclear fueling and investigates the gas dynamics from the outskirts of spiral galaxies to the very center in order to understand the inflow mechanisms and their relations to AGN and galaxy evolution scenarios. This work is based on high resolution observations of emission lines from neutral atomic (HI) and molecular gas (CO) with interferometers operating at centimeter (NRAO VLA) and millimeter (IRAM PdBI) wavelengths, respectively.

2.1 Probing Nuclear Fueling

Up to now a general picture for AGN fueling is still missing: What mechanisms are responsible for the different kinds of AGN observed? How is the angular momentum removed from the fueling material? As described in §1.2.5, the presence of possible drivers for the loss of angular momentum, such as bars, and the activity of the nuclear region seems to be not correlated (see for an overview Martini, 2004). A plausible explanation is that bars are working on large scales (> 1 kpc), and thus, are not sufficient enough to bridge smaller scales to the central BH. The bar-driven loss of angular momentum mainly occurs within the corotation radius (CR), leading the gas towards the inner resonances, e.g. the inner Lindblad resonance (ILR) if present, where the torques are cancelled out. Gas accumulates at this radius, forming an inner ring in which clumps of vigorous star formation are often observed (Schwarz, 1984). Even less known are the processes responsible for fueling the innermost regions: secondary or inner bars were first proposed (Shlosman et al., 1990) to bridge the last few 100 pc, but recently other mechanisms, such as m=1 modes (Emsellem et al., 2001), warped gas disks (Schinnerer et al., 2000) and/or gas density waves (e.g. Englmaier & Shlosman, 2000; Maciejewski, 2002, 2004a,b) have been suggested to be equally or more important. Thus the long-standing problem of fuel transport in the central kpc remains unsolved.

In order to distinguish models for nuclear fueling, observations of neutral gas with high angular and velocity resolution are required. Therefore, the IRAM key project NUclei of GAlaxies (NUGA; see García-Burillo et al., 2003) was established - a spectroscopic imaging survey of gas in the centers of nearby low luminosity AGN. The main goal of the NUGA project is to determine the distribution and dynamics of molecular gas in the inner 1 kpc of the nuclei with resolutions of ∼10-50 pc, and to study systematically the different mechanisms for gas fueling of the AGN.

Most CO interferometer surveys of nearby spirals (Regan et al., 2001; Helfer et al., 2003) mapped CO (1-0) disk emission at low spatial resolution ($4''$-$7''$) and moderate sensitivity (detectability thresholds $\Sigma_{gas} > 180$ $M_\odot/pc^2$). Given the small (∼50-100 pc) linear scales involved, a study of the gas fueling in AGN requires high (∼$0.5''$-$1''$) spatial resolution. Besides, high sensitivity is required to provide a high dynamic range in the synthesized maps. Nearby AGN galaxies are ideal targets to test state-of-the-art dynamical models for the feeding and evolution of a galaxy's central region and black hole.

2.2 Observations and Sample

The NUGA project relies on a multi-wavelength approach: the sample of galaxies with D $\leq$ 54 Mpc has been defined based on the availability of high-quality optical and near-infrared (NIR) images. These images have been obtained with both ground-based telescopes and the Hubble Space Telescope (HST). The optical and NIR counterpart of NUGA provides the stellar potentials, the star formation history and the dust distributions for the sample galaxies. The NUGA core sample (García-Burillo et al., 2003) consists of 12 nearby AGN observed with the IRAM PdBI at 1mm and 3mm with maximum angular and spectral resolutions of $0.5''$ and 3.6 km s^{-1}, respectively. The NUGA supersample adds another 16 galaxies with CO data of similar quality obtained by the NUGA team with the IRAM array as part of other projects. To detect other molecules besides CO (e.g. HCN) in these galaxies additional observations using the IRAM 30m Single Dish Telescope have been undertaken for some galaxies out of the NUGA sample. This allows one to probe denser gas regions to reveal better insight into the distribution of the gas and also information about excitation conditions and abundances of the elements.

For the NUGA sample a total of about 30 nearby (mainly) Seyfert and LINER galaxies were selected based on the following criteria:

1. The ^{12}CO(1-0) emission in the nuclei of all galaxies has been detected in single dish surveys made at FCRAO, NRO and/or IRAM.
2. Galaxies are close enough to have a high spatial resolution, namely $V_{sys} < 2000$ km s^{-1} with a typical spatial scale ranging from $1''$=30pc-100pc.
3. Inclinations lie between 30° and 60° which enables the study of velocity fields and gas morphology. The declination of the galaxies is generally $> 10°$ in order to allow for round beams.

4. Optical and/or NIR high resolution images either with HST or ground-based telescopes are available for all galaxies in the sample.

2.3 Brief Summary of the Results for Nuclear Fueling

Several papers have exploited mainly on a case-by-case basis the data obtained in the context of the NUGA project. The results so far revealed surprisingly that there is no single obvious nuclear molecular gas feature connected with the nuclear activity. Instead a variety of molecular gas morphologies (Fig. 2.1) are found by the NUGA survey: One- and two-armed instabilities for NGC 4826 (García-Burillo et al., 2003), well-ordered rings and nuclear spirals for NGC 4826 (Combes et al., 2004), circumnuclear asymmetries for NGC 3718 (Krips et al., 2005), large-scale bars for NGC 4569 (Boone et al., 2007), and and a combination of nucleus, bar, spiral arms winding up into a pseudo-ring for NGC 6574 (Lindt-Krieg et al., 2008). Additional studies revealed extended radio emission in 3 out of 7 NUGA sources (Krips et al., 2007a) and a very compact ($\leq$50 pc) HCN emission detection in the nucleus of NGC 6951 (Krips et al., 2007b). Moreover, an analysis of the torques exerted by the stellar gravitational potential on the molecular gas in four galaxies found a mostly positive torque inside r<200 pc and no inflow on these scales suggesting that viscous torques may act as fueling mechanism at these scales (García-Burillo et al., 2005).

Much of this variety of morphologies could be related to timescales (García-Burillo et al., 2005). In this scenario the activity in galaxies is related to that of bar instabilities, expecting that the active phases are not necessarily coincident with the phase where the bar has its maximum strength. The resulting implication is that most AGN are probably between active accretion episodes. A potential "smoking gun" for such a scenario was found by Hunt et al. (2008) for NGC 2782 where molecular gas inside the ILR of the primary bar is transported by a second nuclear bar. This suggests that the gas is fueling the central starburst, and in a second step might fuel directly the AGN.

The results of the CO-NUGA project (Fig. 2.1) show a wealth of nuclear gas kinematics that can be broadly classified as:

(a) m=1 gravitational instabilities (one-arm spirals and lopsided disks) develop on multiple scales traceable from few 10 to 100s of parsec, and in at least one case (NGC 4826: García-Burillo et al., 2003), these modes even seem to prevent fueling of the AGN.

(b) m=2 instabilities (two-arm spiral wave) expected to form in stellar bar potentials show only small amounts of molecular gas coincident with the AGN (e.g. NGC 4569: Boone et al., 2007, and NGC 6951: Schinnerer et al., in prep.), and in some cases the distribution appears asymmetric with respect to the AGN.

(c) Rings, and stochastic spirals that are related to self-gravitating and non self-gravitating

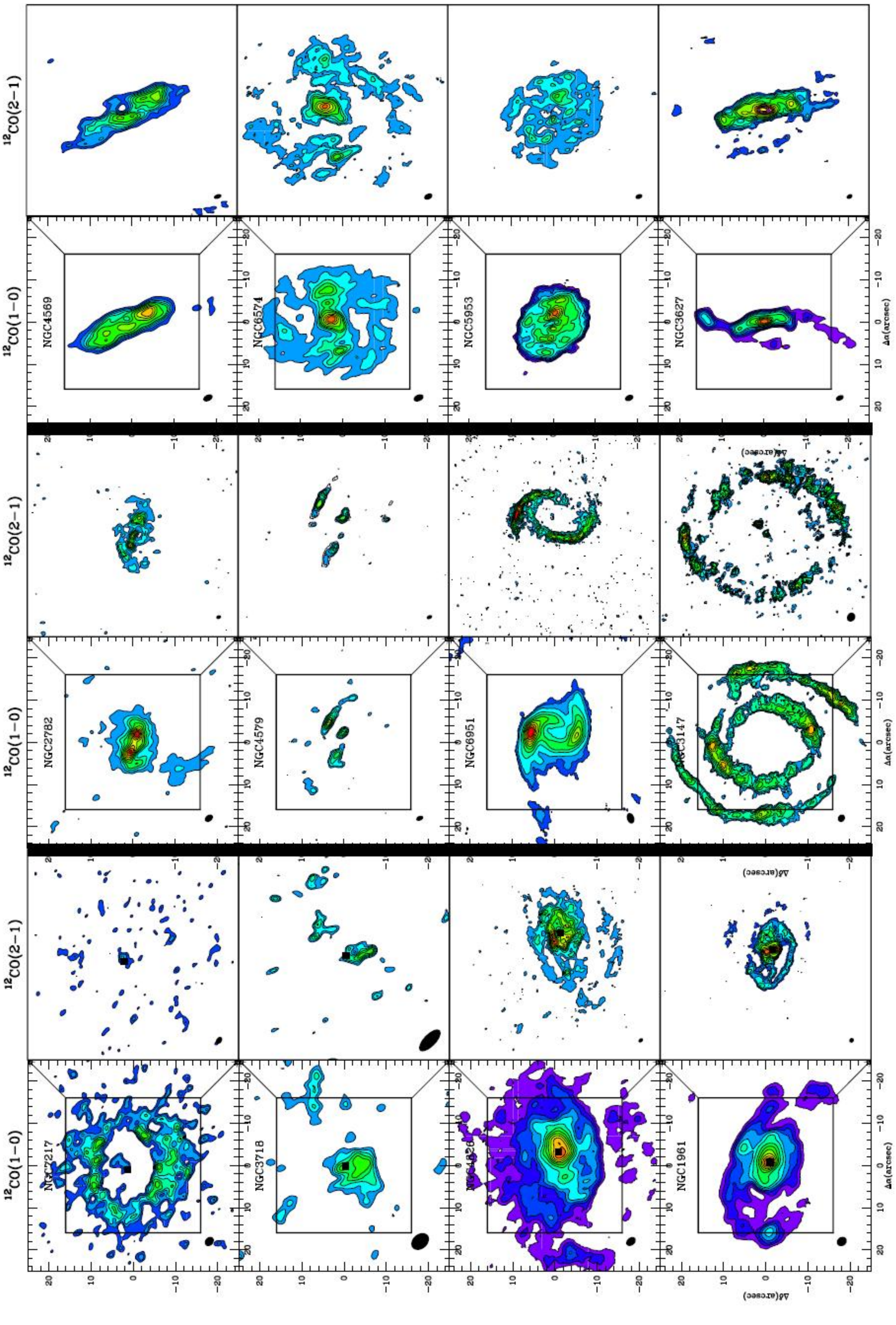

Figure 2.1: All NUGA core sample sources as observed in their ^{12}CO(1-0) (*left*) and (2-1) (*right*) lines per panel. The distribution of the molecular gas shows a wealth of dynamical modes from rings (e.g. *top left*) to m=1 modes (e.g. *second bottom left*) and m=2 modes (e.g. *top middle*). The beam is indicated in the lower left corner of each panel.

instabilities seem not to support nuclear fueling in your detailed case study of (NGC 7217: Combes et al., 2004).

(d) large scale warps that might extend into the central kiloparsec (NGC 3718: Krips et al., 2005).

2.4 The HI-NUGA Project: Gas Dynamics from the Outskirts to the Center in AGN Galaxies

2.4.1 Goals

Models of the gas flow in the disks of galaxies suggest a close link between the nuclear gas kinematics and the kinematics in the outer disk (see review by Combes , 2003). For example, large-scale stellar bars can drive inflow of molecular gas into the central kiloparsec of spiral galaxies (e.g. Shen & Sellwood, 2004). However, the link between the gas kinematics on the 100 pc to the central parsec, i.e. the black hole, is less clear. As already pointed out for our CO-NUGA results, several models have been suggested ranging from dynamical modes with m=1, m=2 to warped disks. The large wealth of nuclear dynamical modes observed in CO line emission of the NUGA sources is adding to this confusing view (see Fig. 2.1). In order to identify the main driving mechanism(s) for nuclear fueling it is essential to connect the observed nuclear kinematics to the observed kinematics of the large-scale disk (see for example the NUGA source NGC 6951 in Fig. 2.2).

Therefore the HI-NUGA project focuses on the following:

- How is nuclear activity related to the gas properties in the outer disk of galaxies? To explain the diverse range of nuclear activity, a possible correlations between the HI properties (e.g. atomic gas content, morphology, dispersion) and the type of nuclear activity (Seyfert, LINER, starburst) is expected. For example, one might aspect a prevalence of Seyfert2 activity with asymmetries in the gas distribution and kinematics. Further, a larger gas fraction for Seyferts than for normal galaxies was suggested by Hunt et al. (1999). Another important trigger mechanisms for nuclear activity might be the galactic environment, like minor mergers and tidal forces (Barnes & Hernquist, 1991). As the atomic gas extends in most disk galaxies much further than the optical disk, it provides an ideal tool to identify interactions and tidal features as well.
- What are the dynamical modes on different scale lengths? Several models suggest that a hierarchy of mechanisms might combine to transport gas from large kpc scales down to the inner pc scales (Shlosman et al., 1990; Combes , 2003; Jogee , 2004). The cross-correlation of dynamical modes (e.g. the corotation resonance of the stellar bar and

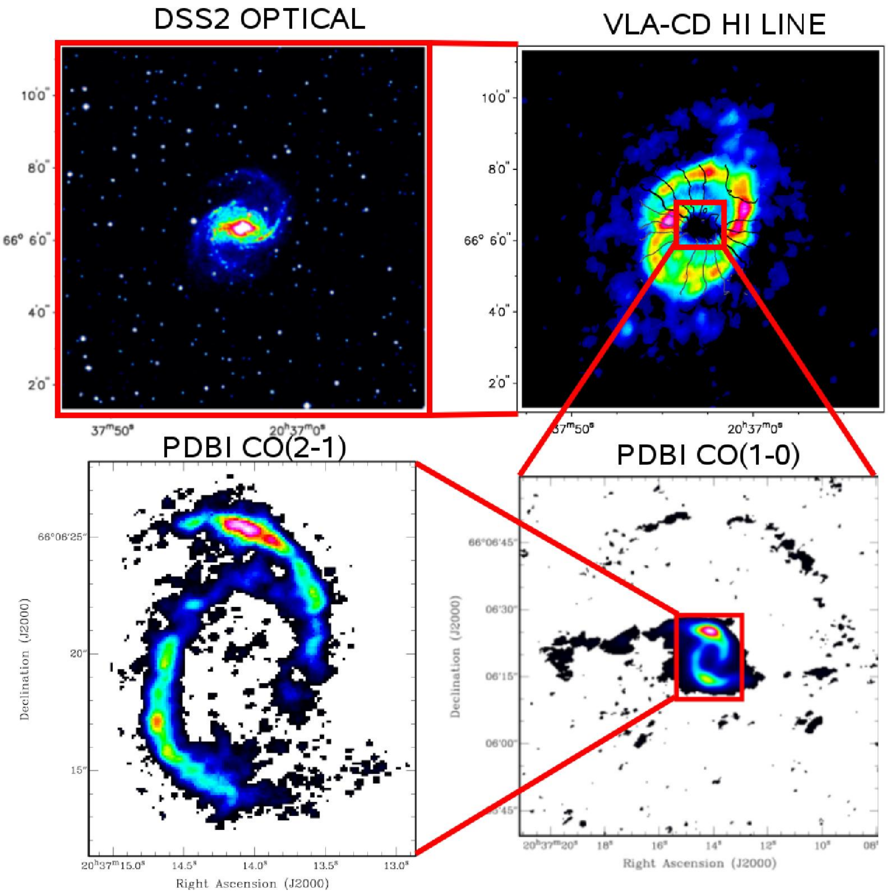

Figure 2.2: The example of the NUGA source NGC 6951 demonstrates the importance of combining HI and CO imaging data to probe the gas kinematics over scale lengths of several orders of magnitude. The VLA D-array HI data (*top right*; sum map in color, velocity field in contours) clearly shows that the galactic gas disk has a much larger extent than the stellar disk seen in its optical light from the DSS2 red survey (*top left*). The CO(1-0) emission as observed by PdBI shows gas lanes along the stellar bar and a nuclear ring like structure. Only the 0.7" resolution CO(2-1) data from PdBI resolves this inner 'ring' into a spiral-like structure and a small amount of gas located close to the Seyfert 2 nucleus.

spiral density waves) probed by the CO and HI gas kinematics allows us to test if the various nuclear modes can be attributed or linked to different large-scale modes. Since from theory a clear link is expected, it is expected that the CO+HI dataset should confirm this picture. However, the effect of external triggers (like tidal interactions, minor mergers) can complicate this simple picture.

- What are the fueling efficiencies and gas inflow rates from the outer disk to the center? As demonstrated with the CO data, gravity torque maps (García-Burillo et al., 2005) are an extremely powerful tool to evaluate whether stellar potentials are efficient enough to drain the gas angular momentum in the inner 1 kpc of these galaxies. Similarly, it is possible to study the torques acting on the entire HI disks and to combine with the torque maps of the molecular disk. These gravity torque maps can be used to estimate gas inflow rates, timescales, and the efficiency of the feeding mechanism for the central black hole. In addition, a decomposition of the observed HI and CO velocity fields into circular and non-circular terms provides possible information about the dynamical states of our galaxies and can be compared to the estimated gas inflow rates from our gravity torque analysis.

- What can we learn from detailed gas dynamical models for individual galaxies? To obtain a realistic dynamical model (for nuclear and large-scale regions together) the determination of the underlying gravitational potential of the whole host galaxy is essential; our NIR/optical wide-field imaging provide initial conditions for deriving the potential, and the combined CO/HI-derived kinematics can constrain models of the gas dynamics. Therefore it is planned to test detailed models of the gas flow from the outer disk to the center for some representative sources of the HI-NUGA sample (e.g. NGC 6951) using N-body and SPH codes.

2.4.2 Sample and Observations

For our HI study, 16 galaxies were selected (15 of which have high quality CO data of $\leq 1''$ resolution): the entire CO-NUGA parent sample, 3 additional galaxies from the CO-NUGA supersample and NGC 5248. The HI-NUGA sample therefore covers a variety of nuclear activity: 7 Seyferts, 7 LINERs and 2 HII galaxies. These galaxies were observed in their 21 cm line emission of neutral HI gas using the NRAO Very Large Array (VLA) interferometer in its C- and D-array configuration ($\sim 20''$ angular and $\sim$5.2 km s^{-1} spectral resolution) and cover roughly a 30' FOV around the targeted NUGA sources. All galaxies (except NGC 5248) have also CO observations from the PdBI. For more than half of the HI-NUGA sample additional VLA B-array data have been obtained. The selection of this subsample was based on the presence of a) sufficient HI signal in the previous C-array observation and b) clearly identified and resolved nuclear modes in the CO data. For 4 galaxies archival BCD-array HI data was available. The combined BCD data provide $\sim 7''$ resolution for more than half of the HI-NUGA sample. An overview of all observations of the HI-NUGA sample is presented in Tab. 2.1.

Table 2.1: The full HI NUGA Sample

Source	Host	AGN	CO (1-0)	CO (2-1)	30m CO
Galaxies with newly obtained B-array:					
NGC 3368	SBab	L	x	x	x
NGC 4321	SBbc	T	x	x	x
NGC 5248	SBbc	H	x	-	-
NGC 6951	SBbc	S	x	x	x
NGC 7217	Sb	L	x	x	x
with archival B-array:					
NGC 3627[a]	SBb	T	x	x	x
NGC 4736[a]	Sab	L	x	-	-
NGC 4826[a]	Sab	T	x	x	-
NGC 2782	SBa	H	x	x	x
only with CD-array data:					
NGC 1961	SBbc	L	x	x	-
NGC 3147	Sbc	S	x	x	-
NGC 3718	SBa	L	x	x	-
NGC 4569	SBab	T	x	x	-
NGC 4579	SBb	S	x	x	x
NGC 5953	SO-a	S	x	x	-
NGC 6574	SBbc	S	x	x	-

Note. — [a] Is observed as part of the VLA Large Proposal "Stuff that Matters: The Physical Conditions of the ISM in Nearby Galaxies". All galaxies have been observed using the VLA in the CD-array configuration. Additional VLA B array data is available for more than half of the HI-NUGA sample. The AGN classification is taken from Ho, Fillipenko & Sargent (1997): S - Seyfert, L - LINER, T - transition object, H - HII galaxy and NED. All CO (2-1) and (1-0) observations have been obtained using the IRAM PdBI, except for NGC5248 (only BIMA-Song data). Additional observations using the IRAM 30m Single Dish Telescope have been undertaken for some galaxies out of the NUGA sample.

3 Atomic Hydrogen Properties of AGN Host Galaxies: HI in 16 NUGA Sources

We present a comprehensive spectroscopic imaging survey of the distribution and kinematics of atomic hydrogen (HI) in 16 nearby spiral galaxies hosting low luminosity AGN, observed with high spectral and spatial resolution (resolution: ∼20″, ∼5 km s^{-1}) using the NRAO Very Large Array (VLA). The sample contains a range of nuclear types, ranging from Seyfert to star-forming nuclei and was originally selected for the NUclei of GAlaxies project (NUGA) - a spectrally and spatially resolved interferometric survey of gas dynamics in nearby galaxies designed to identify the fueling mechanisms of AGN and the relation to host galaxy evolution. Here we investigate the relationship between the HI properties of these galaxies, their environment, their stellar distribution and their AGN type. The large-scale HI morphology of each galaxy is classified as ringed, spiral, or centrally concentrated; comparison of the resulting morphological classification with AGN type reveals that ring structures are significantly more common in LINER than in Seyfert host galaxies, suggesting a time evolution of the AGN activity together with the redistribution of the neutral gas. Dynamically disturbed HI disks are also more prevalent in LINER host galaxies than in Seyfert host galaxies. While several galaxies are surrounded by companions (some with associated HI emission), there is no correlation between the presence of companions and the AGN type (Seyfert/LINER).

3.1 Introduction

Active Galactic Nuclei (AGN) represent some of the most extreme conditions and include the most powerful individual objects to be found throughout the Universe. Nowadays, the phenomena of nuclear activity is generally understood to be the result of accretion of material onto a SuperMassive Black Hole (SMBH); very likely through the infall of gas from its host galaxy (e.g. Rees, 1984). Although SMBHs exist in most galaxies, only a small fraction of all galaxies exhibit nuclear activity (Huchra & Burg, 1992; Ho et al., 1997; Miller et al., 2003). The majority of AGNs show low-ionization narrow emission-line regions (LINERs), which have luminosities lower than Seyfert galaxies and quasars. Originally, LINERs and

Seyferts were considered to form a continuous distribution in the usual line-ratio classification diagrams. Recent investigations of the host properties of emission-line galaxies from the Sloan Digital Sky Survey (Kewley et al., 2006) confirmed that their nuclear activities are due to accretion by a SMBH. But interestingly, LINERs and Seyferts are also clearly separable in emission line ratio diagrams (Groves et al., 2006), and that these two classes have distinct host properties (Groves et al., 2006), implying that their distinction is in fact not simply an arbitrary division. An open question is therefore what mechanisms give rise to the different AGN types observed.

A coherent picture of AGN feeding, e.g. how to remove the angular momentum from host galaxy gas so that it can reach the central parsec, is still missing. Therefore it is expected that a hierarchy of mechanisms might combine to transport gas from large kpc scales down to the inner pc scales (Shlosman et al., 1990; Combes , 2003; Jogee , 2004). Additionally, trigger mechanisms driven by the galactic environment, like minor mergers and tidal forces, might play a role as well (Barnes & Hernquist, 1991). A larger gas fraction for Seyferts than for normal galaxies was suggested by Hunt et al. (1999) and a prevalence of stellar rings (RC3 classification) in active galaxies (Seyfert and LINERs) compared to non-active galaxies was suggested (Hunt & Malkan, 1999). NICMOS imaging of the centers of 250 nearby galaxies (Hunt & Malkan, 2004) revealed systematic morphological differences between HII/starburst (most disturbed), Seyfert (intermediate disturbed), LINER and normal galaxies (most regular). The study of the circumnuclear regions of 24 Seyfert2 galaxies using HST images (Martini & Pogge, 1999) revealed a dominance of nuclear spirals, suggesting that spiral dust lanes may be responsible for feeding gas to the central engines.

Theoretical simulations have also made progress in addressing the nature of nuclear fueling with respect to different types of gravitational instabilities and their feeding efficiency: nested bars (e.g. Shlosman et al., 1989; Friedli & Martinet, 1993; Maciejewski & Sparke, 2000; Englmaier & Shlosman, 2004), gaseous spiral density waves (e.g. Englmaier & Shlosman, 2000; Maciejewski, 2002, 2004a,b), $m = 1$ perturbations (e.g. Shu et al., 1990; Junqueira & Combes, 1996; García-Burillo et al., 2000) and nuclear warps (Schinnerer et al., 2000) have all been suggested as possible transport mechanisms.

In order to distinguish models for nuclear fueling, observations of neutral gas with high angular and velocity resolution are required. Therefore, the IRAM key project NUclei of GAlaxies (NUGA; see García-Burillo et al., 2003) was established - a spectroscopic imaging survey of gas in the centers of nearby low luminosity AGN. As most of the gas in galaxy nuclei is in the molecular phase, the survey used millimeter CO lines to conduct a detailed mapping of molecular gas dynamics at *high-resolution* ($0.5''$) in the central kiloparsec of AGN hosts. The CO-NUGA survey (using the IRAM Plateau de Bure Interferometer) reveals a wealth of nuclear gas distribution and kinematics which are studied in detail: (a) $m=1$ gravitational instabilities (one-arm spirals and lopsided disks; NGC 4826: García-Burillo et al. (2003)), (b) $m=2$ instabilities (two-arm spiral wave) expected to form in stellar bar potentials show only small amounts of molecular gas coincident with the AGN (e.g. NGC 4569: Boone et al. (2007), NGC 4579: García-Burillo et al. (2005) NGC 6951: Schinnerer et al., in prep.), (c) stochastic spirals that are related to non self-gravitating instabilities, and rings (NGC 7217: Combes et al., 2004), and (d) large scale warps that might extend into the central kiloparsec (NGC 3718: Krips et al., 2005). Besides the CO studies also extended radio continuum components resembling jet emission from AGN were detected (Krips et al., 2007a) and a molecular gas disk/torus of dense gas was observed in the HCN line emission (NGC 6951: Krips et al., 2007b). Additionally, García-Burillo et al. (2005) derived in a pilot study the gas inflow rates via measurements of the gravitational torque onto the molecular gas in the central kiloparsec for 4 galaxies.

To complement these CO data and provide a more complete census of the ISM and gas flows from the outskirts of the galaxy disks to the very center, the HI-NUGA project was initiated. HI-NUGA provides observations of the HI gas distributions and kinematics for 16 galaxies (including archival data for 2 galaxies) of the NUGA sample using NRAO's Very Large Array (VLA). Determining the HI distribution and kinematics is necessary to establish whether characteristics of the nuclear dynamics, and hence the nuclear activity, depend on overall host galaxy properties. Possible dependencies might also exist between nuclear modes and large scale drivers (i.e. tidal forces exerted by companions), or the overall content/distribution of the atomic gas. Since the HI gas extends in most disk galaxies much further than the optical disk, it is more loosely bound in the outer region because of the decrease of the gravitational potential. Hence, it provides an ideal tool to identify interactions and tidal features (e.g., Simkin et al., 1987; Mundell et al., 1995). Furthermore, due to its dissipative nature the gas is more sensitive to dynamical disturbances, both internal ones such as non-axisymmetric potentials or external ones (e.g. tidal interactions). Thus, one could expect, for example, to find a prevalence of Seyfert activity with asymmetries in the gas distribution and kinematics.

In this study we present for 16 nearby active galaxies data obtained in the 21 cm emission line of neutral hydrogen using the VLA. The relation between HI properties, such as the large scale environment (HI/optical companions, HI disk asymmetries) and the AGN type (Seyfert, LINER, HII) are analyzed in detail. The outline of this chapter is as follows: We describe the HI-NUGA sample, the observation and data reduction in §3.2. The results and derived HI properties are presented in §3.3, along with a discussion of the presence of companions and tidal disturbances of the HI disks and any correlation with AGN type. A comparison of AGN types and optical (stellar) light distribution is also examined. The results are discussed in the context of correlations with the HI environment (e.g. tidal forces) and the AGN type (§3.4). A summary is presented in §3.5.

3.2 Sample Description, Observations and Data Reduction

3.2.1 Sample Selection and Survey Goals

The NUGA project is a multiwavelength study of the nuclei of nearby AGN. The core sample (García-Burillo et al., 2003) consists of 12 nearby AGN with D $\leq$ 54Mpc selected for the availability of high-quality optical and near infrared (NIR) images obtained with both ground-based telescopes and the Hubble Space Telescope (HST). The distribution and kinematics of molecular gas in all galaxies in the sample have been observed with the IRAM PdBI at 1mm and 3mm with maximum angular and spectral resolutions of $0.5''$ and 3.6 km s^{-1}, respectively. The NUGA supersample adds another 16 galaxies with CO data of similar quality obtained by the NUGA team with the IRAM array as part of other projects.

For our detailed HI study using the VLA, 16 galaxies were selected (15 of which have high quality CO data of $\leq 1''$ resolution): the entire CO-NUGA parent sample, 3 additional galaxies from the CO-NUGA supersample and NGC 5248. The HI-NUGA sample therefore covers a variety of nuclear activity: 7 Seyferts, 7 LINERs and 2 HII galaxies. All galaxies in our sample are spiral galaxies, ranging in Hubble type from Sa to Sbc in disk type. Typical spatial resolution of the HI data is $21''$=(1.9 kpc) for a mean distance of $\sim$20 Mpc; the distance of our sample ranges from 4 Mpc to 54 Mpc. An overview of the general properties of our HI sample is given in Tab. 3.1.

The overall aims of the HI-NUGA project are to 1) determine the global HI properties of the sample galaxies and their large scale environment to search for relations between the nuclear activity and the HI environment, for all disk properties of the full sample, 2) to trace the gas inflow on various spatial scales for the best candidates of the HI-NUGA sample with high angular resolution HI data (VLA B+CD array) and to determine the fueling rates by using gravity torques, 3) to obtain detailed dynamical models (using SPH codes with a fixed gravitational potential and/or N-body codes.) describing the gas flow in the galactic disk over several radii for the most representative galaxies. In this paper we concentrate on goal 1).

3.2.2 AGN Classification

Active galaxies can be separated into the categories of emission-line AGNs and HII region-like galaxies (starburst) based on the differing nature of the photoionization source. Emission-line AGNs can be divided into Seyferts and LINERs. The majority of AGN are LINERs with nuclear optical spectra that are dominated by emission lines of low-ionization species such as [OI] λ6300, [OII] λ3726,9 and [SII] λ6717 (Ho et al., 1997). The main difference between

Table 3.1: Sample Overview

Name	RA (J2000)	DEC (J2000)	Hubble Type	Bar	AGN HFS	AGN Kewley	v_{hel} [km/s]	Dist [Mpc]	Res. [kpc]
NGC 3147	10 16 53.65	+73 24 02.7	S(rs)bc		S2	S	2820	40.9	5.0
NGC 3627	11 20 15.03	+12 59 29.6	SB(s)b	x	L/S2	S	727	6.6	0.5
NGC 4569	12 36 49.80	+13 09 46.3	SB(rs)ab	x	T2	S	-235	16.8	1.6
NGC 4826	12 56 43.69	+21 40 57.5	(R)S(rs)ab		T2	S	408	4.1	0.3
NGC 5953	15 34 32.39	+15 11 37.7	SO-a		S2	S	1965	36	3.3
NGC 6574	18 11 51.23	+14 58 54.4	SB(rs)bc	x	S	S	2282	38	3.3
NGC 6951	20 37 14.09	+66 06 20.3	SB(rs)bc	x	S2	S	1424	24.1	2.4
NGC 1961	05 42 04.80	+69 22 43.3	SB(rs)bc	x	L2	L	3934	53.9	4.4
NGC 3368	10 46 45.74	+11 49 11.8	SB(rs)ab	x	L2	L	897	8.1	0.8
NGC 3718	11 32 34.85	+53 04 04.5	SB(s)a	x	L1.9	L	994	17.0	1.1
NGC 4321	12 22 54.90	+15 49 20.6	SB(s)bc	x	T2	L	1571	16.8	1.4
NGC 4579	12 37 43.52	+11 49 05.5	SB(rs)b	x	S1.9/L1.9	L	1519	37	1.8
NGC 4736	12 50 53.06	+41 07 13.7	(R)S(r)ab	x	L2	L	308	4.3	0.4
NGC 7217	22 07 52.38	+31 21 33.4	(R)S(r)ab		L2	L	952	16.0	1.4
NGC 2782	09 14 05.11	+40 06 49.2	SB(rs)a	x	H	H	2562	37.3	6.2
NGC 5248	13 37 32.07	+08 53 06.2	(R)SB(rs)bc	x	H	H	1153	15	1.4

Note. — Summary of the properties of the complete HI-NUGA sample. Listed are only parameters from LEDA, NED and the resolution of the VLA observations for all galaxies (beam). The AGN classification listed in column (6) is taken from Ho, Fillipenko & Sargent (1997): S - Seyfert, L - LINER, T - transition object, H - HII galaxy and NED. The galaxies are divided into separated classes as described in §3.2.1: Seyfert galaxies(top part), LINER galaxies (mid part) and HII/Transition objects (bottom part), additionally indicated in column (7). The velocities listed in column (8) are the assumed systemic velocities. In column (10) the spatial resolution of our HI images is listed.

Seyferts and LINERs is thought to be accretion rate, which explains why LINERs have lower AGN luminosities than Seyfert galaxies. Although Seyferts and LINERs are basically powered by the same engine, i.e. accretion onto a SMBH, the Seyfert/LINER distribution is bimodal (Groves et al., 2006), implying different accretion mechanisms (for a general review see Ulrich et al., 1997; Combes, 2001; Netzer & Shields, 2007). Furthermore, LINERs seem in general to be hosted by older, more massive, less dusty galaxies with higher stellar velocity dispersions and lower nuclear [OIII] luminosities than Seyfert galaxies (Kewley et al., 2006). Despite numerous studies in this field of research, the origin of their differences (e.g. different stages in evolution) is still under debate.

Although all the galaxies in our sample have several nuclear classifications available in the literature, we reclassified their nuclear types as described in the following, in order to have a coherent scheme for our sample. The most common method to select star-forming galaxies is based on the Baldwin, Phillips & Terlevich (1981) empirical diagnostic diagrams using the optical line ratios of [OI]/Hα, [SII]/Hα, [NII]/Hα, and [OIII]/Hβ. For the purpose of this

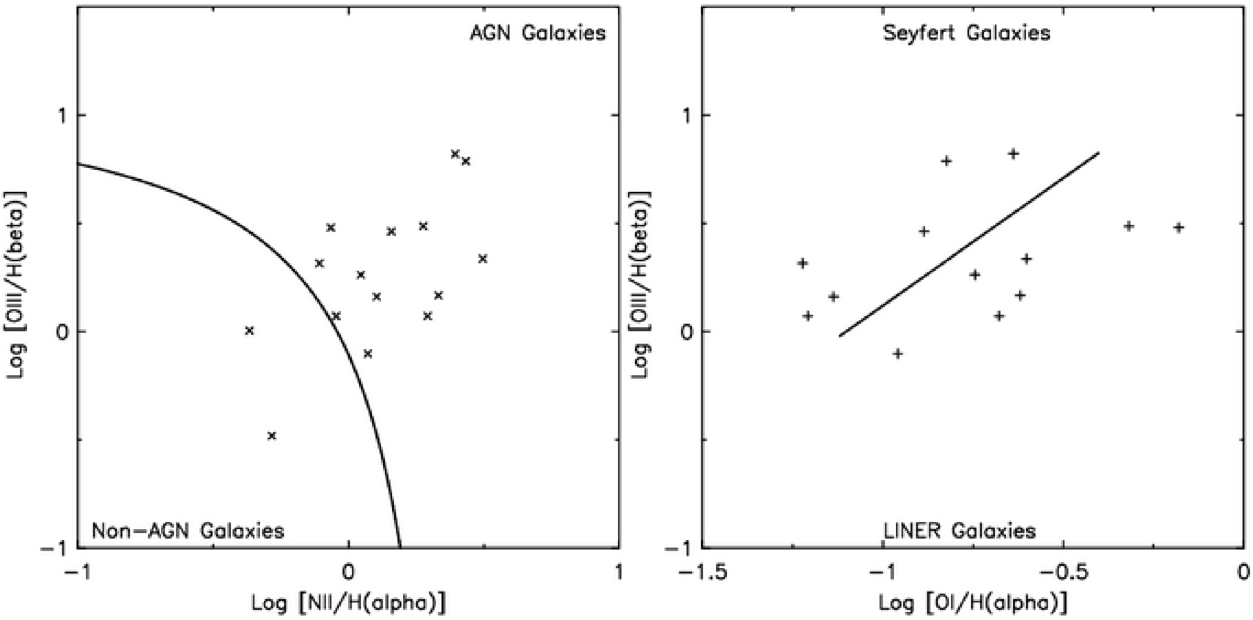

Figure 3.1: AGN classification for our sample following the definition of Kewley et al. (2006). The left panel shows the separation between AGN (upper right part) and non-AGN (lower left part) galaxies using the optical line ratios of [OIII]/Hβ versus [NII]/Hα as described in the text. In the right panel the dividing line between Seyfert (top part) and LINERs (bottom part) is indicated by using the [OIII]/Hβ versus [OI]/Hα line ratios (see text). Note that NGC 6574 is excluded in these diagrams, as no accurate ratios of the lines used were available in the literature. We used the classification as Seyfert given by NED.

paper we separated our sample in Seyferts, LINERs and non-AGN (HII+Transitions) objects following the most recent method of Kewley et al. (2006): First we distinguished AGN galaxies from non-AGN galaxies by using the optical line ratio [OIII]/Hβ versus [NII]/Hα (left panel Fig. 3.1). The line ratios are taken from the cataloged data of Ho et al. (1997) and Kim et al. (1995). For NGC 6574 no accurate line ratios were available in the literature for this method and we used its classification listed in NED as Seyfert. The line separating AGN and Starburst/Transition galaxies is given by (Kewley et al., 2006):

$$log(\frac{[OIII]}{H\beta}) = \frac{0.61}{log(\frac{[NII]}{H\alpha}) - 0.47} + 1.19 \tag{3.1}$$

Secondly, we divided the AGN galaxies in Seyfert and LINERs by using the [OIII]/Hβ versus [OI]/Hα diagram (right panel Fig. 3.1) with a separating line defined by:

$$log(\frac{[OIII]}{H\beta}) = 1.18 \cdot log(\frac{[OI]}{H\alpha}) + 1.30. \tag{3.2}$$

The classification of our sample results in 2 non-AGN galaxies (HII and transition objects), 7 Seyferts and 7 LINERs. Since only 2 non-AGN galaxies are present in our sample, we will mainly focus on a comparison between the properties of Seyferts and LINERs. A detailed comparison of HI properties between Seyfert and non-AGN galaxies is carried out by Mundell et al. (in prep.). The average morphology type taken from Hyperleda is roughly the same for Seyferts (t=2.81) and LINERs (t=2.69). Hence, effects due to bias of the morphology type are unlikely.

3.2.3 VLA Observations and Data Reduction

The 16 galaxies presented here were observed in 2003 and 2004 in their HI line emission using the VLA in its C- and D-configuration. Three galaxies (NGC 3627, NGC 4736, NGC 4826) were also observed as part of the THINGS project (Walter et al., in prep., BC-array data) while adequate data for NGC 2782 and NGC 3718 were already available in the VLA archive. For NGC 3718, only the C-array data has been analyzed as the D-array data was lacking good phase calibrator measurement required for our purposes.

Flux calibrator measurements were performed at the beginning and at the end of each observation cycle. The phase calibrator was observed before and after each source cycle with a maximum distance between source and phase calibrator of 12°. The correlator spectral setup used was spectral line mode 4 with Hanning smoothing and 64 channels per 1.5625 MHz channel width per frequency band providing a frequency resolution of 24.414 kHz/channel ($\sim$ 5.2 km s^{-1}). NGC 2782 was observed with a resolution of only 48.83 kHz ($\sim$ 10.48 km s^{-1}). Our observations have an average on-source integration time of 2.7h in the C-array and 2.8h in the D-array configuration. Thus, the corresponding RMS flux sensitivity of 0.6 and 0.8 mJy/beam/channel gives a 3-σdetection limit of $\sim 4 \times 10^{19}$ cm^{-2} and $\sim 0.38 \times 10^{19}$ cm^{-2} column density for the C- and D-array, respectively.

The data reduction was performed following the standard procedure of the Astronomical Image Processing System (AIPS; Greisen , 2003). Calibration solutions were first derived for the continuum data-set (inner 3/4 of the spectral band width) and then transferred to the line data. The bandpass solutions were determined from the phase calibrator measurements to account for channel to channel variations in phase and amplitude.

After the calibration was applied, the two-IF data set was split into single-source data sets with 64 channels each. For each set the first 8 and last 8 channels were discarded, resulting in two 48-channel data sets. These were then combined into a final cube of 96 channels with an effective bandwith of 2343.7 kHz ($\sim$ 500 km s^{-1}) and a channel width of 24.4kHz ($\sim$ 5.2 km s^{-1}). For the THINGS data and NGC 2782 only the first 4 and last 4 channels were discarded which resulted in 112-channel sets with an effective bandwith of 2734.4 kHz and 5469kHz (NGC 2782), respectively. For NGC 1961 two independent frequency setups were used with an effective bandwith of 4687.5 kHz ($\sim$ 1018 km s^{-1}). After that, the calibrated C and D array data cubes were combined.

The task UVLIN within AIPS was used to subtract the continuum emission. The continuum emission was measured only in channels without line signal (usually the first 10 and last 10 channels of a data cube). The fit was done with a first order polynomial, namely a DC term (offset from zero) and a slope. For NGC 5953 only the first 8 channels were used (simple offset fit) because of additional line signal in the last channels. Channels affected by galactic HI emission (NGC 4569, Channel 4-7) and internal RFI (NGC 1961, Channel 17-18) were dismissed and have been excluded from the further analysis. However, these channels were well outside line emission in both cases.

After the continuum substraction, the data were CLEANed using the task IMAGR within AIPS. The calibration of each observation (C and D configuration) was verified individually (by a check of the imaged cubes). The flux-limit for CLEANing was set to a peak value in the residual image of 2×RMS with a maximum iteration number of 10^5 steps. After CLEANing the residuals were rescaled by the ratio of the restoring beam area to the dirty beam area. The reason for this rescaling is that typically the residual flux of the source in cleaned channel maps is overestimated due to the different shape of the dirty and CLEAN beams. However, the results of the rescaling method turned out to not be significantly different from the results obtained without rescaling (less than 5%). We produced two CLEANed data cubes for each galaxy: 1.) Naturally weighted imaging with a velocity resolution of $\sim$20.8 km s^{-1} and an average angular resolution of $33''$, in order to obtain a datacube with maximum sensitivity to the outer HI disk and for HI companions around it. 2.) Robust weighted imaging for a high angular ($20''$) and spectral ($\sim$5.2 km s^{-1}) resolution data cube to study the galactic HI disk itself. A description of naturally and robust weighting is given in App. A.1. To find the best compromise between angular resolution and RMS, several robust weighting parameters were tested and a robust weighting parameter of 0.3 was selected. The cellsize of each grid was set to $4''$/pixel for natural and $2''$/pixel for robust weighting with a resulting mapsize of 1024 × 1024 pixel. That corresponds to a field of view of $\sim 68'$ (natural) and $\sim 34'$ (robust) such that the $30'$ primary beam is fully mapped in both cases. The RMS values and beam sizes for natural/robust weighting are listed in Table 3.2 with an average achieved RMS value of 0.34/0.46 Jy beam^{-1} respectively. The channel maps for the naturally weighted cubes are presented in the appendix (see Fig. 3.2 as an example). All further analysis was performed on these data cubes. A primary beam correction was only applied for the flux measurement.

The subsequent analysis has been done with the Groningen Image Processing SYstem (GIPSY; van der Hulst et al., 1992). The channel maps were combined to produce zeroth (intensity map), first (velocity field) and second (dispersion field) moments of the line profiles using the task MOMENT. The RMS values have been measured in two regions where no line signal was apparent and averaged over all channels of the cubes. A flux cut-off of three times the channel-averaged RMS value was used for the moment maps. In order to exclude one channel wide noise peaks from the moment maps, two adjacent channels with flux values above the cut-off level were required (corresponding to a width of 10.4 km s^{-1} for the robust weighted cubes). However, for the natural weighted data cube we did not apply such a requirement

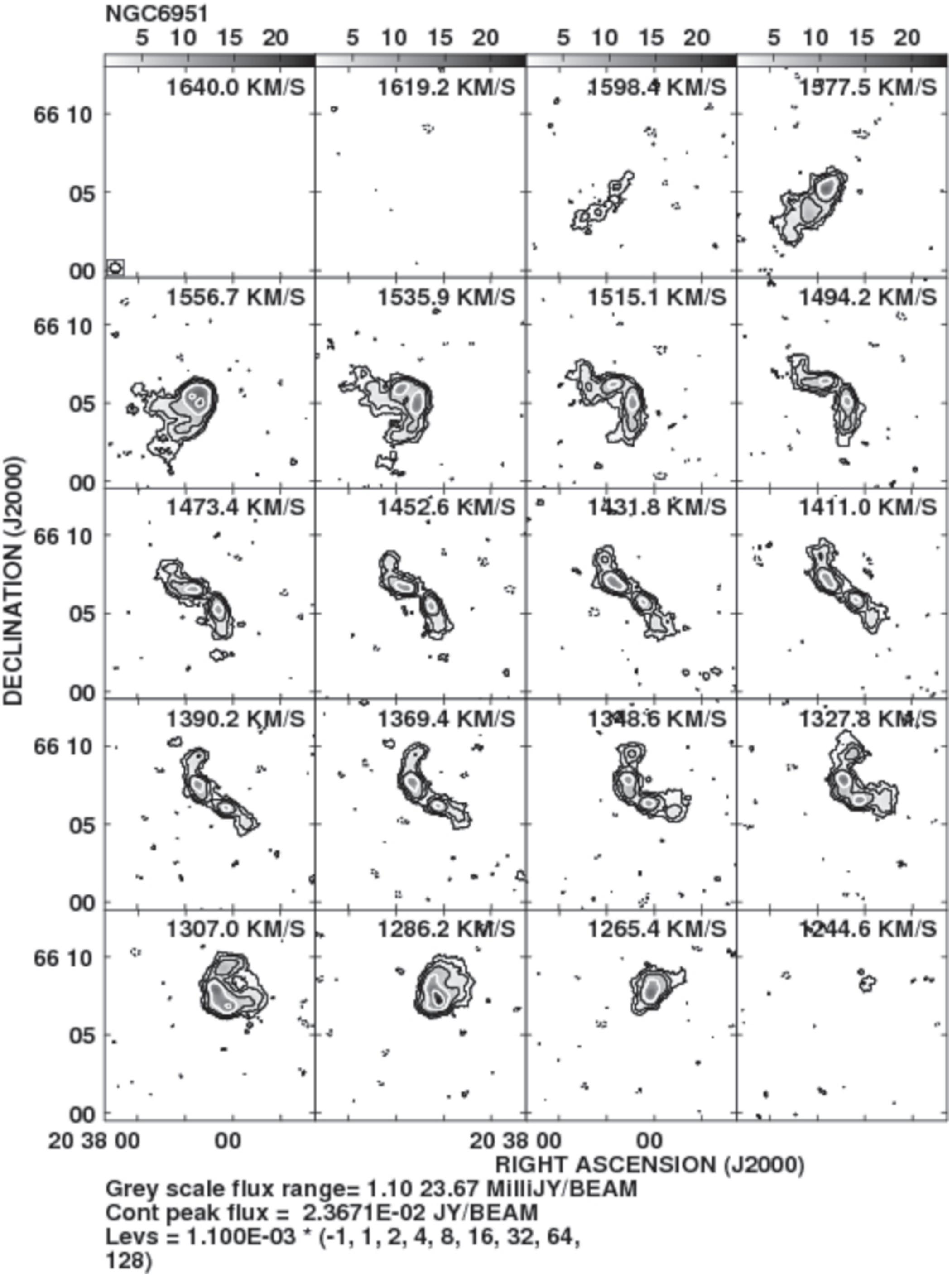

Figure 3.2: Channel maps of the natural weighted data cube for the example NGC 6951. Each channel has a velocity width of ∼20.8 km s^{-1}. The flux cut-off was set at 3σ of the RMS value (for NGC 6951: 0.0011 Jy/Beam) and the contours are in steps of $3\sigma \cdot 2^n$Jy (n=1,2,3...). The channelmaps for all galaxies are presented in App. A.3.

Table 3.2: Observational Setup

Name	nat. weight Beam [″]	rob. weight Beam [″]	RMS nat. [mJy/beam]	RMS rob. [mJy/beam]	FWZI. [km/s]
NGC 3147	45.4 × 43.6	29.2 × 22.0	0.44	0.59	430
NGC 3627	22.5 × 19.2	16.8 × 15.2	0.34	0.68	431
NGC 4569	41.8 × 36.0	21.2 × 19.2	0.48	0.63	396
NGC 4826	25.6 × 21.6	16.3 × 14.8	0.32	0.28	372
NGC 5953	42.1 × 32.5	22.9 × 18.3	0.31	0.41	349
NGC 6574	30.5 × 28.0	20.2 × 18.3	0.31	0.41	340
NGC 6951	39.6 × 34.9	22.2 × 18.6	0.35	0.45	338
NGC 1961	24.6 × 20.1	18.7 × 15.0	0.34	0.49	767
NGC 3368	44.3 × 35.6	23.0 × 19.9	0.28	0.39	399
NGC 3718	17.4 × 15.9	13.9 × 13.5	0.47	0.84	465
NGC 4321	31.3 × 25.6	18.2 × 15.9	0.24	0.30	291
NGC 4579	43.5 × 38.6	23.1 × 21.6	0.33	0.51	374
NGC 4736	29.2 × 28.3	18.9 × 15.5	0.32	0.28	284
NGC 7217	33.4 × 29.6	18.4 × 17.0	0.34	0.41	326
NGC 2782	52.6 × 48.6	35.1 × 33.0	0.25	0.37	246
NGC 5248	35.5 × 28.5	19.9 × 17.5	0.39	0.27	311

Note. — Overview of the observational properties (VLA) beam size and RMS for natural (nat) and robust (rob) weighting. In addition the Full Widths at Zero Intensity (FWZI) of the velocities are listed for all galaxies. The velocity resolution is ∼20.8 km s^{-1} (natural) and ∼5.2 km s^{-1} (robust). Only NGC 2782 has a velocity resolution of ∼10.4 km s^{-1} for robust weighting.

since a single channel has already a width of 20.8 km s^{-1}, which is also the range of the minimal velocity width of an expected HI emission line.

3.3 Analysis and Results

In the following the distribution and kinematic properties of the HI gas disks of the HI-NUGA sample will be derived, compared to optical properties of the host galaxies and analyzed as a function of the AGN type.

3.3.1 HI Distribution and Environment

HI Gas Morphology

The velocity-integrated HI intensity maps and the optical light distribution (DSS2-blue maps) are presented in Fig. 3.3. The HI intensity maps show a large variety of morphologies in the disk gas distribution including spiral (e.g. NGC 6951), ringed (e.g. NGC 7217) and centrally concentrated geometries (e.g. NGC 5953). A simple classification by eye has been used to assign a ring or spiral morphology. In cases where the distinction was unclear, the intensity map was projected into polar coordinates, giving the azimuthal variation of the intensity around a given center. If the intensity was constant along a radius, a ringed geometry was assumed.

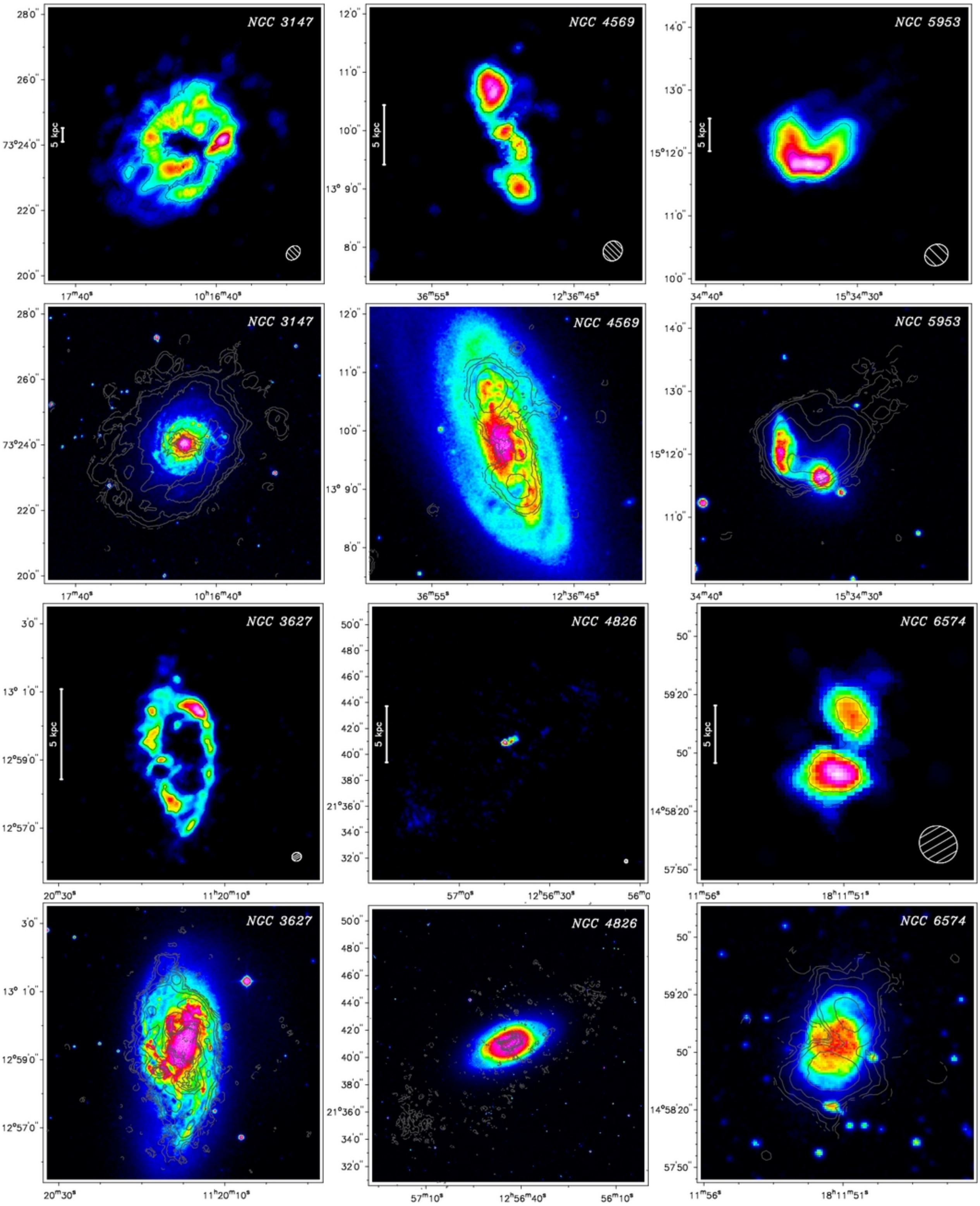

Figure 3.3: HI intensity maps (upper panel) and the optical emission from DSS2-blue (lower panel with HI in contours) of our HI-NUGA sample sorted by AGN type (Seyfert, LINER, HII). The contours are in n steps of $5 \cdot 2^n \cdot 10^{19}$ cm^{-2} of the HI column density (with $n = 1, 2, 3, ...$).

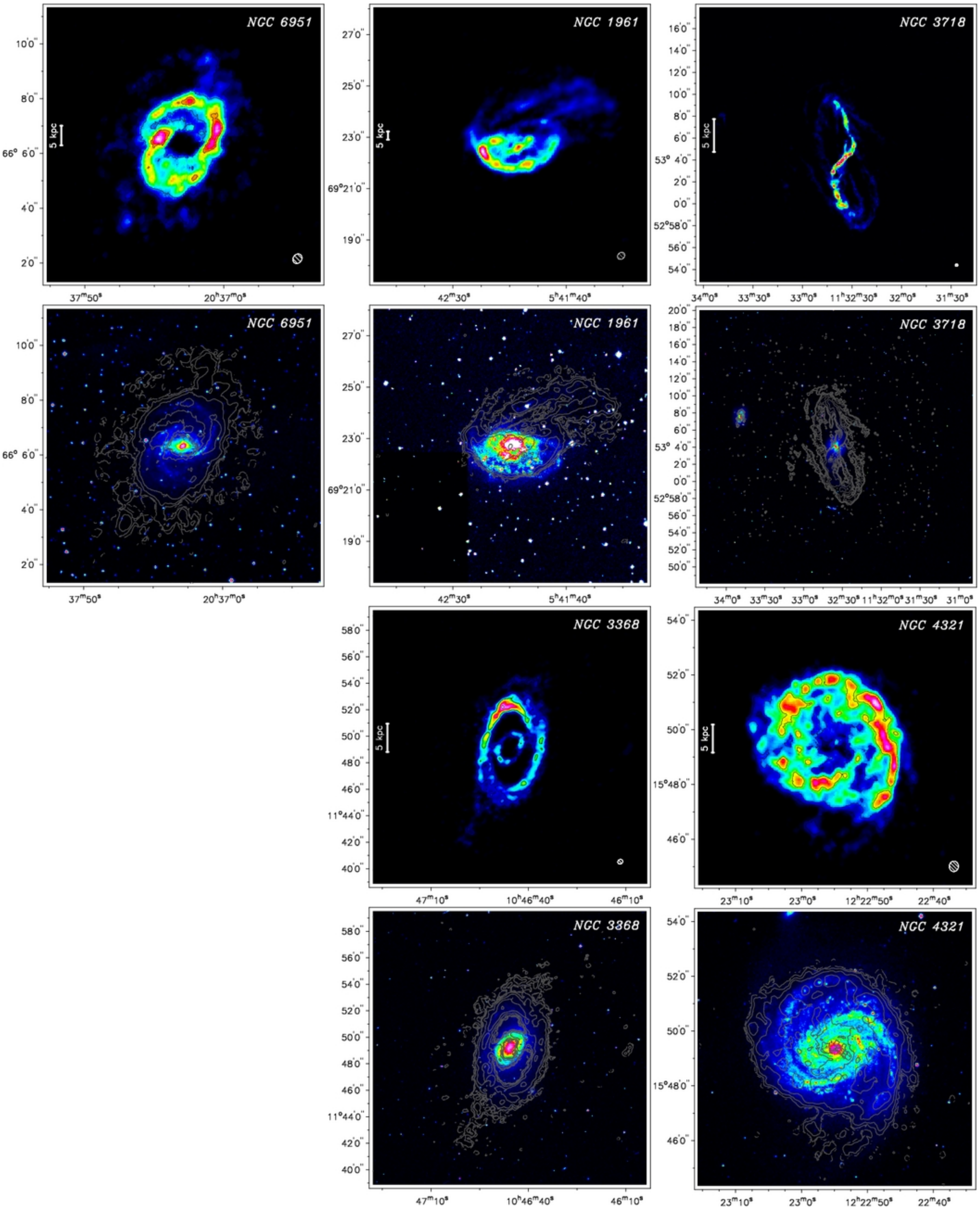

Fig. 3.3 (Continued)

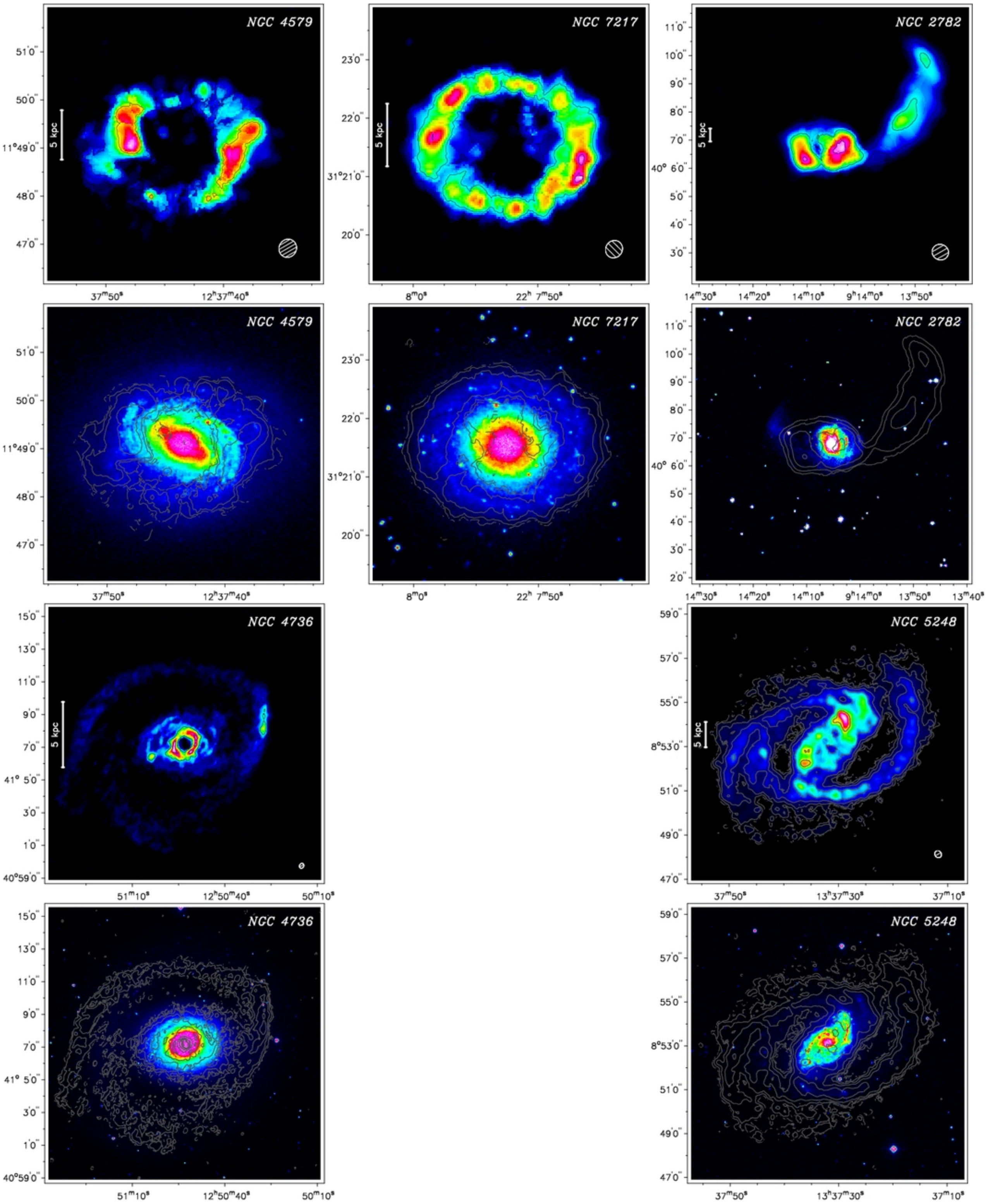

Fig. 3.3 (Continued)

Table 3.3: HI and Optical Morphology

Name	Morphology Type	R_{HI} [″]	R_{opt} [″]	R_{HI}/R_{opt}	Disturbed Disk	Companion HI detected
NGC3147	sp	200	122.1	1.64		
NGC3627	sp	193	267.3	0.72		
NGC4569	c	134	286.5	0.47		
NGC4826	sp/c	578	300	1.93		
NGC5953	c	153	36.9	4.15	x	x
NGC6574	c	71	45.3	1.57		
NGC6951	sp	255	97.2	2.62		
NGC1961	sp	130	125.1	1.04	x	x
NGC3368	r/sp	393	227.4	1.73	x	x
NGC3718	warped	460	161	2.86	x	x
NGC4321	sp	237	228	1.04	x	
NGC4579	r	147	168.6	0.87		
NGC4736	r/sp	427	300	1.42	x	
NGC7217	r	121	119.4	1.01		
NGC2782	c	120	101.7	1.18	x	
NGC5248	sp	334	143.7	2.32		x

Note. — Overview of the HI morphology compared to the size of the stellar disk. The HI morphology is classified as ring (r), spiral arms (s) and/or bar (b). The values of R_{opt} are taken as $d_{B25}/2$ (Length of the projected major axis at the isophotal level 25 mag/arcsec^2 in the B-band) from LEDA. An equivalent radius for the HI disk R_{HI} is defined at a HI column density of 5.0×10^{19} cm^{-2}. The fraction of the radius of the HI disk (R_{HI}) to the radius of the stellar disk (R_{st}) is given as R_{HI}/R_{opt}. In addition disturbed disks and companions are marked by an ”x” (see text for details).

An overview of the HI-morphology of our sample is presented in Tab. 3.3. In summary, we find spiral geometry in 8 galaxies, ringed geometry in 4 galaxies, and concentrated geometry in 5 galaxies, whereby NGC 4826 shows concentrated/spiral geometry and NGC 3368 ringed/spiral geometry in the central/outer disk. For NGC 3718 no classification is possible as its disk is nearly edge-on and shows in addition a large warped disk.

In the following, we describe the HI morphology of the disk for the three galaxies which clearly differ from the rest of the HI-NUGA sample: NGC 5248 is the only galaxy of our sample which shows a large-scale HI ”gas bar” (13 kpc in length). This HI bar coincides with a stellar bar (see left panel of Fig. 3.3). In addition, NGC 5248 shows two large HI spiral arms located outside the HI bar itself. Thus its HI morphology is remarkably similar to NGC 4151 which has a gas-rich bar and optically faint but gas-rich outer spiral arms (Mundell et al., 1999).

NGC 3368 exhibits two rings with radii of about 78 $''$ (~3.1 kpc) and 220 $''$ (~8.6 kpc) for the inner and outer ring, respectively. The outer ring could also be two closely wound spiral arms which are not resolved at our resolution of $19''$. The inner ring is ~15 times larger than the small-scale ($r \approx 5''$) nuclear "mini-bar" (seen in the optical and NIR, Moiseev et al., 2004), which extends along a position angle of $120°-125°$.

NGC 4826 has two counter-rotating HI gas disks (Braun et al., 1992) where the inner HI disk has a radius of ~70 $''$ (~1.4 kpc) and the outer HI disk a radius of ~700 $''$ (~13.9 kpc). No obvious asymmetries are seen, neither in the inner disk nor in the outer disk. Here the radius of the optical disk (~$300''$) lies between the radii of the two counter-rotating parts of the HI disk.

Two galaxies in our sample show very distorted outer HI distributions in the form of HI tails and large faint extensions stretching from only one side of the main galaxy. NGC 2782 has a large HI tail with a projected length of $\sim 6'$ (~3 times the HI radius, see 3.3.2 and Smith, 1991, 1994) extending from its center to the north-west. NGC 1961 shows a large HI extension to the north-west with a projected length of $\sim 4'$ ($\sim$ 2 times the HI radius; see also Shostak et al., 1982) from the center. NGC 3718 exhibits a large HI warp (Schwarz, 1985).

Finally, two galaxies show large differences between the distribution of the stellar light and the HI gas: For NGC 6574 the HI gas distribution shows two HI peaks inside the stellar disk well separated by $30''$ even at our angular resolution of $19''$ (see Fig. 3.3). NGC5953 forms a close binary (likely merging) pair with NGC5943 (see left panel Fig 3) with the two galaxy centers separated by only $60''$ and a difference in systemic velocity of ~53 km s^{-1}. The HI distribution shows a wing-like structure whose velocity field could be interpreted as a single disk, roughly uniformly distributed with a faint HI extension to the north. Also the HI velocity field shows no obvious tidal asymmetries which could be associated with the merging of the two optical galaxies. Our study of the mass content (described in §3.3.4) revealed a larger value for NGC 5953 (Log(M_{HI}/D^2) = 7.1) than the typical HI mass content (Bettoni et al., 2003) for a galaxy of that Hubble type (Log(M_{HI}/D^2) = 6.5). Hence an additional contribution of the gas content from NGC 5954 (Hubble type: Sc) might explain the gas surplus since the typical HI mass content for a Sc galaxies is Log(M_{HI}/D^2) = 6.9. Thus we conclude that the ongoing merger already has changed the HI appearance of NGC 5953 and/or NGC 5954.

HI Environment and Tidal Interactions

In order to search for the presence of HI companions we used widefield maps (described in §3.2) with a field of view (FOV) of $\sim 60'$ which are sensitive to companions with HI masses of $\gtrsim 10^7 M_\odot \cdot d^2$ (lower detection limit near the center of the image) and $\gtrsim 10^9 M_\odot \cdot d^2$ (at radial distances of 30′). Note that the sensitivity scales with the galaxy distance squared, indicated as d in units of [10Mpc]. We found that 5 galaxies are surrounded by at least one HI-detected companion with a range in HI mass of (0.01 - 2.8) 10^9 $M_\odot$. In addition, potential optical companions were identified by using NED within our FOV (equivalent to a radial distance of 30′) and a velocity difference of ±500 km s^{-1} from the host galaxy ($\simeq 2$ times the HI velocity bandwith). Optical companions (within these constrains) were found for ∼56% of our galaxies. All cataloged optical companions (NED, within the constraints described above), their systemic velocity difference to the host galaxy and their distance from the host galaxy center are listed in Tab. 3.4. We assume that the relative velocity between galaxy and companion is inversely proportional to the disruption time of the galaxy disk. For companions with associated HI gas detection (10 companions in total, ≡ 38% of the optical companions) also the derived HI-flux, HI-mass and their velocity width are provided.

To estimate the total tidal strength of companions on each galaxy, we used the formalism developed by Dahari (1984). The strength of a tidal force affecting a galaxy with the mass M_G and the diameter D_G is primarily determined by the mass of the companion M_c and the distance R_{GC} to the power of three between the companion and the galaxy. We approximated the absolute distance by the projected distance and the mass of the companion by using the relation to its size, $M_C \propto D_C^\gamma$ with $\gamma = 1.5$ (Dahari, 1984; Verley et al., 2007). The tidal strength Q_{GC} is defined as the ratio between the tidal force and binding force:

$$Q_{GC} \equiv \frac{F_{tidal}}{F_{bind}} \propto \frac{\frac{M_c \times D_G}{R_{GC}^3}}{\frac{M_G}{D_G^2}} \propto \frac{(\sqrt{D_G D_C})^3}{R_{GC}^3} \tag{3.3}$$

The sum of the tidal interaction strengths (listed in Tab. 3.4) created by all the companions in the field is then calculated as $\mathbf{Q} = log(\sum_C Q_{GC})$. A value of $\mathbf{Q} < 0$ indicates that the tidal forces affecting the primary galaxy are smaller than the internal forces, and vice-versa.

Disturbances were characterized by using the divergence of the rotation curves between the approaching and receding side (see for example NGC 4321 in Fig. 3.4) as well as obvious asymmetries in the HI intensity maps (see for example NGC 1961 in Fig. 3.3). A divergence of at least 5σ (statistical error, roughly corresponding to 60 km s^{-1}) of the velocity difference (see §3.3.3) in the outer disk between approaching and receding side was required (apart from deviations due to streaming motions along spiral arms). From these requirements we found that 7 galaxies have a disturbed outer HI disk (the individual galaxies are indicated in Tab. 3.3). The origin of the disturbances (e.g. tidal forces, ram pressure) and the influence of the companions onto the HI disks are discussed in §3.4.1

Table 3.4: HI and Optical Companions

Target	$\log(\sum Q)$	Candidate Companions	Distance [kpc]	Companion coordinates RA	Dec	Δv_{sys} [km/s]	HI flux [Jy km/s]	HI mass [$10^9 M_{sun}$]	Δv [km/s]
NGC 3147	-2.8	UGC 05570	215	10h20m47.0s	+73d17m03s	96			
NGC 3627	-1.0	SDSS J111857.87+130500.3	38	11h18m57.9s	+13d05m00s	136			
		MESSIER 065	39	11h18m55.9s	+13d05m32s	80			
NGC 4569		-							
NGC 4826		-							
NGC 5953	0.9	NGC 5954	7	15h34m35.1s	+15d11m54s	-6			
		UGC 09902	38	15h34m33.2s	+15d08m00s	-269	1.5	0.39	110
		NGC 5951	171	15h33m43.0s	+15d00m26s	-185	10.7	2.75	300
		4C +15.49	204	15h33m14.4s	+15d16m41s				
NGC 6574	-								
NGC 6951	-								
NGC 1961	-1.4	CGCG 329-011	119	05h43m23.0s	+69d25m51s	174	1.08	0.74	230
		CGCG 329-009	141	05h42m36.9s	+69d14m12s	-62	1.09	0.75	210
			163	05h42m46.0s	+69d13m3s	-184	0.89	0.61	150
		UGC 03342	213	05h44m29.6s	+69d17m56s	40	3.92	2.69	320
		UGC 03344	315	05h44m56.6s	+69d09m34s	348	3.93	2.69	150
		UGC 03349	422	05h45m38.8s	+69d03m38s	358			
		CGCG 307-021	426	05h43m39.7s	+68d56m43s	-67			
NGC 3368		-	37	10h47m43.2s	+11d55m50s	78	0.6	0.01	40
NGC 3718	-1. 2	NGC 3729	58	11h33m49.3s	+53d07m32s	66	19.6	1.34	250
NGC 4321	-0.8	NGC 4323	26	12h23m01.7s	+15d54m20s	262			
		IC 0783A	49	12h22m19.6s	+15d44m01s	-364			
		VCC 0530	56	12h22m07.6s	+15d47m57s	-272			
		IC 0783	92	12h21m38.8s	+15d44m42s	-304			
NGC 4579	-2.4	[GKP2005] 106	184	12h38m41.1s	+11d58m45s	-483			
		VCC 1794	274	12h39m27.1s	+11d46m35s	-291			
		VCC 1642	304	12h35m53.1s	+11d40m55s	-189			
		NGC 4564	318	12h36m27.0s	+11d26m22s	-377			
NGC 4736		-							
NGC 7217		-							
NGC 2782	-3.5	SDSS J091258.41+395540.5	183	09h12m58.4s	+39d55m41s	-42			
NGC 5248	-2.2	CGCG 073-051	103	13h36m43.6s	+08d32m48s	-11			
		UGC 08575	117	13h35m45.6s	+08d58m09s	10	8.36	0.44	140

Note. — Overview of all cataloged companions within a FOV of 60 arcmin and within a velocity difference of ±500 km s^{-1} from the host galaxy (similar to the area probed by the HI data). The position, the projected distance from the host galaxy center and their systemic velocity (NED) relative to the systemic velocities of their host galaxies Δv_{sys} are listed. The sum of the tidal strength created by all companions in the field is given as Q=log($\sum Q$) (see text for detailed description). A value of $\mathbf{Q} < 0$ indicates that the tidal forces affecting the primary galaxy are smaller than the internal binding forces, and vice-versa. In case of associated detection in HI gas also the derived HI properties flux, gas mass and velocity width Δv are specified.

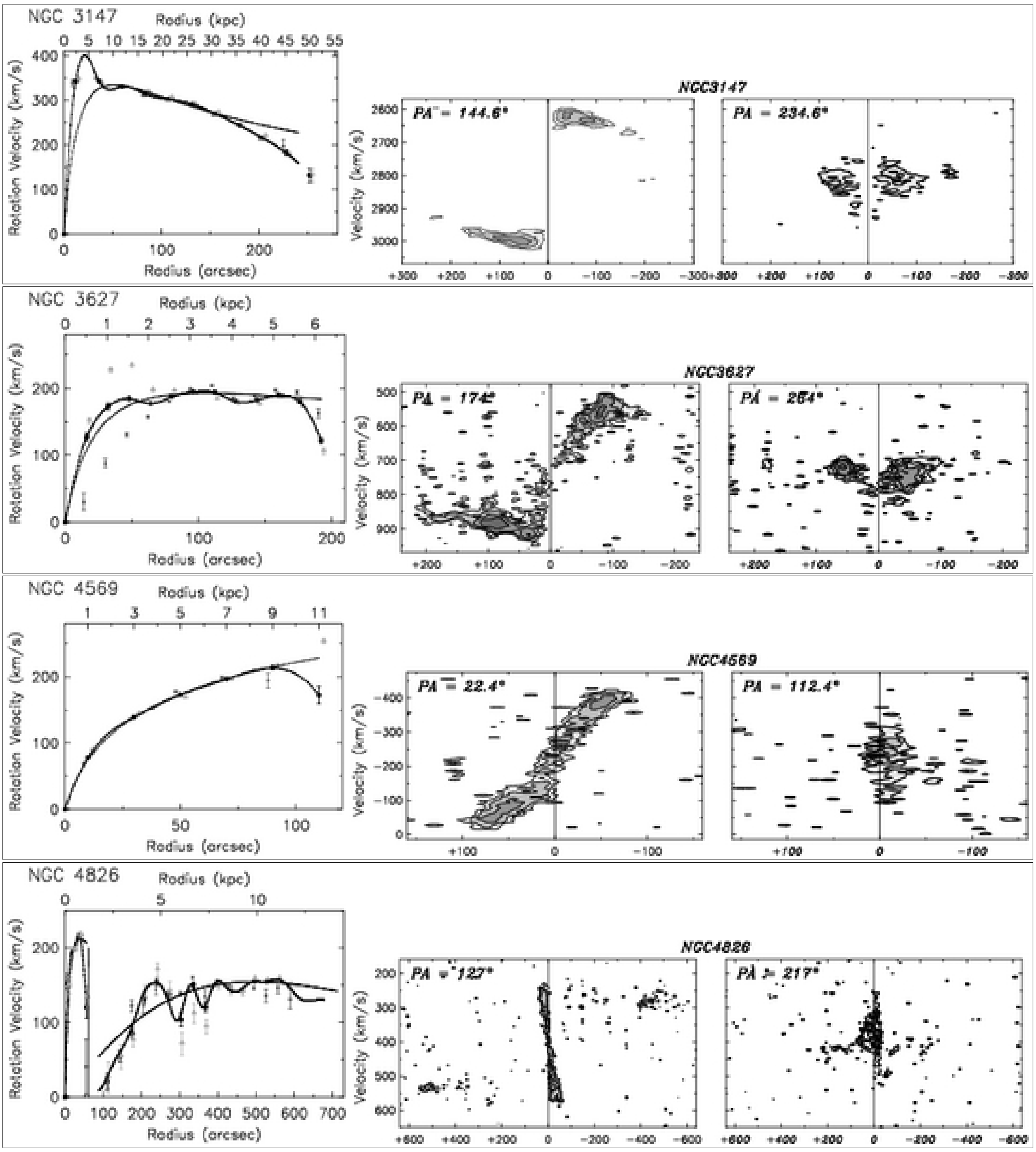

Figure 3.4: Presentation of the rotation curve and pv-diagrams for each galaxy. The rotation velocities have been plotted in the left panel for a) the whole disk (black dots), b) the approaching side of the disk only (dark grey dots), and c) the receding side of the disk only (light grey dots). A Brandt curve (Brandt, 1960) is fitted (thin black line) as well as a spline interpolation (thick black line) to the derived rotation velocities of the whole disk. The center and right panel show the pv diagram of the major and minor axis, respectively. The contours are in n steps of the column density at $1.8 \cdot 2^n \cdot 10^{19}$ cm^{-2} ($n = 1, 2, 3, ...$). Note that the values for NGC 2782 are likely incorrect, as there is a short tidal tail to the east which is barely resolved at our resolution (see Smith, 1994).

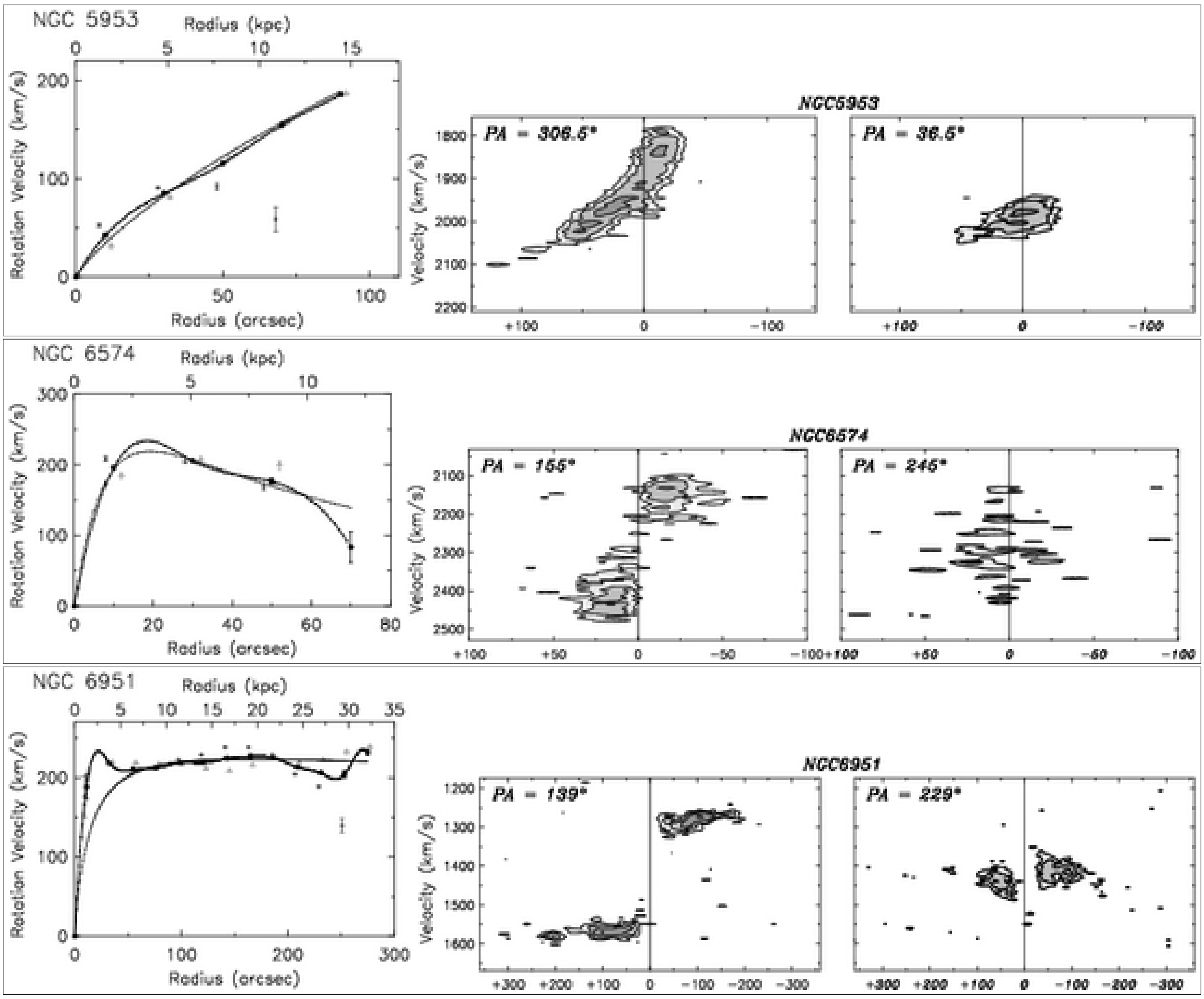

Fig. 3.4 (Continued)

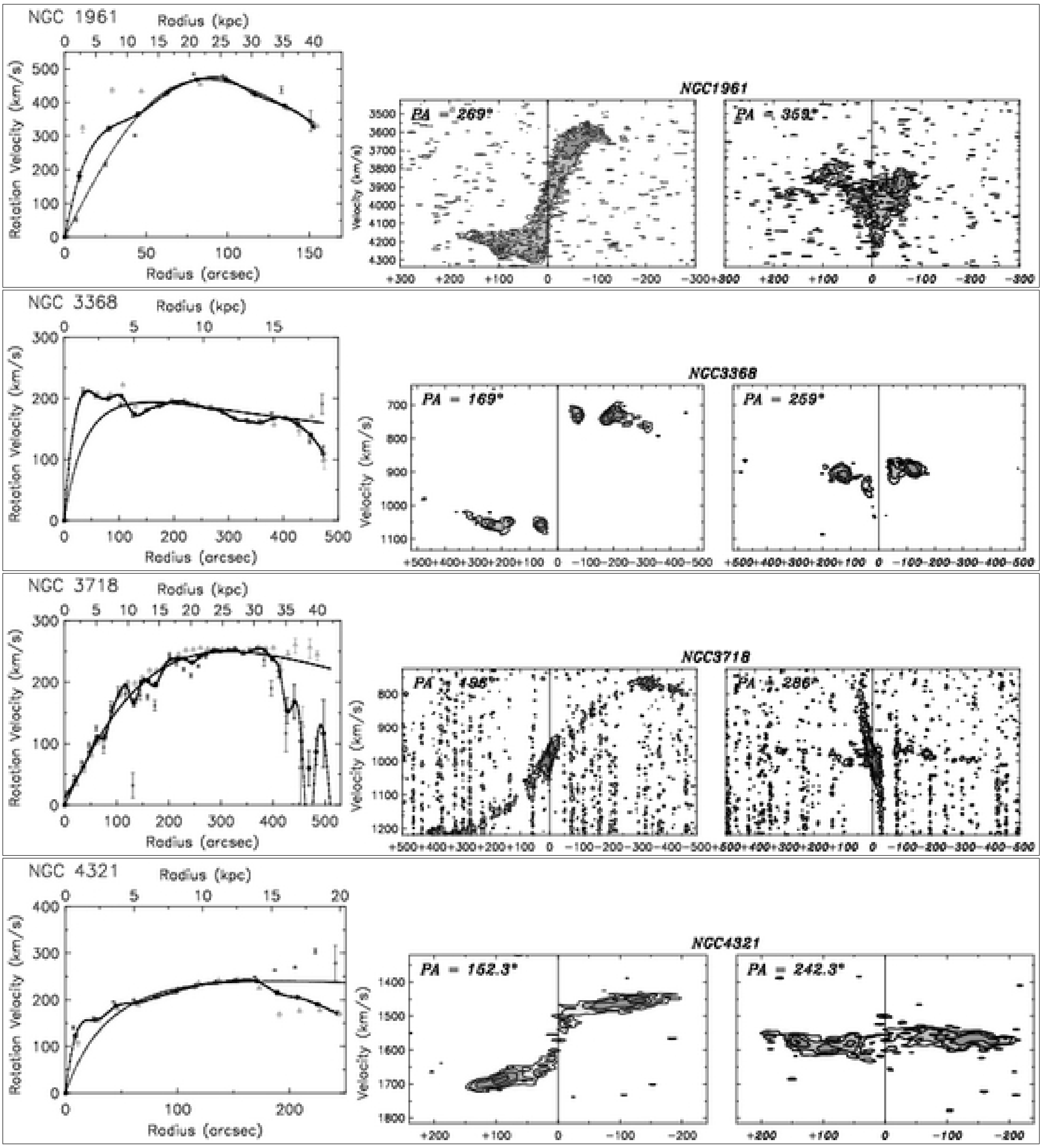

Fig. 3.4 (Continued)

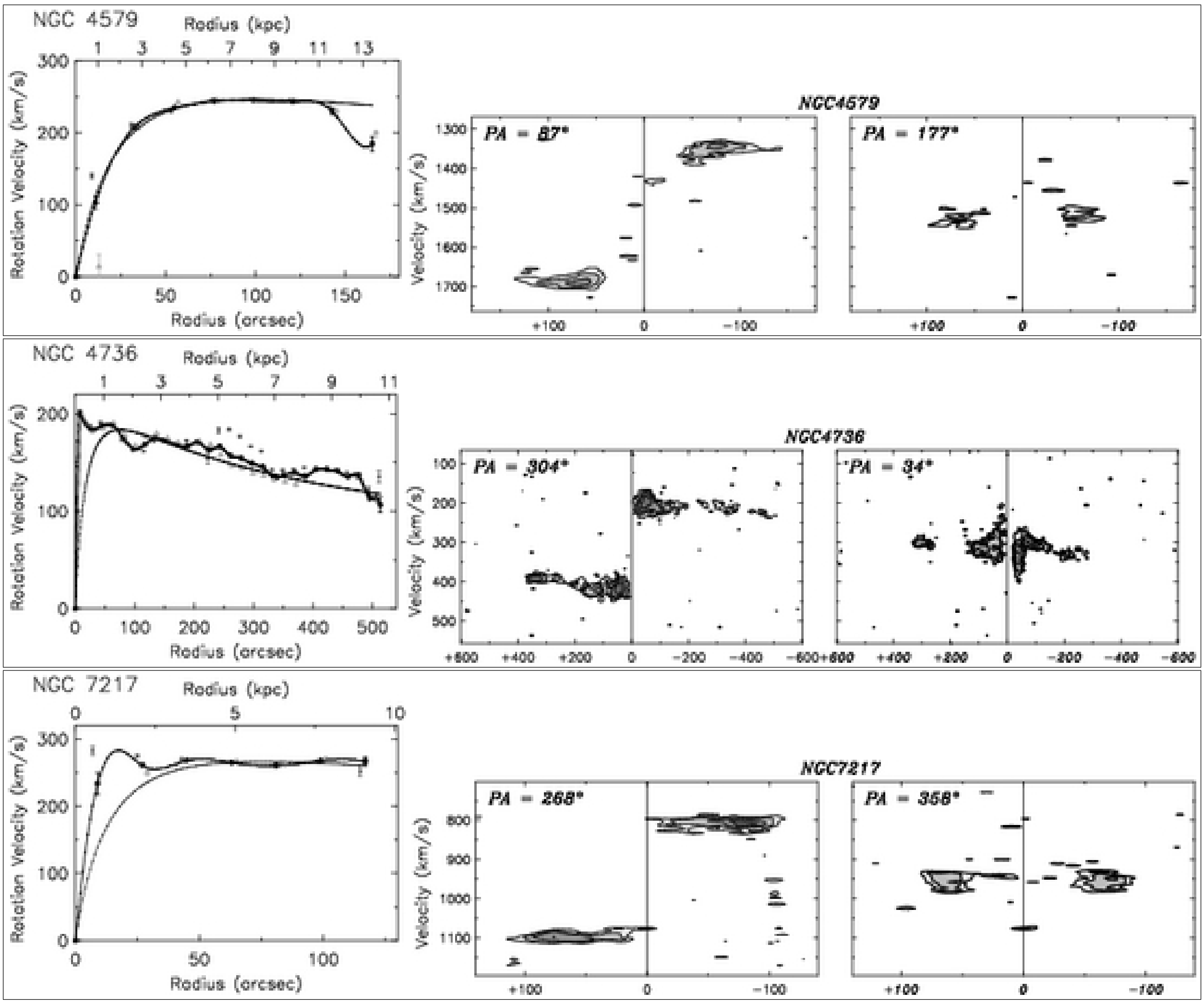

Fig. 3.4 (Continued)

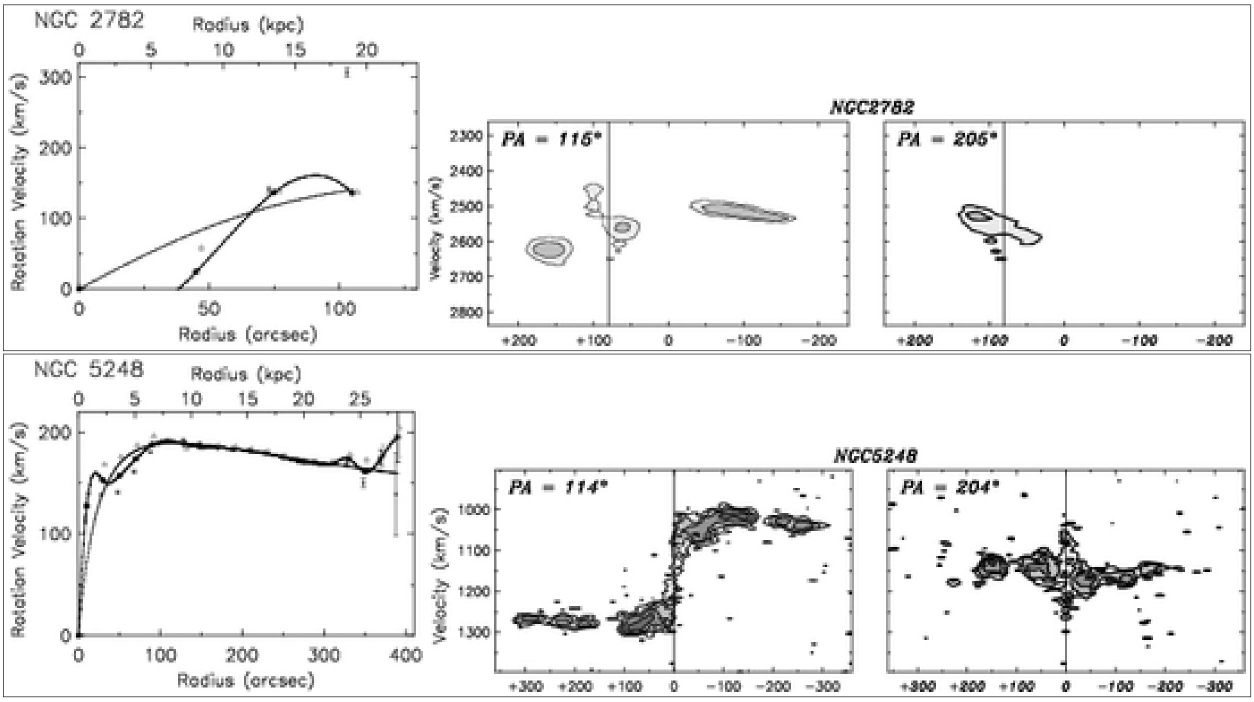

Fig. 3.4 (Continued)

3.3.2 Comparison of Stellar and Gaseous Distribution

In order to compare the stellar distribution with the HI gas distribution, radial profiles were obtained by ellipse fitting using the task ELLINT within GIPSY. The radial profiles of the mean density and the cumulative sum of the optical light (from DSS2-blue images) and HI intensity maps were calculated. The widths of the radii were set to the HI angular resolution which is significantly lower than the typical angular resolution of $\sim 2''$ of the DSS2-blue images. In Fig. 3.5 the mean radial HI and optical profiles are presented (top panel) as well as the cumulative distribution of the HI and optical emission (bottom panel).

To allow for comparison of the spatial extent of the HI gas distribution with the stellar component, the ratio between the radius of the HI disk (R_{HI}) and the radius of the stellar disk (R_{opt}) is calculated. The optical radius R_{opt} was set to the Holmberg radius defined as the parameter log D_{B25} [1] (Hyperleda). In order to obtain an equivalent radius R_{HI} for the HI disk, we measured the radius at a fixed column density of 5.0×10^{19} cm^{-2} for all our galaxies. The radius of the optical disk (R_{opt}) and the HI disk (R_{HI}) are indicated as a dashed and a solid line in Fig. 3.5, respectively. The results are listed in Tab. 3.3 for all galaxies and the mean ratio of $\frac{R_{HI}}{R}{}_{opt}$ is ~ 1.7. In addition the physical radii of the HI disks to this limiting column density are given in Tab. 3.3 with a mean absolute HI radius of 20.6 kpc.

---

[1] Length of the projected major axis at the isophotal level 25 mag/arcsec^2 in the B-band

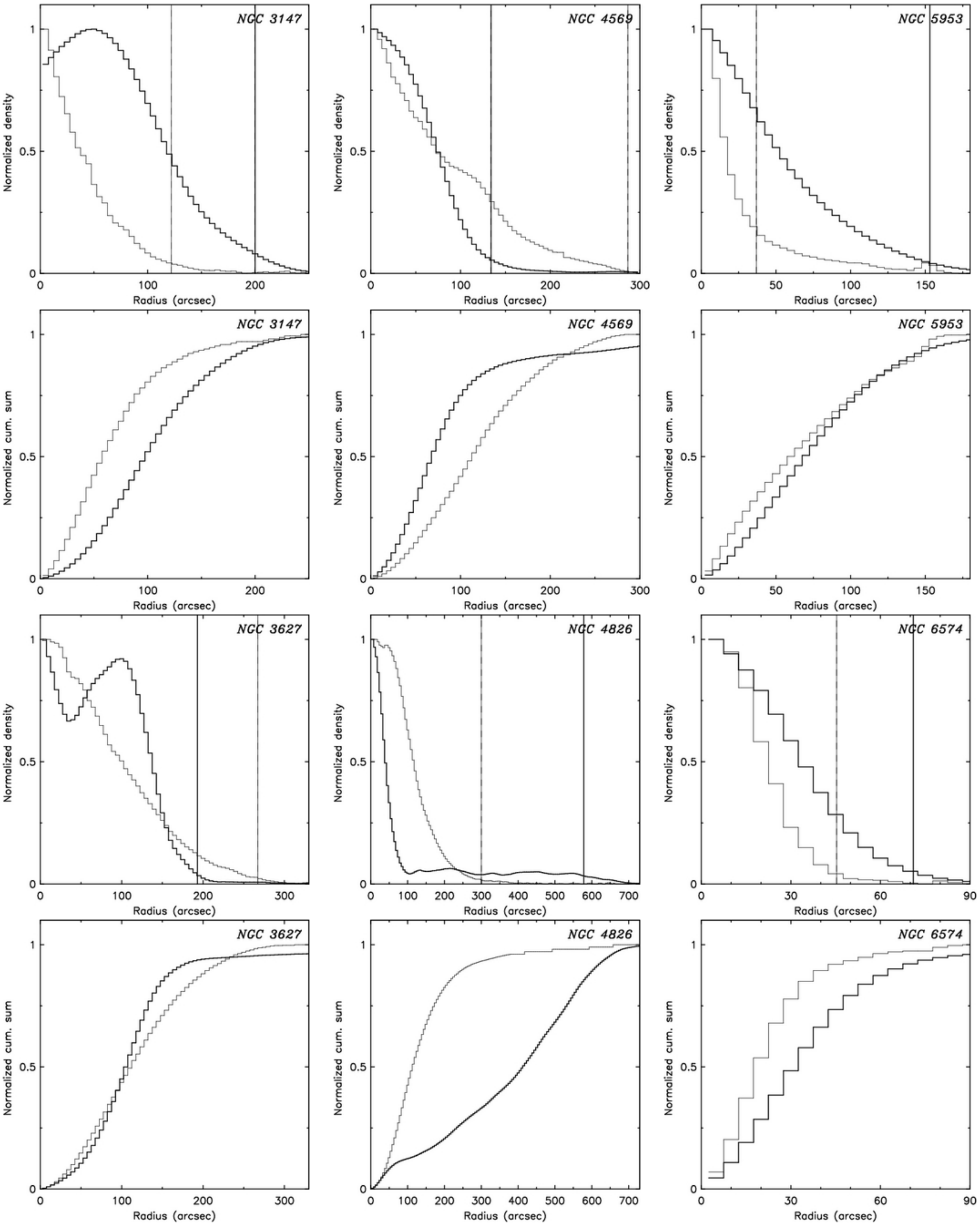

Figure 3.5: Comparison between the optical (thin line) and HI (thick line) radial distribution. The mean radial HI and optical profile are presented in the top panel and the cumulative profiles of the HI and optical emission in the bottom panel for each galaxy. The radius of the HI disk R_{HI} (thick line) and the radius of the stellar disk R_{B25} (thin line) are indicated. The values of R_{B25} are taken from the parameter log(d_{B25}) found in the literature (Hyperleda) and the radius R_{HI} for the HI disk corresponds to a measured column density of 5.0×10^{19} cm^{-2}.

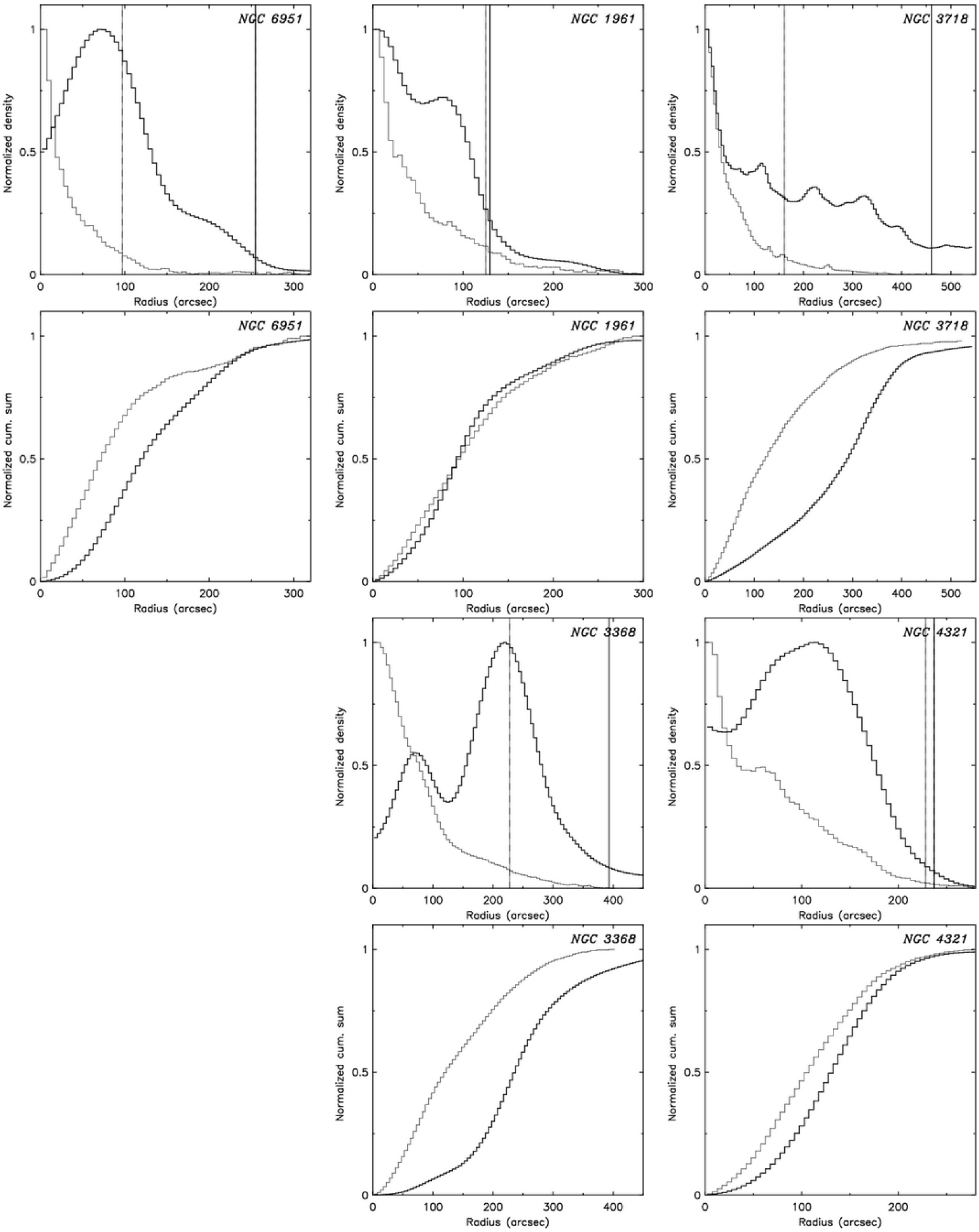

Fig. 3.5 (Continued)

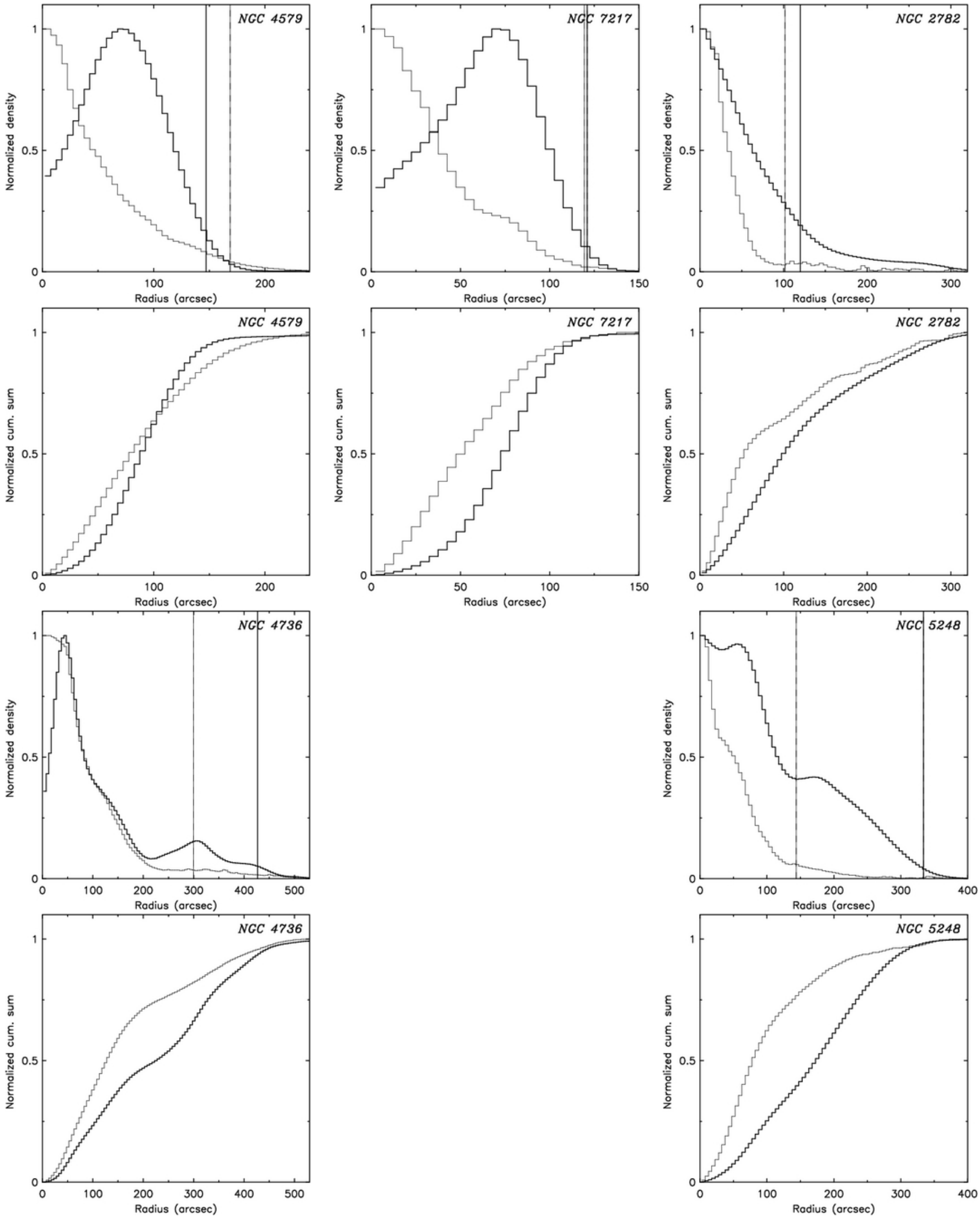

Fig. 3.5 (Continued)

3.3.3 HI Kinematics

Kinematic Parameters and Rotation Curve

The HI morphology provides detailed information about the spatial distribution of the gas, but only in combination with their kinematics can the complete dynamical phase space of the atomic gas be analyzed. Therefore we have performed a detailed kinematic analysis for all galaxies, which includes velocity fields, rotation curves, and residual velocity fields. Fig.3.6 shows (from the left to the right) the intensity-weighted HI mean velocity fields, the HI intensity (color) overlaid with the velocity field (contours), the HI velocity dispersion and the residual velocity field derived from a smooth fit to the rotation curve. The following kinematic parameters (listed in Tab. 3.5) have been derived from the observed velocity field (derived from the robust weighted cubes):

- The dynamical center and its offset from the optical center (taken from Hyperleda).
- The systemic velocity (Heliocentric radial velocity) v_{sys} in km s^{-1}.
- The position angle (PA) in degrees, defined as the angle between the north-direction on the sky and the major axis of the receding half of the galaxy in anti-clockwise direction.
- The inclination (i) in degrees.

These parameters were derived by fitting tilted rings to the velocity field using the task ROTCUR within GIPSY. Initial starting parameters have been taken from cataloged data (NED or Hyperleda). For the fit we excluded data points within an angle of 20° of the minor axis. The widths of the radii were set equivalent to the corresponding angular resolution of each galaxy (see Tab. 3.2). No radial velocity component was fitted. The kinematic parameters have been derived in an iterative way following Begeman (1989). The parameters were assumed to be the same at all radii (unless specified otherwise), except for the circular velocity. Therefore we weighted the obtained value in each ring with its standard deviations, in order to obtain the mean parameter. The iterative process of deriving the kinematic parameters is as follows: we began by fitting both sides of the velocity field in order to determine the systemic velocity (with PA, i held fixed, everything else was free to vary), then the kinematic center (with a fixed PA, i, v_{sys}) and checked again the systemic velocity (with a fixed PA, i and center). Next, the derived center, the inclination and the systemic velocity were held fixed in order to determine the position angle. The position angle was well constrained by the model fits to within $\pm$(1-5)°. The center, the position angle and systemic velocity were held fixed in order to obtain the inclination angle. In case of insufficient precision (statistical error of the inclination fit was $\geq 8°$) for the derived inclination (for NGC 2782, NGC 4569, NGC 6574) we applied an ellipse fit to the optical image. The inclination derived from the optical axial ratio measured at the Holmberg radius was then used to fit the rotation velocity. Finally, the rotation velocities were obtained with fixed inclination, position angle, center and systemic velocity. We used for NGC 4826 two different

PA (inner part: R=0 to 64″; outer part: R=64 to 700″) to account for its counter-rotating HI disk. For NGC 3718, the inclination was required to increase from i=48° to 60° to model its warped HI disk. The derived PA was constant over the disk within ±5°. The derived rotation curves for each galaxy are presented in Fig. 3.4 for a) the entire disk (black line), b) the approaching side of the disk only (dark grey dots), and c) the receding side of the disk only (light grey dots).

The derived kinematic parameters and rotation curves have been verified by using INSPECTOR in GIPSY. This task allows us to overlay the circular HI velocities on position-velocity (pv) diagrams in order to verify the tilted ring parameters on the 3-dimensional datacube. Comparison between the derived rotation curves and corresponding pv slices from the data cubes (center and right panel of Fig. 3.4) show the effect of beam smearing (particularly in the inner 20″) and some small misalignments (∼ spatial and spectral resolution) between our modeled parameters and observed kinematics (e.g. center, systemic velocity). Otherwise, the correspondence between model and data is good in all cases (see next subsection).

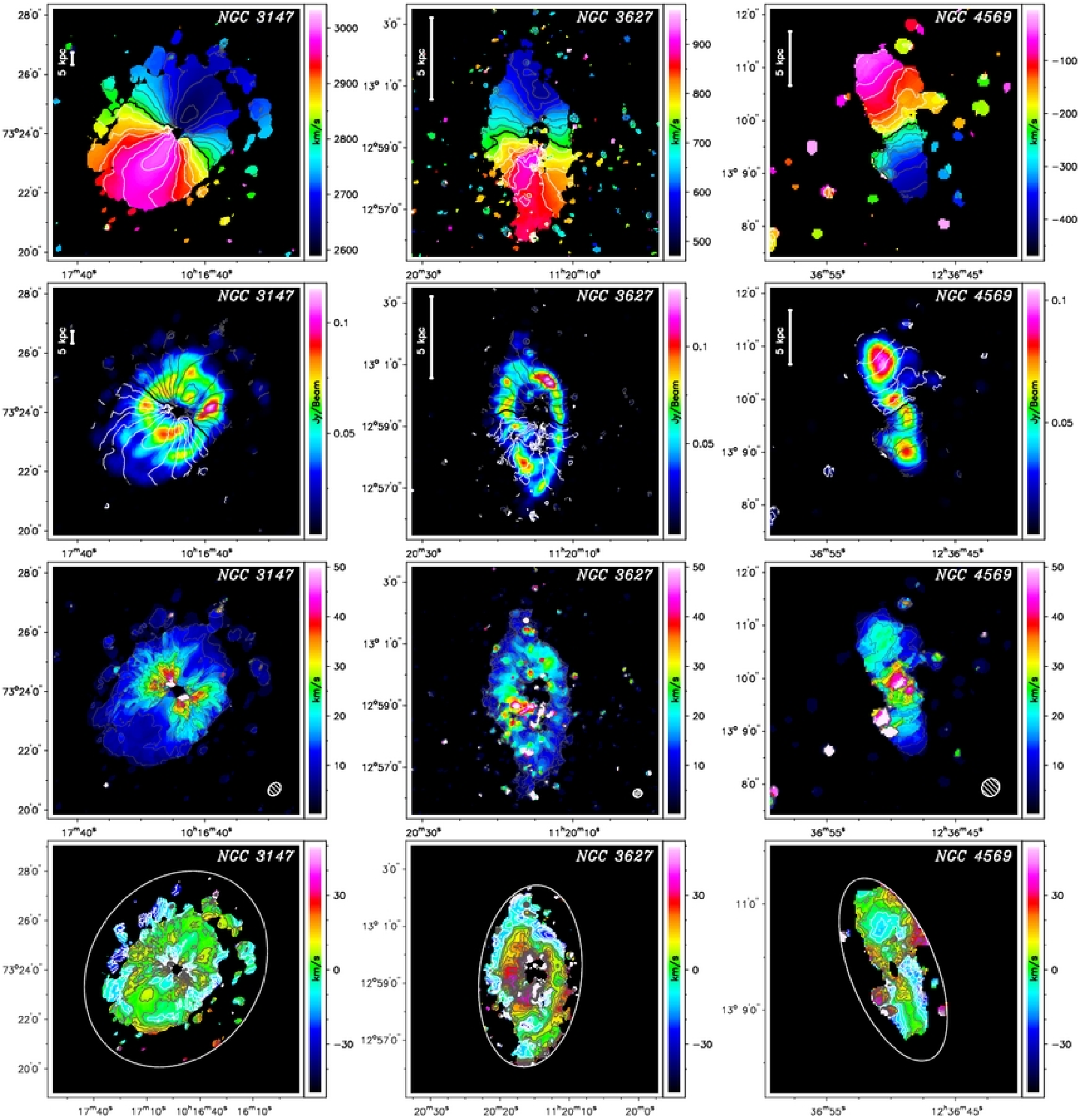

Figure 3.6: Overview of all HI kinematic maps for each galaxy. The intensity-weighted HI mean velocity field, the comparison of HI intensity map and velocity field, the velocity dispersion map, and the residual velocity field are presented (from the top to the bottom). The contours are set in an interval of 25 km s^{-1} for the isovelocity lines (first and second panel from the top), the central line (thick dark line) represents the systemic velocity and white (grey) lines the approaching (receding) velocities. For the dispersion and residual field contours are set in 5 km s^{-1} intervals. The residual velocity field was created by subtracting a model velocity field, derived from a smooth fit to the rotation curve, from the observed velocity field (see text for details). The white ellipse in the residual field (bottom panel) indicates the maximum radius of the model velocity field.

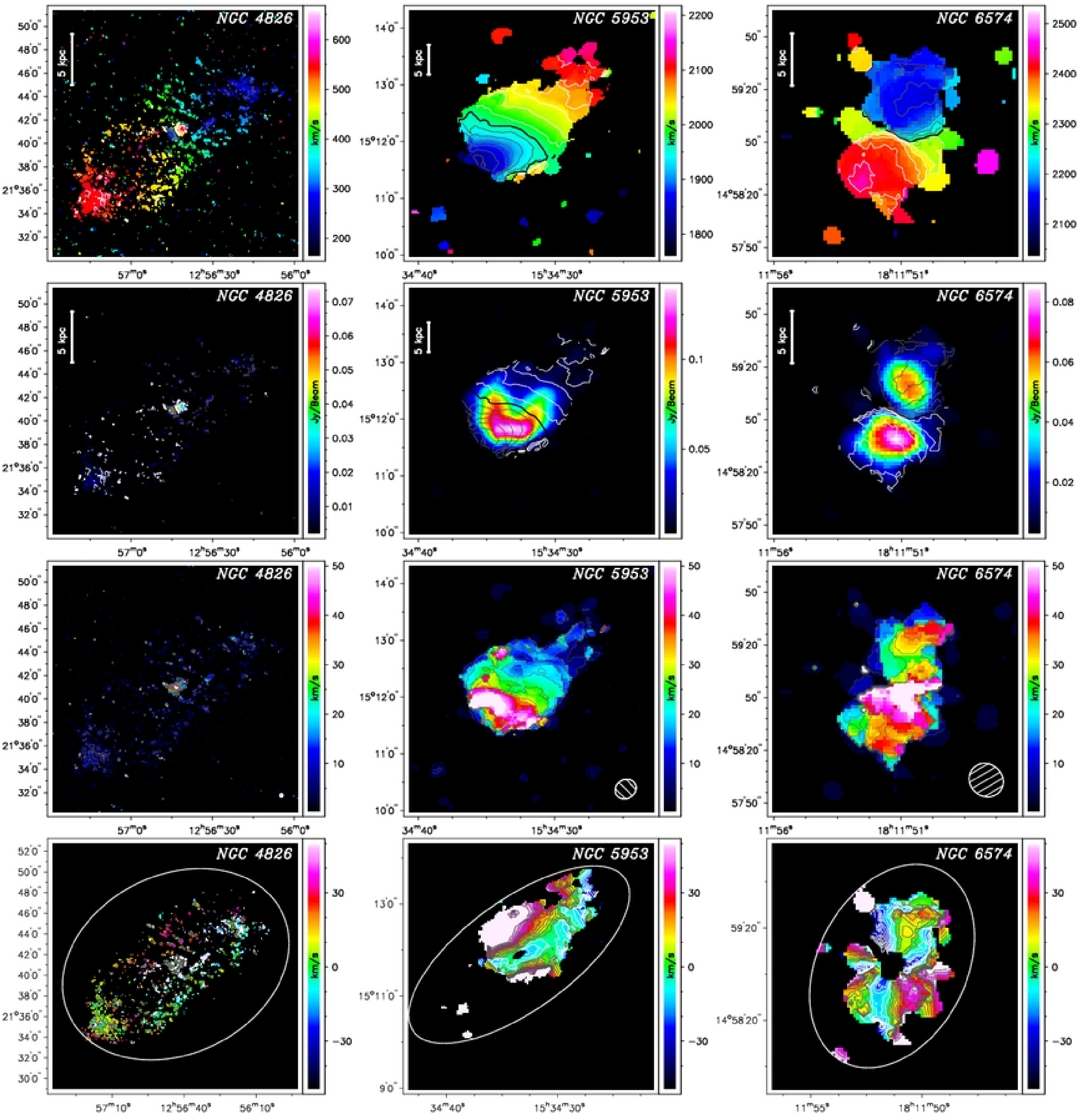

Fig. 3.6 (Continued)

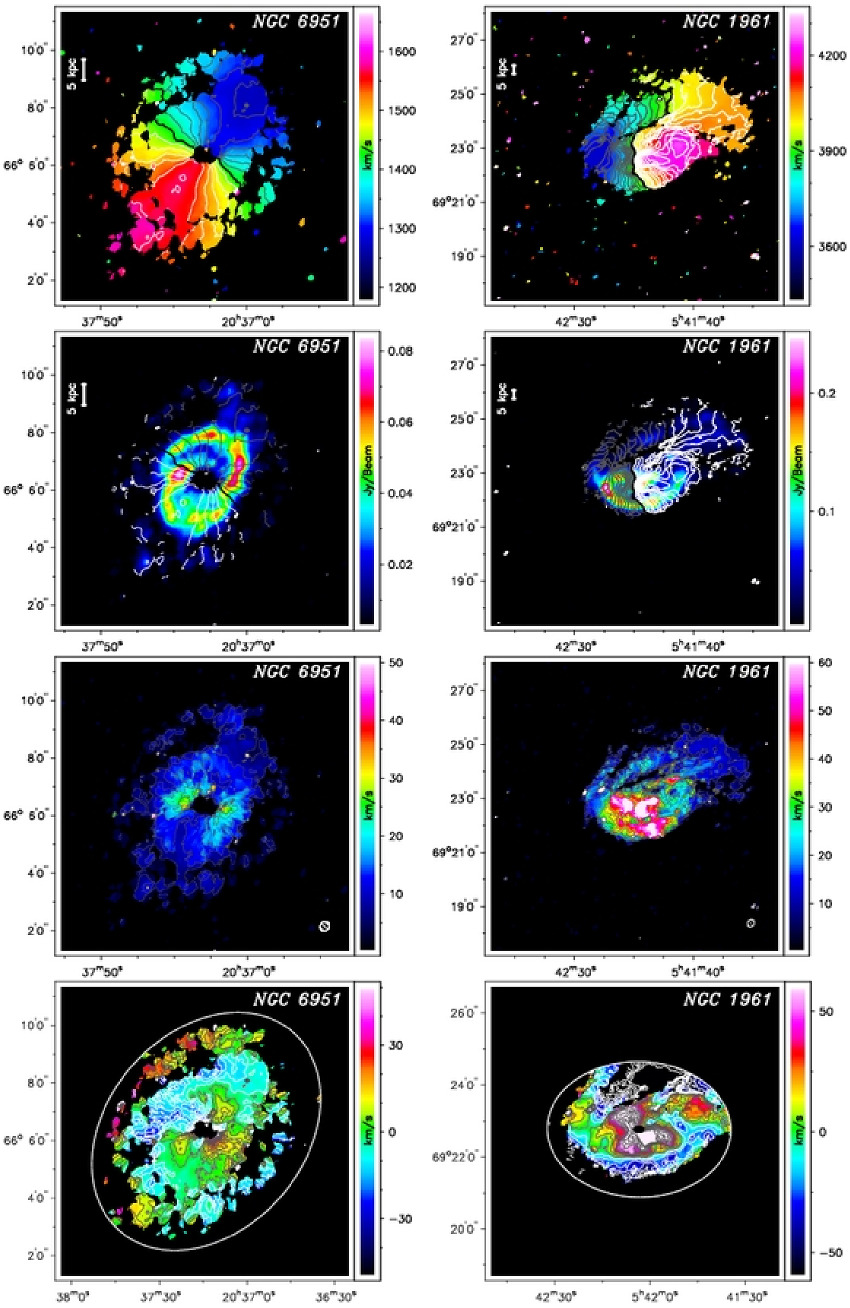

Fig. 3.6 (Continued)

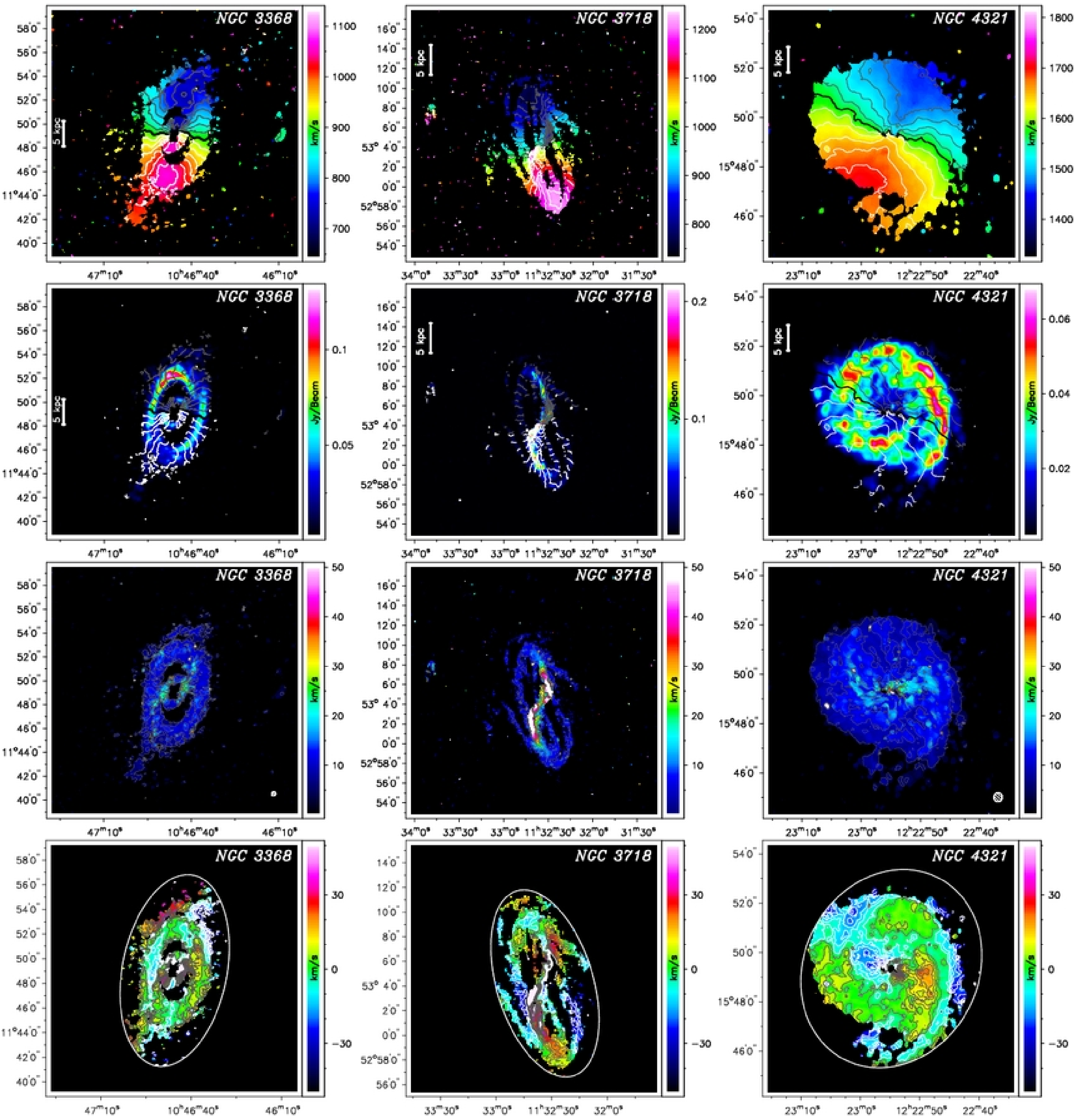

Fig. 3.6 (Continued)

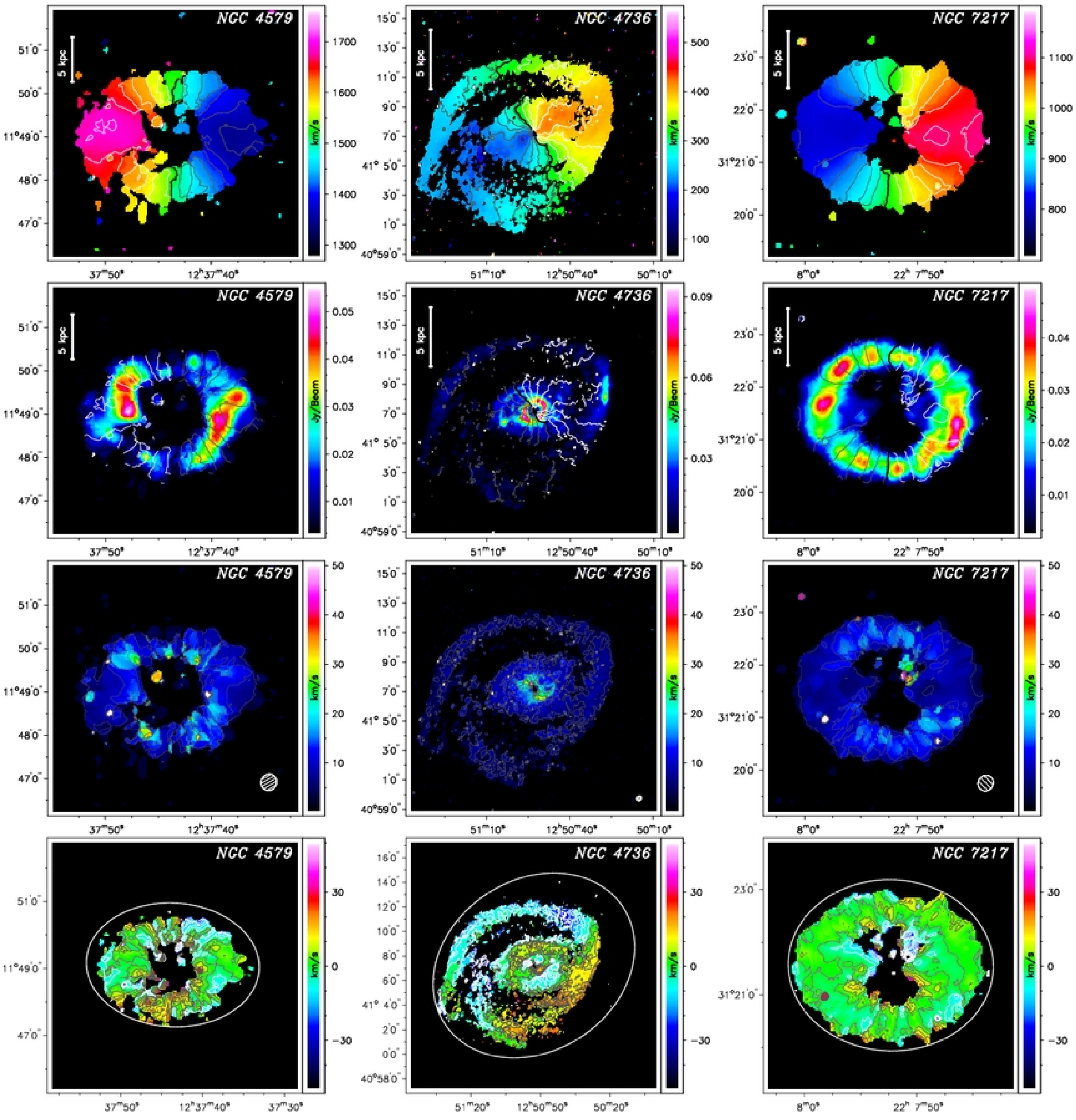

Fig. 3.6 (Continued)

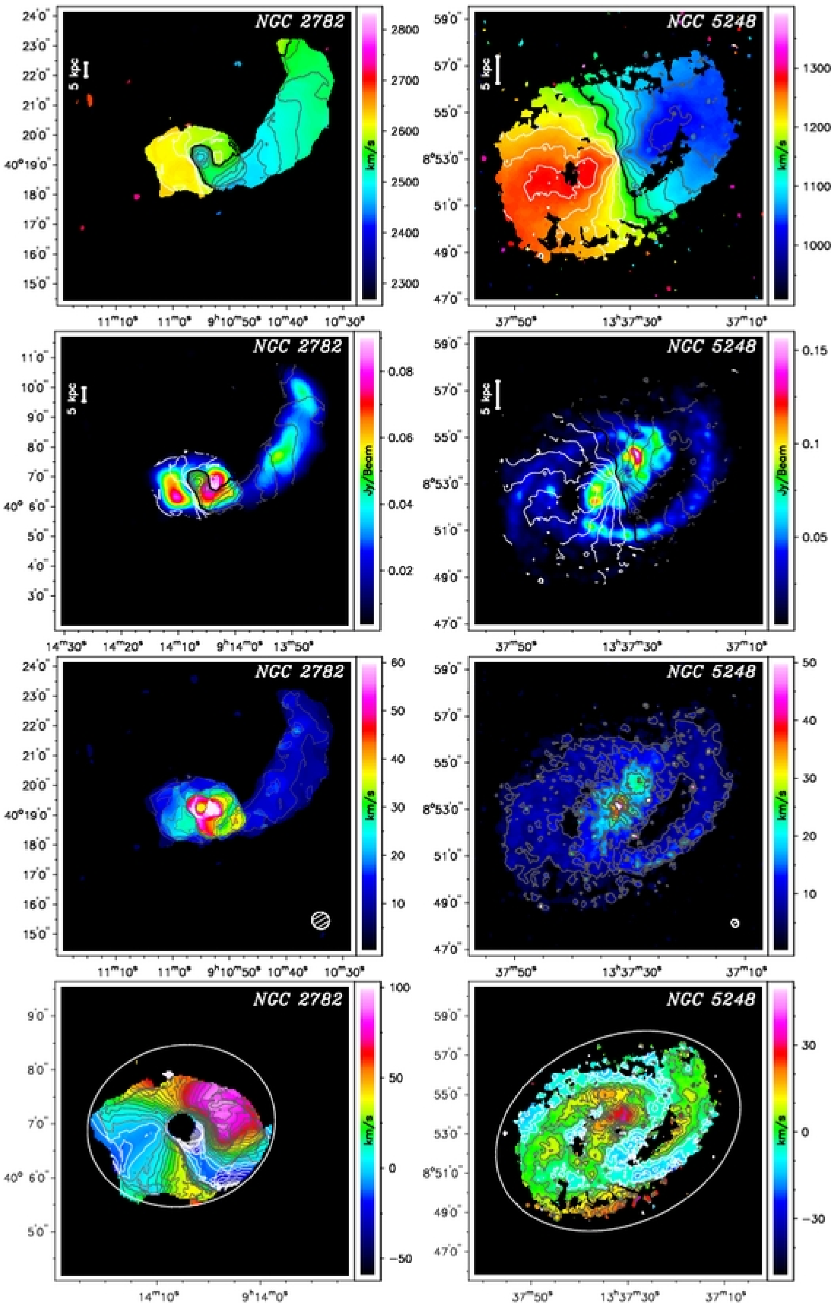

Fig. 3.6 (Continued)

Velocity Fields and Velocity Dispersion

2-D model velocity fields have been created from the derived interpolated rotation curves using the program *VELFI* within GIPSY. These model velocity fields were subtracted from the observed velocity fields to obtain residual velocity fields. The typical range of the residual velocities is ± 25 km s^{-1}. Furthermore, the residual velocity fields (Fig. 3.6) can also be utilized to identify systematic misalignments of the derived kinematic parameters (Warner et al., 1973). However, no obvious misalignments were identified.

Most of the galaxies in our sample exhibit fairly regular velocity fields that are dominated by circular motion. The three exceptional cases are described in the following: NGC 2782 exhibits a large gaseous tidal tail (see §3.3.1) with a velocity gradient of ∼100 km s^{-1} over ∼65kpc (360″) across that tail. The residual velocity field shows that the HI kinematics in the inner HI disk (which coincides with the stellar disk) are fairly different. Smith (1991; 1994) using HI data at ∼9″ resolution found in addition 1) a shorter HI structure extending toward the east (with $6.6{\cdot}10^8 M_{\odot}$) and 2) that the HI gas in the inner disk is counterrotation with respect to the tidal material, suggesting a merging of two galaxies of unequal masses. Due to the resolution of 34″ of our HI data, this disk is basically unresolved and the derived rotation curve reflects partially the kinematic properties of the tidal tails.

NGC 5953 exhibits significant streaming motions, inconsistent with global rotation, with a velocity gradient of ∼60 km s^{-1} over 100″ (∼17kpc). Also NGC 1961 shows streaming motions in the northern part of its HI distribution (velocity gradient ∼400 km s^{-1} over 180″, ∼47kpc), in addition to a rotating disk which is coinciding with the optical one. The residual velocity fields revealed for some galaxies of our sample (e.g. NGC 5248, inner disk of NGC 6951) indications for non-circular motions. Such motions can be caused by a bar potential or spiral waves (van der Kruit & Allen, 1978).

The velocity dispersion maps show that the majority of our galaxies have an average velocity dispersion between 10 and 30 km s^{-1}. The reason for the larger dispersion along the minor axis seen in almost all galaxies is likely caused by an observational effect: the angular distance between adjacent velocities becomes smaller along the minor axis, and hence the beam covers a larger velocity gradient. For NGC 3147, NGC 6574, NGC 3627 and NGC 4569 we found slightly higher dispersion with an average of 15-25 km s^{-1} and maxima of 40-70 km s^{-1}. Further, the highly-disturbed galaxies (NGC 1961, NGC 2782, NGC 5953) exhibit very large velocity dispersion with maxima of 60-100 km s^{-1}.

Table 3.5: Kinematic Parameters

Source	RA (J2000)	Dec (J2000)	Offset [arcsec]	v_{sys} [km/s]	PA [deg]	i [deg]	v^{Br} [km/s]	R^{Br} [arcsec]	n^{Br}
NGC 3147	10 16 53.66	+73 24 02.8	0.2 ± 1.0	2811.7 ± 0.6	144.6 ± 1.0	34.7 ± 3.4	332±12	61±22	1.03±0.04
NGC 3627	11 20 15.59	+12 59 15.1	16.8 ± 0.7	719.7 ± 6.8	173.6 ± 1.6	56.0 ± 3.2	192±8	123±87	1.04±0.13
NGC 4569	12 36 49.81	+13 09 46.0	0.3 ± 1.9	-228.7 ± 4.0	22.4 ± 2.9	63.7 ± 3.2	167±64	45±41	0.76±0.07
NGC 4826	12 56 43.70	+21 40 54.7	2.8 ± 1.2	404.0 ± 3.3	296.2 ± 6.0	48.1 ± 17.8	207±87	53±122	1.06±0.07
outer disk				127.4 ± 2.6	64.7 ± 5.5	70±28	1446±96	1.57±0.21	
NGC 5953	15 34 33.43	+15 11 53.8	22.4 ± 5.8	1906.2 ± 6.5	306.5 ± 2.8	65.2 ± 2.6	139±640	60±366	0.50±0.20
NGC 6574	18 11 51.35	+14 58 55.1	1.9 ± 5.0	2285.6 ± 6.2	155.4 ± 1.9	46.3 ± 3.2	196±30	35±15	1.20±0.15
NGC 6951	20 37 14.26	+66 06 19.3	2.7 ± 0.5	1425.6 ± 1.3	138.7 ± 1.2	41.5 ± 1.5	193±13.8	41±17	0.88±0.02
NGC 1961	05 42 04.35	+69 22 46.5	7.5 ± 2.4	3928.5 ± 15.8	269.1 ± 5.0	42.6 ± 4.0	104±4	274±1	1.95±0.02
NGC 3368	10 46 45.53	+11 49 02.6	9.7 ± 0.5	896.9 ± 2.1	169.0 ± 1.5	57.5 ± 2.1	193±5	177±102	1.02±0.08
NGC 3718	11 32 34.59	+53 04 07.9	5.2 ± 0.6	986.4 ± 6.9	196.0 ± 5.7	48-60	150±29	849±46	1.43±0.11
NGC 4321	12 22 54.83	+15 49 20.6	1.1 ± 0.8	1577.5 ± 2.1	152.3 ± 1.4	31.7 ± 3.5	240±5	176±117	0.99±0.16
NGC 4579	12 37 43.64	+11 49 06.4	2.0 ± 0.5	1517.7 ± 1.0	87.2 ± 1.3	44.5 ± 5.2	244±9	83±50	0.97±0.09
NGC 4736	12 50 53.00	+41 07 14.3	1.1 ± 0.1	310.4 ± 0.3	303.8 ± 1.1	36.6 ± 2.4	183±2	27±5	0.92±0.01
NGC 7217	22 07 52.31	+31 21 33.8	1.1 ± 1.6	951.9 ± 2.5	268.0 ± 1.7	33.7 ± 3.3	261±32	50±64	0.94±0.14
NGC 2782	09 14 05.96	+40 06 53.3	13.4 ± 0.9	2559.0 ± 7.4	115 ± 21.8	31.7^b ± 3.2	55±474	456±448	1.69±4.2
NGC 5248	13 37 32.02	+08 53 08.1	2.0 ± 0.8	1151.1 ± 1.1	114.4 ± 1.0	43.1 ± 1.6	188±2	97±19	0.97±0.02

Note. — Overview of the kinematic parameters derived from the observed velocity fields by tilted-ring model fits: The dynamical center of the HI disk and its offset from the optical center, the systemic velocity v_{sys}, the position angle PA and the inclination i are listed for all galaxies. A Brandt curve fit has been applied to the rotation velocities where v^{Br} is the maximum rotation velocity, R^{Br} the radius of maximum rotation velocity, and n the Brandt curve index as a parameter of the steepness of the curve. Note that the values for NGC 2782 are likely incorrect, as there is a short tidal tail to the east which is barely resolved at our resolution (see Smith, 1994).

Table 3.6: Mass Properties

Source	Flux [Jy km/s]	M_{HI} [$10^9 M_{sun}$]	M_{HI}/M_{dyn}	$v(R_{HI})$ [km/s]	R_{HI} [kpc]	M_{dyn} [$10^{11} M_{sun}$]	M_{dyn}^{Brandt} [$10^{11} M_{sun}$]
NGC3147	22.7	8.96	0.016	249	39.7	5.7	10.1
NGC3627	32.8	0.34	0.007	185	6.2	0.5	0.9
NGC4569	7.5	0.5	0.003	245	10.9	1.5	1.2
NGC4826	45.9	0.18	0.003	149	11.5	0.6	2.5
NGC5953	6.9	1.77	0.004	276	24.5	4.3	4.9
NGC6574	2.93	0.85	0.019	126	12.0	0.4	1.5
NGC6951	34.8	4.77	0.014	221	29.8	3.4	1.7
NGC1961	68	46.62	0.037	402	34.0	12.8	3.4
NGC3368	64.2	0.99	0.010	169	15.4	1.0	2.0
NGC3718	115.1	7.85	0.016	234	37.9	4.8	8.6
NGC4321	51.1	3.4	0.013	238	19.3	2.5	6.6
NGC4579	8.5	0.57	0.004	241	12.0	1.6	3.3
NGC4736	87	0.38	0.009	141	8.9	0.4	0.2
NGC7217	9.7	0.59	0.004	263	9.4	1.5	2.2
NGC2782	14.8	4.86	0.046	145	21.7	1.1	1.2
NGC5248	81.3	4.32	0.028	166	24.3	1.6	2.0

Note. — Overview of the mass properties, including the measured HI flux, the dynamical mass M_{dyn}^{Brandt} obtained from the Brandt fit and the dynamical mass M_{dyn} derived from the deprojected circular velocity $v(R_{HI})$ at the HI radius R_{HI}. The ratio of the HI mass and the dynamical mass M_{dyn} of a galaxy is given by $M_{HI}/Mdyn$. Note that M_{dyn} for NGC 2782 is likely incorrect, as there is a short tidal tail to the east which is barely resolved at our resolution(see Smith, 1994).

3.3.4 Gaseous and Dynamical Masses

The HI fluxes of the galactic disks were measured in the intensity maps of the naturally weighted cubes. The intensity maps were corrected for the response of the VLA primary beam. In Tab. 3.6 the HI flux and the corresponding HI mass are listed for each galaxy. The average HI mass of our sample is $5.4 \times 10^9 M_\odot$ with a maximum mass of $46.6 \times 10^9 M_\odot$ (NGC 1961).

To obtain the dynamical mass we used two approaches. A Brandt curve (Brandt, 1960) was fitted (black curve) to the measured rotation velocities of the whole disk. The Brandt curve is an approximation of a solid-body rotation at small radii and a Keplerian-type velocity decrease at large radii and can be described by (see equation [26] and [28] of Brandt)

$$\frac{v(R)}{v^{Br}} = \frac{R}{R^{Br}} \left[1/3 + 2/3 \left(\frac{R}{R^{Br}} \right)^{n} \right]^{-3/2n}, \tag{3.4}$$

where v^{Br} is the maximum rotation velocity at the radius R^{Br} and n is an index parameterizing the steepness of the curve. From the derived parameters the dynamical mass M_{dyn}^{Br} can be calculated (equation [29] of Brandt) via

$$M_{dyn}^{Br} = 1127 \left(\frac{3}{2} \right)^{3/n} R^{Br} \, v^{Br} \, D \tag{3.5}$$

with M_{dyn}^{Br} in solar mass units, the distance D in [Mpc], the velocity parameter v^{Br} in [km s^{-1}] and the radius parameter R^{Br} in [$''$]. For all galaxies the derived dynamical masses are listed in Table 3.6. In addition, we have calculated the dynamical mass via the spherical symmetry approximation:

$$M_{dyn} = \frac{R\, v^2}{G}, \quad M_{dyn}[M_\odot] = 232407 \; R_{HI}[kpc] \; v^2[(km \; s^{-1})^2], \tag{3.6}$$

with the circular velocity v from the rotation curve at the HI radius R_{HI} (see §3.3.2). Note that the mass could be 40% lower, if a disk geometry would be assumed instead of a spherical one. The dynamical mass M_{dyn}^{Br} obtained by the Brandt fit and the dynamical mass derived at the HI radius M_{dyn} are presented in Tab. 3.6. The comparison between both methods shows that the mass derived by the Brandt fit is on average a factor of two larger as the mass derived at the HI radius. This difference might be expected since the Brandt method is based on the assumption that the rotation curve reaches a Keplerian fall off quite rapidly, which is not exactly the case for most of our galaxies (probably due to dark matter contribution in the outer disk regions). Hence we will use in the following calculations of this paper the dynamical mass derived from Eq. 3.6. The ratio of the HI mass to the dynamical mass of a galaxy is given by M_{HI}/M_{dyn} which lies for our sample in a range of 0.003 to 0.046 with an average ratio of 0.015.

3.3.5 HI Properties as a Function of AGN Type

Here, we investigate possible correlations between the observed HI properties of our galaxies and their type of nuclear activity. Since our sample, as described in §3.2.1, consists mainly of Seyfert (Sy) and LINER (L) host galaxies, we will focus on a comparison of these two classes. A summary of the average properties for each AGN type is listed in Tab. 3.7. The error calculation is based on the bootstrapping method (Efron , 1979) by taking the standard deviation of the mean values from 1000 replications.

Table 3.7: AGN Type Relations

Properties	Seyfert	LINER	non-AGN
Distance [Mpc]	22.9	20.0	26.2
Morph. Type t	2.8 ± 0.5	2.7 ± 0.4	2.6
Disturbed (%)	14 ± 13	71 ± 17	1
HI detected companions (%)	14 ± 13	43 ± 18	1
R_{HI} [kpc]	19.2	19.6	23.0
R_{B25} [kpc]	12.4	14.7	14.4
$\frac{R_{HI}}{R_{B25}}$	1.9 ± 0.43	1.4 ± 0.25	1.8
HI Mass [$10^9 M_\odot$]	2.5 ± 1.1	8.6 ± 5.9	4.5
$\frac{M_{HI}}{M_{dyn}}$	0.009 ± 0.002	0.013 ± 0.004	1.8
Ring (%)	0	80 ± 18	0
Spiral (%)	60	60	100

Note. — Overview of the mean HI properties as a function of AGN type, for Seyferts, LINERs and non-AGN galaxies. For each AGN type the number of galaxies, the average distance, the percentage of galaxies with disturbed disk and HI companions, the mean HI radius R_{HI} at a HI column density of 5.0×10^{19} cm^{-2}, the mean optical radius R_{B25}, the ratio R_{HI}/R_{B25}, the average HI mass of the disk, the average morphology type t, and the percentage of ringed, spiral and concentrated HI structure are listed. In addition, also the corresponding standard deviations are specified (using Bootstrapping method, see §3.3.5).

Environment and HI Morphology

As already described in §3.3.1 we found in our sample several galaxies which are surrounded by companions and/or have disturbed outer disks. No significant statistical relation is found between HI environment and AGN type: The percentage of optical companions is roughly the same for each AGN-type (Sy: 3/7, L: 4/7), and the number of galaxies with HI-detected companions (Sy: 1/7 ; L: 2/7; HII: 1/2) is also similar given our small number statistics. Galaxies with disturbed outer disks seem to be more abundant in LINER hosts (5/7) than in Seyfert hosts (1/7). The origin of these disturbances will be discussed in §3.4.1.

In order to search for a possible correlation between the HI morphology and the AGN type, we excluded the following galaxies from the analysis, as their HI disk morphology is highly asymmetric and hence their morphology can not reliably be assigned: NGC 1961 (large gas extention to NW), NGC 5953 (interacting system NGC 5953/54), NGC 3718 (warped HI disk with inner disk close to edge-on), NGC 4826 (very concentrated in center, counter-rotating HI disks). Thus the number of Seyferts and LINERs is reduced to 5 galaxies for each type. Only LINER host galaxies show ringed HI morphology (LINERs: 80%, Sy: 0%), while gas spiral arms appear as frequently in both types (Sy: 60%, L: 60%). We used the bootstrapping method (Efron , 1979) to calculate the statistical significance of this result: The confidence interval (at percentiles of [5, 95]%) for LINERs is [40, 100]% for ringed structure. The standard deviation of the mean values for HI rings is found to be (80±17)%. Furthermore, the radii of the HI rings were determined but neither the absolute radius was found to be the same for all ringed galaxies (range between 0.9-5.7 kpc), nor the relative radius of the ring to the optical disk (R_{ring}/R_{opt}: 0.15-0.6) or to the HI disk (R_{ring}/R_{opt}: 0.11-0.6) shows any obvious trend.

Masses

In order to search for a possible relation between the mass properties and the nuclear activity type, we compared the dynamical mass (within the HI radius R_{HI}) as well as the HI mass as a function of the AGN type. The mean dynamical mass is slightly larger for LINERs ($3.5{\cdot}10^{11} M_{\odot}$) than for Seyfert galaxies (M_{dyn} is $2.4{\cdot}10^{11} M_{\odot}$) but similar within a range of $[0.45\text{-}5.7]{\cdot}10^{11} M_{\odot}$ (Sy) and $[0.4\text{-}12.3]{\cdot}10^{11} M_{\odot}$ (L). For the HI gas content, we found for Seyfert galaxies a smaller mean HI mass ($2.5{\cdot}10^{9} M_{\odot}$) than for LINERs ($8.6{\cdot}10^{9} M_{\odot}$) with a range of $[0.2\text{-}9.0]{\cdot}10^{9} M_{\odot}$ and $[3.8\text{-}46.6]\ {\cdot}10^{9} M_{\odot}$, respectively. In order to study the relative gas content we calculated the ratio of M_{HI}/M_{dyn} for each galaxy and averaged it for a given AGN type. The mean ratio of M_{HI}/M_{dyn} is 0.009 for Seyfert and 0.013 for LINER host galaxies. Interestingly, the two non-AGN galaxies in our sample have a larger HI gas content of 0.046 and 0.028. The mean Hubble type is roughly the same for our Seyfert (t=2.8), LINER (t=2.7), and non-AGN (t=2.6) sample.

A comparison between the relative gas content (M_{HI}/D_{25}) versus Hubble type for our samples (Sy, L, non-AGN) and typical values for a larger sample (Bettoni et al., 2003) is presented in Fig 3.7. On average the relative gas content of the sample of Bettoni et al. seems to be larger compared to our sample. Note that Bettoni et al. (2003) excluded galaxies cataloged as having distorted morphology and/or any signature of peculiar kinematics (such as polar rings, counterrotating disks or other kinematically decoupled components) and thus their sample does not contain galaxies similar to ours.

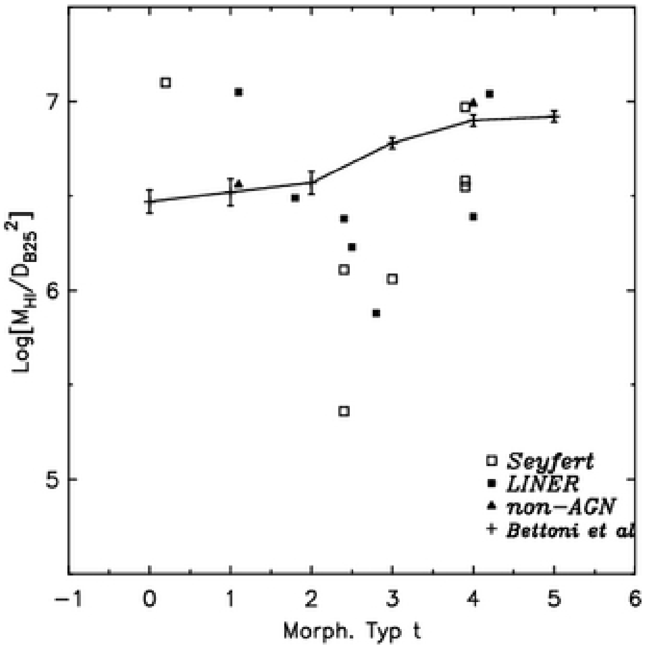

Figure 3.7: Comparison of the relative gas content versus Hubble type (Morphology type t) between our sample (Sy, LINER, non-AGN) and a larger sample of 1916 galaxies by Bettoni et al (2003; the average values are plotted and connected with a solid line). The relative gas content is given as the ratio of the atomic gas mass to the square of the diameter in kpc at the isophote of 25 mag arcsec^{-2} M_{HI}/D^2_{B25}.

HI versus Optical Extent

In order to compare the relative gas disk size between different AGN types, we averaged the ratio R_{HI}/R_{opt} of the HI radius R_{HI} to the optical radius R_{opt} (as described in §3.3.2) for each AGN type. This analysis shows that the gas disk in Seyfert galaxies is slightly larger with an average ratio of 1.9 for Seyferts than for LINERs (1.4). However, the difference is within the statistical deviation ($\pm \sim$0.6). If we neglect galaxies which are part of a galaxy group or cluster (NGC3627, NGC4569, NGC4579), the ratios increase to 2.4 and 1.5, respectively (which corresponds to a difference of 0.9 ± 0.6). Thus, there is a hint that Seyfert galaxies might eventually have more extended HI gas disks than LINER galaxies.

3.3.6 Synopsis of Results

The atomic gas distribution and kinematics for a sample of 16 galaxies have been presented. There is a large variety of HI distribution in the sample (spiral-, ringed- and centrally concentrated geometries) and some galaxies show strongly disturbed HI disks. Most of our galaxies exhibit fairly regular HI gas distribution, exceptions are discussed below. The analysis of the large environment revealed that 5 galaxies have HI-rich companions and for several galaxies potential optical companions are present. The distributions of the gaseous and stellar component are compared, kinematic properties of the HI gas are analyzed (i.e. rotation curves, residual velocity maps), and the gaseous and dynamical masses are derived. Furthermore, a comparison of HI properties and AGN type suggest correlations with HI morphology and host disturbance: LINER host galaxies seem to have a larger fraction of disturbed HI disks, a significant higher percentage of HI ring geometry, and tend to possess a smaller HI extent (relative to the optical radius) than Seyfert host galaxies. No correlation between the presence of companions and the AGN type was found.

3.4 Discussion

The relationship between large scale environment and nuclear activity has been long debated in the literature. Several studies have found indications for correlations between the environment and nuclear activity (Storchi-Bergmann et al., 2001; Chatzichristou, 2002; Márquez et al., 2003). In particular it was suggested that interacting galaxies or galaxies with companions exhibit a significant excess of nuclear activity compared to isolated galaxies (Dahari, 1984; Keel et al., 1985; Rafanelli et al., 1995). On the other hand no relation was seen by other studies (Virani et al., 2000; Schmitt, 2001; Fuentes-Williams & Stocke, 1988; MacKenty, 1989; Laurikainen & Salo, 1995). Hence the issue of possible relations between the environment and nuclear activity appears to be still controversial. Furthermore, results from

Keel et al. (1985) suggested that nuclear phenomena might likely be triggered by a tidally induced inflow of gas from the disk to the nuclear regions, rather than gas transfer between the interacting galaxies themselves. Keel (1996) also found that Seyfert galaxies in pairs actually display smaller kinematic disturbances than non-Seyfert galaxies in pairs, which is obviously in disagreement with the hypothesis that tidal interactions are necessary for the transport of angular momentum and the fueling of the SMBH. Since most of these studies are based on optical/IR imaging, they are in principle less sensitive to distortions than our study of the atomic gas that reacts most readily to tidal disturbances. It should be pointed out that a detailed study of HI gas properties for active versus non-active galaxies (Mundell et al., in prep.) is under-way.

In the context of different AGN types, the analysis of a sample of 451 active galaxies (Sy, LINER, Transition, HII, and absorption-line galaxies) from the Palomar survey (Schmitt, 2001) showed no correlation between AGN-type and the percentage of galaxies with nearby companions after taking morphological differences of the host galaxies into account. We also see no evidence for a correlation between the fraction of companions and the AGN type present (Seyfert, LINER galaxies), neither from our HI study nor for cataloged optical companions listed in NED (see §3.3.1). Note that our sample has a limited number of LINERs (7 galaxies) and Seyfert galaxies (7) and hence the existence of possible relations can not be completely excluded.

3.4.1 HI Environment: Tidal Forces and their Correlation with Disturbed HI Disks

Companion galaxies can possibly disturb the HI gas in a galactic disk via tidal forces and hence affect the fueling of the center with gas (e.g. Keel et al., 1985). The sensitivity and endurance of HI to trace the strength and prevalence of tidal interactions among Seyfert galaxies is discussed in detail by Greene et al. (2004). In our analysis we found companions for about half of our sample. In almost all cases the produced tidal forces are smaller than the binding forces of the affected host galaxy (indicated as $\mathbf{Q} < 0$, see §3.3.1 and Tab. 3.4).

Only the system NGC5953/54 exhibits signs for very strong gravitational interaction as mentioned in §3.3.1. Therefore, most of the disturbances in our sample (6/7 galaxies) can not be explained simply by tidal forces presently at work. The most probable explanations for these disturbances are described in the following, listed in decreasing relevance:

- Interaction with a companion now further or far away. If we assume a relaxation timescale of the disturbance of $3{\cdot}10^8$yr (typical time for one rotation of a galaxy) and a maximum fly-by velocity of $\sim$ 500 km s^{-1}, the involved companion is expected to be found within a radial distance of $\sim$ 150 kpc from the disturbed galaxy. Since 71% of the disturbed disks show companions in a reasonable distance (projected distance is less than 150 kpc), tidal interactions in the past seem to be primarily responsible of the disturbances identified in the HI disks.

- Ram pressure stripping (Cayatte et al., 1990; Vollmer et al., 2000, 2001). In particular for NGC 1961 stripping by intergalactic material was suggested (Shostak et al., 1982). But since none of our galaxies with disturbed HI disk lie in a massive group or cluster environment, gas stripping due to ram pressure is not very likely to explain the presence of disturbances in our sample where no nearby companion is found. Furthermore, the outer HI disk, where disturbances are usually seen, has been removed in clusters due to ram pressure stripping, indicated also by a small HI radius (e.g. NGC 4569, NGC 4579 as part of the Virgo cluster; see §3.4.2)
- Minor merging, whereby the companion has now fully merged and has left no optical trace. This might be the case for NGC 4736 and NGC 2782 where no companions are found in a reasonable distance for tidal interaction.
- Large gas accretion from cosmic filaments: Asymmetries in the gas accretion may cause disturbances (for effects of gas accretion on spiral disk dynamics see Bournaud & Combes, 2002).

3.4.2 HI Morphology and Comparison with the Stellar Distribution

The comparison of the radial density profiles between the HI gas distribution and the stellar distribution revealed significant deviations as expected: 1.) The extent of the HI disk is on average 1.7 times the optical radius, indicated by the Holmberg radius. Only NGC 3627, NGC 4569 and NGC 4579 show a smaller HI radius than optical radius. This can be explained by the fact that they are all members of interacting groups and/or by their rapid motion through an intracluster medium. NGC 3627 is part of the Leo Triplet group and the past encounter with NGC 3628 could explain the spatial conincidence of both the stars and the gas (Zhang et al., 1993). The truncated disks of NGC 4569 (and NGC 4579) are most probably a signature of strong ram pressure stripping in the past by the intracluster medium which pervades the Virgo Cluster (Cayatte et al., 1994). However, most of the galaxies in our sample show a larger HI disk than their optical one. 2.) The radial density profiles exhibit for most of our galaxies a deficiency of HI gas in the inner part of the galaxy disk. This is in general explained by the phase transition from atomic to molecular gas in neutral ISM (Young & Scoville, 1991).

3.4.3 Correlations between HI Gas Properties and AGN Activity Type

As described in §3.3.5 our analysis revealed that the number of galaxies with disturbed HI disks is higher for LINER galaxies than for Seyfert galaxies. But since several mechanisms which can not easily be distinguished can cause these asymmetries (see §3.4.1), it is not possible to draw any strong conclusions explaining the higher fraction for LINERs.

Our study of the HI morphology revealed a significantly higher percentage of galaxies with a HI gas ring for LINER than for Seyfert galaxies. Interestingly, only the study of the Extended 12μm Galaxy Sample (Hunt & Malkan, 1999) indicated a prevalence of stellar rings in active galaxies (Seyfert and LINERs), where LINERs have elevated rates of inner rings, while the Seyfert host galaxies have outer ring fractions several times those in normal galaxies. However, we found no HI gas rings in Seyfert host galaxies. Note that stellar rings are not preferentially found in Seyfert, LINERs, or non-AGNs for our sample by using the optical classification from RC3 listed in NED (see classification in Tab. 3.1; indicated as R or r). To summarize, HI rings are more often found in LINERs while no strong correlation with stellar rings is present.

One possible explanation for an abundance of HI gas rings in LINERs may be a common evolution of the gas distribution in the disk together with the nuclear activity where both are subject to the influence of a present bar or previous one which has now dissolved. This becomes important since rings are linked observationally and phenomenologically to barred galaxy dynamics (for a general review see Buta & Combes, 1996), and hence, expected to be seen after the bar had enough time to redistribute the gas toward the end of its lifetime. Thus, a time evolution of AGN types seems to be possible, where Seyfert and LINERs represent different phases of the galaxy activity cycle: Seyfert galaxies are the ones where the fueling process has just been triggered (e.g. through disturbances and/or bar dynamics) while LINERs are the ones where the triggering mechanism has already distributed the gas in a more stable new configuration (rings) that does no longer support the massive inflow of gas. Interestingly, disturbances, which are assumed to be a sign for a recent trigger of gas inflow, are preferentially found in LINERs in our sample. That would suggest that LINERS are the first stage of activity, just after the triggering: The gas is still distributed in rings, and the fueling of the AGN has just started by the redistribution of the gas. However, as most of the disturbances in our sample are probably due to tidal interactions in the past, as explained in §3.4.1, the currently observed nuclear activity must not be identical to the one during the ongoing tidal interaction.

A general scenario for self-regulated activity in low-luminosity AGNs was developed by García-Burillo et al. (2005), in which the onset of nuclear activity is explained as a recurrent phase during the typical lifetime of any galaxy. In this scenario the activity in galaxies is related to that of bar instabilities, expecting that the active phases are not necessarily coincident with the phase where the bar has its maximum strength. Since the infall of gas driven by a bar is self-destructive (Bournaud & Combes, 2002), i.e. it weakens and destroys the bar, the potential returns to axisymmetry and the gas piles up in a stable configuration (i.e. in rings at the resonances). At this stage, torques exerted by the gravitational potential are negligible and other competing mechanisms, e.g. viscous torques, must transport the gas in the center of the galaxy. The periods of Seyfert/LINER activity (each lasting $\sim 10^8$ years) are suggested to appear during different evolutionary stages of a bar episode (typically characterized by a lifetime $\sim 10^9$ years), depending on the competition between viscosity and gravity torques. The prevalence of HI rings in LINERS, derived in this work, could be explained by the scenario proposed by García-Burillo et al. (2005), where AGN activity is linked to the evolutionary state of the bar-induced gas flow. However, to further substantiate this link requires deriving the complete gravity torque budget based on the HI distribution (see Haan et al. in prep.).

Regarding the relative HI radius ($R_{HI}/R_{optical}$) we found a slightly larger HI extent for Seyfert galaxies than for LINERs, which increases even more when neglecting galaxies which lie in galaxy clusters or groups. In contrast, our study of the large environment, the HI gas content (by using the ratio M_{HI}/M_{dyn}), and the relative HI mass (M_{HI}/M_{dyn}) revealed no significant correlation with the AGN-type. This might be due to the limited number of galaxies in our sample. Hence we conclude that a detailed HI study with a larger sample may reveal more additional information on the interplay between the gaseous component and the AGN type present.

3.5 Summary

We present results on the atomic gas distribution and kinematics of 16 nearby spiral galaxies. This sample forms the part of the NUGA survey which studies the neutral (atomic and molecular) gas dynamics of nearby low luminosity AGN galaxies. We investigated relations between the atomic gas properties, the environment and the stellar distribution as well as possible relations to the AGN type present (Seyfert, LINER). Several galaxies are surrounded by companions with associated HI emission and half of our sample has dynamically disturbed disks. No evidence for a correlation between the presence of companions and Seyfert and LINER galaxies is found, neither from our HI study nor for cataloged optical companions.

The HI morphology of our galaxies revealed rings, spiral arms, and centrally concentrated peaks. The comparison with the AGN type present showed that ring structure is significantly more often present in LINER than in Seyfert host galaxies. Since bars are dynamically linked to the presence of gas rings, a time evolution of the AGN activity together with the redistribution of the neutral gas seems to be a plausible explanation for this finding. Additionally, we found a slightly larger HI extent and less prevalent disturbed HI disks for Seyfert hosts than for LINER host galaxies. A detailed study with a larger HI sample may reveal more relations with respect to the AGN type and would improve the significance of our results.

4 Dynamical Evolution of AGN Host Galaxies - Gas In/Out-Flow Rates in 7 NUGA Galaxies

Gas flow rates from the outer disk regions at several kpc down to the inner disk at a few 10 pc are presented for seven nearby spiral galaxies selected from the NUGA sample (NUclei of GAlaxies). The goal of this study was to examine the role of host galaxy dynamics in the fueling of nuclear activity. Based on high angular resolution interferometric observations of molecular (CO using PdBI) and atomic (HI using the VLA) gas and NIR images, we calculated gravitational torques and determined gas in/out-flow rates as a function of radius and location within the galactic disks. The results are compared with kinematic evidence for radial gas flows (e.g. streaming motions) and the dynamical state of the galaxies (via resonances) derived from several different methods. We show that gravitational torques are very efficient at transporting gas from the outer disk all the way into the galaxy center at ∼100 pc; previously assumed dynamical barriers to gas transport, such as the Corotation Resonance of stellar bars, seem to be overcome by gravitational torque induced gas flows. The transported gas masses range from 0.01 to 50 $M_\odot$ *yr*$^{-1}$ *and are larger for the galaxy center than for the outer disk. Our gas flow maps show the action of nested bars within larger bars for 3 galaxies. Streaming motions indicated by non-circular motions from our kinematic study are larger in the center than in the outer disk and appear to correlate only sparsely with the in/out-flow as function of radius. We demonstrate that spiral disks are very dynamic systems that undergo strong secular evolution on timescales of a few rotation periods (e.g.* $5 \cdot 10^8$ *yrs at a radius of 5 kpc), due to the effectiveness of gravitational torques in redistributing cold galactic gas.*

4.1 Introduction

The study of gas inflow rates has long been recognized to be important for understanding the secular evolution of galaxies, star formation, and nuclear activity. Generally gas inflow can be caused by two different dynamical mechanisms, gravitational and hydrodynamic mechanisms: galaxy interactions and asymmetries in galactic potentials remove angular momentum through torques, while hydrodynamic mechanisms, such as turbulence in the ISM, remove angular momentum through gas dynamical effects (e.g. viscous torques or shocks). Here we focus on the first mechanism with emphasis on the gas response to gravitational torques exerted by the stellar potential. It is well established that asymmetries in galactic potentials, such as large-scale bars, transport gas very efficiently inward (e.g., Mundell et al., 1999; Combes , 2003; Jogee , 2004), and that bars can fuel powerful starbursts (e.g., Jogee et al., 2005). Further, the inflow of gas from the outer regions of a galaxy is necessary to maintain nearly constant star formation in the inner disks of spirals (Blitz, 1996) and to form (and refuel) an Active Galactic Nuclei (AGN) accretion disk around a central black hole (Rees, 1984; Shlosman et al., 1990).

However, searches for low-luminosity AGN fueling mechanisms have not found any strong correlation between the presence of morphological features, e.g. bars, and AGN activity (see for an overview Martini, 2004). One explanation might be that smaller-scale phenomena are responsible for AGN fueling. Thus, only observations with very high spatial resolution provide the possibility to find correlations between AGN fueling and dynamical perturbations. Martini & Pogge (1999) suggested that nuclear spiral dust lanes may be the channels by which gas from the host galaxy disks is being fed into the central engines. But also a high spatial resolution study with the Hubble Space Telescope (HST) of the circumnuclear region (on 100 pc scales) has still not found a significant differences between AGN and control samples, at least not for late-type galaxies (Martini et al., 2003; Simões Lopes et al., 2007). Another possibility is that a hierarchy of mechanisms combine to transport the gas from the outer disk (kpc scales) down to the center (pc scales). As these various mechanisms are working at different spatial scales, also the mass accretion involves different time scales (Shlosman et al., 1990; Combes , 2003; Wada & Koda, 2004). This time-scale conspiracy could explain the lack of any correlation between the presence of non-axisymmetric perturbations and the onset of activity (Wada & Koda, 2004; García-Burillo et al., 2005). Recent spectroscopic studies of the ionized gas in the central kiloparsec seem to confirm this picture by showing evidence for kinematic perturbations linked with Seyfert galaxies at small radii (Dumas et al., 2007). For larger scales ($>$ 1 kpc) first results of a detailed study of HI gas properties for active and non-active disk galaxies indicate possible relationships between Seyfert activity and HI properties (Mundell et al., 2007).

As the neutral gas is distributed in a rotating disk and extends out to kpc scales, the problem of radial gas transport is basically a problem of angular momentum removal from the gas. To transfer angular momentum, effective torques are required.

In particular, gravitational torques, exerted by the stellar and effective dark matter potential are expected to play a major role. In addition, viscous and magnetic torques might contribute significantly. For example, viscous torques are expected to be very efficient in high gas density regions such as the centers of galaxies (García-Burillo et al., 2005). However, normal viscosity is not efficient, due to the very low density of the gas. Even with macroturbulent viscosity, the time-scales are longer than the Hubble time at large radii, and could be effective only inside the central 1 kpc (Lynden-Bell & Kalnajs, 1972). The role of magnetic torques is more uncertain since the interplay between magnetic fields and gas is still not very well understood. Although magnetic fields seem to pervade the interstellar gas in spiral galaxies

(Beck et al., 1999; Beck, 2004), it is more likely that magnetic fields follow the gas flow rather than acting as incitement.

The quest for a quantitative estimation of radial gas flows from observations has been pursued by different methods: One approach is to use the gas kinematics from radio-interferometric observations of moderately inclined spiral galaxies and a decomposition of the velocity field into Fourier components whose radial variations are used to search for evidence of radial gas flows (e.g. Schoenmakers et al., 1997; Schoenmakers , 1999; Fathi , 2004; Wong et al., 2004; Krajnović et al., 2006, Trachternacht et al., submitted). This method has also been successfully applied using optical spectrography in order to search for perturbations in the stellar dynamics (Dumas et al., 2007; Dumas , 2007; Emsellem et al., 2006). Using a slightly different approach, Boone et al. (2007) derived gravitational torques by fitting a model based on analytical solutions for gas particle orbits for the barred spiral galaxy NGC 4569. Spekkens & Sellwood (2007) developed a bisymmetric flow model for non-circular motions that can be fitted to data (applied to the galaxy NGC 2976) by a generalization of the technique developed by Barnes & Sellwood (2003). However, the conversion of the model derived from the velocity field into radial gas flows depends strongly on the chosen model for the gas orbits. As the gas orbits are generally not known, it is impossible to recover the velocity structure from the line-of-sight component of motion alone without further assumptions (e.g. using isophote fits on complementary optical images, Wong et al., 2004).

Another approach for measuring inflow velocities is to derive the gravitational potential on the basis of the observed near-infrared (NIR) light distribution of a galaxy and then to compute the gravitational torques exerted by the stellar potential on the gas (Garcia-Burillo et al., 1993; Quillen et al., 1995; García-Burillo et al., 2005).

In combination with observed rotation curves this method does not depend necessarily on assumed mass-to-light ratios (hereafter M/L ratio) which are derived, e.g. by population synthesis techniques, and are inaccurate for the outer disk where dark matter is expected to have a significant contribution. Instead, the azimuthal averaged calculated velocities from the derivatives of the gravitational potential can be scaled with the actual observed rotation curve and hence allow one to obtain a more realistic scaling of the gravitational potential (assuming a constant azimuthal M/L ratio).

In fact, gravitational torques arise from non-axisymmetric components of the gravitational potential, such as stellar bars, spirals, and oval distributions. The effect of large-scale bars has been studied in detail by simulations which have successfully shown that bars are very efficient for transporting the gas towards the center (e.g. Sparke & Sellwood, 1987; Athanassoula, 2003). As these mechanisms may work on different spatial scales, secondary bars within large-scale bars (e.g. Shlosman et al., 1989; Friedli & Martinet, 1993; Maciejewski & Sparke, 2000; Englmaier & Shlosman, 2004), gaseous spiral density waves (e.g. Englmaier & Shlosman, 2000; Maciejewski, 2002, 2004a,b), m = 1 perturbations (e.g. Shu et al., 1990; Junqueira & Combes, 1996; García-Burillo et al., 2000) and nuclear warps (Schinnerer et al., 2000) have been suggested to transport the gas into the center.

In order to distinguish models for nuclear fueling, observations with high angular and velocity resolution are required. Therefore, the IRAM key project NUclei of GAlaxies (NUGA; see García-Burillo et al., 2003) was established - a spectroscopic imaging survey of gas in the centers of nearby low luminosity AGN. As most of the gas in galaxy nuclei is in the molecular phase, the survey used millimeter CO lines to conduct a detailed mapping of molecular gas dynamics at high-resolution ($\sim 0.5''$) in the central kiloparsec of AGN hosts. To provide a more complete view of gas dynamics from the outer disk to the center, the HI-NUGA project has been initiated: a spectroscopic imaging survey of the atomic gas distribution and kinematics over the entire galaxy disks (~25 kpc) for 16 galaxies of the NUGA sample (Haan et al., 2008). Results of this study indicate that the type of nuclear activity (Seyfert/LINER) is linked to the gas distribution in the outer gaseous disk (at several kpc scales), suggesting a time evolution of AGN activity together with the redistribution of the neutral gas due to the non-axisymmetric potential. As the dominant phase of the neutral ISM transitions from atomic to molecular gas towards the center of galaxies, the combined HI and CO NUGA observations cover all scale lengths from the outer disk at > 10 kpc to the center at ~ 100 pc.

In this chapter we are studying in detail the gas dynamics and the gas response to the gravitational potential for 7 well-chosen targets from the HI-NUGA sample. We present a novel approach to derive gas inflow rates via a combination of gravitational torque computation based on the stellar distribution and a kinematic analysis of the observed gaseous velocity fields. To derive gravitational torques, high spatially resolved maps of the stellar and gaseous distribution are required. Therefore we have obtained for our 7 galaxies VLA HI data with $\sim 7''$ spatial and ~10 km s^{-1} velocity resolution. Our sample and the observational setups (HI-, CO- line emission, and NIR data) are described in §4.2. The dynamical models, the geometrical disk parameters, and the amount of non-circular motions are derived in §4.3 from our observed velocity fields using the atomic and molecular gas kinematics. We have computed gravitational torques and their efficiency to transport the gas over galaxy disks on the basis of NIR images (Spitzer, HST) and a combination of our HI data and NUGA CO data with $\sim 0.5''$ spatial and ~5 km s^{-1} velocity resolution. The methods used for this study and its results are described in §4.4. Finally, we compared in §4.5 the total amount of non-circular motions from our observed velocity fields to the non-circular motions that are induced by the gravitational torques and discuss our findings in the context of AGN fueling mechanisms.

Table 4.1: Sample Overview

Name	RA (J2000)	DEC (J2000)	Hubble Type	AGN HFS	AGN Kewley	v_{sys} [km s^{-1}]	Dist [Mpc]
NGC 3368	10 46 46	+11 49 12	SB(rs)ab	L2	L	897	8.1
NGC 3627	11 20 15	+12 59 30	SB(s)b	L/S2	S	727	6.6
NGC 4321	12 22 55	+15 49 21	SB(s)bc	T2	L	1571	16.8
NGC 4736	12 50 53	+41 07 14	(R)S(r)ab	L2	L	308	4.3
NGC 5248	13 37 32	+08 53 08	(R)SB(rs)bc	H	H	1153	15
NGC 6951	20 37 14	+66 06 20	SB(rs)bc	S2	S	1424	24.1
NGC 7217	22 07 52	+31 21 33	(R)S(r)ab	L2	L	952	16.0

Note. — Summary of the properties of our 7 galaxies. Listed are only parameters from LEDA and NED. The AGN classification listed in column (5) is taken from Ho, Fillipenko & Sargent (1997): S - Seyfert, L - LINER, T - transition object, H - H II galaxy and NED. In addition, our AGN classification (Haan et al., 2008) in Seyfert and LINER following the method of Kewley et al (2006) is indicated in column (6). The velocities listed in column (7) are the assumed systemic velocities.

4.2 Sample Description and Observations

For our study we have used observations of the neutral gas component as traced by HI and CO, as well as the stellar component as described in the following.

4.2.1 Sample Description

For a detailed study of gas inflow rates, we selected 7 galaxies from our HI-NUGA sample (Haan et al., 2008). The selection of the targets is based on the presence of bright HI emission as well as a fairly regular HI morphology (i.e. no highly disturbed gas disks). All the galaxies are spiral galaxies ranging in Hubble type from Sa to Sc and are barred, except for NGC 7217. The distance of our sample ranges from 4 to 24 kpc with a mean distance of ∼13 kpc. A complete overview is given in Tab. 4.1. The galaxies host various kinds of nuclear activity[1]: LINERs (4 galaxies), Seyferts (2 galaxies), and starburst (1 galaxy).

---

[1] The nuclear classification is adopted from Haan et al. (2008) and based on optical emission line ratios following the method of Kewley et al. (2006)

4.2.2 Atomic Gas Data

To trace the dynamics of the outer disk we observed the atomic gas distribution and kinematics in the HI emission line at 21cm using the NRAO Very Large Array (VLA). Previous data obtained with the VLA in C and D array configuration ($\sim$20″ resolution) were already presented by Haan et al. (2008). For the 7 galaxies analyzed here we combined these data with newly obtained VLA B-array data resulting in a final resolution of $\sim 7''$. Two galaxies (NGC 3627, NGC 4736) were already observed as part of the THINGS project (Walter et al., 2008). The data reduction was performed using the Astronomical Image Processing System (AIPS; Greisen , 2003) following the data reduction scheme of the previous CD array data (Haan et al., 2008). Flux calibrator measurements were performed at the beginning and at the end of each observation cycle. The phase calibrator was observed before and after each source cycle with a maximum distance between source and phase calibrator of 12°. The data have an average on-source integration time of 8.5h (B-array), 2.7h (C-array), and 2.8h (D-array). The correlator spectral setup used was set to line mode 4 with Hanning smoothing and 64 channels per 1.5625 MHz channel width per frequency band providing a frequency resolution of 24.414 kHz/channel ($\sim$ 5.2 km s^{-1}). Calibration solutions were first derived for the continuum data-set (inner 3/4 of the spectral band width) and then transferred to the line data. The bandpass solutions were determined from the phase calibrator measurements to account for channel to channel variations in phase and amplitude. The B and CD data have been combined. The CLEANing parameters are adjusted to the new combined BCD data, as described in the following. The cellsize of each grid was set to 1.3″/pixel with a field of view (FOV) of $\sim 22'$. We produced the CLEANed data cubes using robust weighted imaging with a velocity resolution of $\sim$ 10.4 km s^{-1} and an average angular resolution of $\sim 7''$. To find the best compromise between angular resolution and RMS, several robust weighting parameters were tested and a robust parameter of 0.3 was selected. The RMS values and beam sizes are listed in Table 4.2 with an average achieved RMS value of 0.32 mJy beam^{-1}.

The RMS flux sensitivity of 0.4 mJy/beam/channel corresponds to a 3-σ detection limit of $\sim 0.55 \times 10^{19}$ cm^{-2} column density for the combined BCD array data. To separate real emission from noise, we produced masks by taking only into account those regions which show emission above a set level (3σ) in cubes that have been convolved to 30″ resolution (task CONVL). Using these masks, we blank the areas that contain noise in our robust weighted data cubes (task BLANK).

The subsequent analysis has been done with the Groningen Image Processing SYstem (GIPSY; van der Hulst et al., 1992). The channel maps were combined to produce zeroth (intensity map), first (velocity field) and second (dispersion map) moments of the line profiles using the task MOMENT. The RMS values have been measured in two regions where no line signal was apparent and averaged over all channels of the cubes. A flux cut-off of three times the channel-averaged RMS value was used for the moment maps. The velocity-integrated HI

Table 4.2: Setup for the VLA HI observations

Name	Resolution Beam [″]	Resolution [kpc]	FWZI. [km s^{-1}]
NGC 3368	6.4 × 5.3	0.23	399
NGC 3627	5.3 × 5.1	0.17	431
NGC 4321	7.6 × 6.5	0.57	291
NGC 4736	5.6 × 5.2	0.11	284
NGC 5248	5.9 × 5.4	0.41	311
NGC 6951	14.4 × 12.5	1.57	338
NGC 7217	7.9 × 5.3	0.50	326

Note. — Overview of the spatial resolution of our VLA observations. The velocity resolution is ~10.4 km s^{-1} for all galaxies. In addition the Full Widths at Zero Intensity (FWZI) of the velocities are listed for all galaxies.

intensity maps are presented in Figure 4.1.

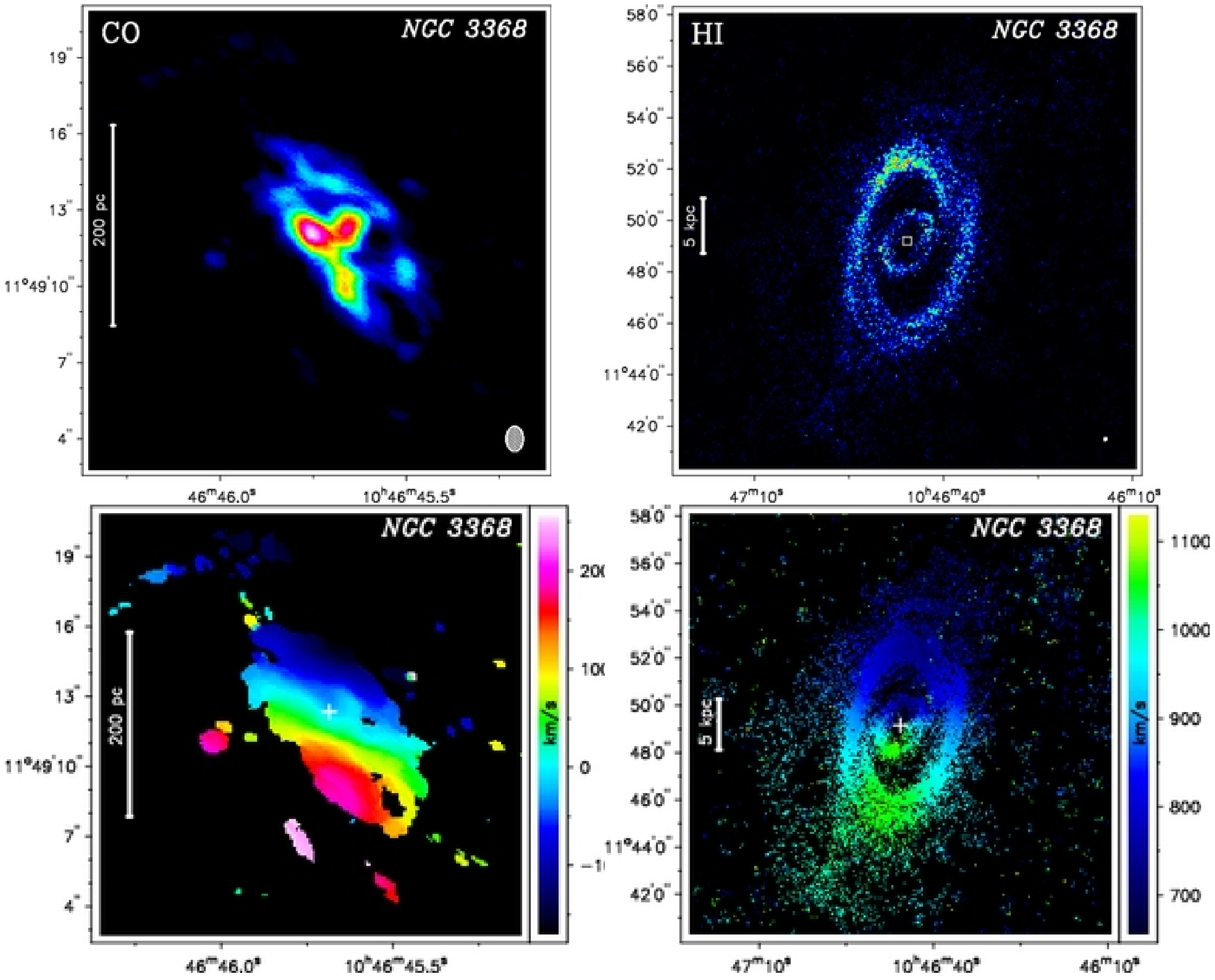

Figure 4.1: - NGC 3368. Overview of the intensity maps (top panels) and intensity-weighted velocity fields (bottom panels) for the molecular (left panels) and atomic gas (right panels). The beam is plotted in the bottom left corner and a scale length of 1 kpc (200 pc) is indicated as bar for the HI (CO) maps at the left. The dynamical center is indicated by a cross in the velocity fields (bottom panels). Colorbars are centered at $v_{center} = 0$ for the molecular gas velocity fields or the systemic velocity ($v_{center} = v_{sys}$) for the atomic gas velocity fields. The square in the HI map indicates the FOV of the CO map. The molecular gas has been observed in the transition of the J=1-0 line of ^{12}CO.

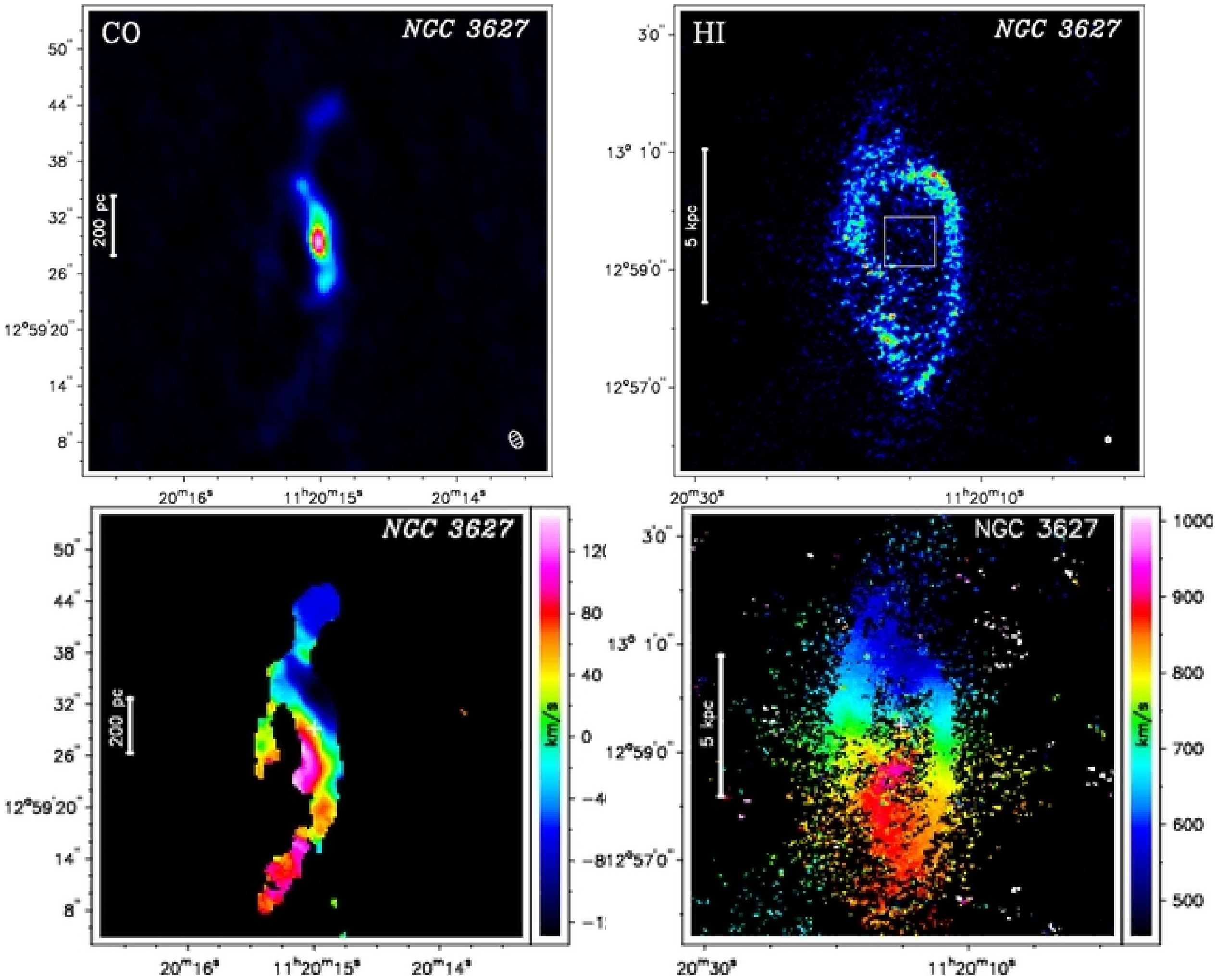

Fig. 4.1 - Continued for NGC 3627. The molecular gas has been observed in the transition of the J=1-0 line of ^{12}CO.

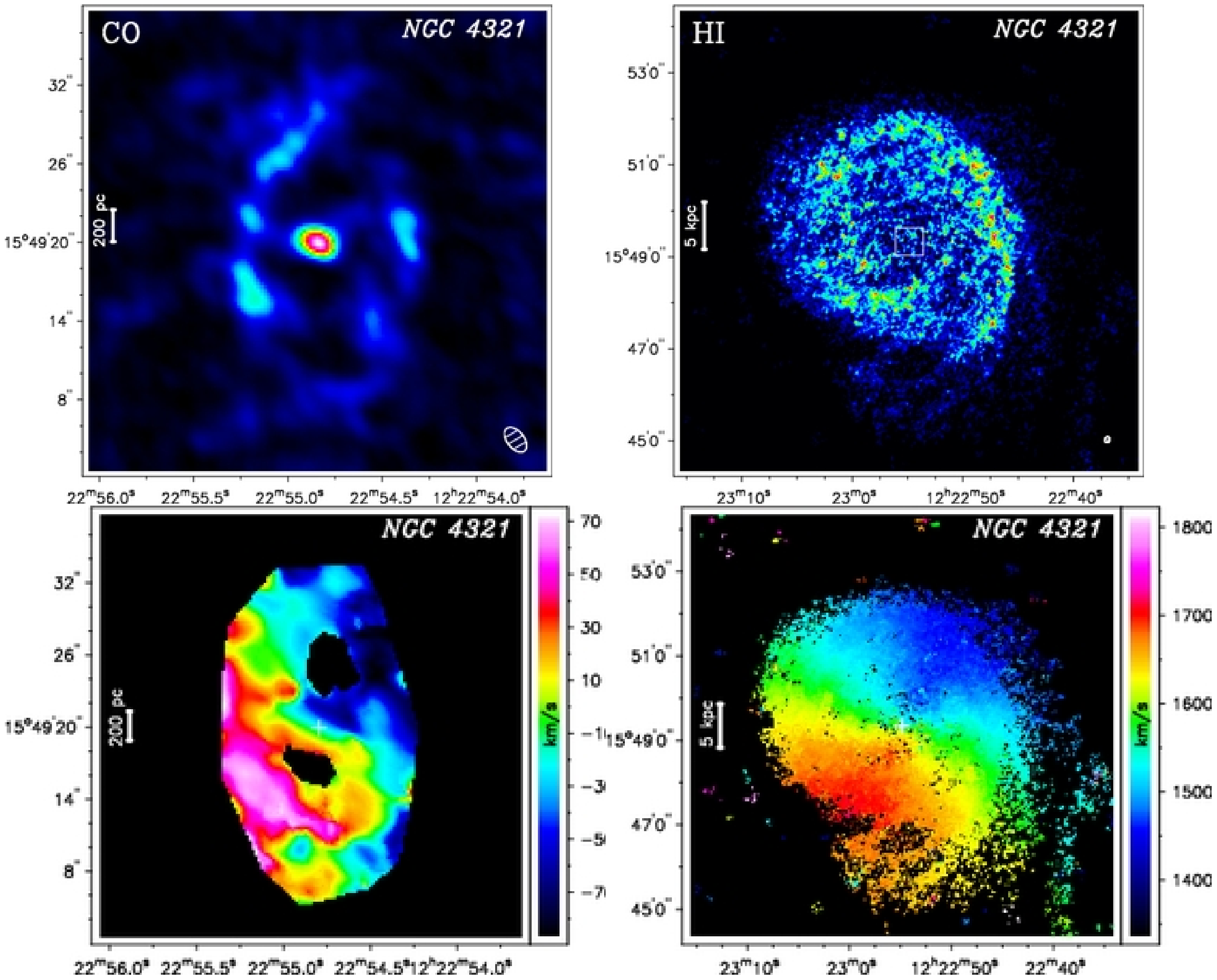

Fig. 4.1 - Continued for NGC 4321. The molecular gas has been observed in the transition of the J=1-0 line of ^{12}CO.

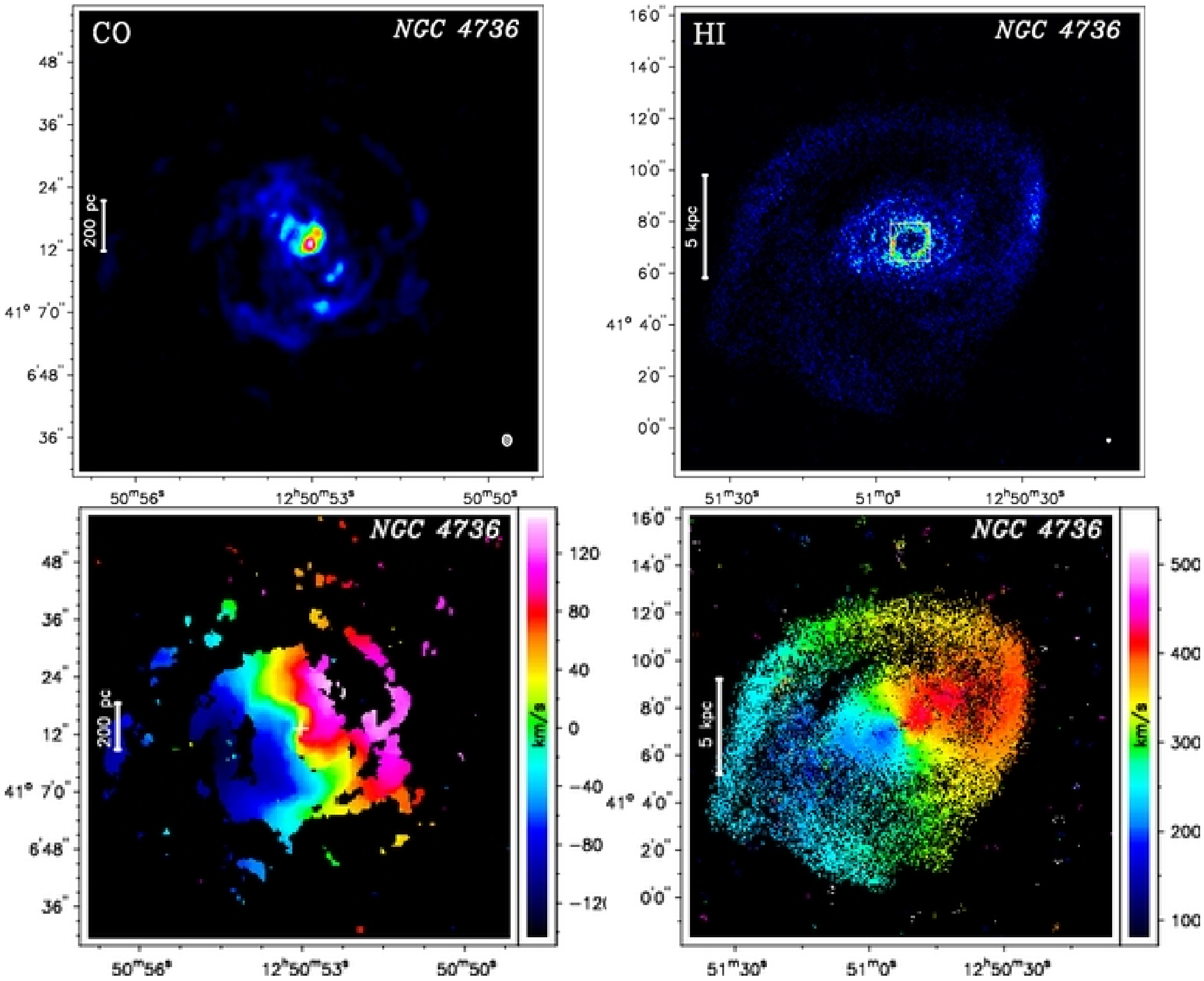

Fig. 4.1 - Continued for NGC 4736. The molecular gas has been observed in the transition of the J=1-0 line of ^{12}CO.

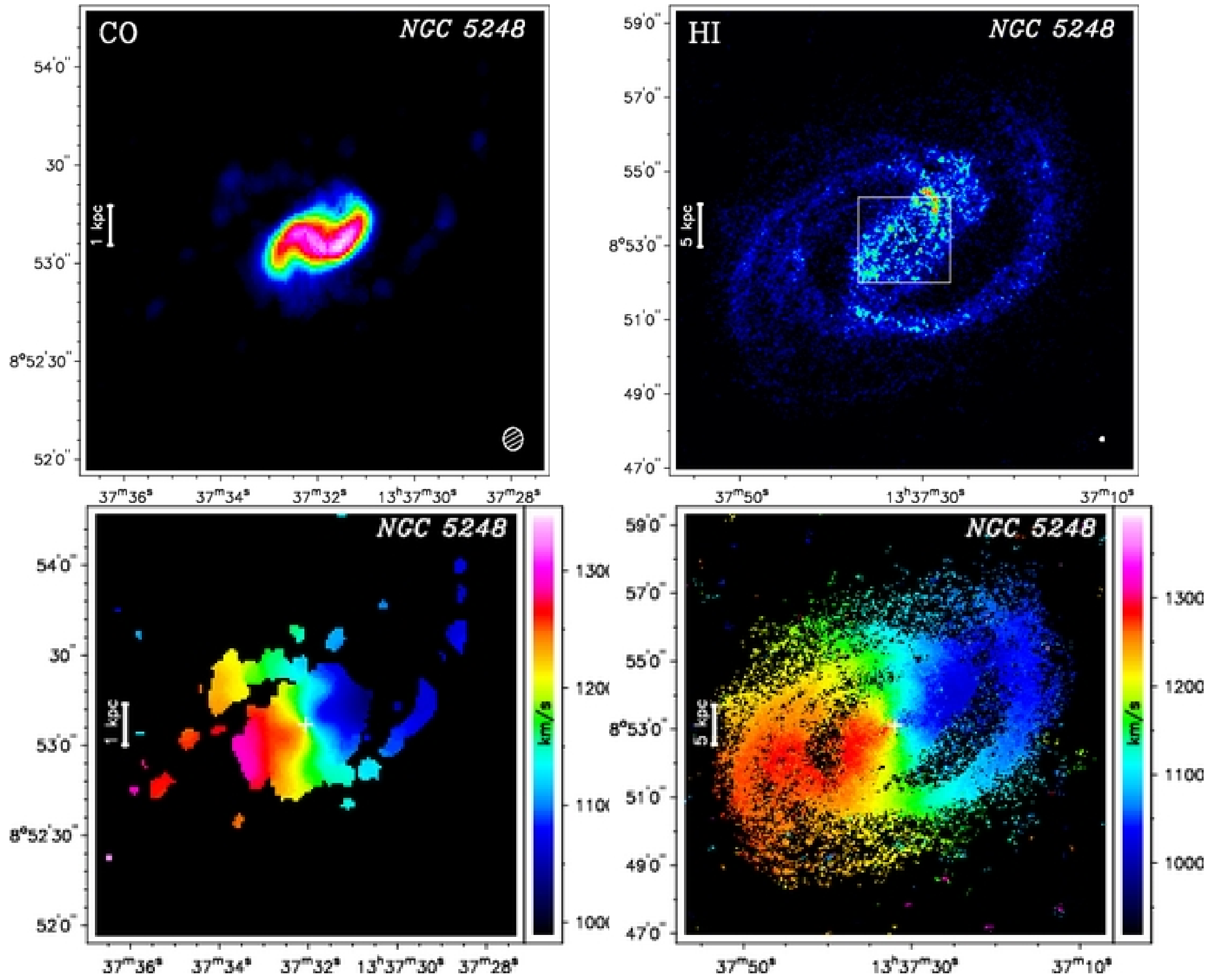

Fig. 4.1 - Continued for NGC 5248. The molecular gas has been observed in the transition of the J=1-0 line of ^{12}CO. Here, the bar indicates a scale length of 1 kpc for the CO and HI maps. Colorbars are centered at the systemic velocity for the molecular and atomic gas velocity fields.

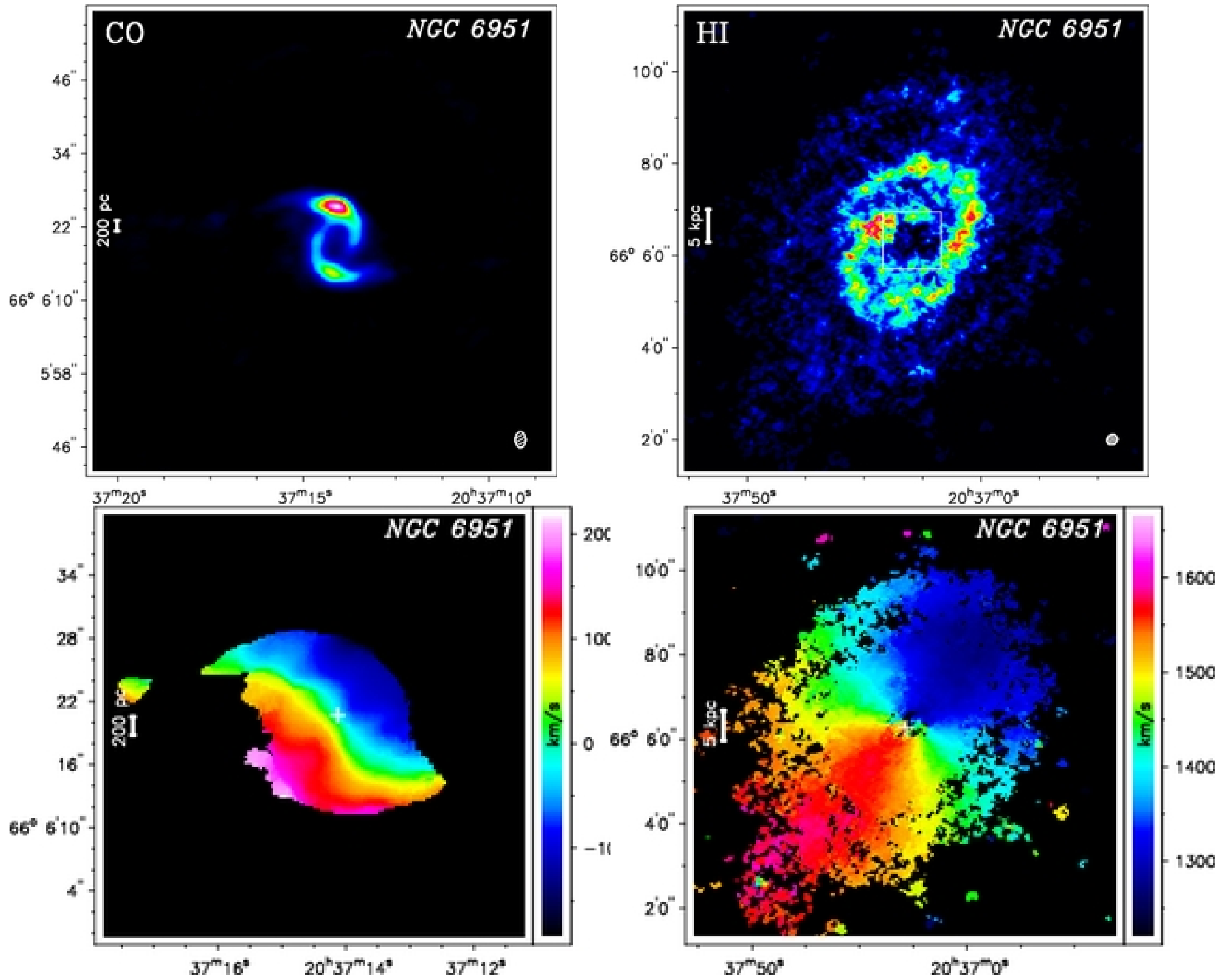

Fig. 4.1 - Continued for NGC 6951. The molecular gas has been observed in the transition of the J=1-0 line of ^{12}CO.

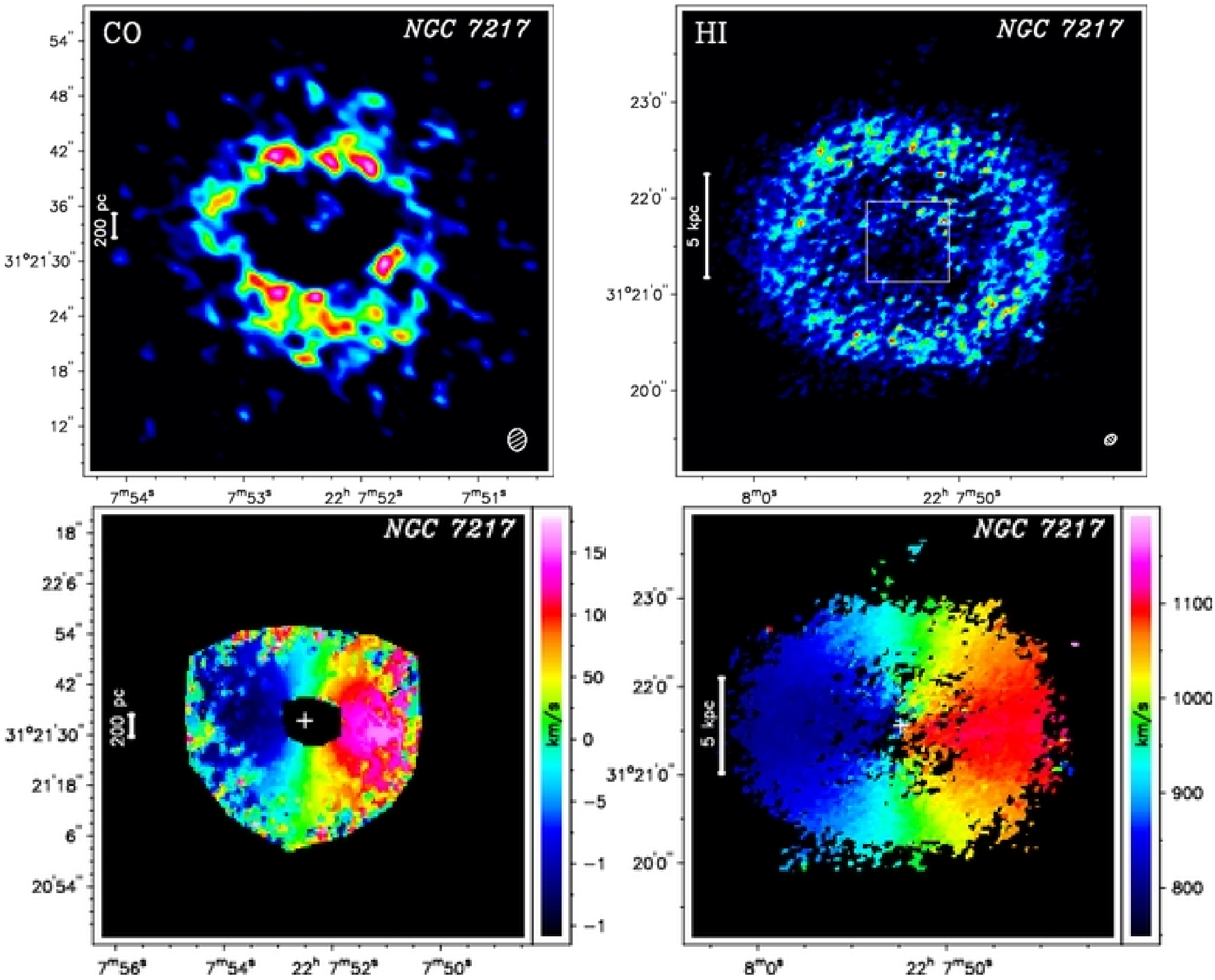

Fig. 4.1 - Continued for NGC 7217. The molecular gas has been observed in the transition of the J=2-1 line of ^{12}CO.

Table 4.3: Setup for the CO observations

Name	CO 1-0 Beam [″]	CO 2-1 Beam [″]	Origin
NGC 3368	2.5 × 1.4	1.0 × 0.67	(PI. Schinnerer)
NGC 3627	1.9 × 1.2	0.9 × 0.6	(NUGA)
NGC 4321	2.2 × 1.3	-	(García-Burillo et al., 2005)
NGC 4736	2.1 × 1.7	-	(PI. Schinnerer)
NGC 5248	6.9 × 5.8	-	(Helfer et al., 2003)
NGC 6951	2.6 × 1.7	0.6 × 0.5	(García-Burillo et al., 2005)
NGC 7217	2.4 × 1.9	-	(Combes et al., 2004)

Note. — Overview of the angular resolution of our CO observations using the transitions of the J=1-0 and J=2-1 lines of ^{12}CO. The velocity resolution is ~5.2 km s^{-1} for all galaxies, except NGC 5248 which has a velocity resolution of ~10 km s^{-1}. In addition, the origin of the data is listed.

4.2.3 Molecular Gas Data

The spectroscopic imaging of CO lines provides information about the distribution and kinematics of the molecular gas. The molecular gas has been observed in the transition of the J = 1−0 and J = 2−1 lines of ^{12}CO with maximum angular (~ 0.5″) and spectral resolution (3-6 km s^{-1}) using the IRAM Plateau de Bure mm-interferometer (PdBI) as part of the NUGA project and the larger NUGA supersample (García-Burillo et al., 2003). The primary beam size is ~42″ (~21″) in all the CO 1−0 (2−1) line observations. Only for NGC 5248 no PdBI data was available. Therefore we used for NGC 5248 the publicly available BIMA-SONG data (Helfer et al., 2003) which was observed in the CO (1-0) line with an angular resolution of 6.1″ and spectral resolution of 10 km s^{-1} with the BIMA mm-interferometer. An overview of the observational parameters is presented in Tab. 4.3.

4.2.4 Near Infrared Images

Archival near infrared images (NIR) from Spitzer, HST and ground-based telescopes have been used to estimate the stellar mass distribution of our galaxies. An overview of all NIR images used is presented in Tab. 4.4. Foreground stars have been removed using the software tool NFIGI (Baillard et al., in prep.) and, in case additional cleaning was necessary, by hand. In addition, background is subtracted from the NIR images by calculating the mean value in the outer region of the image outside the galaxy disk to ensure that no light contribution from the galaxy itself is subtracted. Other methods for background subtraction

Table 4.4: NIR data

Name	Instrument	P.I.; Proposal ID	Instrument	P.I.; Program ID
NGC 3368	NICMOS F160w	J. Mulchaey; 7330	IRAC CH1	G. Fazio; 69
NGC 3627	NICMOS F160w	J. Mulchaey; 7330	IRAC CH1	R. Kennicutt; 159
NGC 4321	K-Band	Knapen et al. (2003)	IRAC CH1	R. Kennicutt; 159
NGC 4736	NICMOS F160w	R. Kennicutt; 9360	IRAC CH1	R. Kennicutt; 159
NGC 5248	NICMOS F160w	D. Maoz; 7879	IRAC CH1	G. Fazio; 69
NGC 6951	NICMOS F160w	J. Mulchaey; 7330	K-Band	Mulchaey et al. (1997)
NGC 7217	NICMOS F160w	M. Stiavelli; 7331	H-Band	Eskridge et al. (2002)

Note. — Overview of all NIR images used.

have been tested (e.g. fitting the radial luminosity profile to find constant background value), but could not be applied successfully to all NIR images because of limited FOVs. After background subtraction all values below zero were set to zero which might be caused by small overestimation of the background value (case only for outer regions of image).

4.3 Kinematic Modeling

To search for kinematic evidence for radial gas flows and non-circular motions, we have performed a detailed kinematic analysis on the basis of our CO and HI velocity fields. In §4.3.1 we first estimate the basic disk orientation parameters which are also required for our gravitational torque calculations. Then, we model non-circular motions and search for evidence of gas inflow or outflow by employing a Fourier analysis of the velocity fields as described in §4.3.2. The results of this study are presented in §4.3.3 and indicate, e.g., a higher ratio of non-circular to circular gas motions for the central (CO) than for the outer gaseous disk (HI).

4.3.1 HI and CO Kinematics

In preparation for our analysis of radial gas flows, we derived the following disk parameters by fitting tilted rings to the CO and HI velocity fields using the task ROTCUR within GIPSY:

- The dynamical center and its offset from the optical center (taken from Hyperleda).
- The systemic velocity v_{sys} in km s^{-1}.

- The position angle (PA) in degrees, defined as the angle between the north-direction on the sky and the major axis of the receding half of the galaxy in anti-clockwise direction.
- The inclination (i) in degrees.

The kinematic parameters have been derived in an iterative way (Begeman, 1989) as described in our analysis for the entire HI-NUGA sample (Haan et al., 2008). The parameters were assumed to be the same at all radii, except for the circular velocity. We weighted the obtained value in each ring with its standard deviations, in order to derive the mean parameter. For the fit we excluded data points within an angle of 20° of the minor axis. The widths of the radii were set to $0.4''$ ($6''$) which corresponds roughly to the angular resolution of our CO (HI) observations. No radial velocity component was fitted as disk parameter. We have applied the same systemic velocity, inclination, and PA derived from our HI velocity field for the CO analysis as we assume that these disk orientation parameters are constant over the entire galaxy disk. We found no evidence for a significant warped disk in our sample using the derived inclination angle as a function of radius (see Fig. 4.2). For the estimation of the dynamical center position we have taken into account only data of the inner third of the HI gas disk to exclude possible shifts of the kinematic center due to spiral arms and disturbances in the outer HI disk. In addition we derived the center position from the CO kinematics for most galaxies of our sample. However, our derived values for the kinematic center show only small offsets from the photometric center with an average offset of $\sim 1.5''$ which is similar to typical errors expected from photometric center fitting. An overview of all derived parameters for each galaxy is presented in Tab. 4.5. Finally, the rotation velocities were obtained for the atomic and molecular gas with fixed inclination, position angle, center and systemic velocity.

4.3.2 Description of Kinematic Modeling of Non-Circular Motions

In this study we attempt to detect non-circular motions and evidence for radial gas flow directly from the observed gas kinematics. In principle, one would expect that non-circular motions are caused by the non-axisymmetric part of the gravitational potential. However in practice, other physical effects such as gas viscosity and shocks in the gas may have significant contributions to any observed non-circular motion. Furthermore, interactions with galaxy companions as well as AGN and star formation feedback might work as additional source for non-circular motions. To estimate the contribution from these effects, we compare the measurement of the non-circular motions with the results obtained via our gravitational torque analysis (see §4.5.3). To obtain a fair estimate of the circular and non-circular part of our gas velocity fields, we have used the GIPSY task RESWRI which performs a harmonic expansion of the velocity fields. This expansion is made by first fitting a tilted-ring model to the velocity field of the gas disk and subsequently decomposing the velocity field along each ring into its harmonic terms. Since the data points may not be uniformly distributed

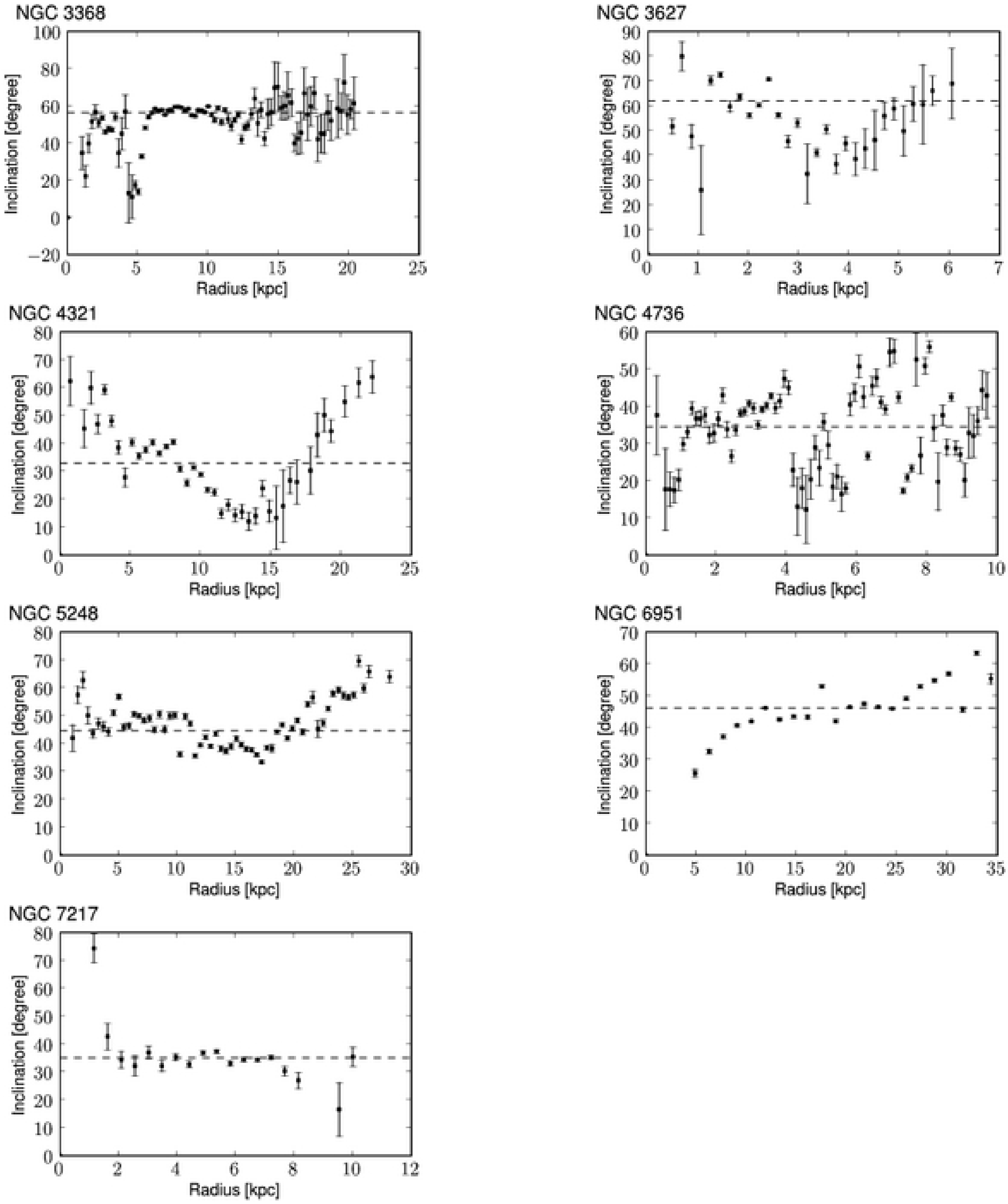

NGC 3368

NGC 3627

NGC 4321

NGC 4736

NGC 5248

NGC 6951

NGC 7217

Figure 4.2: Overview of the inclination angle parameters as a function of radius derived from fitting the HI velocity field. The dashed line indicates the calculated mean inclination angle.

Table 4.5: Disk and Kinematic Parameters

Source	x-offset [″]	y-offset [″]	v_{sys} [km s^{-1}]	PA [°]	i [°]
NGC 3368	2.2 ± 0.7	-2.1 ± 0.9	895.5 ± 0.3	168.5 ± 0.5	56.5 ± 0.5
NGC 3627	-0.2 ± 1.0	1.1 ± 2.1	720.3 ± 2.2	174.2 ± 0.7	62.0 ± 2.2
NGC 4321	1.5 ± 0.5	0.4 ± 0.5	1577.5 ± 0.4	152.1 ± 0.4	33.0 ± 1.5
NGC 4736	0.4 ± 0.3	0.5 ± 0.4	309.0 ± 0.5	299.0 ± 0.9	34.5 ± 1.2
NGC 5248	1.6 ± 0.6	-1.1 ± 0.6	1151.3 ± 0.3	113.2 ± 0.5	44.6 ± 0.9
NGC 6951	1.5 ± 1.0	-1.7 ± 1.0	1424.6 ± 0.8	138.1 ± 0.9	46.2 ± 1.1
NGC 7217	-0.3 ± 0.5	0.3 ± 0.4	951.8 ± 0.2	265.3 ± 2.0	35.1 ± 0.6

Note. — Overview of the disk and kinematic parameters derived from the observed velocity field by fitting tilted-rings to the velocity field: The offset of the dynamical center of the HI disk to the photometric centers from NED, the systemic velocity v_{sys}, the position angle PA and the inclination i are listed for all galaxies. Note that the errors are statistical errors and are interdependent for each galaxy.

in azimuth, RESWRI performs a least-square fitting (singular value decomposition) rather than a direct Fourier expansion. In practice, after the convergence of the ROTCUR part, RESWRI makes a harmonic expansion of the line-of-sight velocity v_{los} along each ring,

$$v_{los}(r) = v_{sys}(r) + \sum_{n=1}^{k} \left[c_n(r)\cos(n\psi) + s_n(r)\sin(n\psi)\right], \tag{4.1}$$

where k is the order of the fit, r the radial distance from the center, ψ the azimuthal angle, measured from the receding side of the line of nodes, and v_{sys} the systemic velocity as 0^{th} harmonic component. The coefficients c_n and s_n are determined by making a least-squares-fit to the data points up to third order, which requires three sine terms (s_1, s_2, s_3) and three cosine terms (c_1, c_2, c_3). Since the line-of-sight velocity is given in the most general case of a velocity field as

$$v_{los}(r) = v_{sys}(r) + v_\theta(r)\cos(\psi)\sin(i) + v_R(r)\sin(\psi)\sin(i) \tag{4.2}$$

where v_θ and v_R are the circular and radial components of the velocity field, respectively. Hencefore, $c_1 = v_\theta(r) sin(i)$ reflects the observed circular velocity, whereas all other terms are contributions to non-circular motions (see for a detailed discussion of the harmonic terms Schoenmakers et al., 1997; Schoenmakers , 1999).

To estimate the total amount of non-circular motions we calculate the quadratically added amplitude of all non-circular harmonic components v_{nc} up to the order of $N = 3$ (see also

Table 4.6: Kinematic Analysis

Source	$\langle v_{nc}/v_{rot} \rangle$	
	HI	CO
NGC 3368	0.071 ± 0.120	0.132 ± 0.211
NGC 3627	0.120 ± 0.084	0.832 ± 2.571
NGC 4321	0.068 ± 0.064	0.330 ± 0.867
NGC 4736	0.130 ± 0.300	0.221 ± 0.153
NGC 5248	0.098 ± 0.063	0.115 ± 0.042
NGC 6951	0.066 ± 0.293	0.137 ± 0.029
NGC 7217	0.054 ± 0.056	0.071 ± 0.093
Mean	0.09	0.26

Note. — Overview of the ratio of non-circular motion to rotation velocity v_{nc}/v_{rot} with the standard deviation of the mean value for CO and HI.

Trachternach et al., 2008):

$$v_{nc}(r) = \sqrt{s_1^2(r) + c_2^2(r) + s_2^2(r) + c_3^2(r) + s_3^2(r)}. \tag{4.3}$$

which is basically the vector sum of all non-circular velocity contributions. The fraction v_{nc}/v_{rot} shows how the contribution of non-circular motions to the total velocity may vary with radius. At the corotation radii (R_{CR}) of a bar or spiral the s_3-terms become dominant over the s_1-terms (Canzian & Allen, 1997).

4.3.3 Results of our Kinematic Analysis

For the outer disk (probed by our HI gas kinematics), most of the galaxies in our sample exhibit fairly regular velocity fields that are dominated by circular motions (see Fig. 4.1). The ratio of non-circular motions to rotational velocity v_{nc}/v_{rot} averaged over the radius for HI is typically in the range of 0.05-0.09, except for NGC 3627 and NGC 4736 which exhibit a slightly larger ratio of 0.12 and 0.14, respectively. For NGC 3627, that can be explained by the fact that it belongs to the Leo Triplet and non-circular motions are very likely induced by the past encounter with NGC 3628 (Zhang et al., 1993). Although NGC 4736 exhibits a one-arm spiral in the outer HI disk which might be a hint for a previous interaction, no optical companion is obvious. The mean values of v_{nc}/v_{rot} are derived by weighting the data points with their standard deviations and are presented together with the standard deviation of the mean value in Tab. 4.6.

Although the mean ratios v_{nc}/v_{rot} are quite small, the ratio of non-circular motions in HI is increasing to 40% as a function of radius, primarily in the inner- and outer-most region of the HI disk. For the center at $\lesssim$1 kpc, a larger fraction of non-circular motions is derived from our CO velocity fields with typical values of (7-14)% for NGC 7217, NGC 5248, NGC 3368, NGC 6951 and very large fractions of (22, 33, 83)% for NGC 4736, NGC 4321, and NGC 3627, respectively. In particular, for NGC 3627 non-circular motions seem to dominate the velocity field not only in the center, but also have significant contributions in the outer disk.

In Fig. 4.3 we plot the rotation curve v_{rot} and the fraction of non-circular motion to circular motion v_{nc}/v_{c_1} as function of radius for each galaxy. The total power of non-circular motions v_{nc} is typically larger for the central (CO kinematics) than for the outer gaseous disk (HI) with mean values of 26% and 9%, respectively. A comparison of non-circular motions and radial flow directions obtained from our kinematics and the ones on the basis of gravitational torques is performed in § 4.5.3. Further, we have compared in §4.5.3 candidate radial gas flow regions derived from our velocity fields with the inflow/outflow rates due to gravity torques. In fact, all studies that have tried to determine an actual inflow/outflow on the basis of the harmonic decomposition alone method were not very successful so far. The main reason for that is that elliptical streaming in a bar or spiral potential seems to be the dominant contributor to noncircular motions (see Wong et al., 2004, for more details). To derive net inflow/outflow a phase shift between the gas and the gravitational potential has to be present, which is the underlying concept for our gravity torque study in the next section.

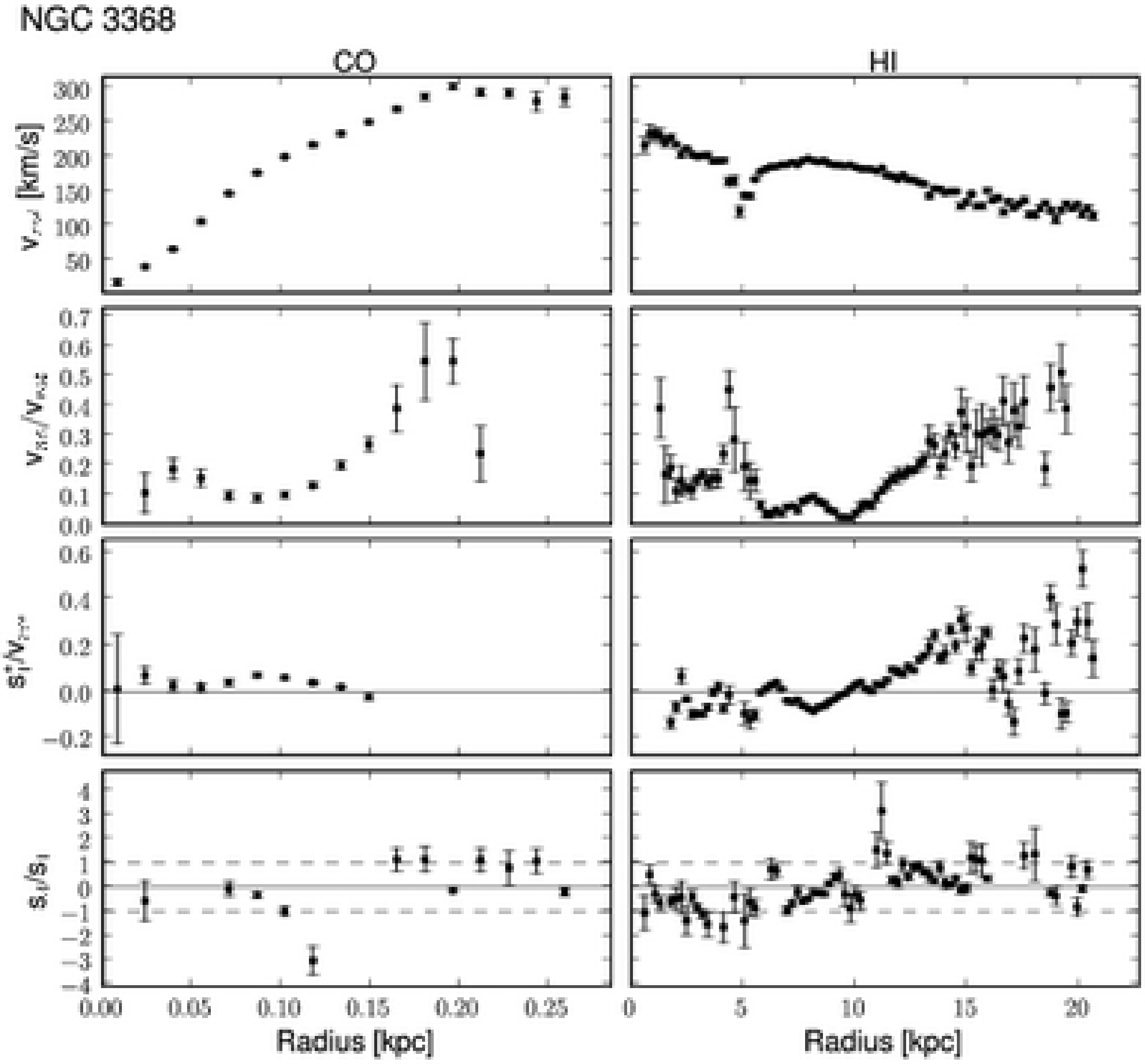

Figure 4.3: Overview of the modeling results based on the CO (left panels) and HI (right panels) velocity fields. From the top to the bottom panels: The rotation curve v_{rot}, the ratio of non-circular motion to rotation velocity v_{nc}/v_{rot}, the ratio of the amplitude of the first sine-term to the rotation velocity s_1^*/v_{rot}, and the ratio of s_3/s_1 as a function of radius for each galaxy. Candidate radial gas outflow and inflow are characterized by a positive and negative sign of the s_1^*/v_{rot} term as long as $|s_3/s_1| \ll 1$. Data with error bars larger than three (two) times the median of the dataset are clipped for HI (CO). At the CR radius R_{CR} the dominance switches from the s_1- to the s_3-terms (Canzian & Allen, 1997) as indicated by the horizontal dashed lines at $s_3/s_1 = \pm 1$.

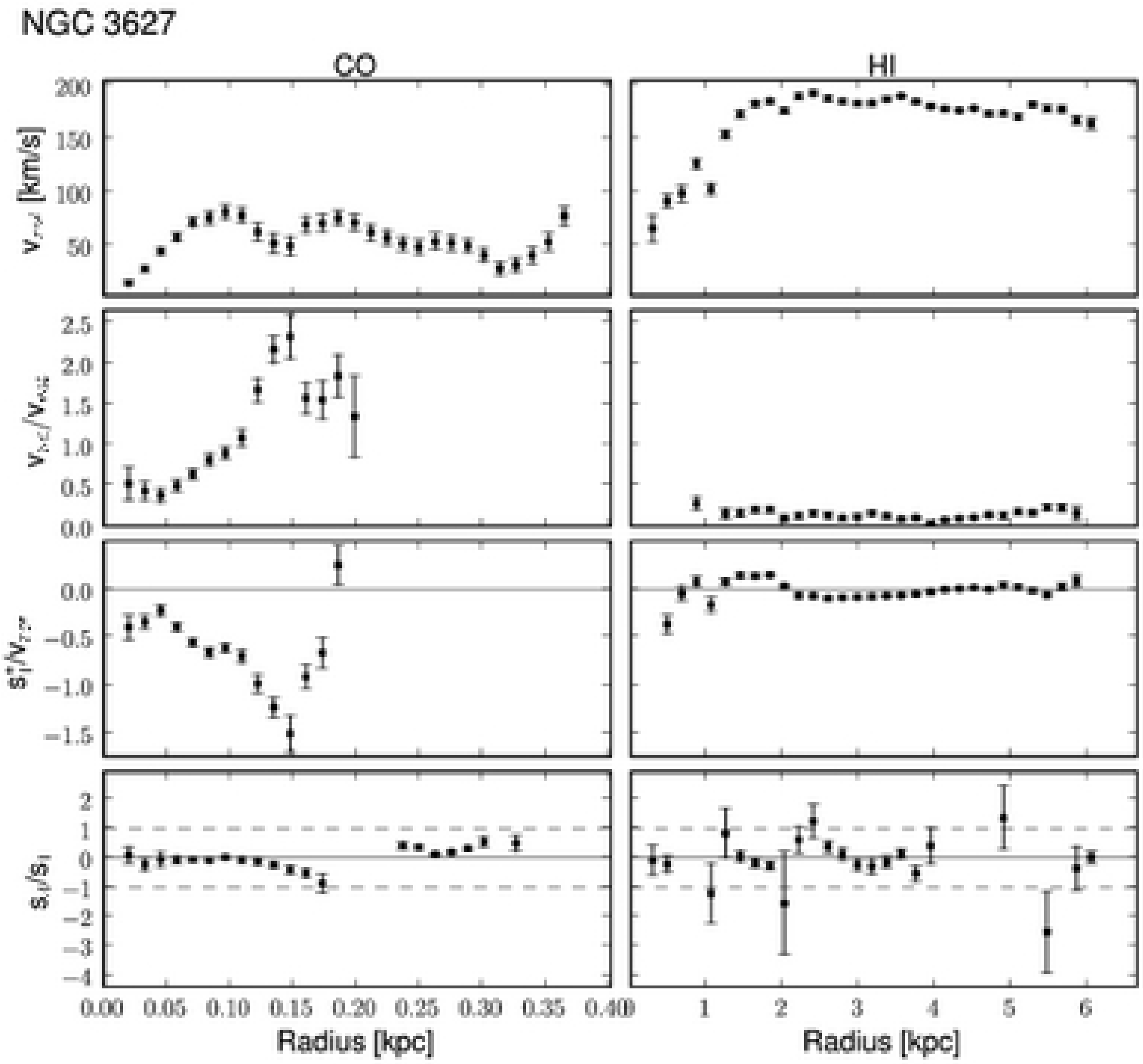

Fig. 4.3 (Continued)

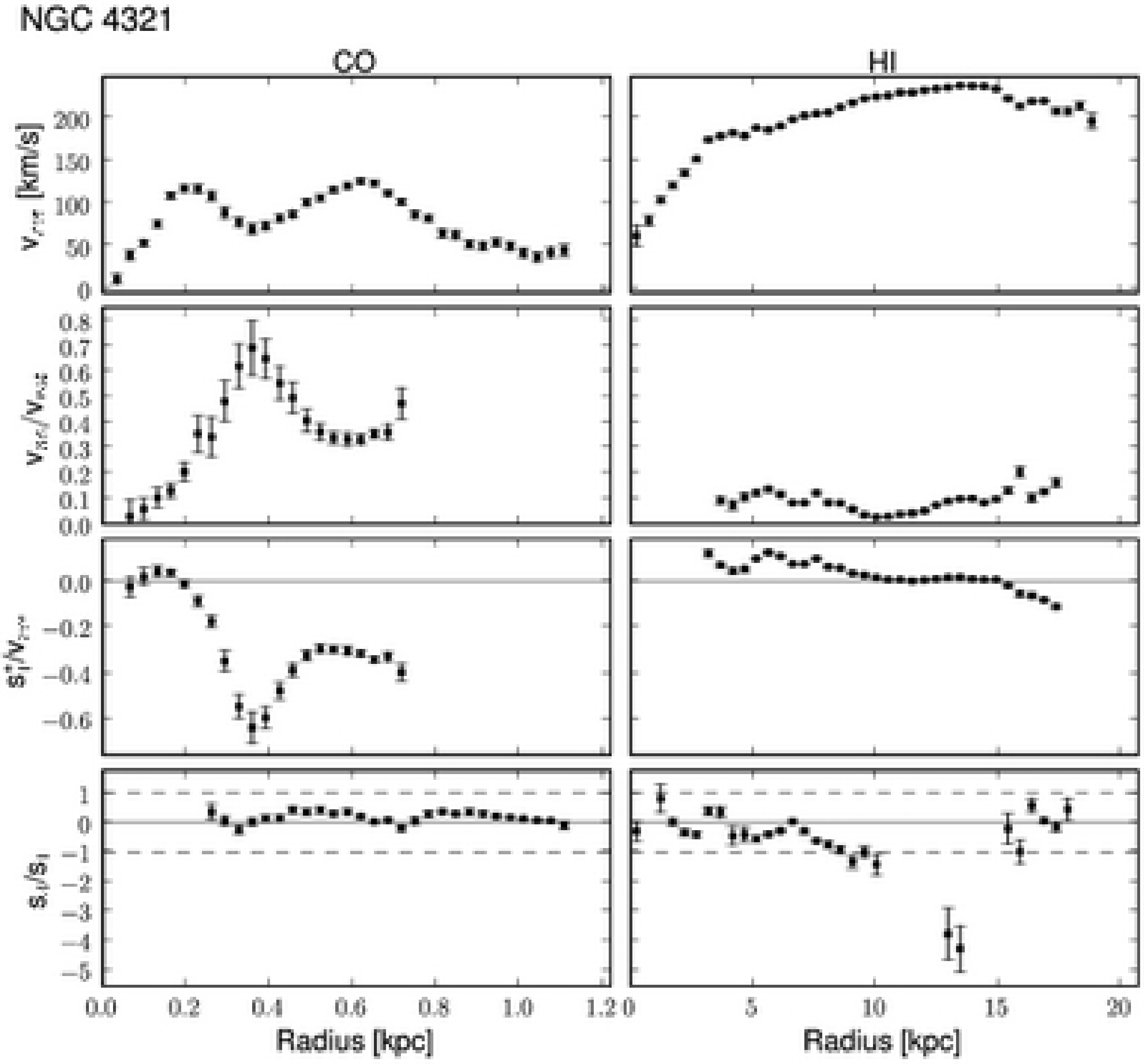

Fig. 4.3 (Continued)

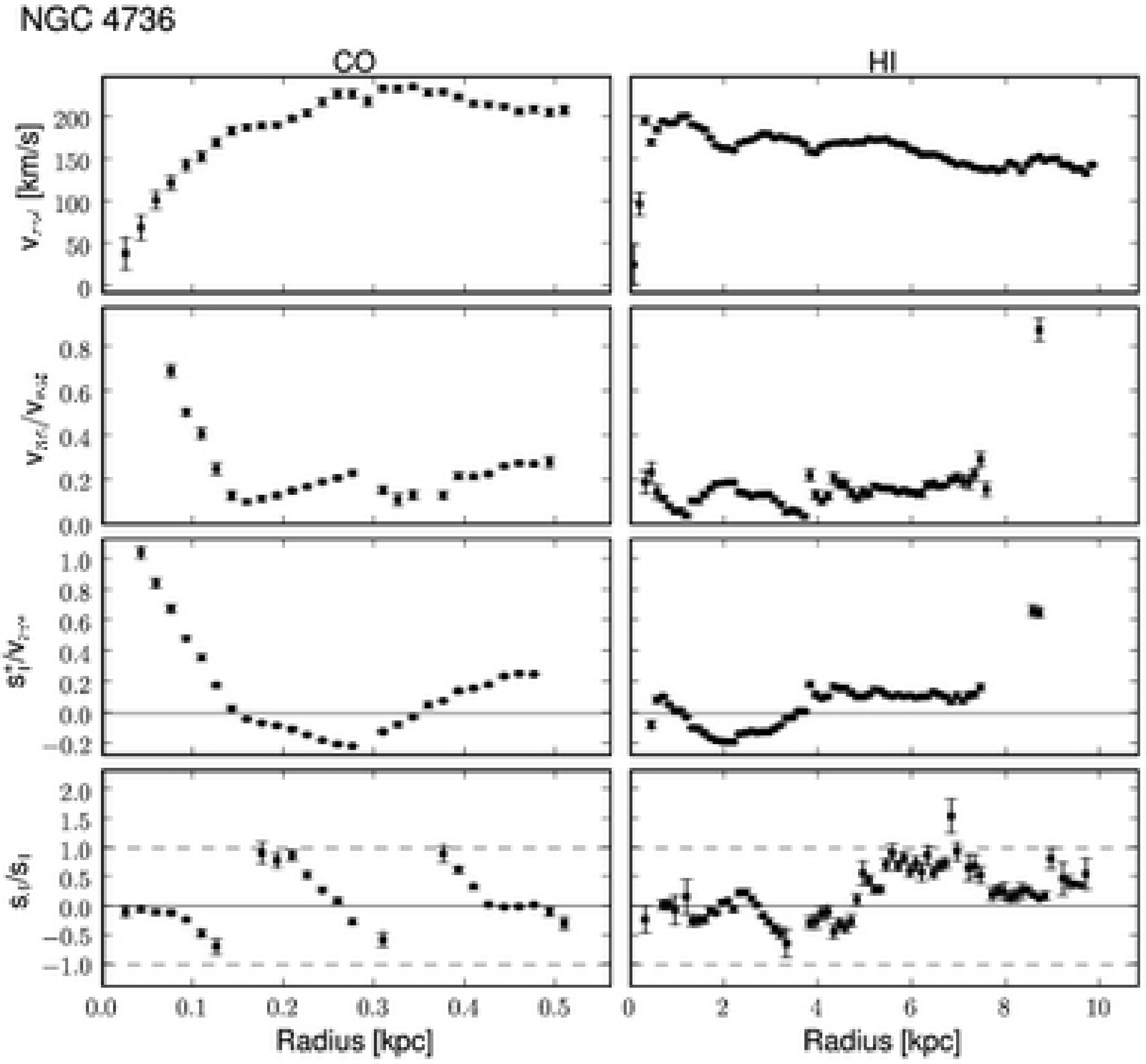

Fig. 4.3 (Continued)

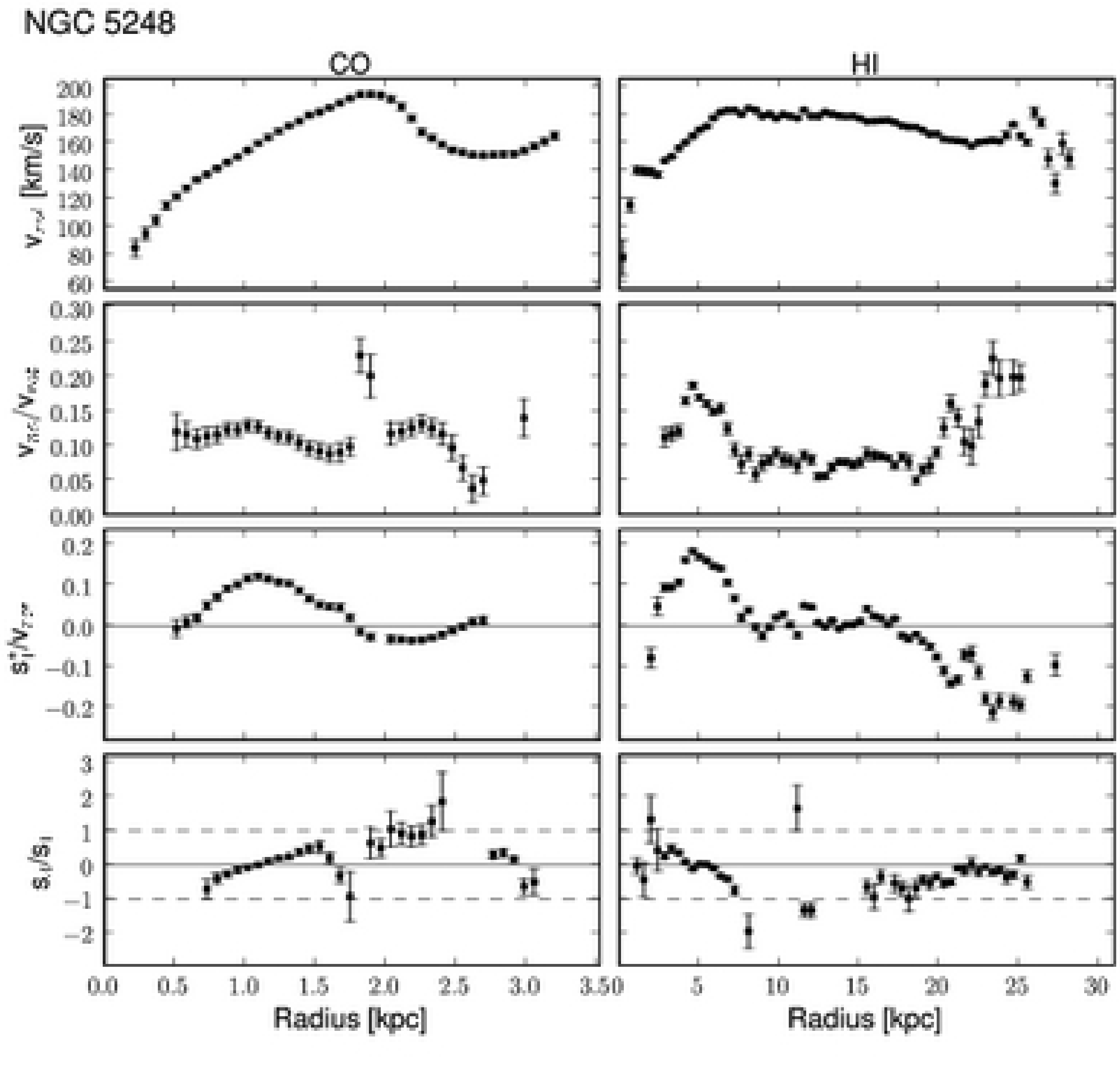

Fig. 4.3 (Continued)

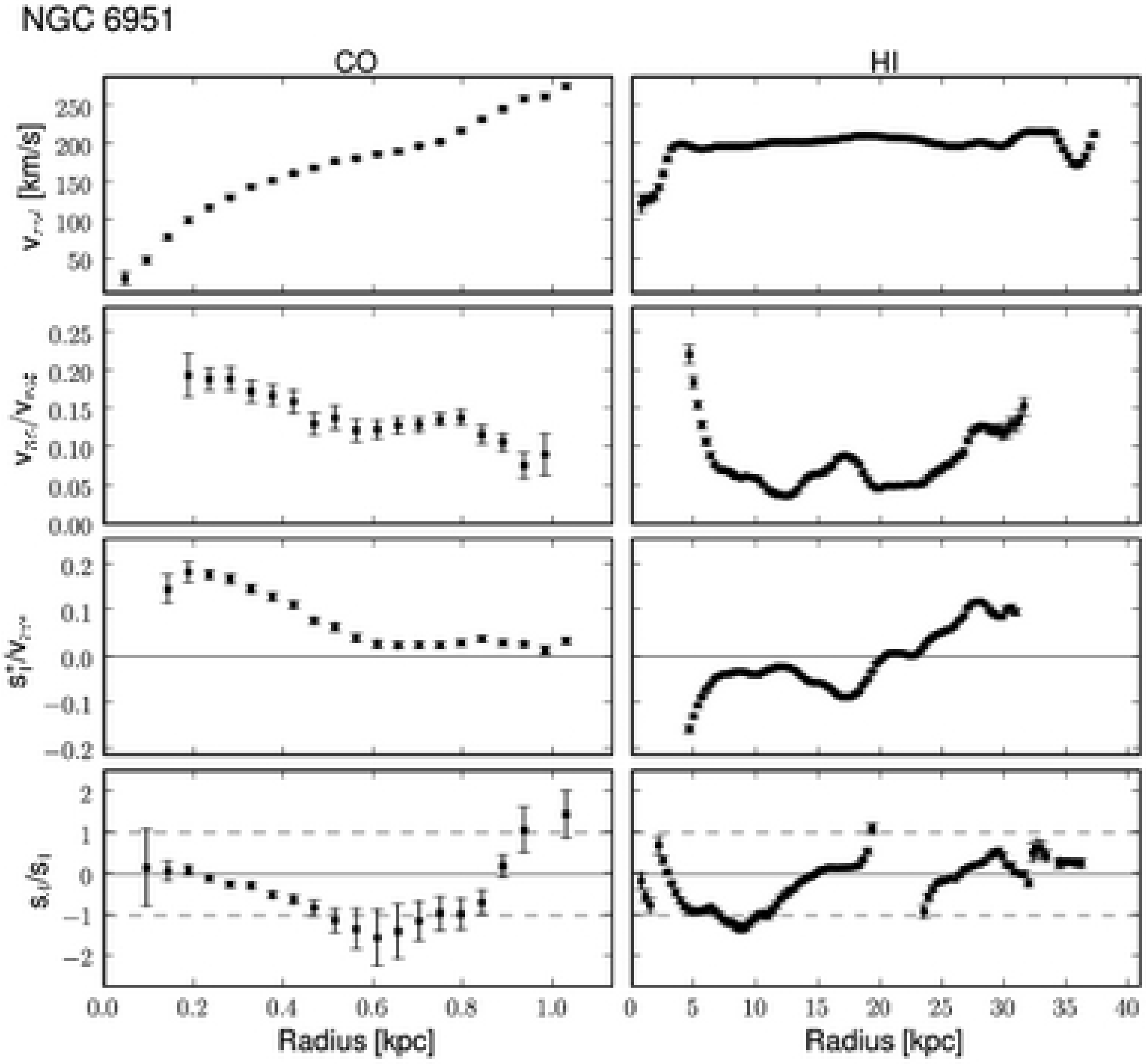

Fig. 4.3 (Continued)

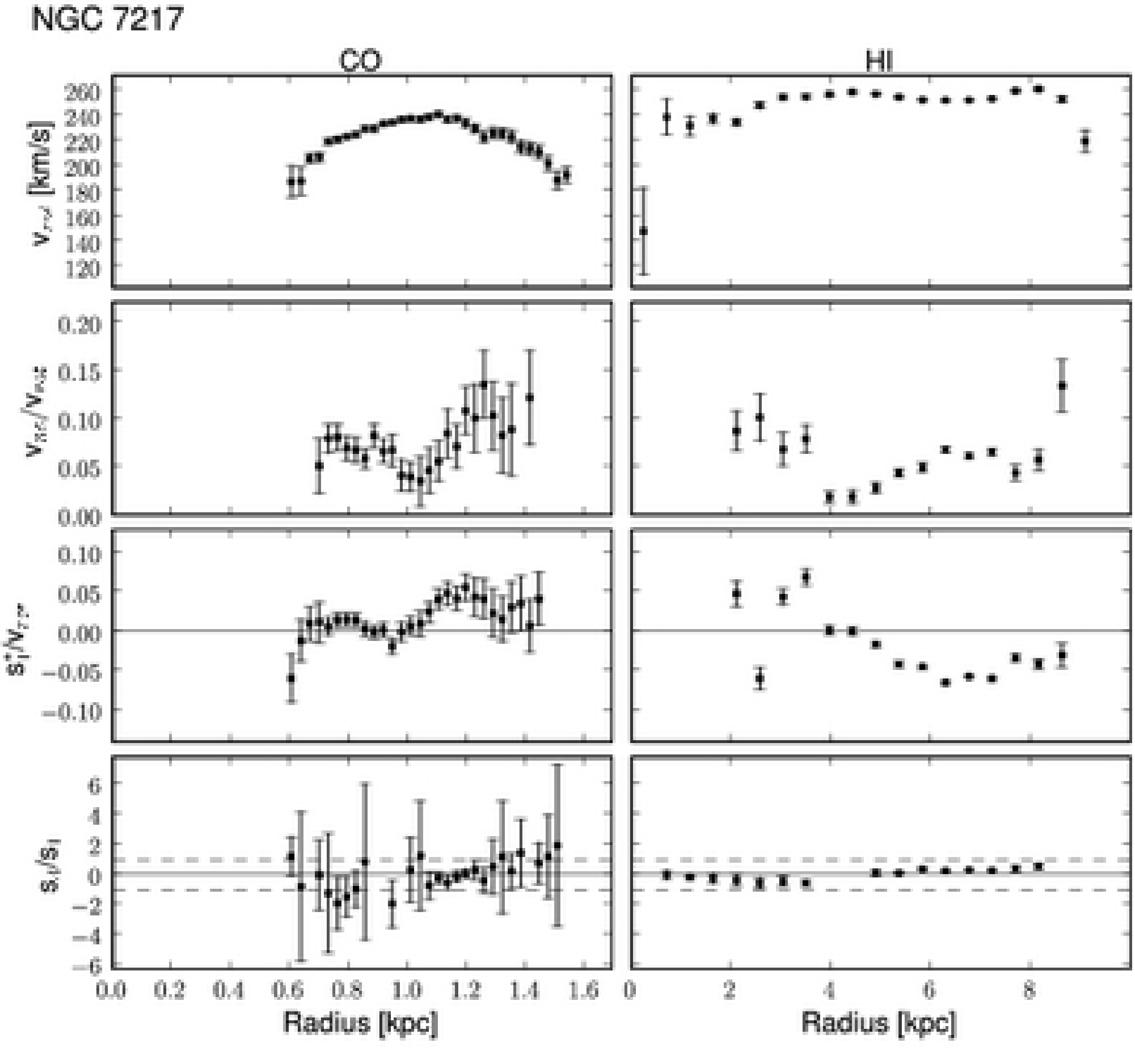

Fig. 4.3 (Continued)

4.4 Gravitational Torques

In this section we focus on the study of gravitational torques exerted by the stellar potential on the gaseous disk. By definition, a torque is a vector $\boldsymbol{\tau}$, which points along the rotation axis it would tend to cause. It can be described mathematically as the cross product $\boldsymbol{\tau} = \boldsymbol{r} \times \boldsymbol{F}$ where $\boldsymbol{r}$ is the particle's position vector relative to the fulcrum and $\boldsymbol{F}$ is the force acting on the particles, or, more generally, as the rate of change of angular momentum, $\boldsymbol{\tau} = \mathrm{d}\boldsymbol{L}/\mathrm{d}t$ where $\boldsymbol{L}$ is the angular momentum vector and t stands for time. The efficiency with which gravitational torques drain the angular momentum of the gas depends first on the strengths of non-axisymmetric components such as bars and oval distributions, but also, on the existence of significant phase shifts between the gaseous and stellar distributions (García-Burillo et al., 2005). To calculate these phase shifts high spatial resolution images of the gas and stars are necessary. The method of mapping the gravitational potential and torques in a non-axisymmetric galaxy is based on its appearance in NIR images using a Fourier transform method (Garcia-Burillo et al., 1993; Quillen et al., 1994; García-Burillo et al., 2005). These gravity torque maps are then utilized to determine the transport of angular momentum, gas inflow rates, and the efficiency of the feeding mechanism for the central black hole. For the computation of the potential and torques we have developed a software toolkit (PyPot) which makes use of the programming language Python and its associated software packages (e.g. Scipy).

The major fraction of the stellar mass of spiral galaxies is made up by old stars such as cool giants and dwarfs rather than from hot young stars which are bright and blue. As near infrared images detect light primarily from these old stars due to their SED, they better trace the mass distribution of a galaxy in comparison to optical images which are biased by the contribution of bright young stars (Aaronson, 1977; Quillen et al., 1994). Furthermore NIR images are less affected from dust-extinction than optical ones and can reveal bars that are not easily observed in the optical (e.g. Quillen et al., 1994).

4.4.1 Method Description

A detailed description of gravitational torques is done by García-Burillo et al. (2005). We used a similar method to derive gravitational torques which is briefly described below and consists of the following steps:

1. Evaluation of the stellar potential using high-resolution NIR images from the Spitzer telescope, ground-based telescopes, and HST. To obtain the total gravitational potential we scale the stellar potential with mass-to-light ratios which are estimated by fitting the gaseous rotation curves derived from our HI and CO observations (see §4.3.1).
2. Computation of gravitational forces and gravity torques based on the stellar potential.

3. Weighting of the torque field with the gas column density in order to link the derived torque field to angular momentum variations.
4. Estimation of the gas flows induced by these angular momentum variations using azimuthal averages of the torques at each radius.
5. Finally, the time-scales and gas masses associated with inflow/outflow are derived by estimating the average fraction of angular momentum transferred in one rotation.

As the average fraction of gas to dynamical mass for our sample is $\sim 5\%$, the total mass budget is expected to be dominated by the stellar contribution, so that we will neglect self-gravity of the gas.

Computation of the Gravitational Potential

The gravitational potential is computed on a cartesian grid based on the NIR images used as tracers for the stellar potential (following the method of Garcia-Burillo et al., 1993). First we deproject the NIR and gas images using the inclination i and position angle PA derived from our kinematic analysis (see §4.2.4). An estimation of systematic errors of our calculations due to possible parameter errors will be presented in §4.4.2. Since a bulge would be artificially elongated by the deprojection, the bulge component has to be excluded from the deprojection. Thus, a bulge model is created first using results from fitting a de Vaucouleurs and exponential function to the radial stellar profile representing the bulge and disk brightness profile, respectively. The bulge model is assumed to be spherical. Then the bulge component is subtracted from the NIR image. After the deprojection of the galaxy (without bulge), the bulge model (with the same scaling as before) is added again to the deprojected galaxy disk. The deprojected NIR and gas images are shown in Fig. 4.4. The gravitational potential of the galaxy,

$$\Phi(\mathbf{x}) = -G \int \frac{\rho(\mathbf{x}')d^3\mathbf{x}'}{|\mathbf{x} - \mathbf{x}'|}, \tag{4.4}$$

can be written as a convolution of the 3D mass density $\rho(x, y, z)$ and the function $g(r) = 1/r$ (the gravitational potential of a point-like source).

$$\Phi(x, y, z) = -G \cdot \rho(x, y, z) \otimes g(r) \tag{4.5}$$

where G is the gravitational constant. We use a smoothing length ϵ, to avoid singularities for distances close to or equal to 0. This results in a slight change of the convolution kernel to:

$$g(r, \epsilon) = \frac{1}{\sqrt{r^2 + \epsilon^2}} \tag{4.6}$$

and we find the normal $1/r$ function when ϵ goes to 0. Further, the thickness of the stellar component of galactic disks is not negligible. Observations have shown that the vertical scale height of stellar disks is roughly constant as a function of radius (van der Kruit & Searle, 1982a,b; Wainscoat et al., 1989; Barnaby & Thronson, 1992). To take this into account we assume a non-infinitesimally thin disk and use a model for the vertical distribution $h(z)$, namely an isothermal plane with

$$h(z) = \frac{1}{2}\, h\; sech^2(z/a), \tag{4.7}$$

and a constant scale height a, equal to $\sim 1/12$ of the radial scale length of the galaxy disk. In that case, the mass density distribution is written as:

$$\begin{aligned} \rho(x,y,z) &= \Sigma(x,y) \times h(z) && (4.8)\\ \text{with} \int_{-\infty}^{\infty} h(z) &= 1 && (4.9) \end{aligned}$$

To compute the potential in the equatorial plane, we integrate the contributions from all heights. This results in a convolution kernel function which can be written as:

$$g(r,\epsilon) = \int_{-\infty}^{\infty} \frac{h(z)}{\sqrt{r^2+\epsilon^2+z^2}}\,\mathrm{d}z \tag{4.10}$$

Hence we still can write the potential in a simple form, at least in the plane of the disk:

$$\Phi(x,y,z=0) = -G \cdot \Sigma(x,y) \otimes g(r,\epsilon) \tag{4.11}$$

In practice, given the vertical thickening function $h(z)$ and the smoothing length ϵ, we tabulate the function $g(r,\epsilon)$ numerically at the beginning of our code. The convolution is then performed using Fast Fourier Transforms. Note that in order to avoid edge effects, we extend the grid to a factor of ~4 times larger than the initial grid.

After that, the potential has to be factorized with the appropriate mass-to-light ratio which is calculated via comparing the observed rotation curve and the rotation velocities derived from the potential,

$$f_{scal}(R) \equiv \frac{v_{model}(R)}{v_{rot}(R)} \tag{4.12}$$

where v_{model} respresents the circular velocity derived from the stellar potential and v_{rot} the rotation curve velocity of our combined and interpolated CO and HI rotation curve at the radius R. Then, we employed a fit on $f_{scal}(R)$ as function of radius using a decomposition into disk, bulge, and dark matter component. The derived scaled circular velocities from the gravitational potential match very well the observed circular velocities within ±5% along the radial axis.

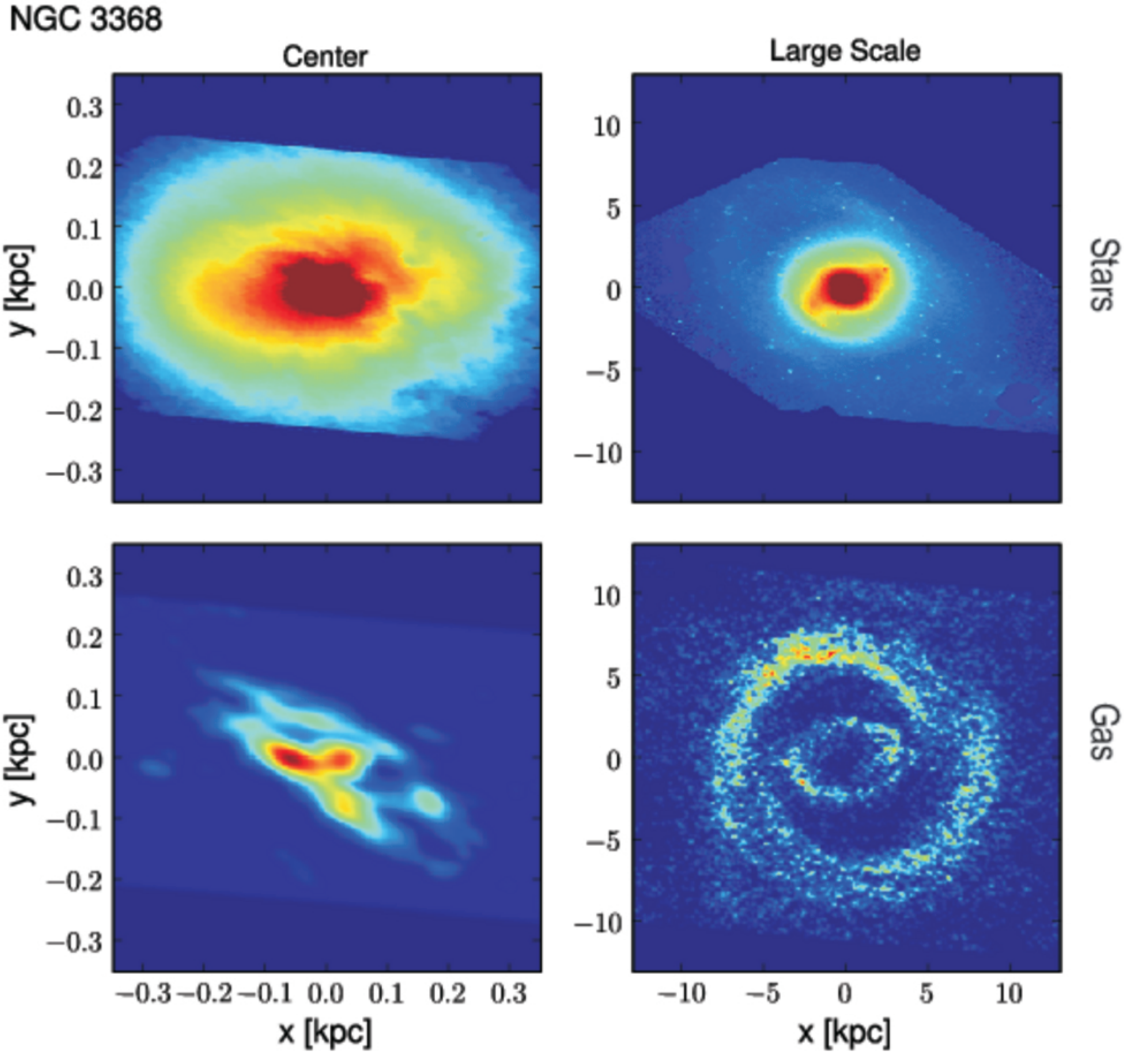

Figure 4.4: Overview of the deprojected stellar (top panels) and gaseous distribution (bottom panels) traced by our CO (left bottom panels) and HI observations (right bottom panels).

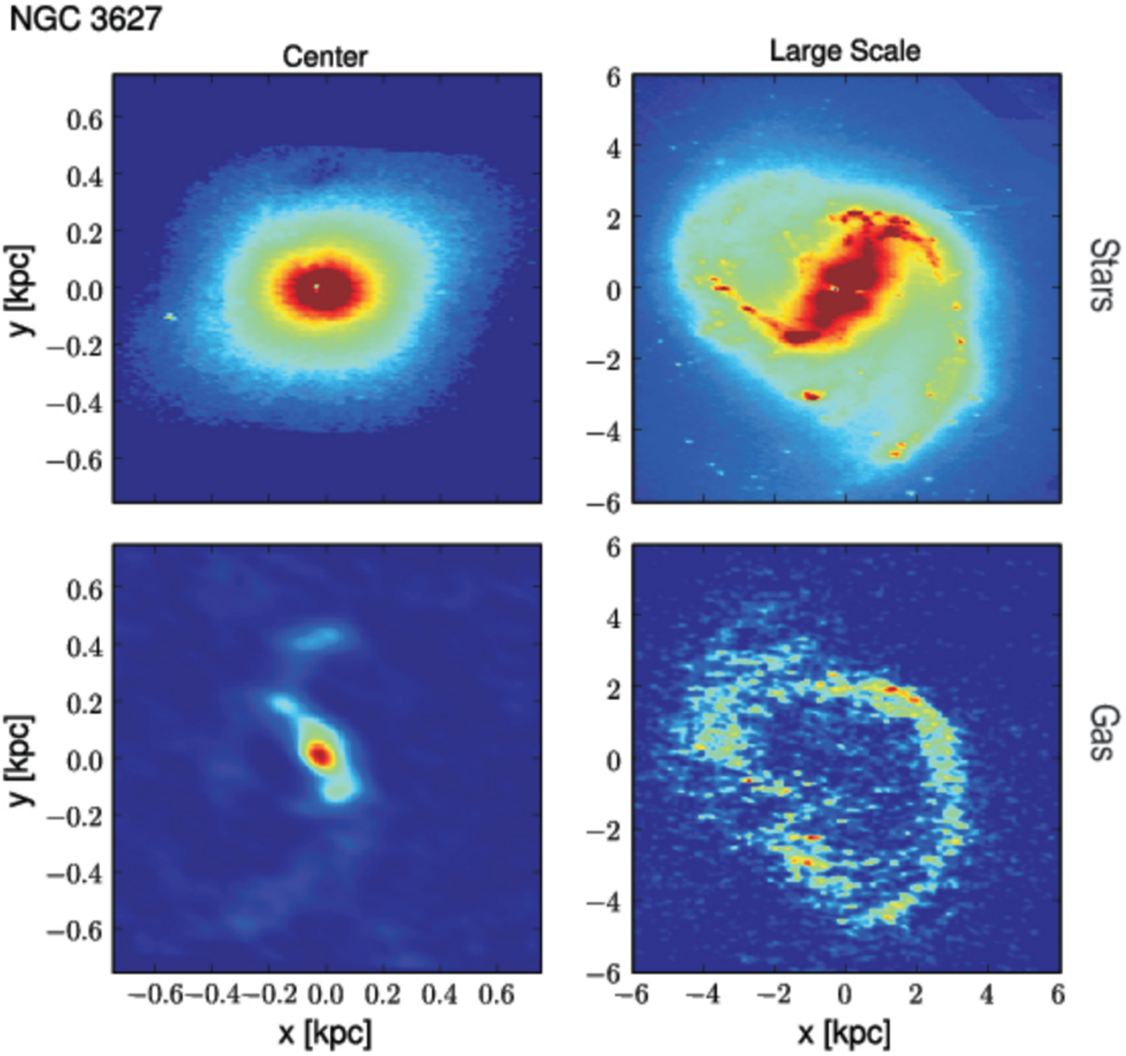

Fig. 4.4 (Continued)

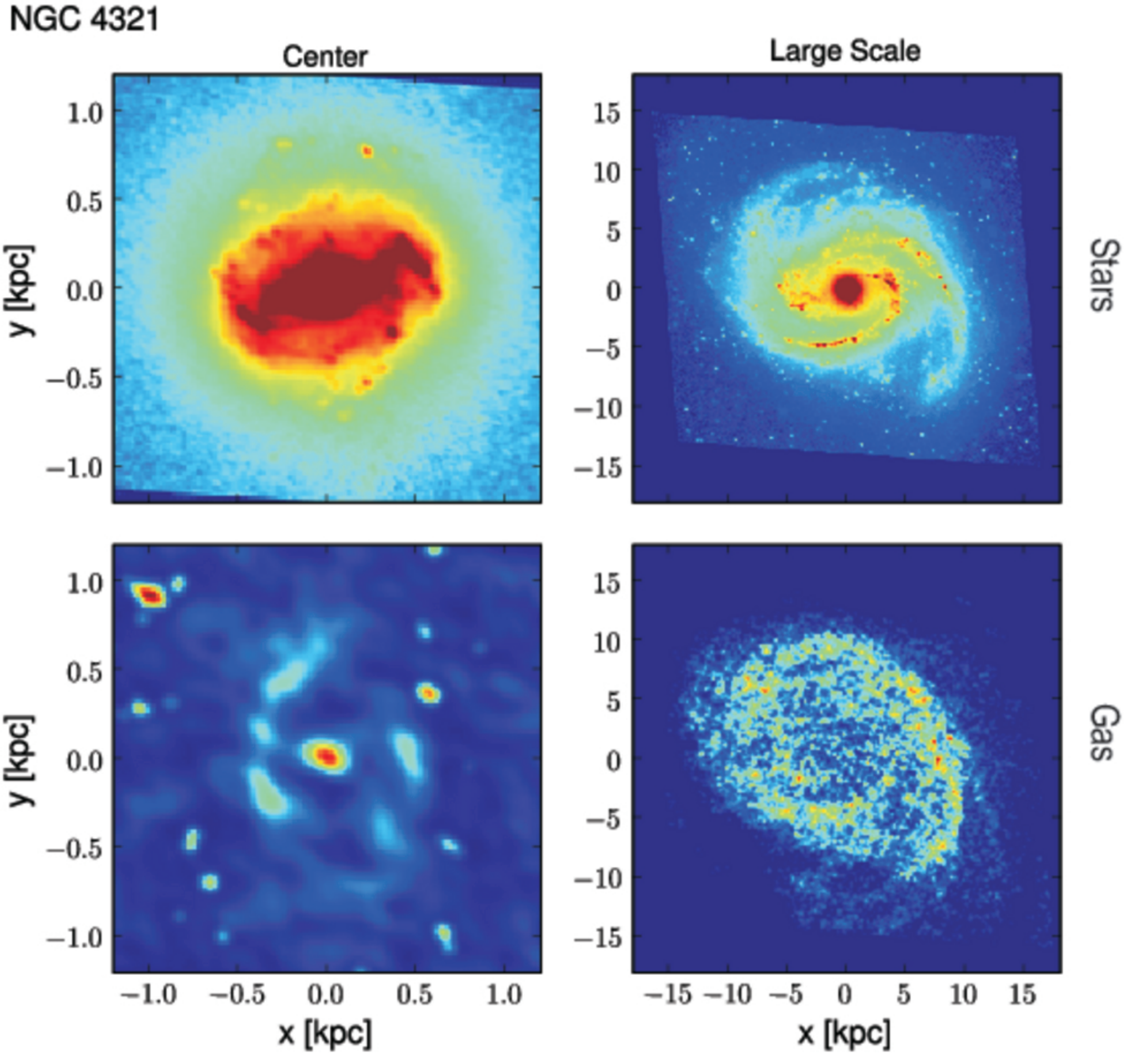

Fig. 4.4 (Continued)

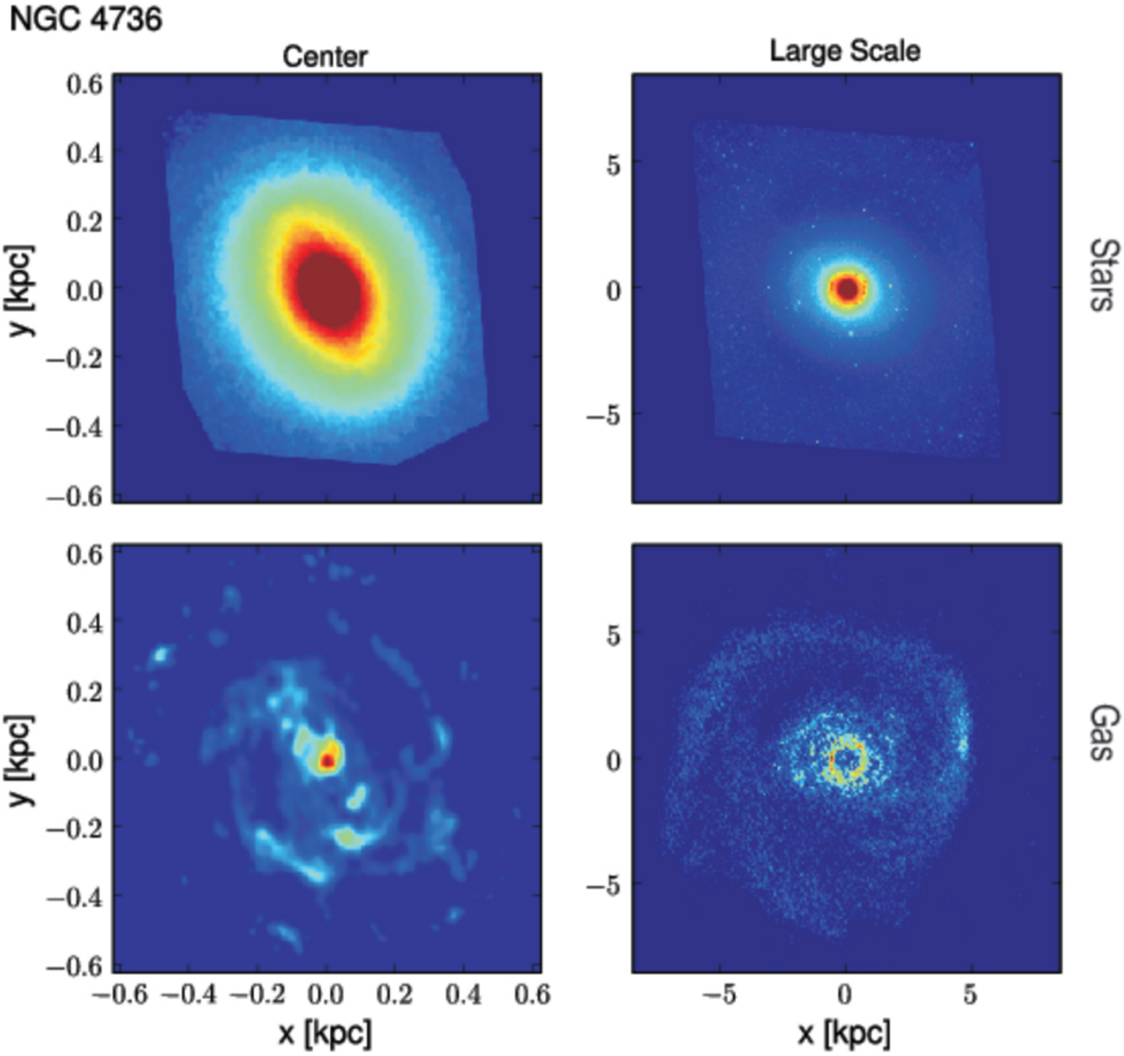

Fig. 4.4 (Continued)

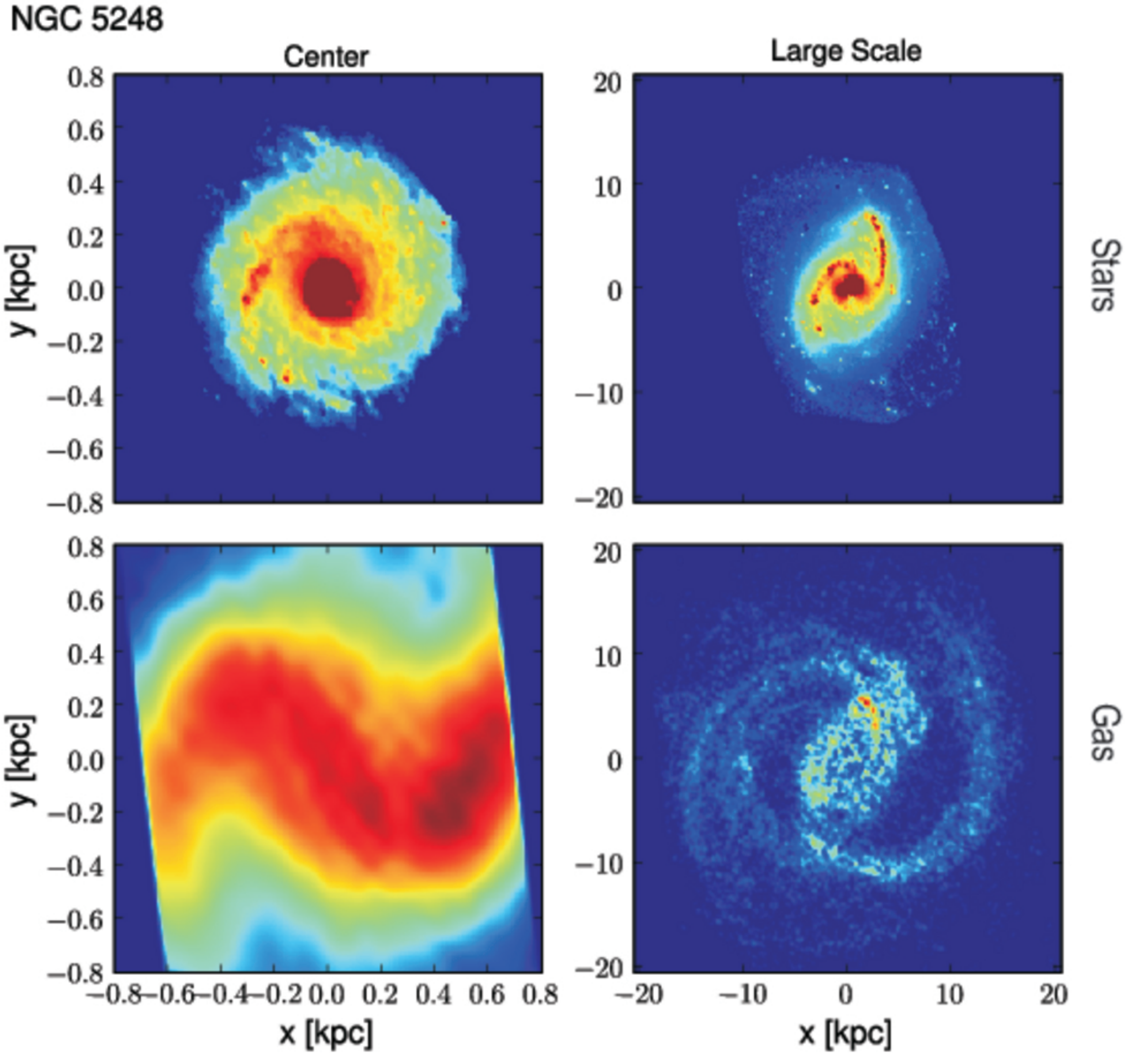

Fig. 4.4 (Continued)

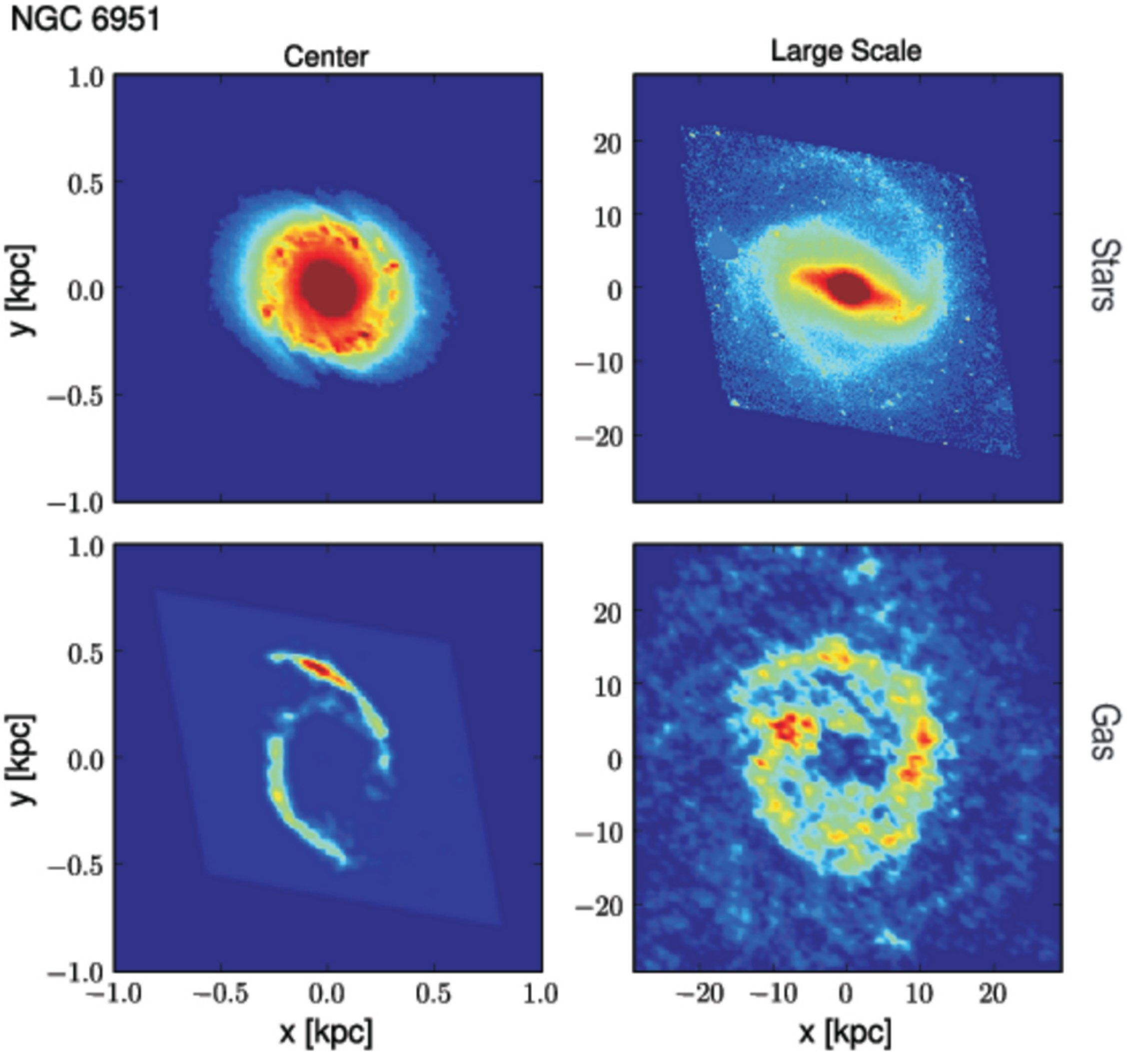

Fig. 4.4 (Continued)

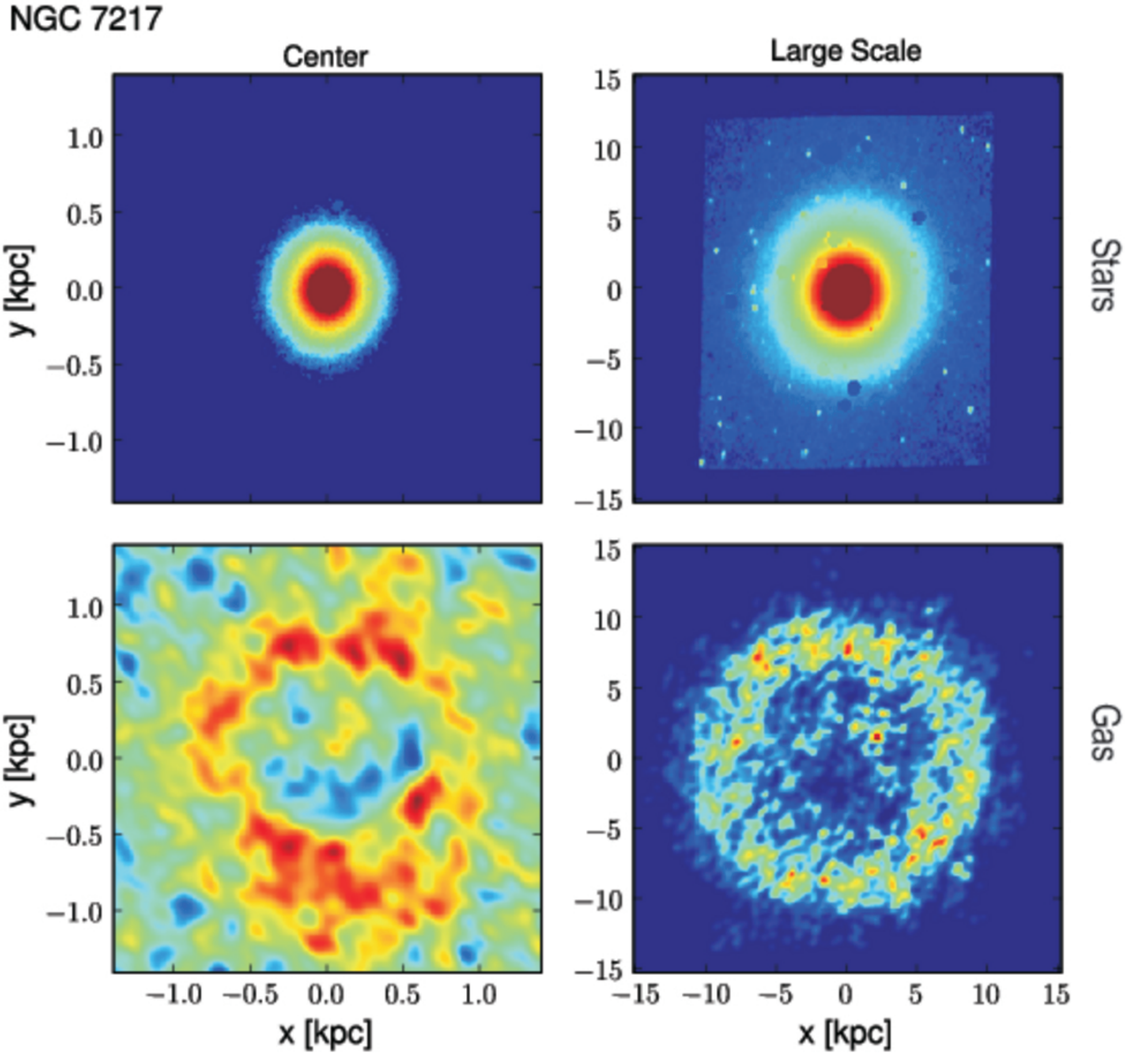

Fig. 4.4 (Continued)

Computation of Gravitational Forces and Gravity Torques

At first, the forces per unit mass in x and y direction $F_{x,y}$ for our derived gravitational potential are calculated at each pixel:

$$F_{x,y}(x,y) = -\nabla_{x,y}\Phi(x,y) \tag{4.13}$$

The gravity torques (per unit mass) $\boldsymbol{\tau}$ are defined as:

$$\boldsymbol{\tau} = \boldsymbol{r} \times \boldsymbol{F}, \tag{4.14}$$

and calculated in the plane:

$$\tau(x,y) = xF_y - yF_x. \tag{4.15}$$

The positive or negative sign of the torque $\tau(x,y)$ defines whether the gas accelerates or decelerates. An example of the gravitational potential and torque is presented in Fig. 4.5 for NGC 6951.

The link between torque field and angular momentum variations is made through the observed distribution of gas (García-Burillo et al., 2005) as explained in the following. At first we assume that the CO and HI emission lines are good tracers of the total gas column density in the center and outer disk, respectively. The reason for using two different lines is due to the fact that the neutral interstellar medium (ISM) undergoes a phase transition from atomic to molecular gas towards the center of a galaxy (Young & Scoville, 1991). Since the gas distribution is the convolution of the gas density with the orbit path density, the gas distribution is indirectly equivalent to the time spent by the gas clouds along the orbit paths. Thus, we implicitly average over all possible orbits of gaseous particles. To do this link between the derived torque field and angular momentum variations, the torques are weighted with the gas column density $N(x,y)$ and averaged over the azimuth:

$$\tau(R) = \frac{\int_\theta [N(x,y) \cdot (xF_y - yF_x)]}{\int_\theta N(x,y)}, \tag{4.16}$$

By definition, $\tau(R)$ represents the azimuthal averaged time derivative of the specific angular momentum L of the gas, i.e.

$$\tau(R) = \frac{\mathrm{d}L}{\mathrm{d}t}|_\theta. \tag{4.17}$$

The positive or negative sign of $\tau(R)$ defines whether the gas may gain or loose angular momentum, respectively. The fueling efficiency can be estimated by deriving the average fraction of the gas specific angular momentum transferred in one rotation (T_{rot}) by the stellar potential, as a function of radius, defined as:

$$\frac{\Delta L}{L} = \frac{\mathrm{d}L}{\mathrm{d}t}|_\theta \cdot \frac{1}{L}|_\theta \cdot T_{rot} = \frac{\tau(R)}{L_\theta} \cdot T_{rot} \tag{4.18}$$

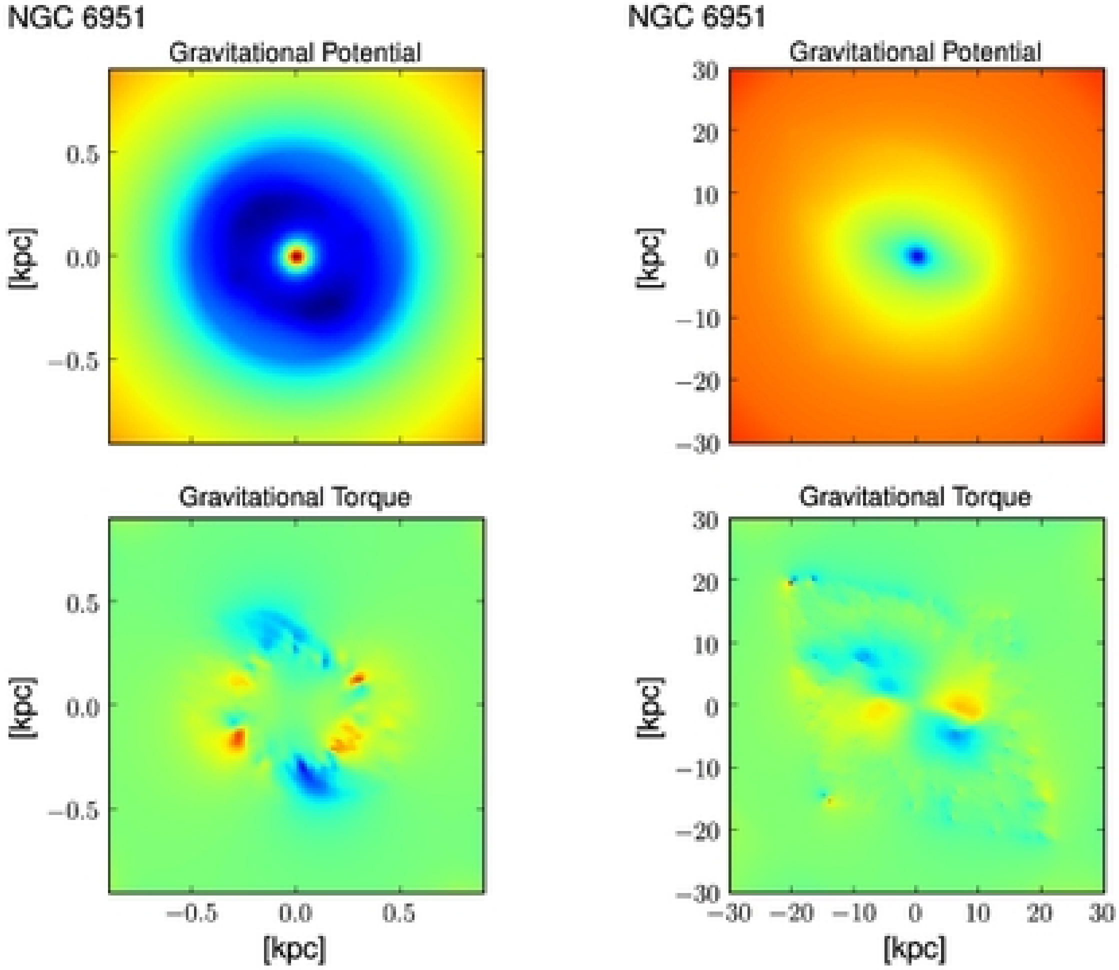

Figure 4.5: Example of the gravitational potential and torque (without weighting with the gas component) for the center (left panels) and the large scale disk (right panels) for NGC 6951.

where the azimuthal averaged angular momentum L_θ is assumed to be well represented by its axisymmetric average, i.e., $L_\theta = R \cdot v_{rot}$. The inverse of $\Delta L/L$ determines how long it will take (in terms of orbital time periods) for the gravitational potential to transfer the equivalent of the total gas angular momentum.

The mass inflow/outflow rate of gas per unit length $\mathrm{d}^2M(R)/(\mathrm{d}R\mathrm{d}t)$ (in units of $\mathrm{M}_\odot\ \mathrm{yr}^{-1}\ \mathrm{pc}^{-1}$) is calculated as follows:

$$\frac{\mathrm{d}^2M(R)}{\mathrm{d}R\mathrm{d}t} = \frac{\mathrm{d}L}{\mathrm{d}t}|_\theta \cdot \frac{1}{L}|_\theta \cdot 2\pi R \cdot N(x,y)|_\theta \tag{4.19}$$

where $N(x,y)|_\theta$ is the gas column density of the atomic (HI) and molecular gas using the conversion factor from CO to H_2 typical for galaxy nuclei of $X = N(H_2)/I(CO) = 2.2\ 10^{20}$ cm^{-2} K^{-1} km^{-1} s (Solomon & Barrett, 1991). Then, the integrated inflow/outflow rates $\mathrm{d}M(R)/\mathrm{d}t$ are derived by integrating from $R = 0$ out to a certain radius R,

$$\frac{\mathrm{d}M(R)}{\mathrm{d}t} = \sum_{0}^{R} \left[\frac{\mathrm{d}^2 M(R)}{\mathrm{d}R\mathrm{d}t} \cdot \Delta R \right] \tag{4.20}$$

with ΔR as radial binning size (in units of pc).

4.4.2 Robustness of the Method: Parameters and Errors

In order to examine the reliability of our results, we estimated how small errors in our assumed parameters will affect the results. One main source for errors arises from uncertainties in the input parameters that were derived from our kinematic study (see previous section). First, we checked the parameters that describe the geometry of the disk given by inclination i, position angle PA, and position of the center (x, y). We assume that these parameters do not vary with radius. To evaluate the effects of changes in these parameters on the derived gravity torque map, we tested two simple disk models (see Fig. 4.6): 1) an exponential disk which produces no torque pattern because of its axisymmetrical distribution, and 2) An exponential disk plus an additional constant oval distribution, which produces a typical torque that changes sign between the 4 quadrants. The oval distribution has a minor-to-major axis ratio of 0.5 and a constant surface brightness of 20% of the maximum brightness of the exponential disk. For comparison, typical torque patterns without parameter errors are presented in Fig. 4.7 for different disk models. We tested the robustness of the results from our code with uncertainties based on our kinematic results:

- An inclination error of 3° at a typical inclination of 45°: The result shows an additional torque pattern that changes sign between the 4 quadrants. This pattern corresponds to one induced by a small oval contribution. Because of its axisymmetry and uniform gas distribution no contribution in the radial profile is seen. In principle an inclination error will produce a fake "bar" or "oval" but it will be along one of the principal axes of the disk (major, minor) and hence might provide a way to disentangle this false pattern from a true one.
- A position angle error of 2°: Here the torque also changes sign between the 4 quadrants, causing a pattern similar to an oval distribution, but along an axis that is rotated by 45° to one of the principal axes.
- An error of the center position of 1 pixel which corresponds to ∼50 pc at a distance of 10 Mpc and a pixel size of 1″: That results in a bimodal pattern, which increases the torque budget of one side of a torque pattern produced by an oval distribution, and decreases the torque at the opposite side.

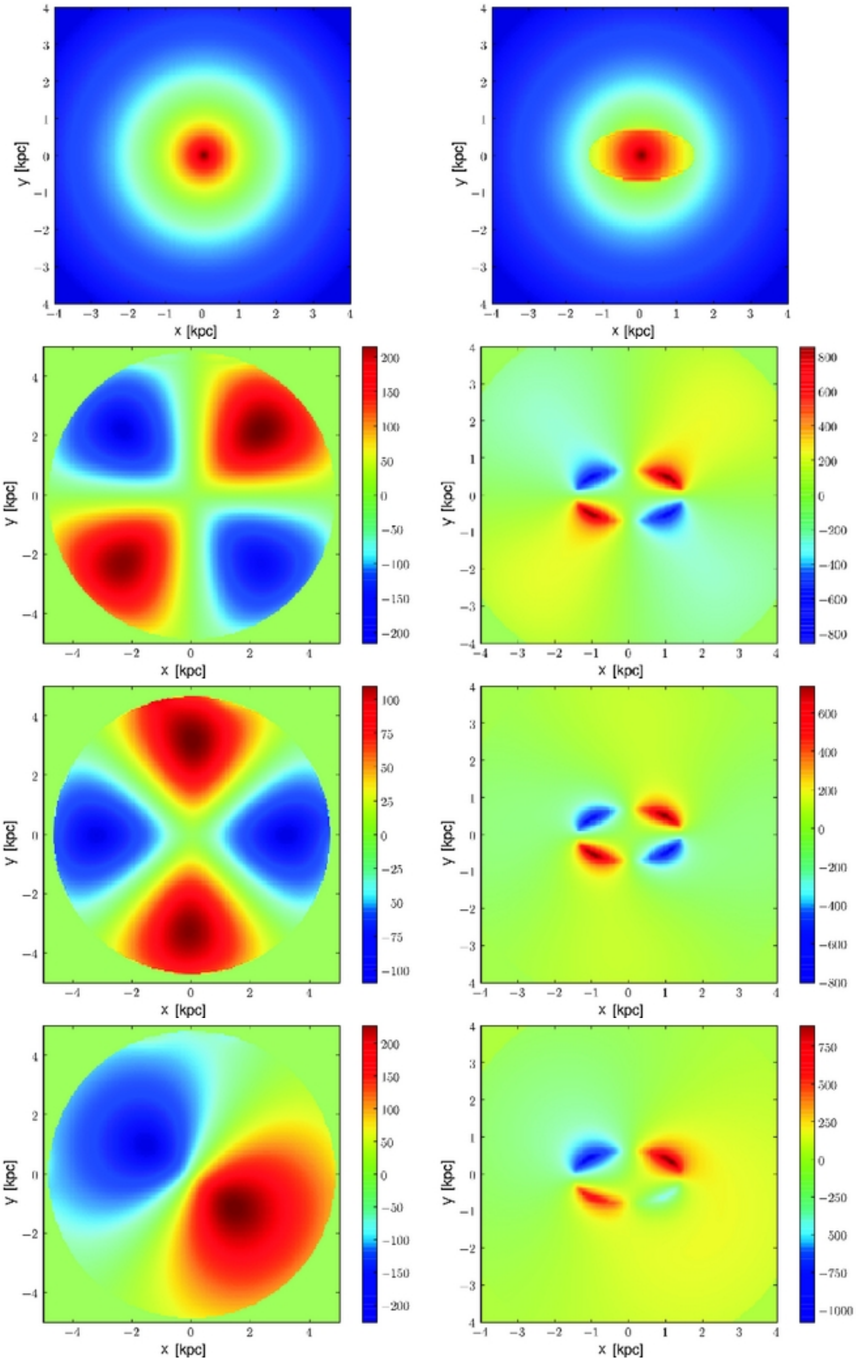

Figure 4.6: Overview of the error estimation from models. The computed torques are calculated for two models: 1) an exponential disk (top left panel) which produces no torque pattern because of its axisymmetric distribution, and 2) an exponential disk plus an additional constant oval distribution (top right panel). The torque calculation is tested with uncertainties of an inclination error of 3° (second row), a position angle error of 2° (third row), and an error of the center position of 1 pixel $\simeq 1''$ (bottom row).

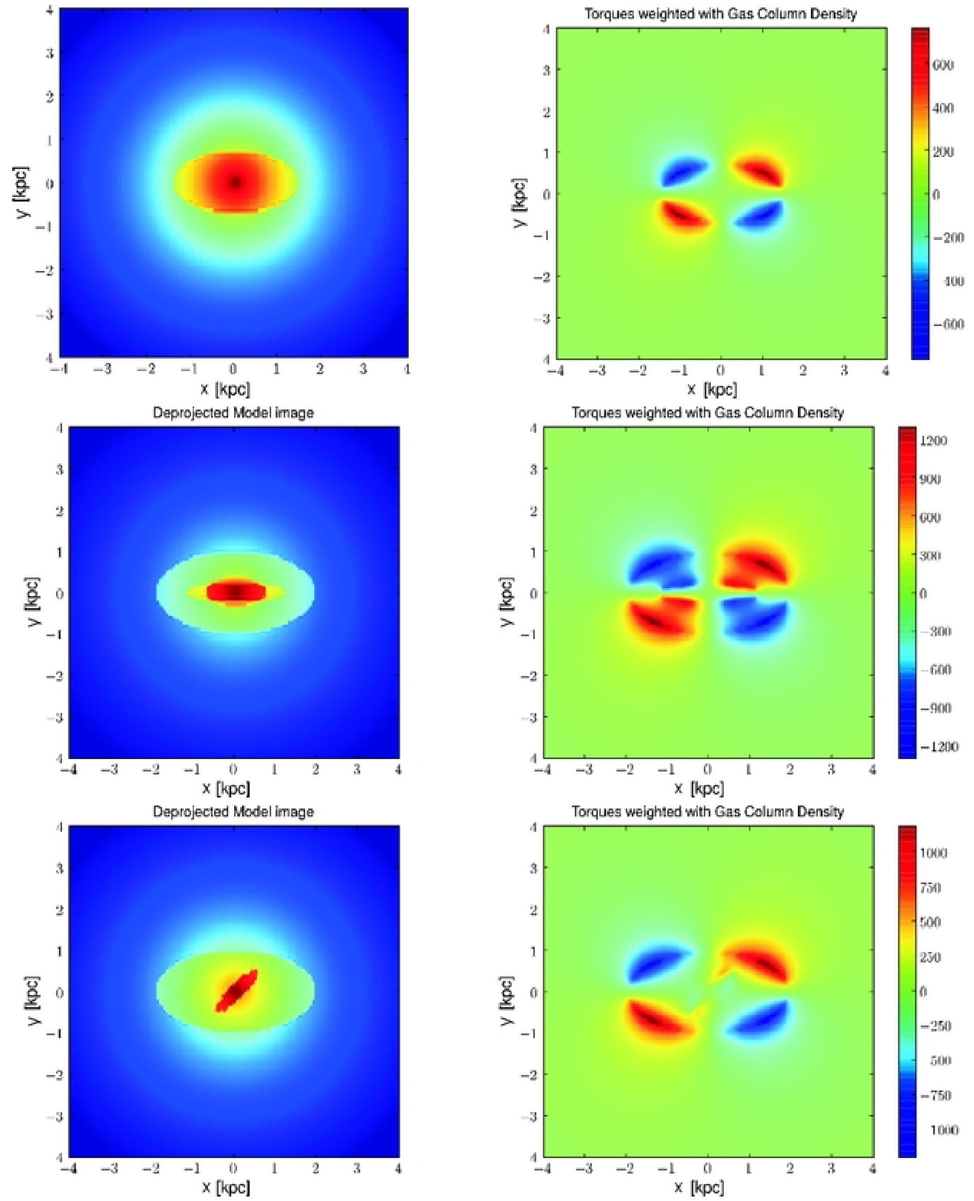

Figure 4.7: Comparison of the torque patterns (right panels) derived from three different models (left panels): 1) exponential disk plus a constant oval distribution (top row), 2) exponential disk plus three parallel aligned constant oval distributions/bars with different lengths and strengths (middle row), and 3) exponential disk plus a constant oval distribution and an inner bar with a difference in PA of 45° (bottom row).

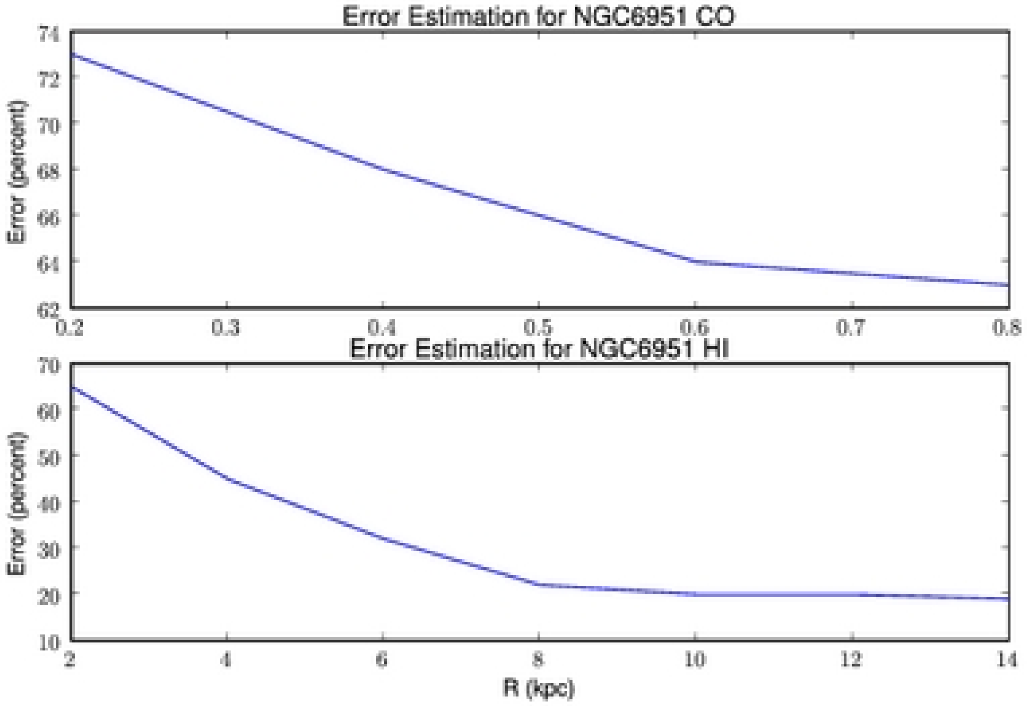

Figure 4.8: Error estimation for CO (top) and HI (bottom) based on radial torque calculation. The errors are the relative differences between the torque results using the best input parameters with those where typical errors of the input parameters were applied.

Since this simple test does not take into account the gas distribution of a "real" galaxy which very likely differs from an homogeneous axisymmetric distribution, we also estimated the effects of these uncertainties using the NIR images and gas maps of a typical galaxy from our sample, namely NGC 6951. In order to estimate the errors in the radial torques, we compared the torque results using the best input parameters with those where typical errors of the input parameter were applied. The total error as a function of radius is shown in Fig.4.8. The results of this test are summarized in Tab. 4.7, separately for the central CO based and outer HI based torque calculation.

Not only geometric uncertainties can have an effect on our results, but also the assumed mass-to-light ratio. Since we scale our potential with the derived (deprojected) rotation curve from the velocity maps, our results do not depend on uncertainties in the mass-to-light ratio, e.g. derived from stellar population models. Instead, our method relies on a scaling factor between the circular velocity derived from the stellar potential and the combined CO and HI rotation curve velocity as given by Eq. 4.12. Since rotation curves are derived from azimuthal averaged velocities, different mass-to-light contributions of non-axisymmetric

Table 4.7: Error estimation

Parameter	dτ (CO)	dτ (HI)
Position Angle (dPA=2°)	4%	<1%
Inclination (di=2°)	24%	<1%
Shift of IR image (0.2″)	10-30%	~13%;
Shift of gas image (0.3″)	5-20%	5-20%
Background subtraction	<5%	<1%
Bulge-nobulge subtraction	< 2%	3-10%
Rot vel (dv=15 km s^{-1})	20%	10%
Sum	60-80%	13-70%
Typical	67%	30%

Note. — Estimation of systematic errors in the radial torques for CO and HI of a typical galaxy from our sample, namely NGC 6951. To do so, the torque results using the best input parameters have been compared with those where typical errors of the input parameters were applied. Note that the errors have a radial dependency (see Fig. 4.8)

components such as spiral arms (cool supergiants or dust glowing star formation regions) and bars will affect the scaling. Furthermore, possible deviations from a constant inclination of the galaxy disk (i.e. warping disk) might have an impact. However, most spiral galaxies show only small variations in the inclination across the stellar disk and we found no evidence for a significant warped disk in our sample as described in §4.3.1

Another possible source of error might be that the gas distribution is not 100% recovered at all spatial scales due to missing short spacings of the interferometer observations. As our HI observations are continuous and traces all spatial scales, HI is a good tracer for the atomic gas distribution in our galaxies. For CO, the PdBI observations do not trace all spatial scales, and thus, might miss some flux from short spacings. However, to estimate the effect of short spacing corrections, García-Burillo et al. (2008) have compared the gravity torque results for NGC 4579 without (only CO PdBI-data) and with short spacing corrections using additional CO data obtained with the IRAM 30m telescope. The result shows that the gravitational torques with short spacings are roughly (5-40)% larger than without short spacings.

4.4.3 Determining the Corotation Radii

The accurate determination of the corotation (CR) radii of density wave patterns is an important parameter for the characterization of the dynamical state of a galaxy and to understand the relation between morphologies and kinematics of galaxies. We have applied the *Potential-Density Phase-Shift* method (Zhang & Buta, 2007) to derive the corotation resonance (CR) radii for our galaxies. This technique is based on the calculated radial distribution of an azimuthal phase shift between the stellar potential and a stellar density wave pattern which results in a torque action between the wave pattern and the underlying disk matter. Consequently, the material inside (outside) the CR radius looses (gains) angular momentum which causes an inflow (outflow).

The validity of the phase-shift method is based on the global self-consistency requirement of the wave mode (i.e., both the Poisson equation and the equations of motion need to be satisfied at the same time). For a self-sustained global spiral mode, the radial density variation of the modal perturbation density, as well as the pitch angle variation, together determine that the Poisson equation will lead to the zero crossing of the phase-shift curve being exactly at the CR radius of the mode (see for more details Zhang & Buta, 2007).

We calculated the CR radius using the method of Zhang & Buta (2007) as follows: The rate of angular momentum exchange between the density wave pattern and the axisymmetric part of the disk can be either expressed as (Zhang, 1996):

$$\frac{dL}{dt}(r) = -\frac{1}{2\pi}\int_0^{2\pi} \Upsilon(r,\phi)\frac{\partial\Psi(r,\phi)}{\partial\phi}d\phi, \tag{4.21}$$

with the perturbation density waveform Υ and the perturbation potential waveform Ψ, or as two sinusoidal waveform,

$$\frac{dL}{dt}(r) = \frac{m}{2}A_\Upsilon(r)A_\Psi(r)\sin\left[m\phi_0(r)\right], \tag{4.22}$$

with the amplitudes of the density wave A_Υ and potential wave A_Ψ, the non-axisymmetric mode number m (e.g. for two spiral arms or a bar: m=2), and the phaseshift ϕ_0 between these two waveforms. Using these two equations, the phaseshift ϕ_0 can be calculated from

$$\phi_0(r,\phi) = \frac{1}{m}\sin^{-1}\left[\frac{1}{m}\frac{\int_0^{2\pi}\Upsilon(r,\phi)\frac{\partial\Psi(r,\phi)}{\partial\phi}d\phi}{\sqrt{\int_0^{2\pi}\Psi^2 d\phi}\sqrt{\int_0^{2\pi}\Upsilon^2 d\phi}}\right]. \tag{4.23}$$

The potential Ψ and the density distribution Υ are taken from our gravity torque calculation (see §4.4.1). We assume that the phaseshift is positive when the potential lags the density wave in the azimuthal direction in the sense of the galactic rotation. For all of our galaxies we derived the phaseshift as a function of radius and we defined the CR radii as the positive-to-negative crossings of the phaseshift ϕ_0 (see Fig. 4.9). At this location the direction of angular momentum transfer between the disk matter and the density wave changes sign.

In fact, the Phase-Shift method of Zhang & Buta (2007) is very similar to our gravity torque study as both rely on a phase-shift between the gravitational potential and a density wave

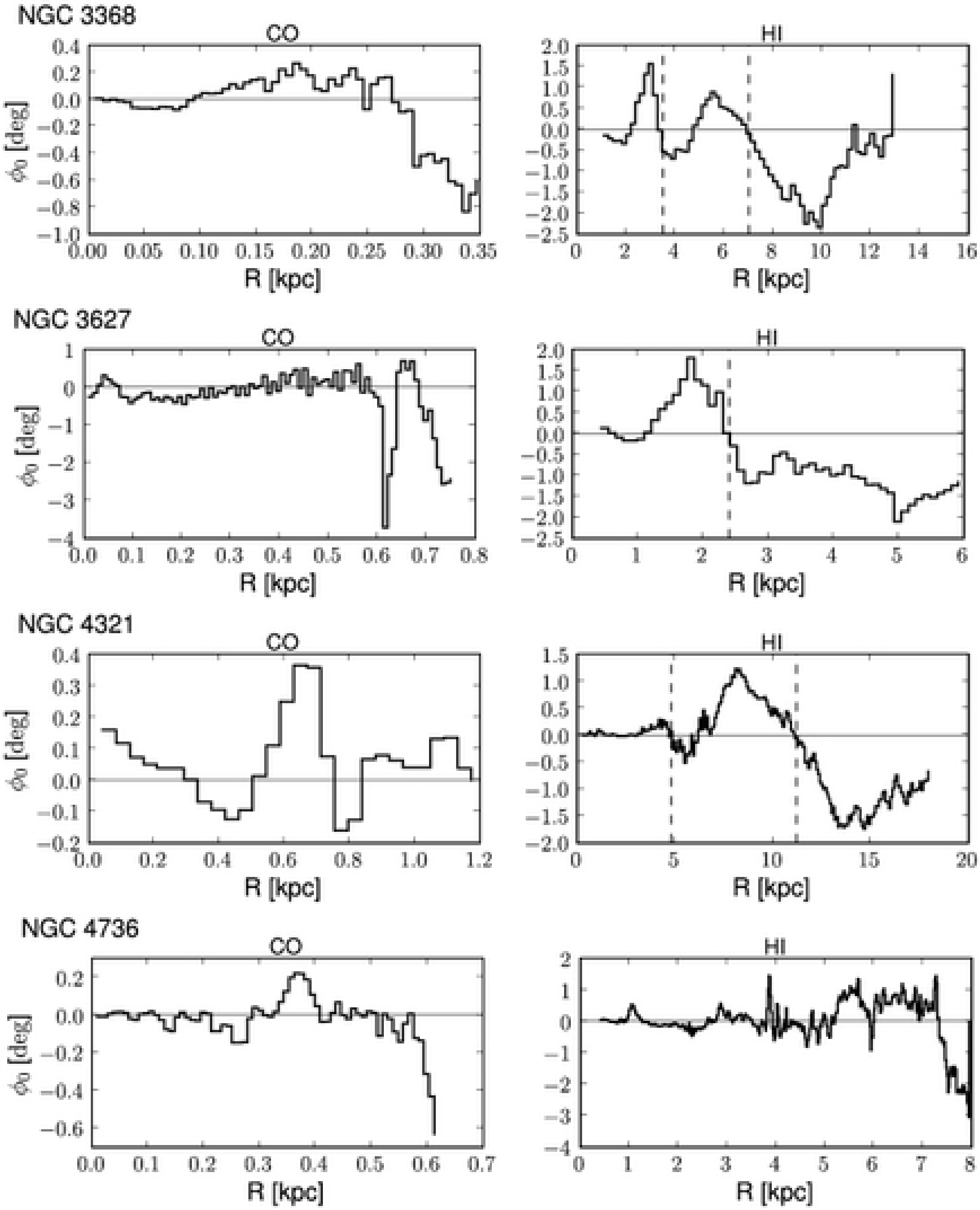

Figure 4.9: Overview of the phaseshift between the potential and density wave patterns for the center (left panels) and the large scale disk (right panels). The CR radii are defined as the positive-to-negative crossings of the phaseshift and indicated by dashed vertical lines.

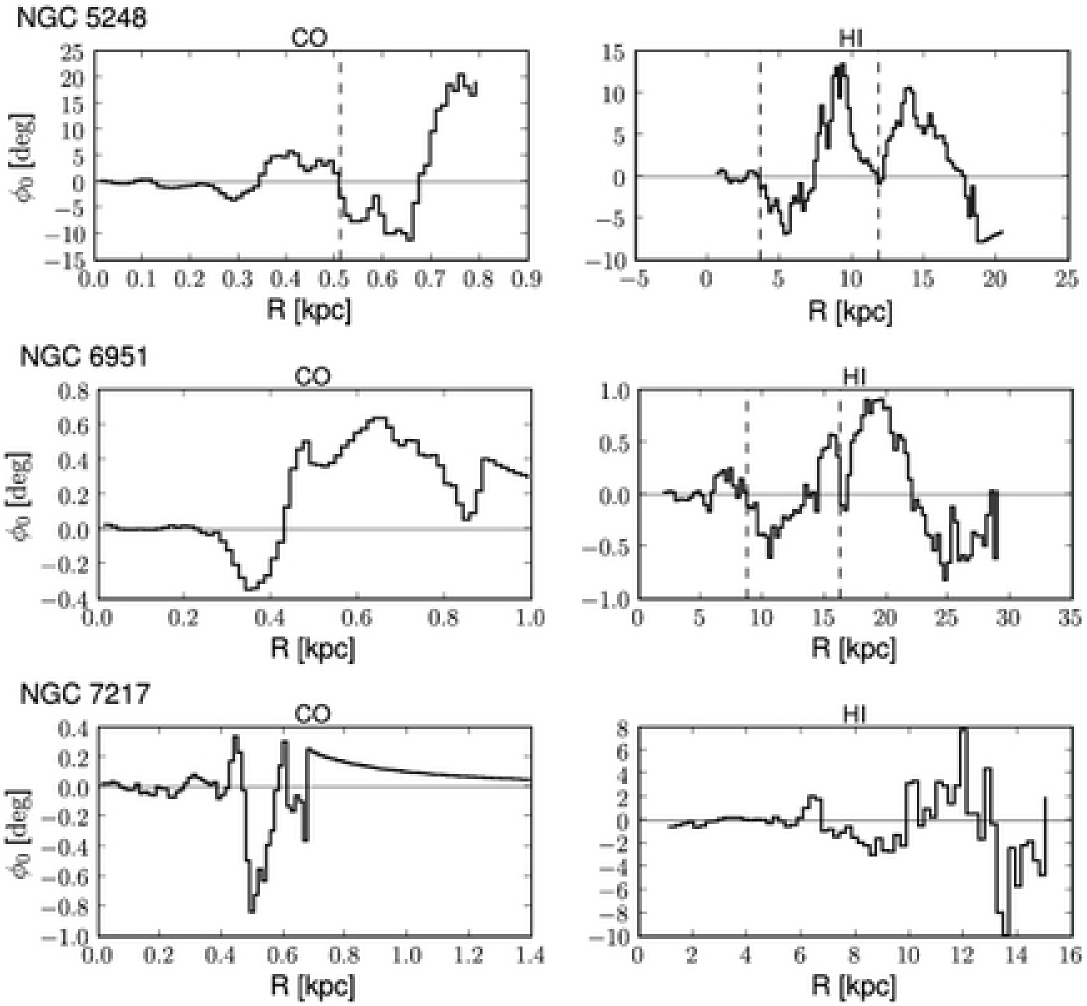

Fig. 4.9 (Continued)

pattern. Thus, also the gravity torque is expected to change sign at each resonance with the gas as test particles for measuring the gravity torques. On the other hand, the gravity torque method might differ from the Potential-Density Phase-Shift in case of a superposition of density patterns or a shift of gas due to viscosity. However, in case of a strong dominating pattern, both methods are expected to reveal a similar location for the CR radius.

To verify our estimation of the CR radii we derived additionally the CR radii using the bar length and the method of Canzian (1993) (see §4.3.2). A comparison of the results derived from these different studies is presented in Tab. 4.8 for all our galaxies. The CR radius is assumed to be 1.1-1.6 times the radius of the bar (Rautiainen et al., 2008) and is visually estimated directly from the deprojected NIR images (Fig. 4.4) using the change in PA and the ellipticity of the bar. All three methods (Canzian, bar length, Phase-Shift) reveal roughly the same radii for the CR of the bar. For our galaxies the Phase-Shift method appeared to be the most precise method with uncertainties of (5 - 10)% and the Canzian method the most unprecise one with uncertainties ranging up to 50%. The estimation of the CR using the bar length suffers from the uncertainty in the estimation of the bar length and its relation to the CR radius, which lies in the range of (10-30)%. The comparison between the CR radii determined by our gravity torques study and the Phase-Shift method of Zhang & Buta (2007) reveals significant differences for the location of the CR radii of the bar for NGC 3368, NGC4321, and NGC 6951 (see Tab. 4.8). One possible explanation for these differences is that all three galaxies exhibit a strong stellar bar and spiral pattern (also visible in the NIR images) which might be superimposed.

To derive the location of the Inner Lindblad Resonance (ILR), the Ultra Harmonic Resonance (UHR), and Outer Lindblad Resonance (OLR) we used a simple method presented in Fig. 4.10 which is described in the following. The angular velocity Ω is calculated from a fit using a cubic spline interpolation to our measured CO and HI rotation curve. After determining the bar pattern speed at the location of the corotation resonance (taken from the Phase-Shift method), the frequency curves $\Omega \pm \kappa/2$ and $\Omega - \kappa/4$ are derived with the epicyclic frequency

$$\kappa = \sqrt{4\Omega^2 + R\frac{\mathrm{d}\Omega^2}{\mathrm{dR}}} \tag{4.24}$$

The derived CR, ILR, UHR and OLR are also listed in Tab. 4.8. Interestingly the OLR caused by the bar seems to overlap for some galaxies (NGC 3368, NGC 6951) with the CR radius of the spiral determined by the Phase-Shift method, suggesting a coupling between bar and spiral resonances. However, as our uncertainties in the estimation of the OLR are quite large, this correlation is not very significant.

Table 4.8: Resonances

Source	CR_{Torque} [kpc]	R_{Bar} [kpc]	CR_C [kpc]	CR_{PS} [kpc]	Ω_{Bar} [km s^{-1} kpc^{-1}]	ILR [kpc]	UHR [kpc]	OLR [kpc]	Comments
NGC 3368	4.5	3.2	2.5-3.5	**3.5**	54	-	2.5	7.4	Outer Bar
			7	**7.0**					Outer Spiral
NGC 3627	2.7	1.5	2	**2.4**	79	-	0.4	3.7	Outer Bar
NGC 4321		5	8.5	**4.8**	39	-	1.7	13.0	Bar
	11.7			**11.2**					Outer Spiral
NGC 4736	-	-	5.5-7						Outer Oval
NGC 5248			1.7-2.0	**3.6**	41	2.3	2.7	8.9	Inner Spiral/Bar
	9.5-11	7	7.5-12	**11.8**					Outer Spiral/Bar
NGC 6951		7	5-7	**8.7**	23	(1.6, 2.5)	3.2	20.0	Bar
	11			**16.2**					Outer Resonance
			20-23	22.1					Outer Resonance
NGC 7217	5.5-7	-							

Note. — Overview of the dynamical resonances derived from different methods: the CR radius from our gravity torque study (column 2), the radius of the bar (column 3) , the CR using the method of Canzian (1993) (column 4), the CR on the basis of the Phase-Shift method of Zhang & Buta (2007) (column 5) and the associated angular speed of the bar Ω_{Bar} (column 6), the Inner Lindblad Resonance (ILR) at $\Omega_{Bar} = \Omega - \kappa/2$ (column 7), the Ultra Harmonic Resonance (UHR) at $\Omega_{Bar} = \Omega - \kappa/4$ (column 8), and the Outer Lindblad Resonance (OLR) at $\Omega_{Bar} = \Omega + \kappa/2$ (column 9) of the bar. All radii are deprojected. The CR values printed in boldface are taken for further interpretation of our torque results as function of the CR locations of spiral arms and bars.

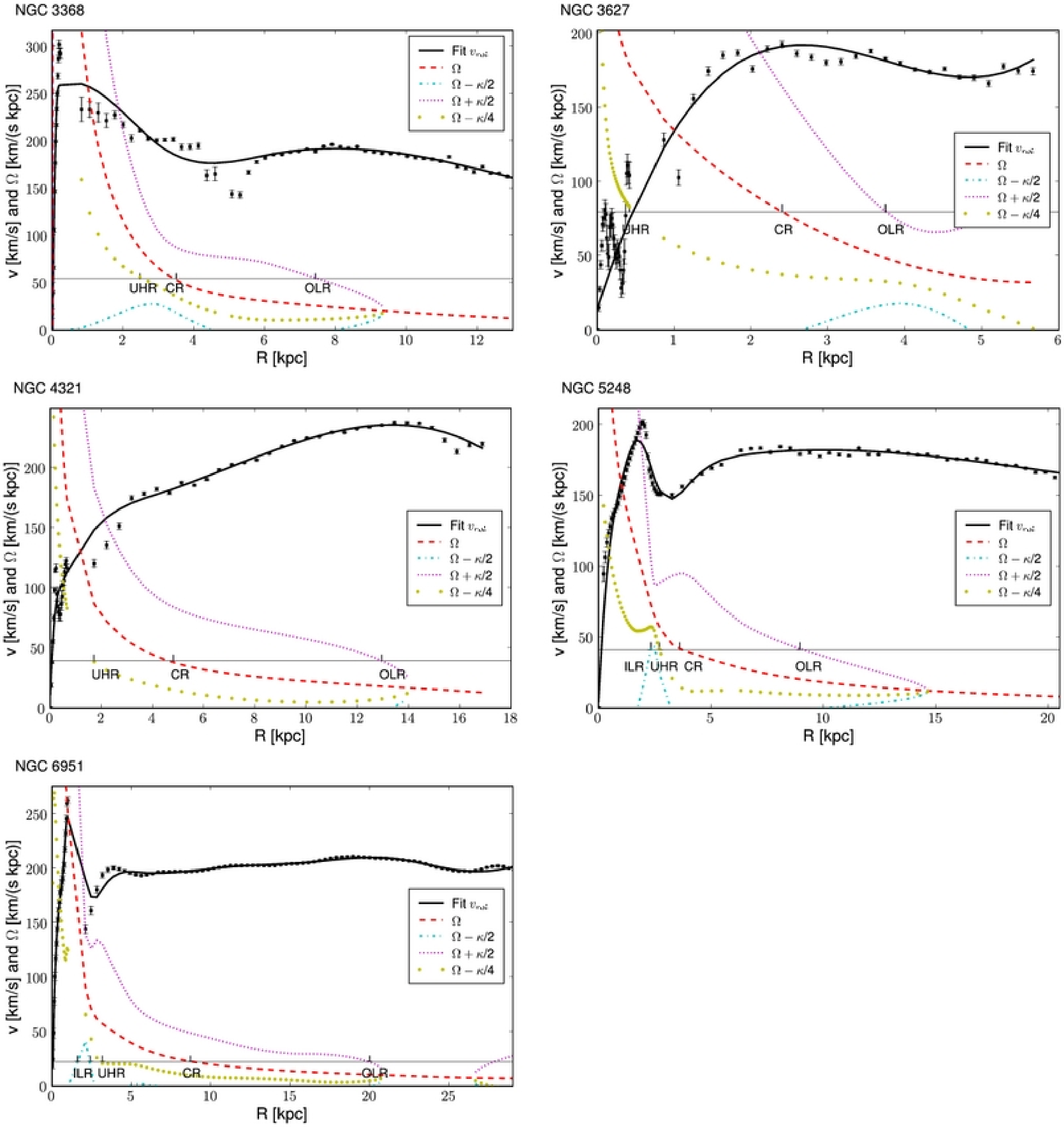

Figure 4.10: Overview of the CR resonance of the bar and the associated bar pattern speed Ω_{Bar} (horizontal solid line, see also Tab. 4.8) , the Inner Lindblad Resonance (ILR) at $\Omega_{Bar} = \Omega - \kappa/2$, the Ultra Harmonic-Resonance (UHR) at $\Omega_{Bar} = \Omega - \kappa/4$, and the Outer Lindblad Resonance (OLR) at $\Omega_{Bar} = \Omega + \kappa/2$ of the bar. The angular velocity Ω is calculated from a fit using a cubic spline interpolation (solid line) to our measured CO and HI rotation curve (points with errorbars). NGC 4736 and NGC 7217 are not shown here as no large-scale bar or oval is present in these two galaxies.

4.4.4 Results

We have derived neutral gas inflow rates for 7 nearby spiral galaxies as a function of radius as well as location within the disks (see top panel of Fig. 4.11). By definition, the torque $\tau(R)$ represents the azimuthally averaged time derivative of the specific angular momentum of the gas. The positive or negative sign of $\tau(R)$ defines whether the gas may gain or loose angular momentum, respectively. For almost all galaxies of our sample the torque changes sign in different quadrants which corresponds to inflow and outflow in adjacent quadrants. As such a pattern is generally expected to be generated by m=2 modes, (e.g. bar or oval potential), we conclude that this mode is the dominant mode in our sample. Only NGC 5248 shows a bipolar torque pattern for the center. In addition, the torque pattern is very sensitive to the presence of stellar spiral arms which cause a positive (negative) torque on the side of the spiral arm towards (away from) the galaxy center. Such a torque pattern is present in all galaxies of our sample, except for NGC 7217 and NGC 4736.

To estimate radial gas flows and time scales we derived the azimuthally averaged torque $\tau(R)$ and the angular momentum transferred in one rotation $\mathrm{d}L(R)/L$ as a function of radius which are presented in Fig. 4.11. Similarly to the torque maps, a positive or negative sign of $\tau(R)$ and $\mathrm{d}L(R)/L$ defines whether the gas may gain or loose angular momentum corresponding to gas outflow or inflow, respectively.

The transferred angular momentum and gas masses averaged over the entire galaxy disk are listed in Tab. 4.9 for each galaxy.

We found that the averaged transferred angular momentum $\langle dL/L\rangle$ over the entire gas disk lies in the range of -0.04 (NGC 6951) to 0.06 (NGC 5248) for HI and -0.5 (NGC 3368) to 0.16 (NGC 3627) for CO. To estimate the mean amplitude of angular momentum exchange within the disk we derive the mean value of the absolute angular momentum transfer, $\langle|dL/L|\rangle$. This parameter is used later in §4.5 for a comparison to the non-circular motions identified in our analysis of the gas kinematics. We found values of $\langle|dL/L|\rangle$ in the range of 0.03 (NGC 7217) to 0.26 (NGC 3627) for HI and 20.03 (NGC 7217) to 0.55 (NGC 3368) for CO. Clearly, NGC 7217 exhibits the lowest torque strength and angular momentum transfer in our sample due to its nearly axisymmetric potential (Combes et al., 2004) whereas NGC 3627 and NGC 3368 exhibit the largest amplitude of angular momentum exchange. In general, the amplitude of $\langle|dL/L|\rangle$ is larger in the center (CO) than in the outer disk (HI).

To estimate the transferred gas mass at a certain radius, we derived the mass inflow/outflow rates $\mathrm{d}^2M(R)/(\mathrm{d}R\mathrm{d}t)$ (in units of $\mathrm{M}_\odot$ yr^{-1} pc^{-1}) as a function of radius (see Fig. 4.12). In addition, we examined the net mass flow $\mathrm{d}M(R)/(\mathrm{d}t)$ (in units of $\mathrm{M}_\odot$ yr^{-1}) outwards to a given radius R by integrating over the gravitational torques of the molecular and atomic gas disk, separately. These values represent the net gas mass inflow/outflow within these regions and can be compared to the typical gas masses required by star formation and AGN fueling

Table 4.9: Gravitational Torque Analysis

Source	$\langle dL/L \rangle$		$\langle \lvert dL/L \rvert \rangle$		dM_{HI}/dt	dM_{mol}/dt	HI R_{max}	CO R_{max}
	HI	CO	HI	CO	[$M_\odot$ yr^{-1}]	[$M_\odot$ yr^{-1}]	[kpc]	[kpc]
NGC 3368	0.02	-0.50	0.12	0.55	0.04	-11.11	13.0	0.35
NGC 3627	-0.00	0.16	0.26	0.24	-0.10	50.13	6.0	0.75
NGC 4321	0.01	0.02	0.10	0.10	-0.18	1.03	18.0	1.2
NGC 4736	0.02	0.01	0.03	0.09	0.06	-0.01	8.5	0.62
NGC 5248	0.06	-0.02	0.13	0.02	0.49	-22.96	20.5	0.8
NGC 6951	-0.04	-0.05	0.09	0.10	-0.16	-4.29	29.0	1.0
NGC 7217	-0.01	-0.02	0.03	0.03	-0.01	-2.37	15.2	1.4

Note. — Overview of the transfered angular momentum and gas masses averaged over the radius for the center (molecular gas traced by CO) and the outer disk (atomic gas traced by HI). A positive (negative) sign corresponds to a net outflow (inflow). The averaged transfered angular momentum $\langle dL/L \rangle$ over the entire gas disk is listed in column 2 & 3 and the mean value of the absolute angular momentum transfer within the disk in column 3 & 4. The net mass inflow/outflow rates $\mathrm{d}M(R)/(\mathrm{d}t)$ (in units of $M_\odot$ yr^{-1}) out to the maximum disk radius (column 8,9) are listed in column 6 (7) for the atomic (molecular) gas. The corotation radii derived from the Potential-Density Phase-Shift method are listed in column 10.

(see §4.5). A positive (negative) sign indicates gas outflow (inflow). The net gas mass flow for the entire molecular and atomic gas disks (integrated from 0 to R_{max}) are listed in Tab. 4.9 with a range of (-0.01 - 0.5) $M_\odot$ yr^{-1} for the atomic gas ($R_{max} \simeq 20$ kpc) and much larger values of (-23 - 50) $M_\odot$ yr^{-1} for the molecular gas in the center ($R_{max} \simeq 1$ kpc). However, to study the redistribution of gas within the galaxy disk, e.g. caused by bar and spiral wave patterns, one has to examine the gas mass flow as a function of radius (see Fig. 4.12). For example, the net gas mass flow over the entire disk can be zero while a large redistribution of gas may occur within the disk. This seems to be the case for, e.g., NGC 3627 where we found a large net gas mass inflow in a region of $0 < R < 3$ kpc ($\sum_0^{3\ kpc}$ $M_\odot$ yr^{-1}=-1 $M_\odot$ yr^{-1}), and a similar value with the opposite sign (gas mass outflow) from 3 kpc to the outer region of the galaxy ($\sum_{3\ kpc}^{6\ kpc}$ $M_\odot$ yr^{-1}=1 $M_\odot$ yr^{-1}), so that the sum over the entire disk results coincidentally in an almost zero net gas mass flow ($\sum_0^{R_{max}}$ $M_\odot$ yr^{-1}=-0.1 $M_\odot$ yr^{-1}). In general, we found for our sample that the amplitude of the gas mass flow within the disk is much larger than the net gas mass flow over the entire gas disk. This indicates that the redistribution of gas within the galaxy exceeds the net gas mass outflow/inflow from the entire galaxy. The significant inflows and outflows within the disk are likely caused by the dynamical action of the stellar bar and/or spiral pattern.

To evaluate in more detail whether the angular momentum transfer changes sign at characteristic dynamical locations within the disk, we derived the corotation (CR) radii as described in §4.4.3 (see Tab. 4.9 for an overview of all CR radii for our galaxies). The CR radius is defined as the radius where the density wave pattern (e.g. bar, spiral) and the differentially rotating disk have the same angular velocity. This leads to a gain of angular momentum outside and loss of angular momentum inside the regions close to the CR radius. Since galaxies can harbor several spiral and/or bar patterns, also multiple CR radii can exist within one galaxy. In Tab. 4.9 we listed all CR radii for our galaxies with a significant phaseshift inversion.

Summarizing, almost all galaxies of our sample (except the center of NGC 5248) exhibit torque patterns typical for m=2 modes (bars, spirals). NGC 3627 seems to have a very strong torque efficiency in the center ($\mathrm{d}L/L > 0.6$) while NGC 7217 shows the lowest torque strength and angular momentum transfer in our sample. In general, we found that the transfer of angular momentum and the gas mass flow is larger in the center ($R \lesssim 1$ kpc) than in the outer disk ($R \gtrsim 1$ kpc).

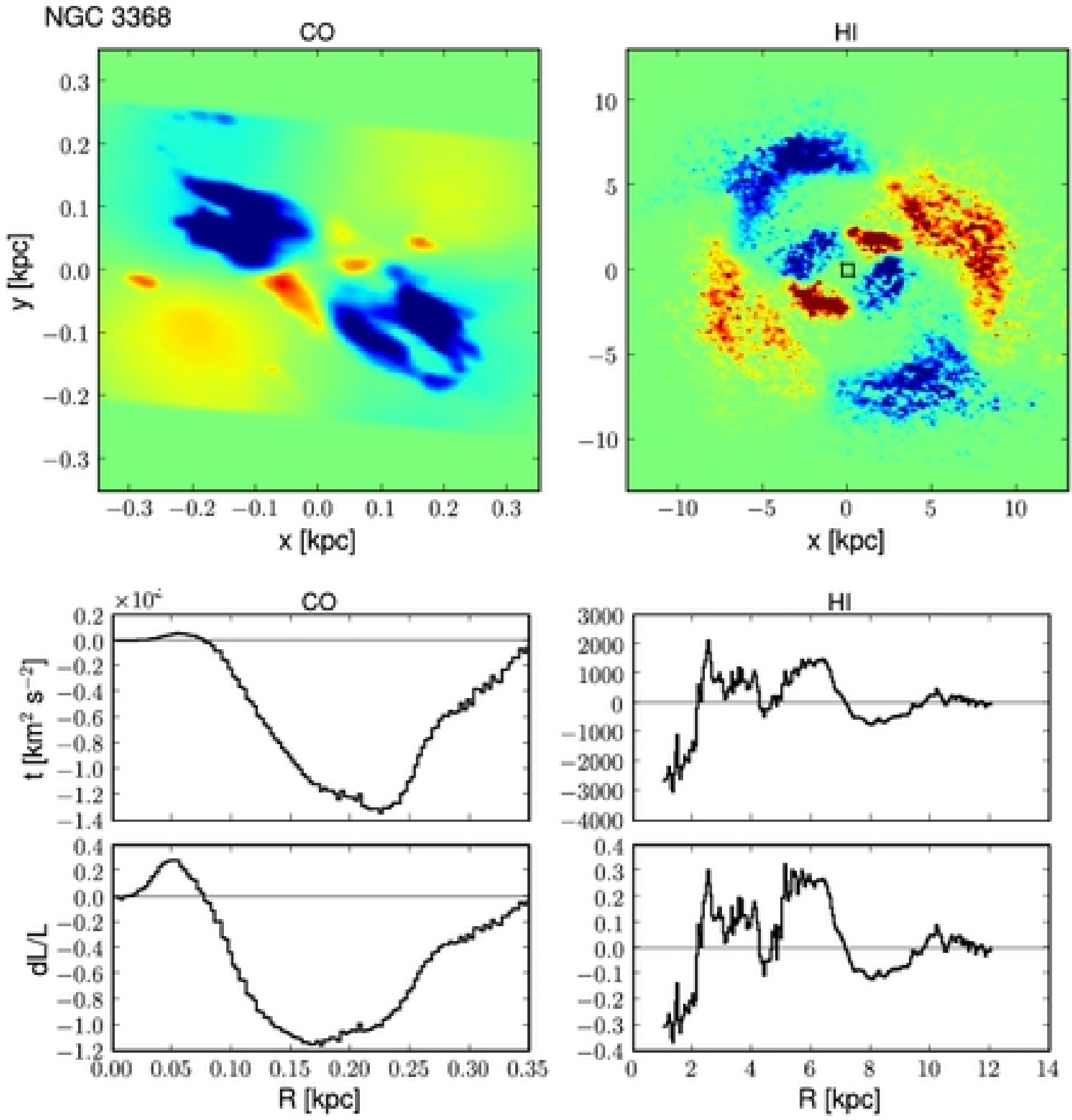

Figure 4.11: Overview of the torque results for the center (CO, left panels) and the large scale disk (HI, right panels). A positive (red colored) or a negative (blue colored) torque corresponds to an outflow or inflow of gas, respectively. The top panels show the gravitational torques weighted with the CO- (left top panel) and HI- (right top panel) gas column density and normalized to their the maximum values. The square in the HI-weighted torque map (right top panel) indicates the FOV of the CO-weighted torque map. The torque per unit mass averaged over azimuth $\tau(R)$ and the fraction of angular momentum $\mathrm{d}L/L$ transfered from/to the gas in one rotation are shown in the center and bottom panels, respectively.

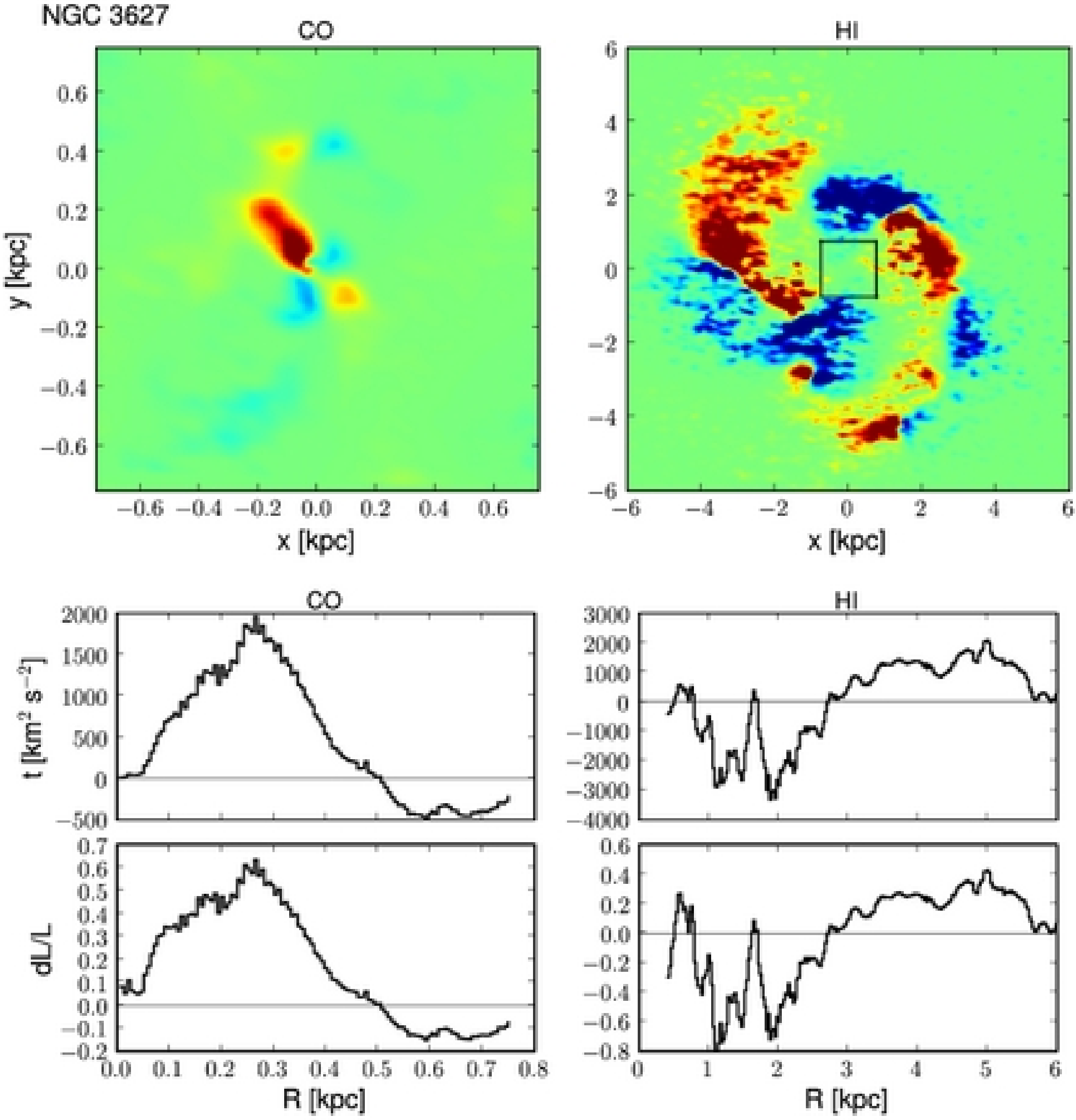

Fig. 4.11 (Continued)

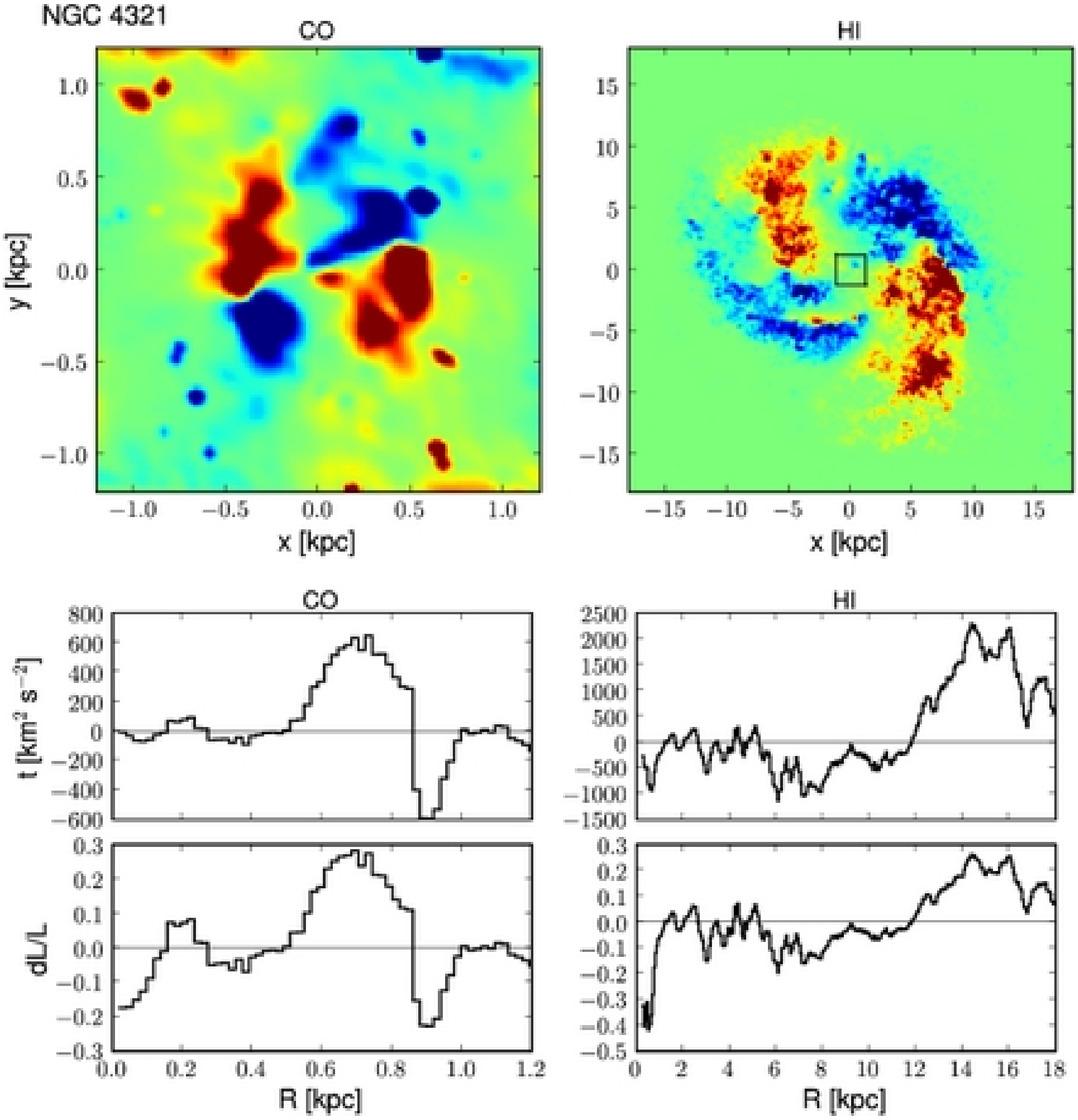

Fig. 4.11 (Continued)

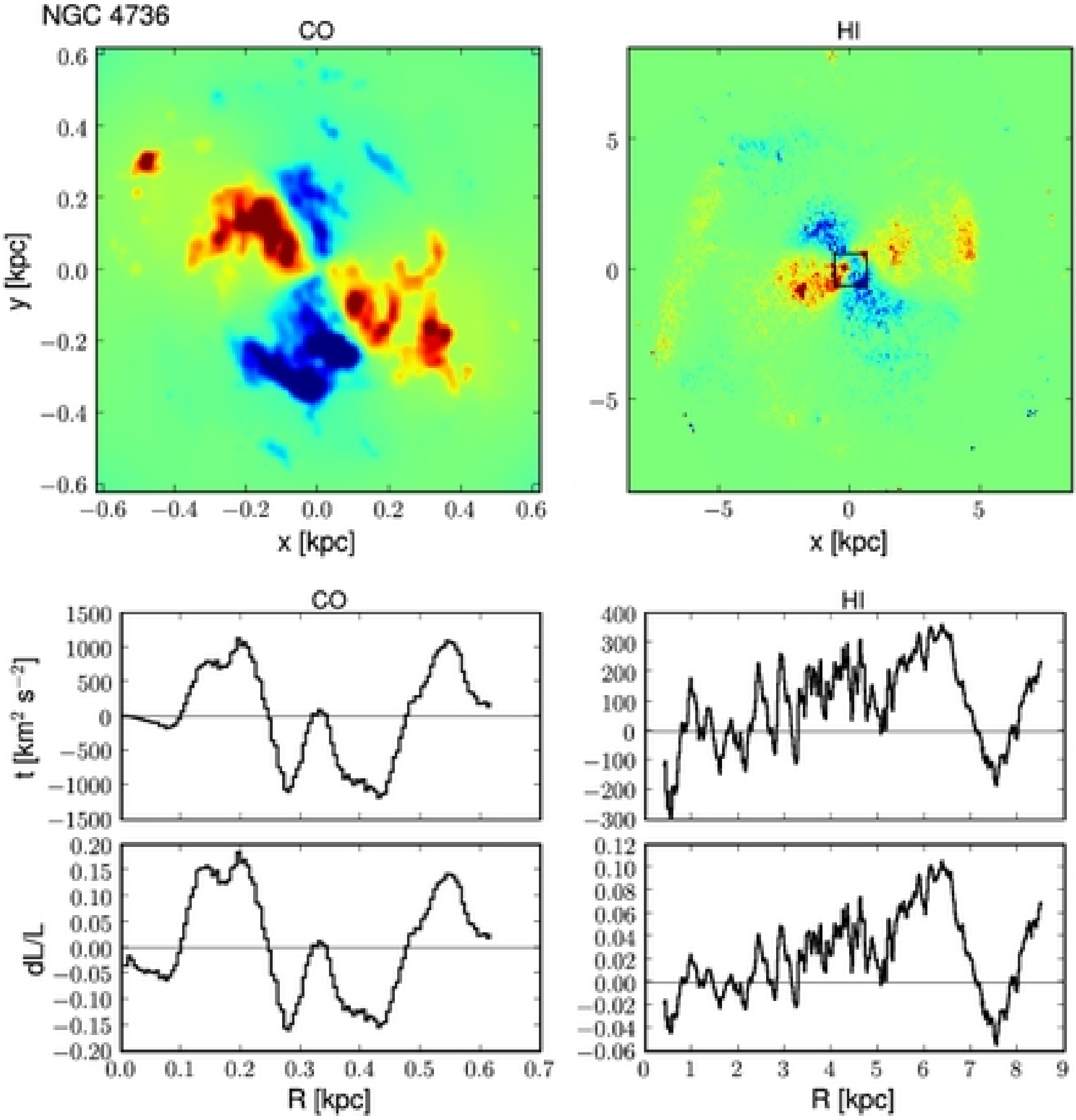

Fig. 4.11 (Continued)

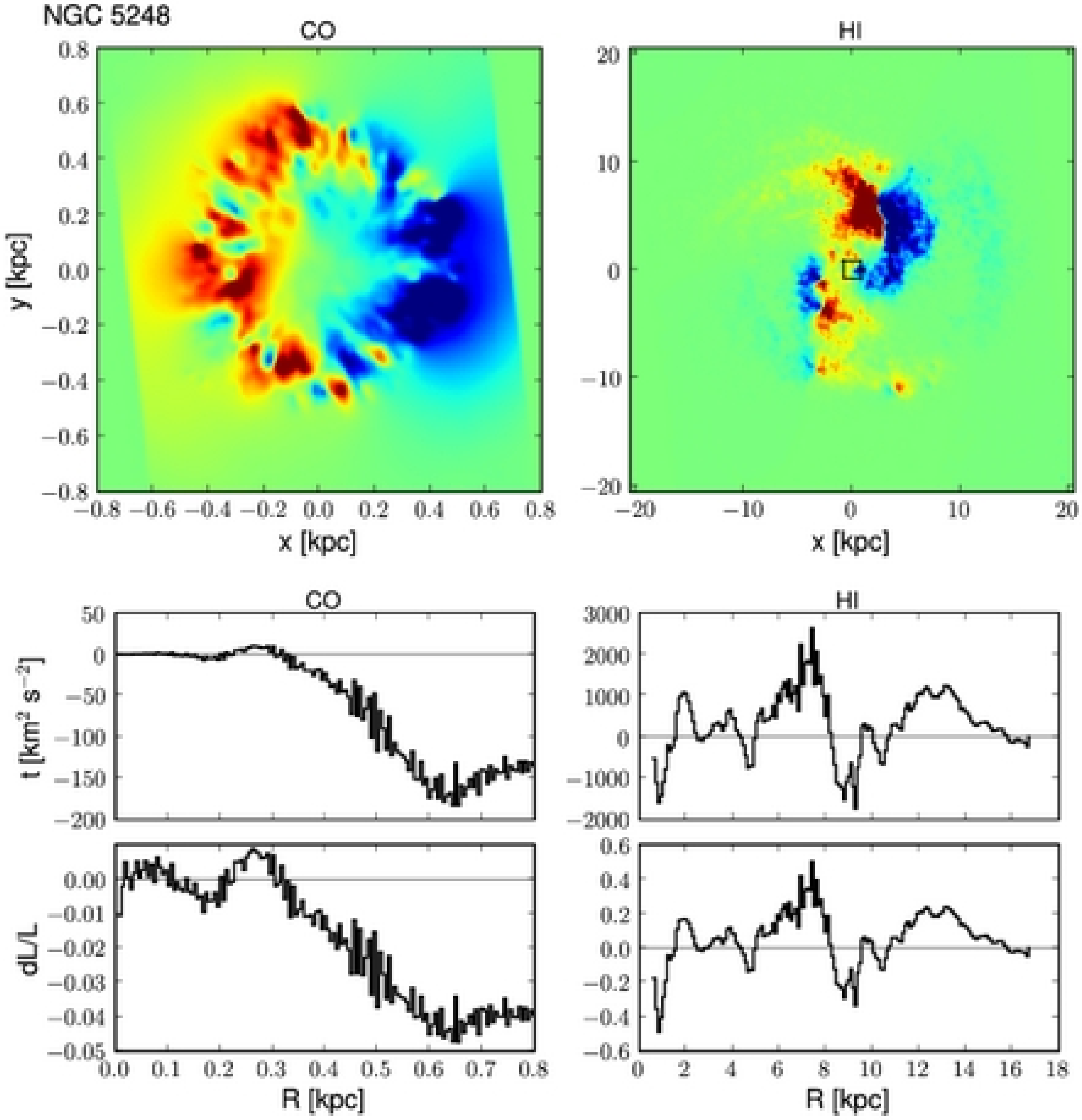

Fig. 4.11 (Continued)

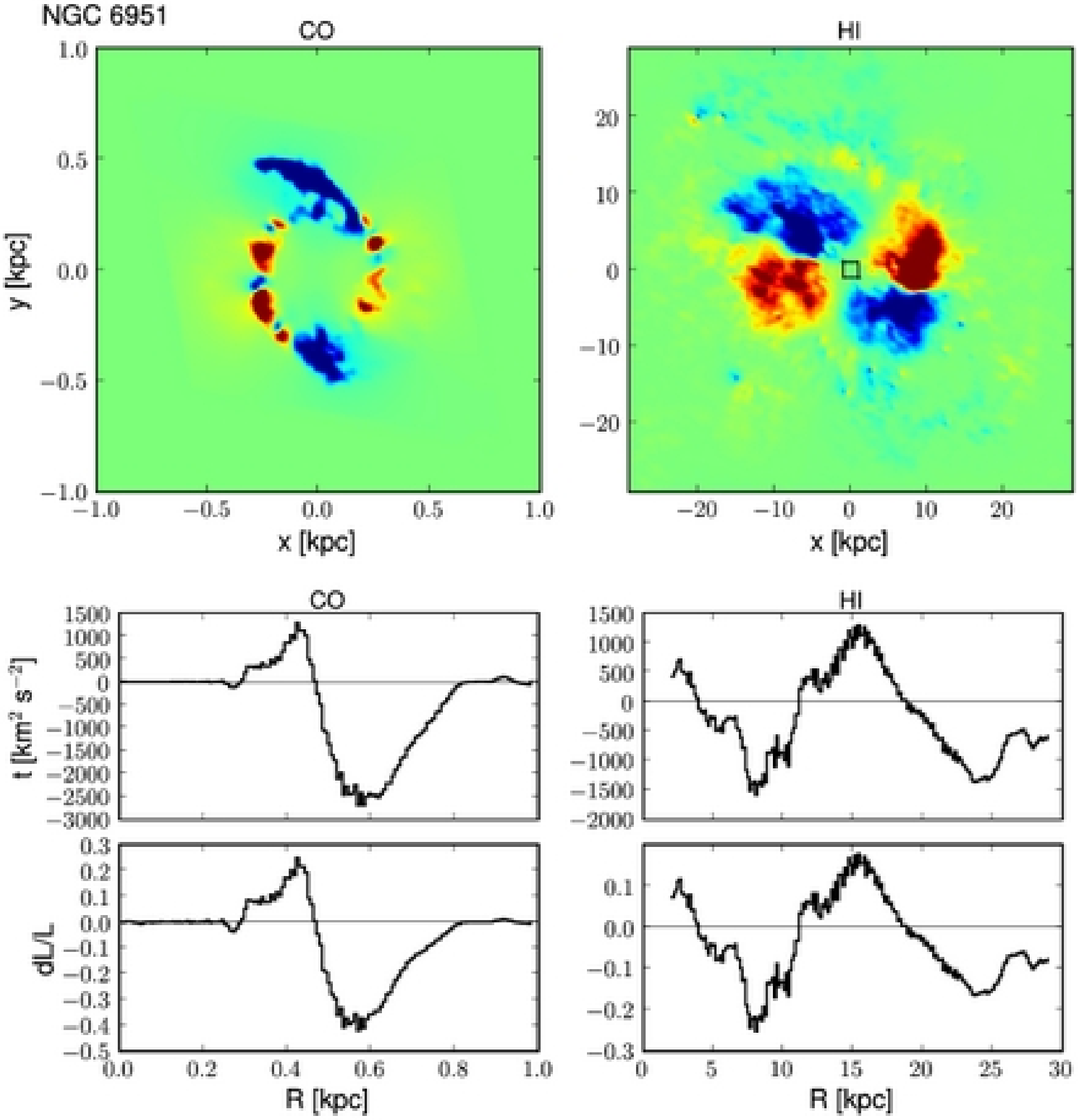

Fig. 4.11 (Continued)

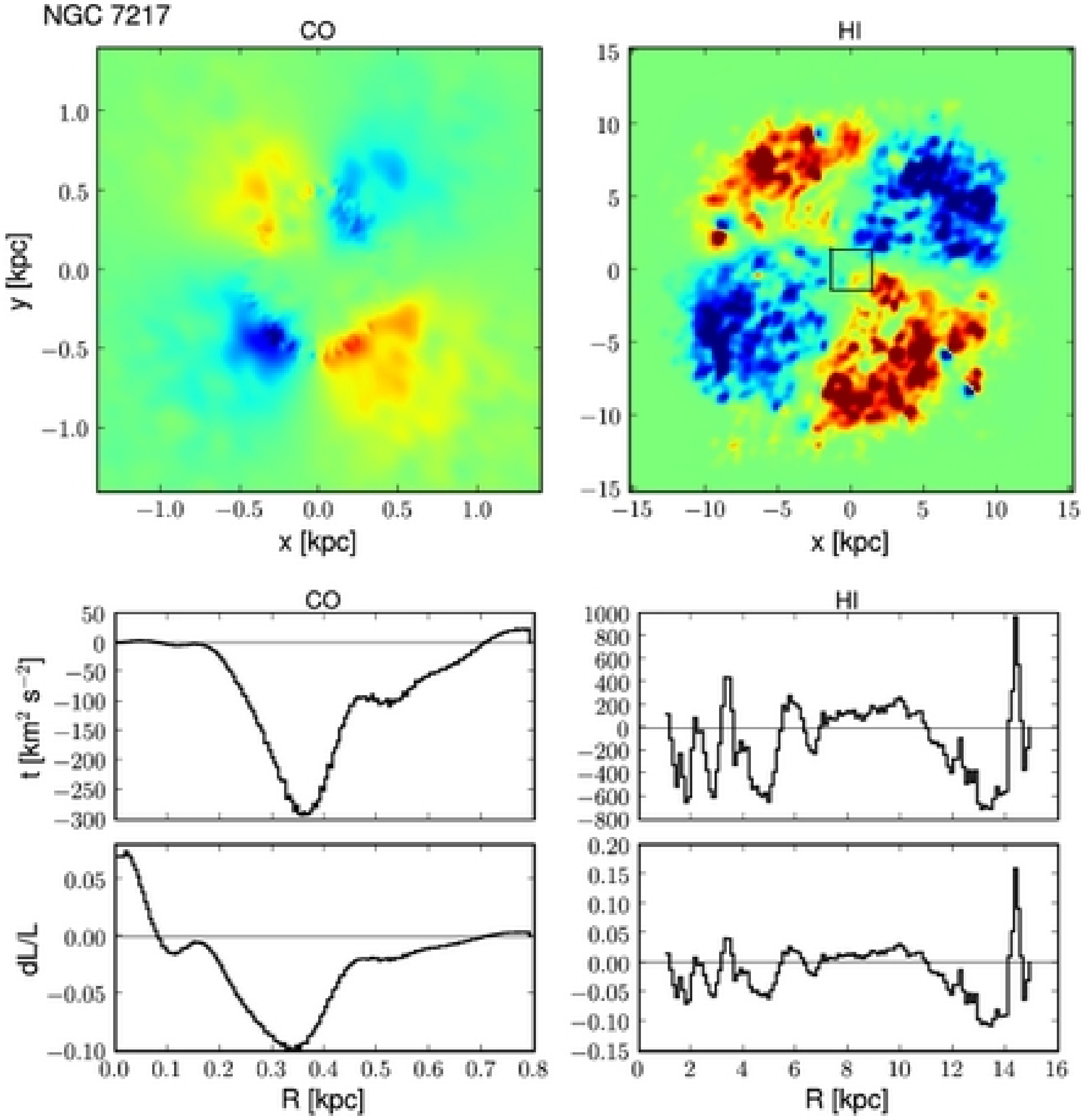

Fig. 4.11 (Continued)

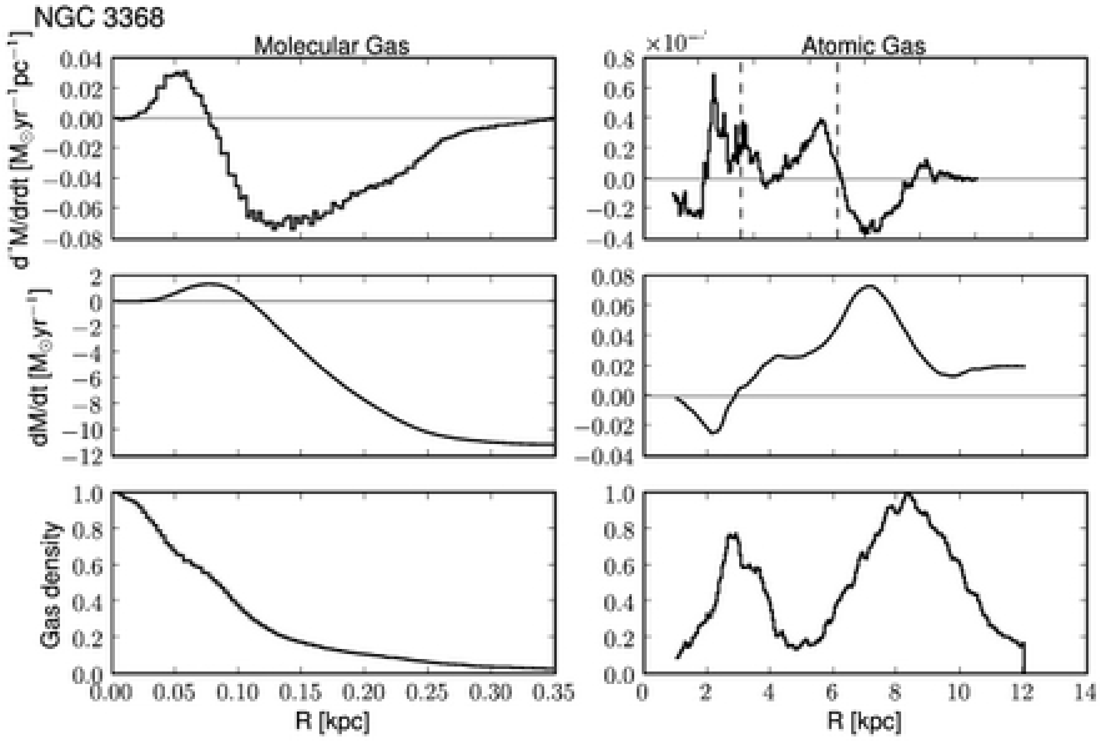

Figure 4.12: Overview of the mass flow rates for the molecular gas (left panels) and the atomic gas (right panels). The upper panels present the mass flow rate of gas per unit length while the central panels show the overall mass flow rate of gas outwards to a given radius. The molecular and atomic gas densities (bottom panels) are normalized to the maximum density. The vertical dashed line indicates the CR radius of single density wave pattern (bar or spiral), if present, derived from the Stellar-Density-Phase-Shift method (see §4.4.3).

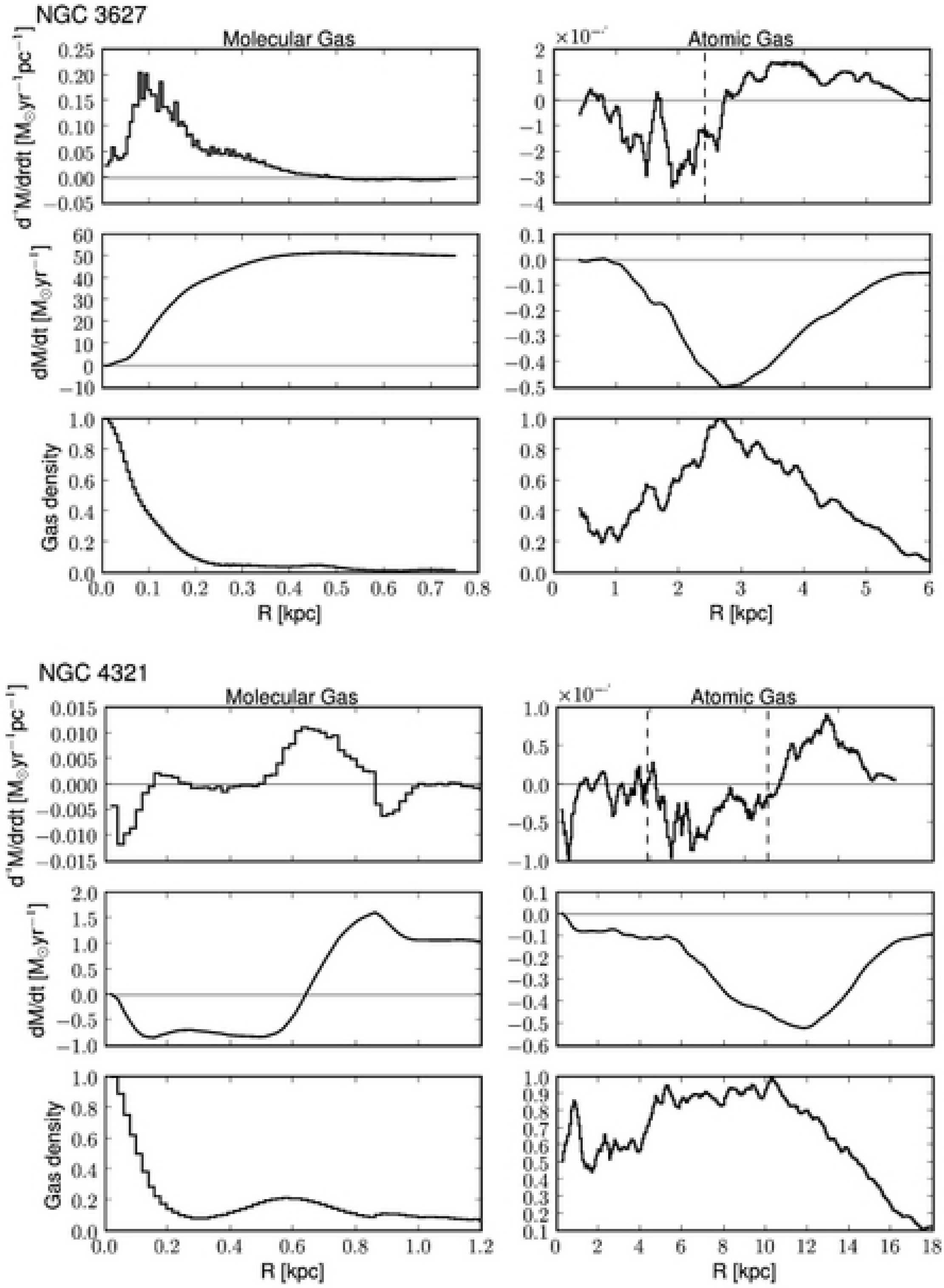

Fig. 4.12 (Continued)

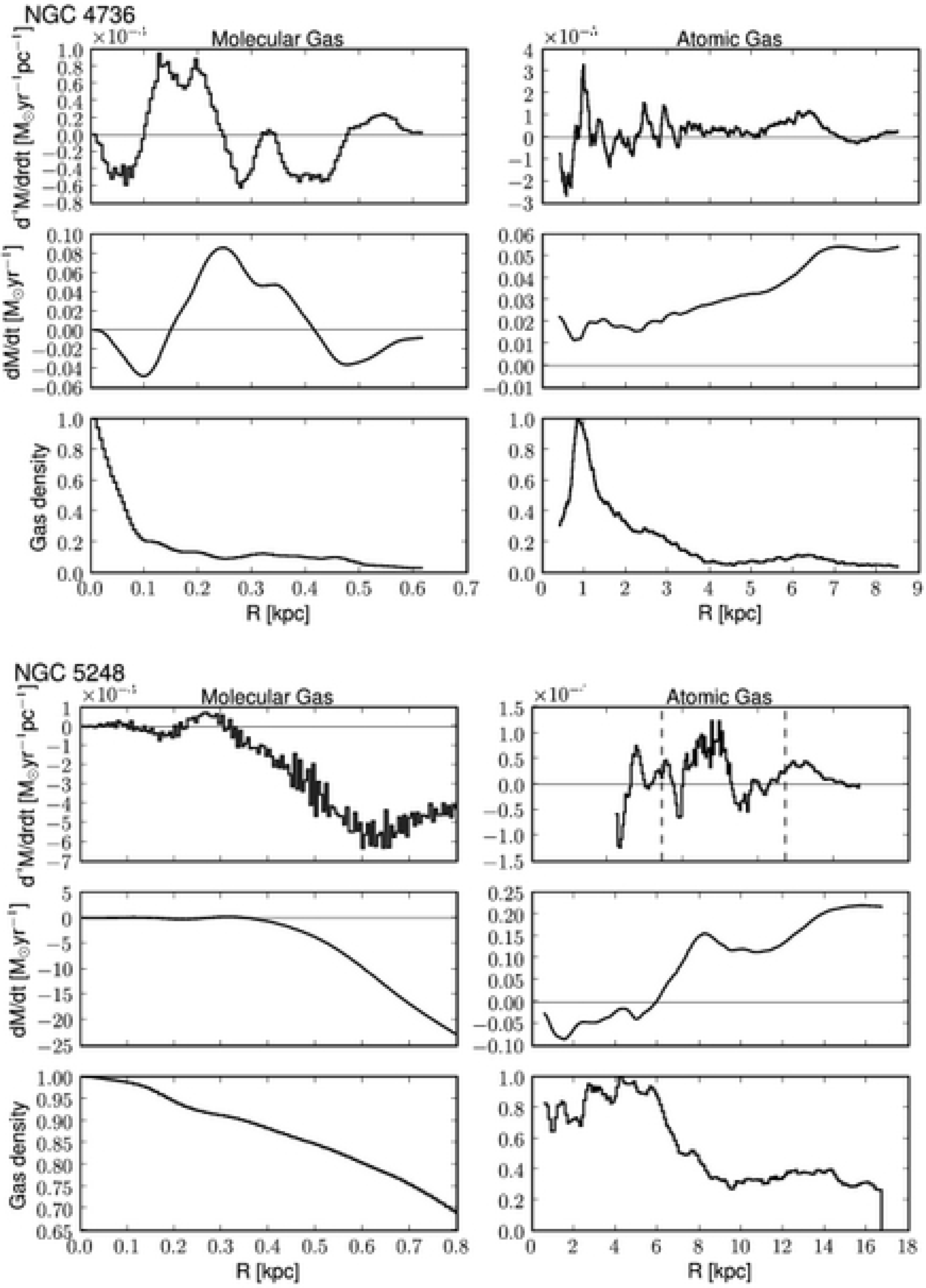

Fig. 4.12 (Continued)

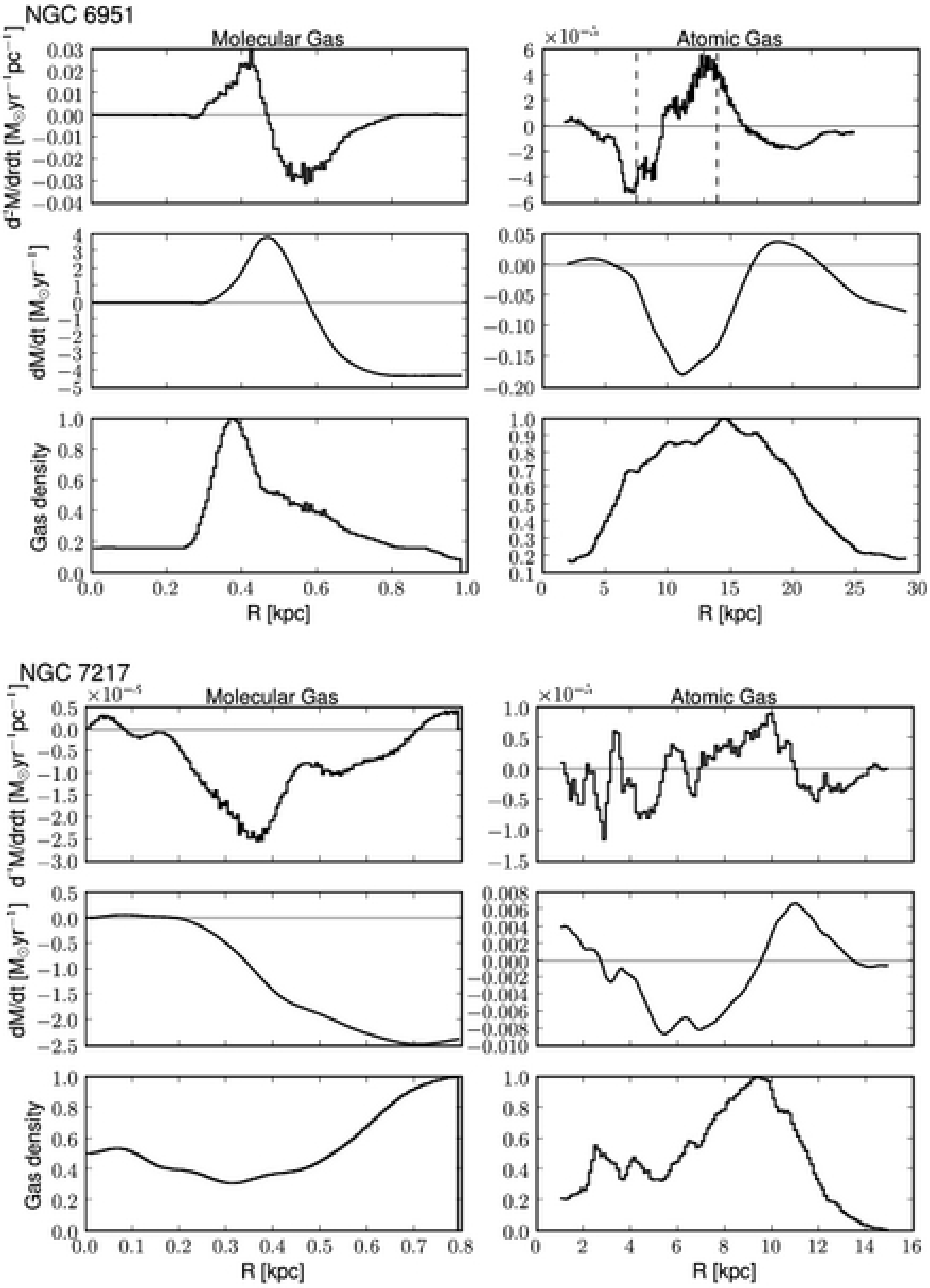

Fig. 4.12 (Continued)

4.5 Discussion

4.5.1 Gas Flows in Individual Galaxies

In this section we describe the gas flow for each of our 7 galaxies and search for relations to their dynamical states and stellar and gaseous morphologies. As most of our galaxies are different in their morphology and kinematics, only case studies can give information about the mechanisms that are acting. A general picture of the gas flow follows from a comparison of these individual studies and is described in §4.5.2.

NGC 3368

NGC 3368 has two stellar bars, an inner one with a radius of ∼1.0 kpc and an outer one with a radius of ∼3.2 kpc, which have a small offset of $\sim 25°$ between their position angles (see Fig. 4.4). Two spiral arms are connected to the ends of the outer bar. The atomic gas distribution shows two gaseous spiral arms which are coincident with the stellar ones and an additional gaseous ring around the outer bar. We found that the two dimensional torque maps of the central and the outer disk show the typical torque pattern that is expected from its stellar bars and spirals. On the basis of our radial torque profiles we found gas inflow for the outer disk region (7-10 kpc) with an average angular momentum transfer $\mathrm{d}L/L$ of 10% of the total angular momentum per rotational period at a given radius, while on intermediate disk scales (2-7 kpc) gas outflow is present (see Fig. 4.11). Because of the switch from out- to inflow, gas is expected to accumulate at this radius which is confirmed by our observed atomic gas distribution (see Fig. 4.12). Interestingly, the shift at 7 kpc in the flow direction is directly contrary to the one that is expected by crossing the CR resonance of the spiral at ∼7 kpc. The lack of a correlation between CR radius of the spiral and the expected gas flow can be likely explained by the fact that the bar potential is still acting at this location and overlaps with the spiral pattern. The UHR ($R \simeq 2.5$ kpc) and OLR ($R \simeq 7.5$ kpc) of the bar seem to correlate with an expected accumulation of gas at $R = 2.5$ kpc and $R = 8$ kpc, respectively, as clearly visible in the radial atomic gas density profile (see Fig. 4.12). For the center we found a large gas inflow from 2 - 0.08 kpc, that seems to transport the gas towards the AGN. Only for the very center from 0 - 0.08 kpc gas outflow is present, suggesting an accumulation of gas at a radial distance of 0.08 kpc, which is also visible as a small bump in the radial molecular gas density profile (see Fig. 4.12).

NGC 3627

The stellar distribution of NGC 3627 exhibits two bars with a radius of 1.5 kpc and 0.2 kpc and two spiral arms at the ends of each of the bars. As the two bars have an offset between their PAs of $\sim 45°$ a possible decoupling of these two dynamical modes might influence the gas kinematics (see also García-Burillo et al., 2008). We found that the torque pattern reflects the shift of the PAs between these two bars. For the outer disk the torques are dominated by the potential of the spiral arms with a CR radius at 2.5 kpc. Within this CR radius the gas is transported inwards, while moving outwards outside the CR radius, which is confirmed by our radial torque profile: A significant inflow ($\mathrm{d}L/L \simeq 0.3$) from 2.8-0.7 kpc and outflow of gas ($\mathrm{d}L/L \simeq 0.3$) from 2.8-5 kpc. For the central disk traced by our CO observation we found a large gas outflow ($\mathrm{d}L/L \simeq 0.4$) from 0 - 0.5 kpc. Thus, gas accumulation might be possible at $\sim$ 0.5 kpc where the flow direction switches from out- to inflow, which is also visible as a small peak in the radial molecular gas density profile (see Fig. 4.12). This gas accumulation at $\sim$ 0.5 kpc seems also to overlap with the UHR of the bar at $R = 0.45$ kpc.

NGC 4321

The NIR image shows a large-scale bar ($R_{Bar} = 5$ kpc) which is parallel to the nuclear bar ($R_{Bar} = 0.5$ kpc). The large-scale bar is coupled to 4 spiral arms. The gas flow follows the spirals in the outer disk and is increasingly dominated by the torques caused by the bar towards the center. For the outer disk (from 12 - 18 kpc) we found a significant outflow ($\mathrm{d}L/L = 0.2$) and on intermediate scales (from 12 - 6 kpc) inflow. The switch from inflow to outflow is roughly occurring at the CR radius of the spirals at 11.2 kpc. At the CR radius of the bar no switch from in- to outflow is found, suggesting that the standard CR determinations are not applicable for this case because of a superposition of bar and spiral wave pattern. A typical torque pattern caused by the bar is present in the center probed by our CO observations. While a shift from out- (0.5 - 0.9 kpc) to inflow (1.0 - 0.9 kpc) is present at 0.9 kpc, no significant angular momentum transport occurs towards the very center of the galaxy (from 0.5 - 0 kpc). The comparison with a previous gravity torque study only for the center (García-Burillo et al., 2005) revealed a similar torque pattern but larger amplitudes. Although similar methods have been used, the difference in the amplitude can be likely explained by differences in the used geometric parameters of the disk (i, PA, and center) as well as a different method for the scaling with the mass-to-light ratios (García-Burillo et al. (2005): constant scaling; our study: scaling as function of radius).

NGC 4736

For NGC 4736 we found that the direction of the torque rotates by about $\sim 60^\circ$ in the region of 2 - 0 kpc. This is likely due to the presence of two oval stellar distributions whose major axes have an offset of $\sim 60^\circ$ suggesting a decoupling between these two dynamical modes. These ovals are clearly visible in the NIR images (see Fig. 4.4). The gravitational torque caused by the outer oval is still dominant for the large gas spiral at 6.2 kpc producing a net outflow at this location (5.5 - 7 kpc). Averaged over the entire atomic gas disk, gas is transported outwards.

NGC 5248

NGC 5248 shows a large-scale bar ($\sim$ 7 kpc) visible in the NIR image and in the gaseous distribution as well. Further, two inner stellar spiral arms are present within the bar and two outer ones continue from the ends of the bar to the outer disk at 15 kpc. The gravitational torque pattern seems to be a mix between the bar and spiral arm contributions. In particular, the outer disk exhibits an additional torque concentration at the end of the north-western spiral arm at a distance of 7 kpc from the center. For the outer disk we found outflow at distances from (11-15), (2-8) kpc and inflow between $\sim$(11-8) kpc. The gravitational torques in the center are very small (maximum of $\mathrm{d}L/L = 0.04$) and show no typical torque pattern for a bar or oval. Instead a bipolar pattern is present, but might be caused by a possible offset between the real center and our used values (see §4.4.2) or is alternatively suggesting the presence of a lopsided disk. Interestingly, NGC 5248 is the only galaxy in our sample without AGN activity, which might be linked to the absence of gravitational torques and/or a possible lopsided disk in the center. However, to test this finding in detail higher spatially resolved data of the molecular gas distribution with sub-arcsecond resolution is necessary as for this galaxy only BIMA-SONG data with $6.1''$ was available for our study.

NGC 6951

NGC 6951 is a representative galaxy with a combination of AGN activity, stellar bars (inner and large-scale) and spiral arms (visible in NIR image and HI map). The gas flow pattern from 15-28 kpc reflects the stellar spiral arms and is increasingly dominated by the gravitational torque caused by the bar towards the center (see Fig. 4.11). The molecular gas distribution in the center shows two gaseous spiral arms whose gas flow underlie the gravitational torque caused by the inner bar. For the outer disk we found that the gas is transported outwards ($\mathrm{d}L/L \simeq 0.15$) from (19-27) kpc. On intermediate scales inflow occurs from (19-11) kpc, while outflow is dominant from (4-11) kpc. The radius where the gas flow is changing from inflow to outflow (11 kpc) does not overlap with any resonances of a single pattern (i.e. bar or spiral). We interprete this as gas is funneled inwards across the CR radius of the bar (at ∼8.5 kpc) and that the gas can overcome the CR barrier. We can exclude this as being due to errors in the gravitational torque calculation or CR estimation, as neither the errors of our torque study (see § 4.4.2) are large enough to eliminate such a significant inflow on the scale between (5-11) kpc, nor the possible range in the CR estimation of (5-9) kpc (including errors) could shift the CR radius to the switch from in- to outflow at 11 kpc. Also viscous torques are not efficient enough at the large scale to change the flow direction, because of the much smaller gas densities than in the center. The most likely explanation for the mismatch between the gravitational torque induced flow direction and the standard CR estimations of the bar is the presence of several pattern speeds (i.e. bar and spiral wave pattern) that combine and allow the gas to overcome the standard CR barrier of a single pattern. For the center we found gas inflow from (0.8-0.45) kpc and outflow from (0.3-0.45) kpc, suggesting a gas accumulation at ∼0.45 kpc. This is roughly coincident with a significant peak in the radial gas density profile at this location (at 0.38 kpc) leading to two inner molecular gaseous spiral arms. The comparison with a previous gravity torque study only for the center (García-Burillo et al., 2005) revealed a similar torque pattern but much larger amplitudes for our study (about a factor of 5-10). This difference in the amplitude might not only caused by differences in the used geometric parameters of the disk (i, PA, and center) as well as a different method for the scaling with the mass-to-light ratios, but eventually also by the use of different NIR images (García-Burillo et al. (2005): J-band, our study: K-band). We tested our code with the NIR image and parameters used by García-Burillo et al. (2005) and found similar torque values as in García-Burillo et al. (2005), so that an error in the calculations can be excluded.

NGC 7217

The two-dimensional torque map shows a pattern typical for an oval potential. Although NGC 7217 has no bar, an oval stellar distribution is possible, however it might be just an deprojection effect due to uncertainties in the inclination angle. The latter case seems to be possible as the torque pattern is aligned with the major axis (PA=265.5°) in such a way as expected from an error in the inclination angle (see §4.4.2). For the outer disk we found no strong evidence for gas transport caused by the gravitational torque. At the center we found only small evidence for gas inflow from (0.5-0.2) kpc with a maximum of $\mathrm{d}L/L = 0.1$, but this is presumably due to the uncertainty in inclination angle.

4.5.2 A General Picture of the Gas Flow from the Outer Disk to the Center

We found that the typical torque pattern changes sign in 4 quadrants. This typical butterfly pattern is characteristic for the action of an oval or barred gravitational potential. The orientation of the torque pattern in the center is coincident with the one of the outer disk (except for NGC 4736). Towards the outer disk, the gas reflects the stellar spiral arms, if present, which cause a positive (negative) torque on the side of the spiral arms towards (away from) the galaxy center. Thus, we conclude that for almost all galaxies in our sample a dominant m=2 mode is present and has roughly the same orientation in the outer disk and the center. We found nested bars within large-scale bars for NGC 3368, NGC 3627, and NGC 4736 whose major axes have an offset of $25° - 60°$ to the large-scale bars. No signs for unidentified patterns (i.e. not showing up as a prominent feature in the NIR image) are found in the torque maps.

The radial profiles of $\mathrm{d}L/\mathrm{L}$ and $\mathrm{d}^2M(R)/(\mathrm{d}R\mathrm{d}t)$ reveal that torques are more efficient in the redistribution of gas in the center of galaxies than in the outer disks, presumably due to larger gravitational torques induced there by the bar component. We found for a majority of our galaxies (5/7) a significant reversal from outflow to inflow in radial direction at radial distances ranging between (0.1 - 0.9 kpc), leading to an increasing gravitational pressure on the gas at this position due to gravitational torques and in case of stable orbits to an accumulation of gas at this position. A comparison of our radial gas density profiles and the torque profiles revealed for most of the outer disks (HI density) no correlation while for some central disks (CO density) an overlap or a shift between both profiles is found (see Fig. 4.12 and §4.5.1). A possible explanation is that gravitational torques will redistribute the gas within a few orbital rotation periods. As the transport of angular momentum per rotation period is on average ~0.3, the expected timescale for the redistribution of the total angular momentum for a given radius is ~3 rotation periods ($\cong 3 \cdot 10^7$ yr at a radius of 0.5 kpc). Another explanation might be that the gas is consumed in star formation and hence does not accumulate as expected. For the very center of (0 - 0.1) kpc we found no significant gas transport towards the AGN due to gravitational torques, suggesting that other torques such as viscous torques might be become important for fueling the AGN (see also García-Burillo et al., 2005).

In the dynamics of galaxies the CR radius is expected to separate inflow (between ILR and CR) from outflow (between CR and OLR). However, in all galaxies of our sample the CR radius of the bar does not correlate with any inflow/outflow separation and thus, sets no barrier for gas transport within the disk. This contradiction can be possibly explained by a coupling of dynamical modes, e.g. of a spiral and a bar or an oval potential. Thus, the orbital paths of the gas may change in comparison to the orbits of a single dynamical mode and allow the transport of gas across the CR. A similar case has been worked out for

NGC 4579 which shows a transportation of gas inwards across the CR of the bar, but in this case due to a (morphological) decoupling of bar and spiral pattern on different spatial scales (García-Burillo et al., 2008).

With regard to the CR of a spiral pattern, most of our galaxies with spirals (NGC 3627, NGC 4321, NGC 5248) show a correlation between CR radius of the spiral and a reversal of inflow/outflow of gas due to gravitational torques. Only for NGC 6951 no correlation is found. Instead a significant outflow due to gravitational torques occurs at the CR radius of the spiral, suggesting that the bar potential is still acting at this radius and may overlap with the spiral pattern. Further, the OLR of the bar (18.6 kpc) does not overlap with the CR of the spiral and, thus, seems to substantiate the dominance of the bar for NGC 6951. Also for NGC 3368 and NGC 4736, which have none or only very weak stellar spiral arms, the gravitational torque is dominated by a bar or oval potential.

Summarizing, gravitational torques can be very efficient in transporting the gas from the outer disk to the center at$\sim$100 pc. Due to a dynamical coupling of bar and spiral arms, the gas can bridge even resonances such as the CR of a bar (which could act as a natural barrier for further gas inflow).

4.5.3 Comparison between Gravitational and Kinematic Derived Gas Flows

Estimation of Radial Motion

In general one would expect that gas inflow/outflow should also be recognizable in the velocity field of a galaxy. In practice, to determine radial gas flows from the line-of-sight velocity alone is very ambitious and controversial (for an overview see Wong et al., 2004). The main reason is that the dominant contributor to noncircular motions (see next section) in a bar or spiral potential seems to be elliptical streaming which cannot be used by itself to derive net inflow/outflow without further assumptions. One of the most promising attempts to derive radial gas motion was conducted by Wong et al. (2004) using the variations of the first- and third-order sine coefficients (s_1 and s_3) as a function of radius to provide a basic approach to diagnose various types of non-circular motions (see for more details Wong et al., 2004): warp streaming (i.e. motion out of the plane of the disk; correlation between s_1- and s_3-term, with a slope $\mathrm{d}s_3/\mathrm{d}s_1 > 0$), elliptical or spiral streaming (anticorrelation between s_1- and s_3-term, with $\mathrm{d}s_3/\mathrm{d}s_1 < 0$), and radial inflow ($s_1 \gg s_3$). Note that these criteria are very idealized and do not permit a clear distinction between the models when applied to real galaxies. However, to definitely test whether this method can clearly identify radial gas motion or not, we have compared the radial gas flows derived from our velocity fields (see §4.3.2) with the inflow/outflow rates due to gravity torques (see §4.4.4).

We have used the following convention (following the method of Wong et al. (2004)): If the s_1-term is interpreted as radial gas flow (for $s_1/s_3 \gg 1$), a positive (negative) sign of the s_1 amplitude corresponds to gas outflow (inflow) for a counterclockwise rotating galaxy. We derived the sense of rotation for our galaxies by presuming that spiral arms as seen in the optical images are always trailing. In order to have a consistent labeling we defined $s_1^* = s_1$ $(-s_1)$ for counterclockwise (clockwise) rotation, so that $s_1^* < 0$ always corresponds to gas inflow (see third panel of Fig. 4.3). In the following we discuss some candidate regions for inflow/outflow: NGC 3627 and NGC 4321 exhibit a significant negative s_1^* term at 0-0.15 kpc and 0.2-0.8 kpc, respectively, which indicates radial inflow at these scales. In contrast, we found for these regions significant outflow rates from our gravitational torque analysis. Further, the outer disk of NGC 6951 shows a significant negative s_1^* term (indicating inflow) at (15-18) kpc, while the torque analysis reveals significant outflow ($\mathrm{d}L/L = 0.1$). Summarizing, we found no correlation between the candidate radial flow regions from our kinematic study and the inflow/outflow caused by gravitational torques. Thus, we conclude in agreement with other studies (e.g. Wong et al., 2004) that the non-circular terms are predominantly caused by elliptical streaming motions and cannot be used as an indicator alone for possible radial inflow/outflow of gas.

Streaming Motions versus Radial Inflow/Outflow

As an alternative to radial gas motion where the gas looses or gains angular momentum, gas clouds with streaming motion can follow under certain assumptions closed orbits and no angular momentum is transferred when collisional shocks and other nonlinear effects are excluded. For instance, if the principal axes of an elliptical orbit are aligned with those of a stellar bar, the phase shift between the bar and the gas is zero and hence no inflow will occur at all, but still strong streaming motions are present. To produce a net inflow/outflow a phase shift between the gas and the potential is required. Streaming motions are present in m=2 perturbation such as in a barlike potential where the gas follows elliptical closed orbits or in a two arm spiral density wave where a phase shift occurs that varies as a function of radius. This collisionless orbit approximation can be simple described by first order Fourier terms (Franx et al., 1994). In a realistic treatment the nonlinear effects will contribute additional Fourier terms and elliptical streaming motions may overlap with radial gas flows.

To estimate a possible dependence of streaming motion on pure inflow/outflow rates, we have conducted the following study. If we assume that the non-circular motions derived from our kinematic harmonic decomposition are dominated by elliptical streaming, it is possible to compare the amplitude of non-circular motions v_{nc}/v_{rot} as tracer for elliptical streaming with the amplitude of angular momentum transport caused by gravitational torques $\langle|\mathrm{d}L/L|\rangle$ as a function of radius (see Fig. 4.13). Note that the absolute scales are not really expected to be similar as they quantify different physical measurements, but indicate the significance of the values obtained with each method.

On average, we find that the amplitude of angular momentum exchange derived from our torque analysis ($v_{nc}/v_{rot} = 0.09$ for HI and $v_{nc}/v_{rot} = 0.16$ for CO) is similar to the amplitude of non-circular motions obtained from our kinematic analysis ($v_{nc}/v_{rot} = 0.09$ for HI and $v_{nc}/v_{rot} = 0.26$ for CO). In more detail, v_{nc}/v_{rot} seems to be larger for the center as $\langle|\mathrm{d}L/L|\rangle$ for most of our galaxies, except for NGC 3368 and NGC 6951. For the outer disk $\langle|\mathrm{d}L/L|\rangle$ is larger than v_{nc}/v_{rot}, at least for those galaxies with a bar. Galaxies without a bar (NGC 4736 and NGC 7217) exhibit very weak gravitational torques and hence small values of $\langle|\mathrm{d}L/L|\rangle$. Interestingly, non-circular motions in unbarred galaxies have roughly the same amplitude for the outer disk than barred galaxies.

The peaks in the amplitude of non-circular motions to the amplitude of inflow/outflow seem to be correlated as a function of radius for some galaxies: Center and outer disk of NGC 3368, outer disks of NGC 3627, NGC 4321, NGC 4736, and NGC 6951. Hence one might infer that non-circular motions are not pure elliptical streaming motions, but include to some extent radial motion as well. On the other hand, we found also cases with significant streaming motions but negligible inflow/outflow rates (e.g. for NGC 4736 and NGC 7217). Thus, our study demonstrates that signatures for streaming motions alone can not be used as reliable tracers for inflow/outflow which requires a phaseshift between the gas distribution and the gravitational potential.

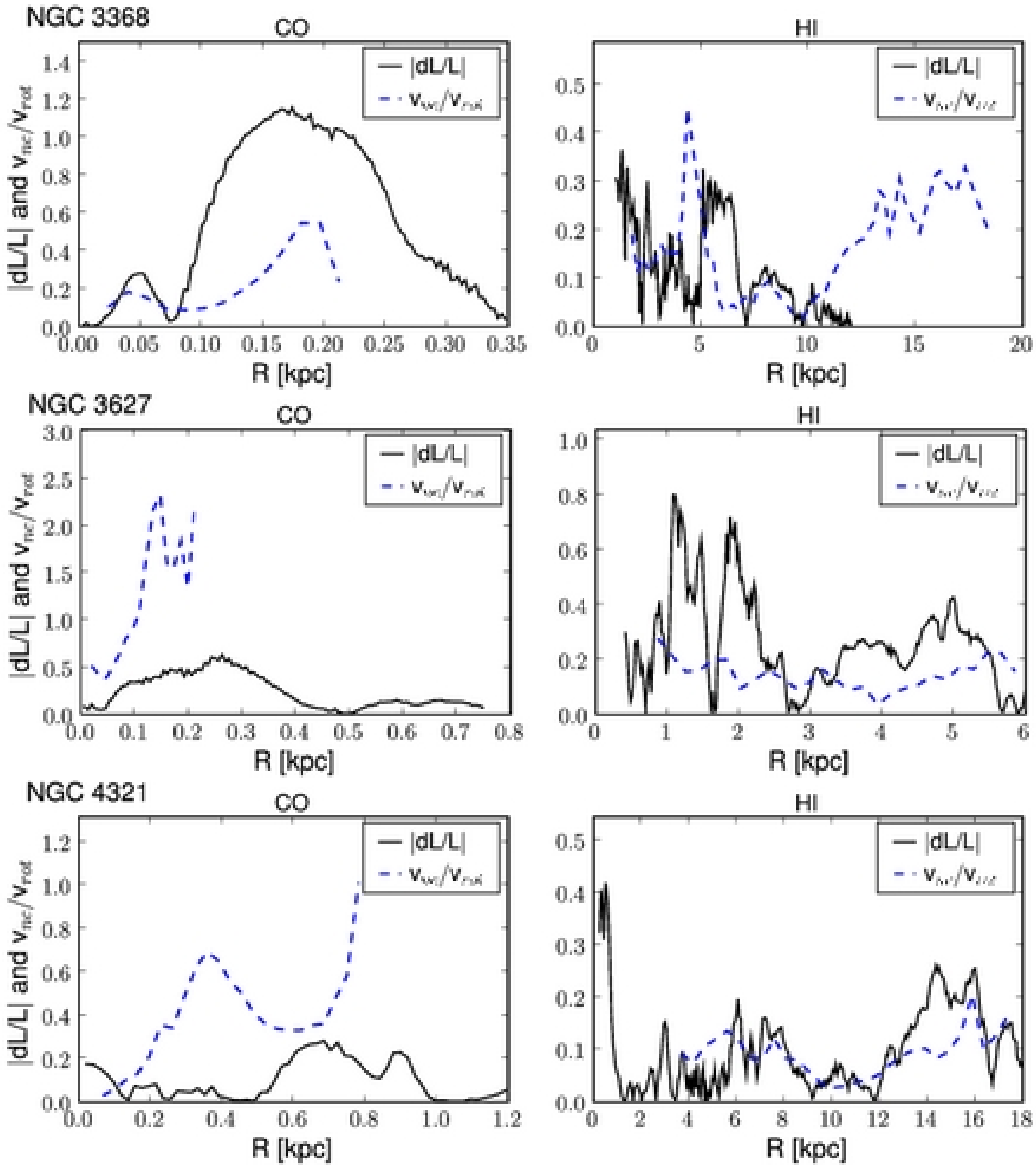

Figure 4.13: Comparison between the absolute value of angular momentum transport per rotation dL/L derived from our torque analysis (see §4.4.4) with the fraction of non-circular to rotation velocity v_{nc}/v_{rot} from the harmonic decomposition of the velocity field (see §4.3.2). As non-circular motions are very likely dominated by elliptical streaming this comparison can be interpreted as elliptical streaming versus inflow/outflow as a function of radius. Values of v_{nc}/v_{rot} with error bars larger than three (two) times the median of the dataset are not displayed for HI (CO).

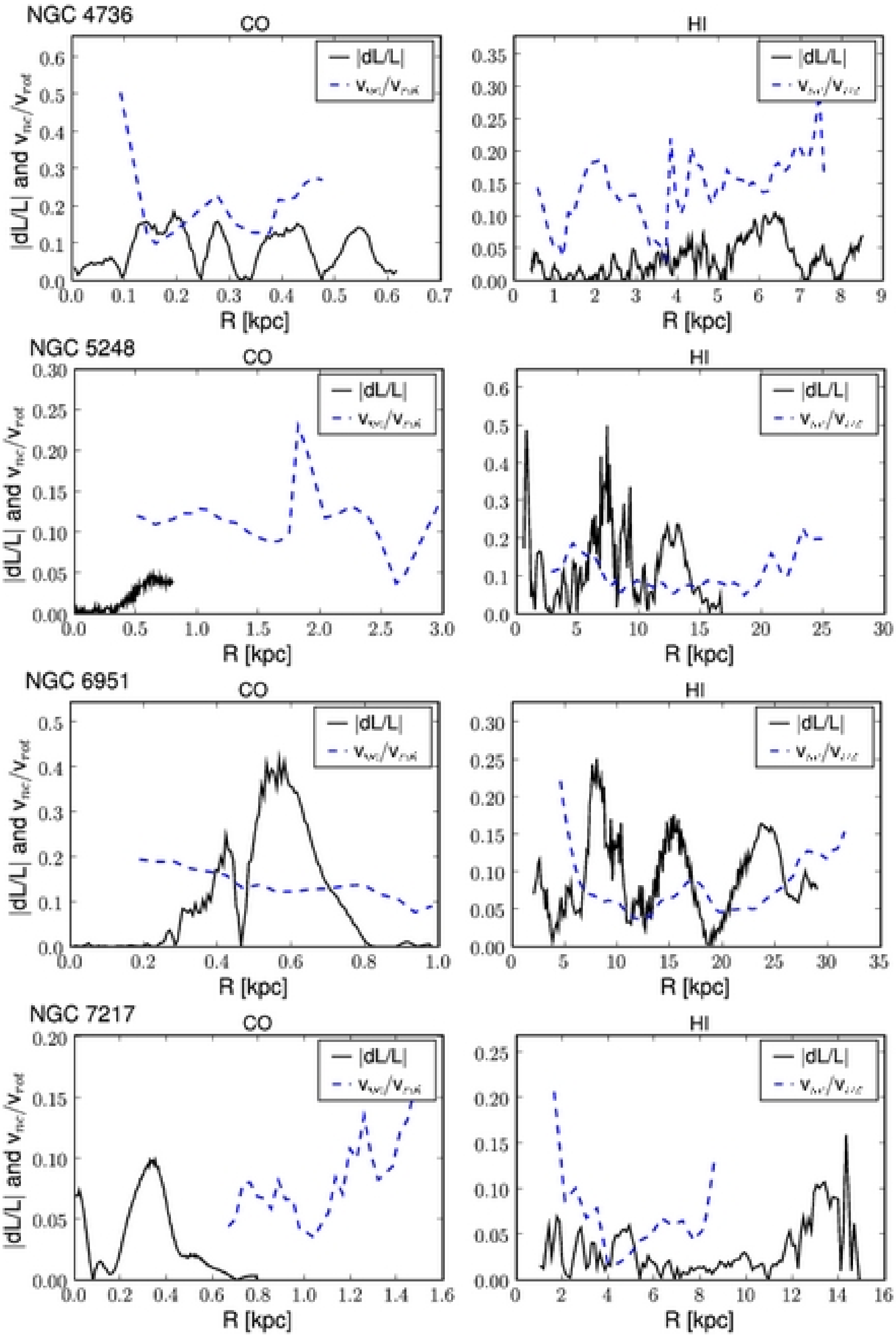

Fig. 4.13 (Continued)

4.5.4 Implications for AGN Fueling

The fueling of AGN requires transportation of gas from large kpc scales down to the inner pc. To bring the gas to the center the angular momentum of the gas must decrease by orders of magnitude. Several types of gravitational instabilities, such as bars, nested bars, spiral density waves, and spiral dust lanes have been proposed that might combine to transport gas from large kpc scales down to the very center (Shlosman et al., 1990; Combes , 2003; Wada & Koda, 2004). Inflow of gas is expected to occur mainly inside the corotation radius (CR), transporting the gas towards the inner Lindblad resonance (ILR), where the gas might accumulate and start to form clumps of star formation. To test this scenario we have compared the gas inflow/outflow rates to the dynamical behavior of the gas at the resonances. Our results suggest for some galaxies of our sample (NGC 3368, NGC 4321, and NGC 6951) that the CR radius of the bar is overcome by gravitational torques, most likely due to a coupling of several patterns (e.g. spiral arms plus bar wave pattern). Thus, the gas reservoir inside the CR can be refueled by gas from the outer disk. However, a generalization of such a scenario is not possible and detailed case studies are required to disentangle the underlying mechanisms. For example, García-Burillo et al. (2008) find for NGC 4579 that a decoupling of bar and spiral patterns on different spatial scales allows the gas to efficiently populate the UHR region inside corotation of a bar and thus explain how the CR barrier can be crossed.

For the central disk, we found that the integrated gravitational torques indicate net outflow (2 galaxies) and inflow (5 galaxies) in our galaxies. In particular NGC 3627 (Seyfert 2 type) shows a large gas outflow ($\mathrm{d}L/L$=0.5) inside the inner 0.4 kpc, suggesting a redistribution of the total angular momentum of the gas in ∼2.5 rotational periods at this radius ($\simeq 2.4 \cdot 10^7$ yrs). Interestingly, the kinematic analysis reveals also a large amplitude of non-circular motions ($\mathrm{d}v_{nc}/v_{rot}$=0.8) at scales of $R \leq 0.15$ kpc which may substantiate this scenario.

These findings are similar to other studies of the gas flow for the molecular gas disk: A gravity torque study for for the NUGA galaxy NGC 6574 using CO as tracer (Lindt-Krieg et al., 2008) has shown that gas is flowing inwards down to a radius of 400 pc which overlaps with a high nuclear gas concentration suggesting that the gas has been piling up at this location quite recently, since no startburst has been observed yet. An analysis of the torques exerted by the stellar gravitational potential on the molecular gas in four other galaxies found a mostly positive torque inside r<200 pc and no inflow on these scales suggesting that viscous torques may act as fueling mechanism as well (García-Burillo et al., 2005). Much of the explanation of this variety of morphologies appears to be related to timescales (García-Burillo et al., 2005). In this scenario the activity in galaxies is related to that of bar instabilities, expecting that the active phases are not necessarily coincident with the phase where the bar has its maximum strength. The resulting implication is that most AGN are probably between active accretion episodes. Evidence for such a scenario was found by Hunt et al. (2008) for NGC 2782 where molecular gas inside the ILR of the primary bar, transported by a second nuclear bar, suggests that the gas is fueling the central starburst, and in a second step might fuel directly the AGN.

The integrated gas mass transfer rates in the center range from 0.01 - 50 $M_\odot$ yr^{-1} based on our assumptions (see §4.4.1) and are sufficient enough to preserve the AGN activity which requires typical mass accretion rates of 0.01-0.1 $M_\odot$ yr^{-1} for LINER and Seyfert activity. However, to bridge the last 100 pc to the AGN other mechanisms (e.g. viscous torques) have to play a major role, since no significant gravity torques are present at these scales (see also García-Burillo et al., 2005).

4.6 Summary

We studied the gas flow in 7 nearby galaxies to identify mechanisms for gas transport towards the center in AGN galaxies. On the basis of high angular resolution CO and HI spectroscopic data and NIR images we calculated the gravitational torques and inflow rates as a function of radius and location within the galaxies. Besides the two-dimensional gravitational torques, we applied for this study a variety of methods including a harmonic decomposition of the residual velocity field, and the Canzian and Phase-Shift methods to identify dynamical resonances. Our study shows that gas redistribution is very effective within the galaxy disks due to gravitational torques indicating that spiral disks are very dynamic systems that undergo strong secular evolution on timescales of a few rotation periods (e.g. $\sim 5 \cdot 10^8$ yrs at a radius of 5 kpc). The main results are summarized as follows:

- Gravitational torques are very efficient in transporting the gas from the outer disk to the center at ~100 pc. Typical rates for angular momentum transport per rotation are 10% of the total angular momentum at a given radius. The transported gas mass rates range from 0.01 to 50 $M_\odot$ yr^{-1} and are larger in the central (< 1 kpc) than for the outer disk (1-20 kpc).
- Dynamical resonances such as the Corotation Resonance (CR) of a bar pattern, which act normally as a barrier for gas transport, can be easily overcome by gravitational torques induced gas flows. A possible explanation is the presence of several patterns with different speeds (e.g. bar and spiral wave pattern) that combine and allow the gas to overcome the standard CR barrier of a single pattern.
- The transport of angular momentum, and thus, the inflow/outflow rates, are larger for the center (< 1 kpc) than for the outer disk (1-20 kpc), suggesting stronger gravitational torques induced by bars in the center of galaxies.
- In our sample the dominant dynamical mode is m=2 (e.g.bar,oval,two spiral-arms) and has roughly the same orientation for the outer disk than for the center (except for NGC 4736).

- Our gas flow maps indicate the presence of nested bars within larger bars for 3 out of 7 galaxies (NGC 3368, NGC 3627, and NGC 4736) with offsets in the position angles of $25° - 60°$ to the major axes of the large-scale bars.
- No signs for unidentified patterns (that are not evident in the NIR images) are found in the torque maps.
- Streaming motions (e.g. due to bar and spiral density waves) indicated by non-circular motions are larger in the center and have the same order of magnitude in the outer disk as the pure inflow/outflow rates caused by gravitational torques. Further, non-circular motions seem to correlate only occasionally with the inflow/outflow as function of radius, and are thus not a reliable tracer of real in/outflow.
- No correlation is found between the candidate radial flow regions from our kinematic study and the inflow/outflow caused by gravitational torques. This might be explained by the fact that the non-circular terms from our residual velocity field are predominantly caused by elliptical motions.
- The change in flow direction of the gas caused by gravitational torques can be used to determine the CR radius similarly to other methods (Canzian, Stellar Density-Potential-Phase-Shift, bar length). In particular this method may be applicable in case that several patterns with different speeds combine.
- For the very center (0-0.1 kpc) no significant gas transport is found towards the AGN due to gravitational torques. Thus, other mechanisms such as viscous torques might be important for fueling the AGN at this scale.

5 Summary and Outlook

The aim of this thesis is to investigate possible fueling mechanisms on several spatial scales and the related galaxy evolution scenarios of nearby active galaxies. The first part of this chapter summarizes the main results and puts them into the broader context of AGN fueling and secular evolution. In the second part, a short outlook on future progress in this area of research is given.

5.1 Summary and Discussion of Results

A sample of nearby spiral galaxies with Active Galactic Nuclei (AGN) is studied using radio interferometric line observations (IRAM PdBI, NRAO VLA) and state-of-the-art modeling tools. This work is part of the CO- and HI-NUclei of GAlaxies project (NUGA), which aims to tests models for nuclear fueling and investigates the gas dynamics from the outskirts of spiral galaxies to the very center in order to understand the inflow mechanisms and their relations to AGN and galaxy evolution scenarios. The results of this thesis are summarized in the following.

5.1.1 Relations between Nuclear Activity and Outer Disk Properties - A possible Indication for an AGN Evolution Scenario?

Nowadays, the phenomena of nuclear activity is generally understood to be the result of accretion of material onto a SuperMassive Black Hole (SMBH); very likely through the infall of gas from its host galaxy (e.g. Rees, 1984). Although SMBHs exist in most galaxies, only a small fraction of all galaxies exhibit nuclear activity (Huchra & Burg, 1992; Ho et al., 1997; Miller et al., 2003). One key question is whether nuclear dynamics, and thus the type of nuclear activity, depends on the host galaxy properties, i.e. are large-scale disk properties (such as gas morphology or kinematic disturbances) correlated with the nuclear activity type (Seyfert, LINER, starburst). In order to address this question the distribution and kinematics of atomic hydrogen (HI) in 16 nearby spiral galaxies hosting low luminosity AGN (7 Seyferts, 7 LINER host galaxies, and 2 starburst galaxies) have been analyzed.

In particular it has been suggested that interacting galaxies or galaxies with companions exhibit a significant excess of nuclear activity compared to isolated galaxies (Dahari, 1984; Keel et al., 1985; Rafanelli et al., 1995). On the other hand no relation was found by other similar studies (Virani et al., 2000; Schmitt, 2001; Fuentes-Williams & Stocke, 1988; MacKenty, 1989; Laurikainen & Salo, 1995). Hence the issue of possible relations between the environment and nuclear activity appears to be still controversial. Since most of these studies are based on optical/IR imaging, they are in principle less sensitive to distortions than our study of the atomic gas that reacts most readily to tidal disturbances. However, in our study we found no evidence for a correlation between the fraction of companions and the AGN type present (Seyfert, LINER galaxies), neither for HI companions from our study nor for cataloged optical companions listed in NED. In almost all cases the produced tidal forces are smaller than the binding forces of the affected host galaxy. These findings are in agreement with an analysis using a larger sample of 451 active galaxies (Sy, LINER, Transition, HII, and absorption-line galaxies) from the Palomar survey (Schmitt, 2001). Thus, we conclude that AGN activity is not correlated with the presence of nearby companions. However, given the fact that half of our sample shows kinematically disturbed outer disks, it is still possible that previous interactions with companions that are now far away might have triggered AGN fueling (see §3.4.1). As the tidal forces are primarily acting on the outer disk of galaxies, the disturbed gas might reach the center and subsequently initiate nuclear activity at time-scales when the companion has long disappeared.

Apart from the environment of galaxies, also the host galaxy properties themselves are suggested to play an important role for nuclear fueling. Recent investigations of the host properties of emission-line galaxies from the Sloan Digital Sky Survey (Kewley et al., 2006) have shown that LINERs and Seyferts are clearly separable in emission line ratio diagrams (Groves et al., 2006), and that these two classes have distinct host properties (Groves et al., 2006), implying that their distinction is in fact not simply an arbitrary division. The question is therefore what mechanisms give rise to the different AGN types observed? Interestingly, our study of the HI morphology revealed a significantly higher percentage of galaxies with a HI gas ring (80%) for LINER than for Seyfert galaxies (0%), while no strong correlation with stellar rings is present. One possible explanation for an abundance of HI gas rings in LINERs may be a common evolution of the gas distribution in the disk together with the nuclear activity where both are subject to the influence of an existing bar or previous one which has now dissolved. Thus, a time evolution of AGN types seems to be possible, where Seyfert and LINERs represent different phases of the galaxy activity cycle: Seyfert galaxies are the ones where the fueling process has just been triggered (through onsetting bar dynamics) while LINERs are the ones where the triggering mechanism has already distributed the gas in a more stable new configuration (rings) that does no longer support the massive inflow of gas. This explanation is an extension of a scenario suggested by García-Burillo et al. (2005) in which the onset of nuclear activity is explained as a recurrent phase during the typical lifetime of any galaxy. In this scenario the activity in galaxies is related to that of bar instabilities, expecting that the active phases are not necessarily coincident with the phase where the bar has its maximum strength. The periods of Seyfert/LINER activity (each lasting $\sim 10^7 - 10^8$ yrs) appear during different evolutionary stages of a bar episode (typically characterized by a lifetime $\sim 10^9$ years), depending on the competition between viscosity and gravity torques. Thus, the prevalence of HI rings in LINERs, derived in this work, could be explained by the scenario proposed by García-Burillo et al. (2005), where AGN activity is linked to the evolutionary state of the bar-induced gas flow.

Other possible relations such as the HI gas content (by using the ratio M_{HI}/M_{dyn}), the relative HI mass (M_{HI}/M_{dyn}), and relative HI radius ($R_{HI}/R_{optical}$) have been studied, however, no significant correlations with the AGN-type have been found, likely due to the small number of galaxies in our sample.

5.1.2 Dynamical Evolution of AGN Host Galaxies - Gas Inflow Rates and Fueling Efficiencies

The fueling of AGN requires transportation of gas from large kpc scales down to the inner pc. To bring the gas to the center, the angular momentum of the gas must decrease by orders of magnitude. To study the role of host galaxy dynamics in the fueling of nuclear activity, we calculated gravitational torques and determined gas in/out-flow rates as a function of radius and location within the galactic disks on the basis of our combined molecular (CO using PdBI) and atomic (HI using the VLA) gas data as well as NIR images. For this detailed study of gas inflow rates, we selected 7 galaxies out of the 16 galaxies from our HI-NUGA sample. To calculate the gravitational potentials and twodimensional gas flow maps, the modeling tool PyPot has been developed. The results are compared with kinematic evidence for radial gas flows (e.g. streaming motions) and the dynamical state of the galaxies (via resonances) derived from several different methods.

We have demonstrated that gravitational torques are very efficient at transporting gas from the outer disk all the way into the galaxy center at ~100 pc. The integrated gas mass transfer rates in the centers ($0 < R \lesssim 1$ kpc) range from 0.01 - 50 $M_\odot$ yr^{-1} based on our assumptions (see §4.4.1) and are sufficient enough to preserve the AGN activity which requires typical mass accretion rates of 0.01-0.1 $M_\odot$ yr^{-1} for LINER and Seyfert activity. The dominant dynamical mode is m=2 (e.g.bar,oval,two spiral-arms) and has roughly the same orientation for the outer disk than for the center for most of our galaxies, suggesting that nuclear modes tend to be directly linked to large scale modes. Interestingly, a possible dynamical m=1 mode (e.g. lopsided disk) is found only for the center of NGC 5248, which is also the only inactive galaxy in our sample. The gas flow maps show also the action of nested bars within larger bars for 3 out of 7 galaxies (NGC 3368, NGC 3627, and NGC 4736). Our results suggest for several galaxies of our sample (NGC 3368, NGC 4321, and NGC 6951) that the corotation resonance (CR) radius of the bar, which acts normally as a barrier for gas transport, is overcome by gravitational torques. The most likely explanation is that an interplay of different patterns (e.g. spiral arms plus bar wave pattern) allow the gas to overcome the standard CR barrier of a single pattern. Thus, the gas reservoir inside the CR can be refueled by gas from the outer disk, and can then subsequently be transported towards the galactic center via the action of one or two bars (large-scale and inner bar), if present.

For the central disks ($R \lesssim 1$ kpc), we found that the integrated gravitational torques indicate net outflow (2 galaxies) and inflow (5 galaxies) in our galaxies. For the very center (0-0.1 kpc) no significant gas transport is found towards the AGN due to gravitational torques. Thus, other mechanisms such as viscous torques (García-Burillo et al., 2005) might be important for fueling the AGN at this scale. These findings are similar to other studies of the gas flow in the molecular gas disk: A gravity torque study for NGC 6574 using CO as tracer (Lindt-Krieg et al., 2008) has shown that gas is flowing inwards down to a radius of 400 pc which overlaps with a high nuclear gas concentration suggesting that the gas has been piling up at this location fairly recently, since no starburst has been observed yet. An analysis of the torques exerted by the stellar gravitational potential on the molecular gas in four other NUGA galaxies found also a mostly positive torque inside r<200 pc and no inflow on these scales suggesting that viscous torques may act as fueling mechanism as well (García-Burillo et al., 2005).

Further this work revealed a) that the transport of angular momentum, and thus, the inflow/outflow rates, are larger for the center (< 1 kpc) than for the outer disk (1-20 kpc), suggesting stronger gravitational torques induced by bars in the center of galaxies, b) that non-circular motions present in our velocity fields are predominantly caused by elliptical motions and cannot be used as reliable tracer for determination of the in/out-flow direction of gas (in agreement with findings of other studies, e.g. Wong et al., 2004), and c) that the change in flow direction of the gas caused by gravitational torques can be used to determine the CR radius, in particular for the case when several patterns are present.

Summarizing, this study demonstrates that gas redistribution is very effective within the galaxy disks due to gravitational torques indicating that spiral disks are very dynamic systems that undergo strong secular evolution on timescales of a few rotation periods (e.g. $\sim 5 \cdot 10^8$ yrs at a radius of 5 kpc). Thus, gas can lose angular momentum and can be transported from the outer disk to the center (overcoming the CR barrier) where it might accumulate at the Inner Lindblad Resonance (ILR), and subsequently fuel the AGN through viscous torques and/or starbursts (e.g. via mass loss of young stars, supernovae, or tidal disruption). This demonstrates that secular evolution processes seem to be efficient enough to transport gas to the center, so that tidal interactions are not implicitly required. The absence of correlations between the presence of stellar patterns (e.g. bars) and AGN activity can be explained by the fact that the episodic lifetime of an AGN ($\sim 10^7$ - 10^8 yrs) is shorter than the inflow time due to one or more fueling mechanisms ($\sim 10^8$ - 10^9 yrs).

5.2 Outlook

This work has shown that nuclear dynamics as well as the type of nuclear activity (Seyfert/LINER) is linked to the state of the gas flow present in the entire gas disk. To substantiate this link a better knowledge of the relation between AGN type, the dynamical state of a galaxy, the gas distribution, and the responsible mechanism (e.g. gravitational torques, viscous forces and/or starformation) in the center (<100 pc) of a galaxy is required. While statistical studies using large samples of galaxies might in principle provide such robust correlations and thus can show evidence for a possible fueling scenario, individual case studies and simulations involving detailed modeling of the gas flow are necessary to reveal the physical processes of AGN fueling. Ongoing and possible projects that tackle the issue of AGN fueling are briefly described in the following.

5.2.1 Detailed Simulation of the Gas Flow in a Representative AGN Galaxy

To probe the complex interplay between the stellar component and the gaseous response, it is crucial to study the gas behavior in detail. Our combined CO/HI datasets provide detailed insight into the gas flow on all scale lengths within a galaxy disk. Thus, current dynamical models which predict a very close link between the large-scale and nuclear gas kinematics can be tested by tailored simulations of individual sources using N-body and SPH codes. To do so, we have started such a project of a detailed model of the gas flow from the outer disk to the center of the representative source NGC 6951. This galaxy is a prototypical Seyfert 2 galaxy with a single stellar bar as well as gaseous and stellar spiral arms. In particular, modeling the gas flow in the inner and outer part of the disk at the same time has not been at all attempted before in models of nearby galaxies. The main aims of such a study are a) to test if the observed gas morphology can be reproduced by simulation and under what conditions (e.g. initial conditions as well as simulation parameter such as viscosity), b) to evaluate typical time scales for building up large-scale and central gaseous spirals, c) to estimate gas inflow rates and to compare them with our gravity torque results, and d) to determine the efficiency of gravitational versus viscous torques as a function of radius within the galaxies disk.

For this project the gravitational potential derived from PyPot is adopted and the simulation tool GADGET-2 has been modified in order to take such a real static potential as input. The gaseous behavior is then probed using the SPH part of the GADGET-2 simulation software on the static potential of NGC 6951. Initial conditions are defined as a thin homogeneous gas disk and are derived from the observed gas distribution and kinematics. In practice, the static potential is implemented in GADGET-2 using an additional computation for the acceleration in three dimensions on the basis of external FITS-files that describe the forces and the potential in the equatorial plane. Further, it includes a smooth initiation (slow increase with time) of the non-axisymmetric component (e.g. bars and spirals) of the external potential and related forces, and a rotation of this component with a defined pattern speed. A detailed description of this work is given in the App. A.2. It is planned to compare the result of this simulation directly to the observations of the gas kinematics on all spatial scales, and thus, to test our current understanding on how dynamical processes proceed in the gaseous component in the disk (see detailed description of aims of this study above).

5.2.2 Future Applications of the Gravity Torque Method

As demonstrated in this work and similar CO studies (e.g. García-Burillo et al., 2005), gravity torque maps (García-Burillo et al., 2005) are an extremely powerful tool to evaluate whether stellar potentials can efficiently transport gas within a galaxy. Without doubt this method will be likely used for further studies of gas flows in galaxies, possibly not only for AGN fueling, but also related to star-formation processes in the disk. Further, the gravitational torque method might be valuable for dynamical studies to determine the CR radius in comparison to other methods (Canzian, Stellar Density-Potential-Phase-Shift, bar length). In particular this method may be applicable in case where several patterns exist (see § 4.4.3).

For large samples (>100 galaxies), a determination of the gas flow may be more difficult given the limited number of galaxies that have high-spatially resolved neutral gas images. The information about the gas distribution is required as the link between the derived torque field and angular momentum variations relies on the weighting of the "pure" gravitational torque field with the gas column density (see §4.4). However, also without the exact knowledge of the gas distribution it is still possible to derive the gravitational potential and to evaluate the dynamical modes in galaxies (e.g. the strength of the bar and/or spiral). This may be useful for the search of statistical correlations with other galactic properties (e.g. AGN type, gas content, Hubble type, and/or evolution of galaxies on cosmological time scales) and hence to evaluate indirectly possible mechanisms to transport angular momentum in galaxies. For example, an analysis of possible correlations between AGN type, gravitational torque (bar strength) and gas mass reservoir for a large sample of inactive and LLAGN galaxies could provide a critical test for the proposed evolutionary AGN scenario which suggest a time evolution of the AGN activity together with the redistribution of the neutral gas through bars (described in § 3.4.3) and may reveal important information on the role of AGN in secular galaxy evolution.

5.2.3 Comparison of the Gas Distribution and Kinematics between Active and Inactive Galaxies

Up to now, most surveys for studying nuclear activity and host properties have been based on optical/IR, but the majority of these studies have failed to find a clear distinction between Seyfert host and inactive galaxy morphology on a range of scales that encompasses nearby companions and interactions, galactic bars and nuclear spirals (see for an overview Martini, 2004) An advantage of probing atomic gas properties instead of the stellar component is that gas is much more sensitive to internal (e.g. bars) and external disturbances (e.g. tidal interactions) than stars.

To investigate in more detail whether the triggering mechanism of AGN is related to the galactic host properties, the VLA Hydrogen Imaging and Kinematics of INactive Galaxies and Seyferts survey (The VHIKINGS survey) has been established (Mundell et al., 2007). The VHIKINGS survey is a high angular resolution HI synthesis imaging spectroscopic survey of 56 Seyfert and inactive control galaxies which aims to compare statistically the structural and dynamical properties of active and inactive galaxies. In particular, possible relationships might exist between the presence of nuclear activity and disk properties such as HI content, distribution, global and detailed kinematics. Further, the gaseous environment of active and inactive galaxies will be compared, such as the prevalence of gas-rich low optical brightness dwarf galaxies.

The VHIKINGS survey is motivated by single dish HI surveys of Seyferts, which found that $\sim$40% of Seyfert galaxies (Heckman et al., 1978; Mirabel & Wilson, 1984) exhibits HI profiles different from the typical profiles of normally rotating spiral galaxies. Further, recent spectroscopic studies of the ionized gas show evidence for kinematic perturbations linked with Seyfert galaxies at small radii (Dumas et al., 2007). Indeed, first results of the ongoing VHIKINGS survey indicate possible relationships between Seyfert activity and HI properties (Mundell et al., 2007) and will hopefully soon reveal more insight into the topic of AGN fueling.

Similar to the large-scale study described above, it is also possible to compare the gaseous morphology and kinematics in the galactic centers (<1 kpc) between active and inactive galaxies. Recent NICMOS imaging of the circumnuclear regions of 250 galaxies (Hunt and Malkan,2004) found significant isophotal twists and disturbances suggesting the possibility of identifiable dynamical differences between active and inactive hosts. On the other hand, Martini et al. (2003) found a comparable frequency of nuclear dust spirals in active and inactive galaxies for late-type galaxies. In combination with similar results for the frequency of bars and interactions, these results suggest that there is no universal fueling mechanism for low-luminosity AGN at scales greater than 100 pc from the center. Hence also the timescale for nuclear activity should be less than the timescale for matter inflow from this spatial scale of 100 pc. If the dynamical timescale on these spatial scales corresponds roughly to the characteristic inflow time, the phase of nuclear activity would have an upper limit of several million years. To tackle the issue of nuclear fueling at smaller spatial scales, a comparison of molecular gas properties between the CO-NUGA sample (active galaxies) and a well matched sample of inactive galaxies (from archive data or follow-up observations using SMA or IRAM PdBI) would be ideally suited. As this study could probe the molecular gas distribution and kinematics at a spatial resolution of a few 10 pc, it would provide also new upper limits for the time-scales of nuclear activity.

A Appendix

A.1 Uniform and Natural Weighting

The minimum noise in an image is produced by weighting each sample by the inverse square of its uncertainty (thermal noise). **Natural** weighting means to have all samples simply weighted by their input weights. Since most interferometers do not sample the *uv* plane at all uniformly the beam pattern produced by natural weighting tends to have a central beam resembling a core-halo source produced by all the short spacing data. To reduce the effects of non-uniformity in data sampling, the concept of **uniform** weighting was deviced, which attempts to give each cell in the *uv* plane grid the same weight. In principal, images with natural weighting tend to have smaller Root Mean Square (RMS) values but larger dirty beams (low angular resolution), while uniform weighted images have smaller dirty beams (higher angular resolution) but larger RMS values. To find the best compromise between angular resolution and RMS, several robust weighting parameters were tested and a robust weighting parameter of 0.3 was selected (see Fig. A.1). This amount of robustness seems to reduce the noise added by weighting significantly while causing only modest increases in the undesirable near-in sidelobes and central lobe width of the dirty beam.

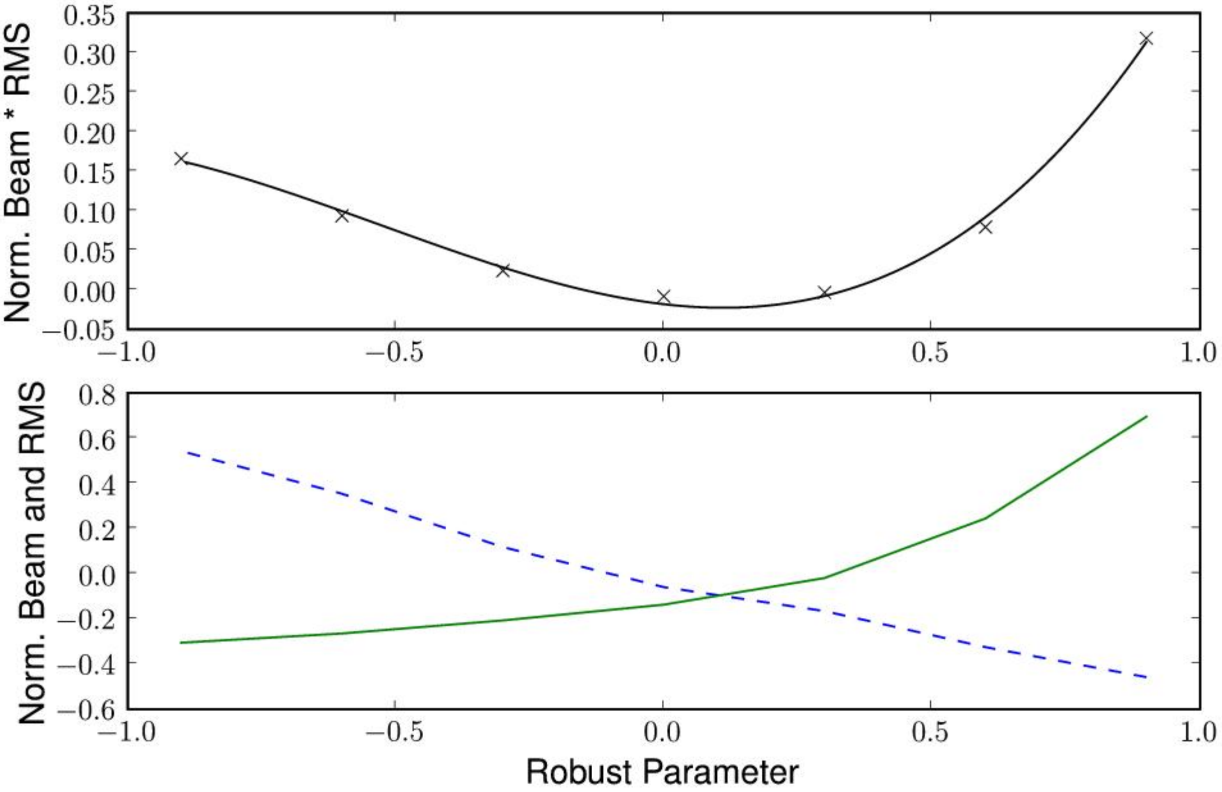

Figure A.1: Comparison of the dirty beam and RMS values for different robust weighting parameters. All values have been normalized to their minimum and maximum obtained with pure natural (robust weighting parameter of 5) and pure uniform weighting (robust weighting parameter of -5). The top panel shows the combination of dirty beam × RMS value as a function of robust weighting parameter, while RMS (blue dashed line) and dirty beam (red solid line) values are plotted separately in the bottom panel.

A.2 Procedures for GADGET-2 Simulation

The simulation is based on the smoothed particle hydrodynamics (SPH) part of GADGET-2 in combination with the static gravitational potential of NGC 6951. GADGET-2 is a cosmological simulation tool with a parallel TreeSPH code for an ideal gas, capable of following a collisionless fluid with the N-body method (for an overview see Springel, 2005). Our initial conditions are derived from our CO and HI gas observations: The gas particles are homogeneously distributed in a thin disk (0.5 kpc height) with a radius of 25 kpc (similar to the HI radius of NGC 6951). The initial velocities in x,y directions are defined as circular orbits corresponding to the gravitational potential of NGC 6951. For each particle a random dispersion term is added to the x,y,z velocities using a Gaussian distribution with $\sigma = 5$ km s^{-1} which is the average dispersion for NGC 6951 (from our kinematic analysis).

The static potential is implemented in GADGET-2 using an additional computation for the acceleration in three dimensions on the basis of external FITS-files that describe the forces $F_x(z = 0)$, $F_y(z = 0)$ and the potential $\Phi(x, y, z = 0)$ in a plane. We assume a non-infinitesimally thin disk and use a model for the vertical distribution, namely an isothermal plane with the scaling height h, so that the force in x directions is calculated in GADGET-2 using

$$F_x = \frac{\mathrm{d}\Phi}{\mathrm{d}x} = F_x(z = 0)\ sech^2(z/(4h)) \tag{A.1}$$

and in the same way for F_y. In z direction the forces are calculated using

$$F_z = \frac{\mathrm{d}(\Phi)}{\mathrm{d}z} = \Phi(x, y, z = 0)\ \frac{\mathrm{d}(sech^2(z/(4h)))}{\mathrm{d}z} \tag{A.2}$$

with

$$\frac{\mathrm{d}(sech^2(z/(4h)))}{\mathrm{d}z} = \frac{-1}{2h}\ \frac{sinh(z/4h)}{(cosh(z/4h))^3} \tag{A.3}$$

It is also possible to multiply the results with an additional scaling relation in case of a thick disk. Then, the additional acceleration is derived for each particle by linearly interpolating the 8 closest neighbor cells in the force array. Further a smooth transition from axisymmetry to non-axisymmetry in time is included,

$$\Phi = \Phi_{axisym} \cdot (1 - G(t)) + \Phi_{non-axisym} \cdot G(t) \tag{A.4}$$

where $G(t)$ is a function starting at 0 at t=0 and being 1 after a certain time so that the gas can settle smoothly in the non-axisymmetric potential. The axisymmetric part Φ_{axisym} is derived by azimuthal averaging the non-axisymmetric part $\Phi_{non-axisym}$ which is given by the gravitational potential of NGC 6951. The non-axisymmetric part of the potential and forces rotates with a defined pattern speed.

A.3 Channel Maps

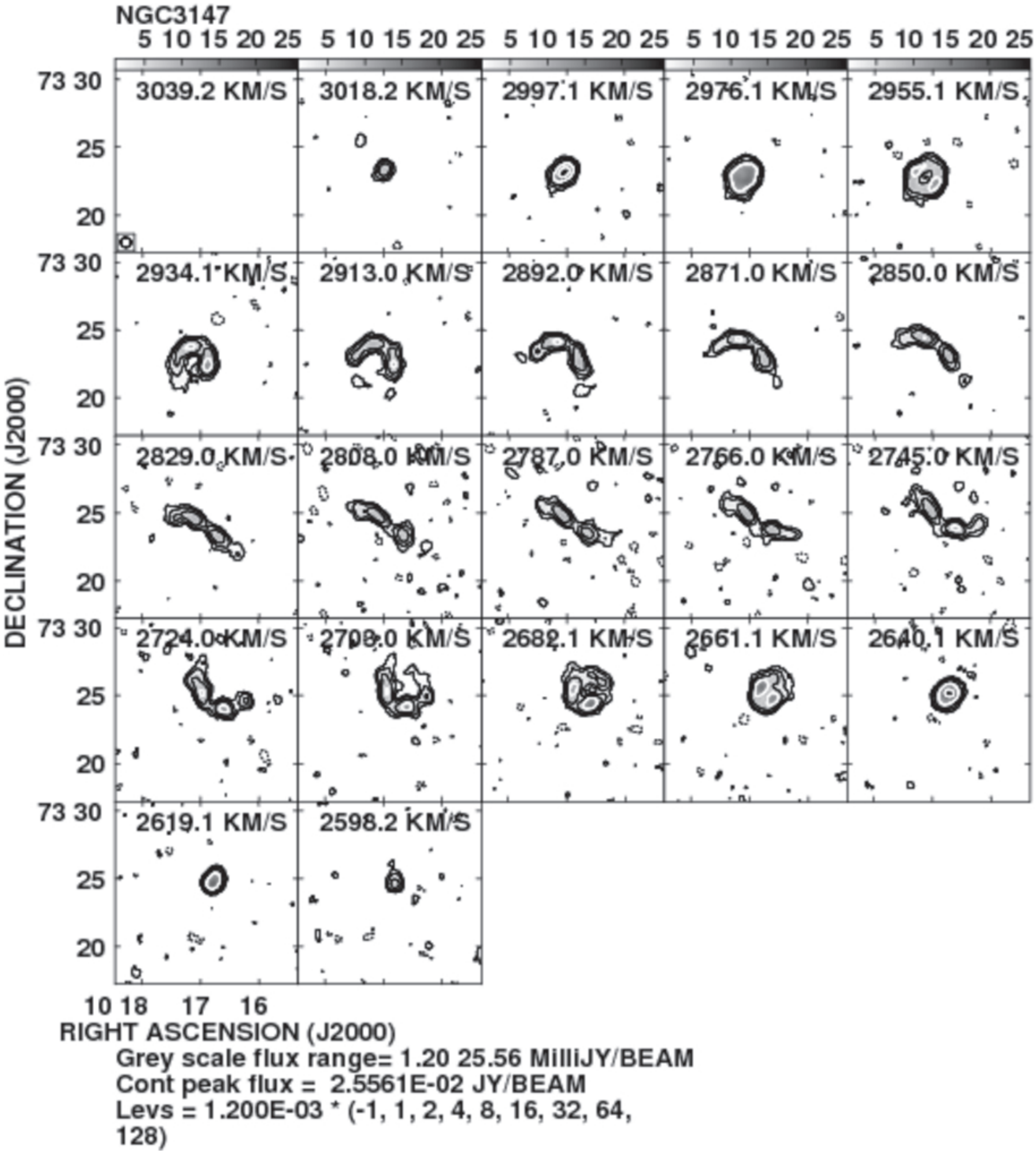

Figure A.2: Channel maps of the natural weighted data cubes. Each channel has a velocity width of ~20.8 km s^{-1}. The flux cut-off was set at 3σ of the RMS value and the contours are in steps of $3\sigma \cdot 2^n$Jy (n=1,2,3...).

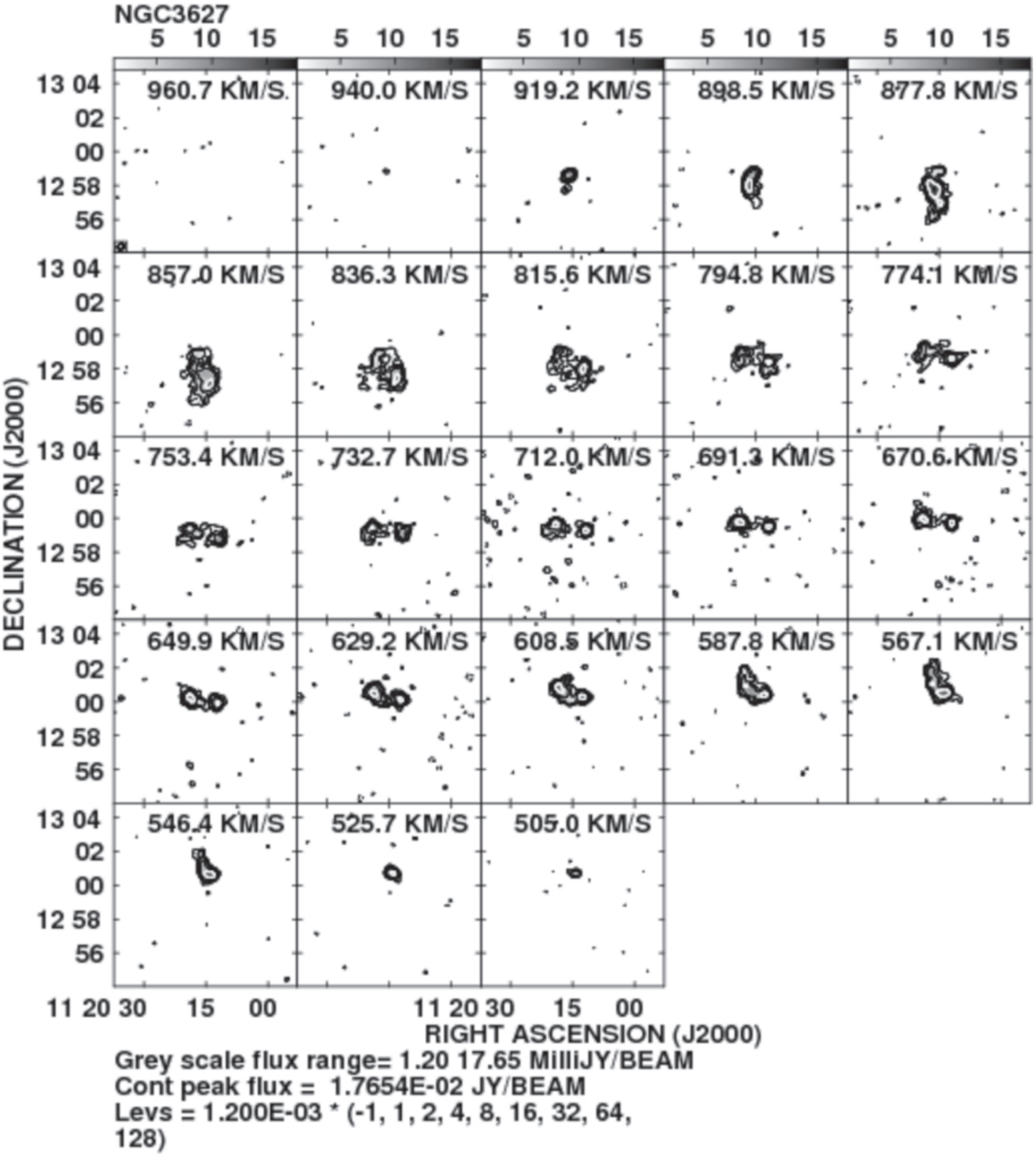

Fig. A.2 (Continued)

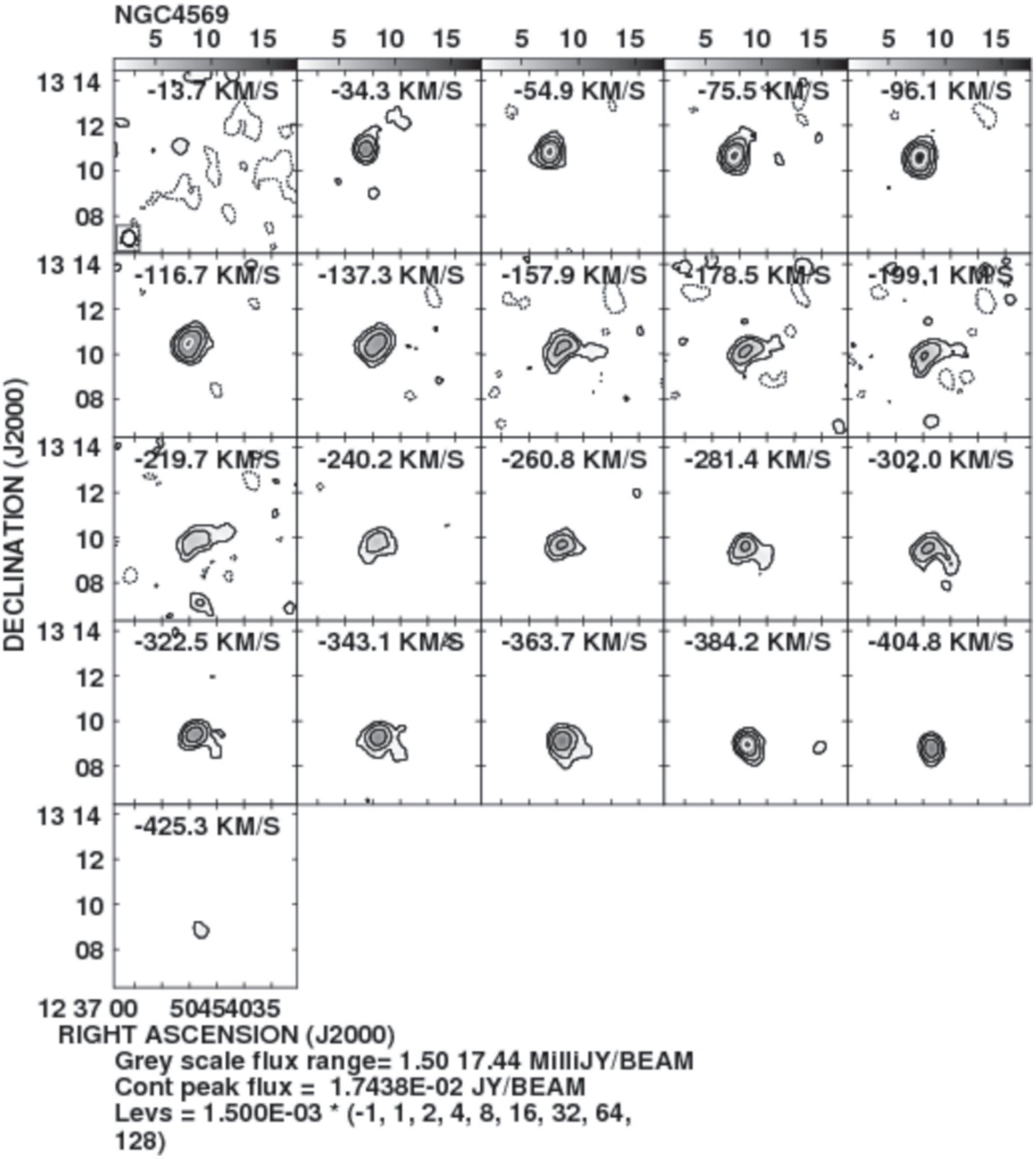

Fig. A.2 (Continued)

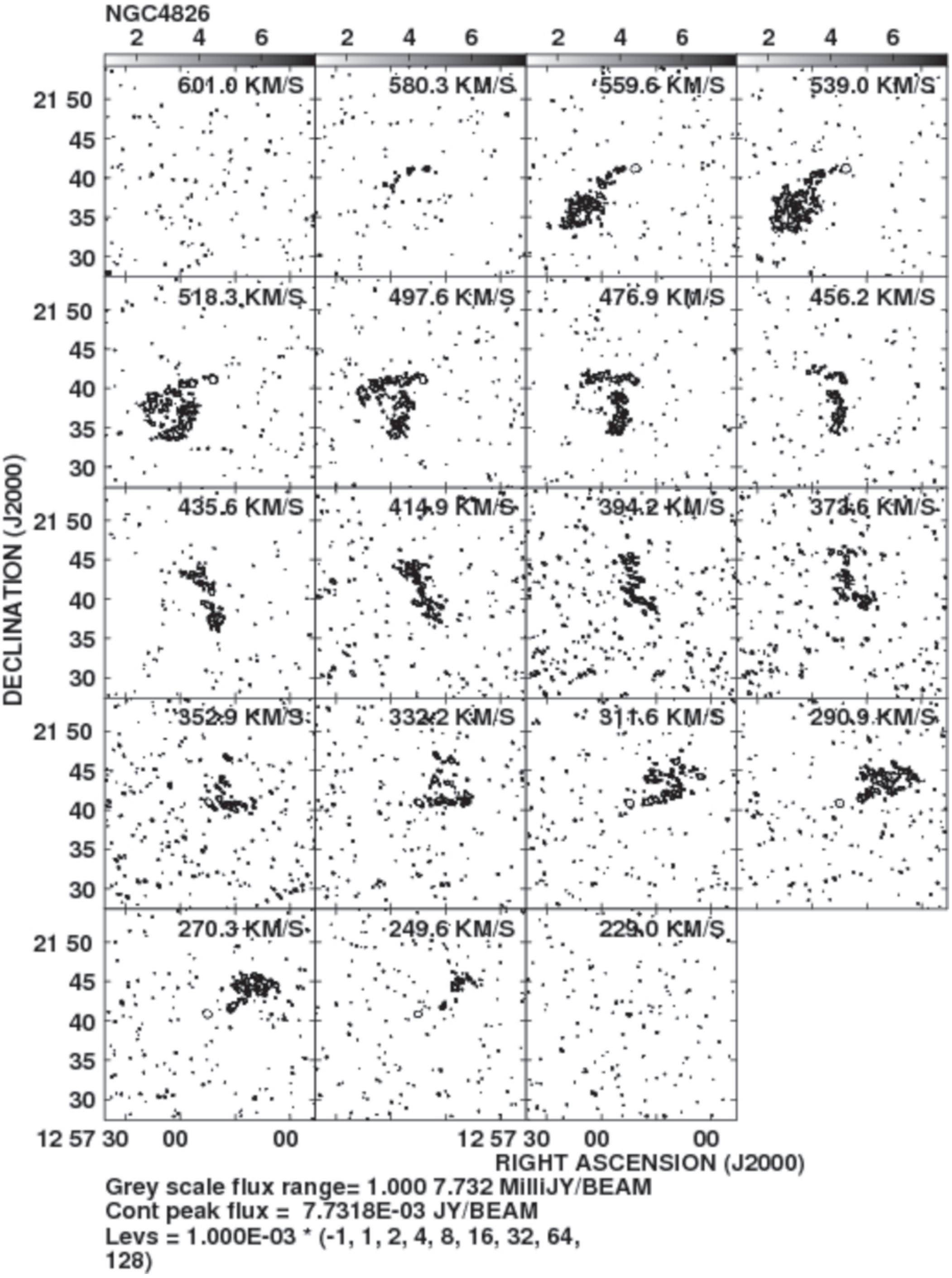

Fig. A.2 (Continued)

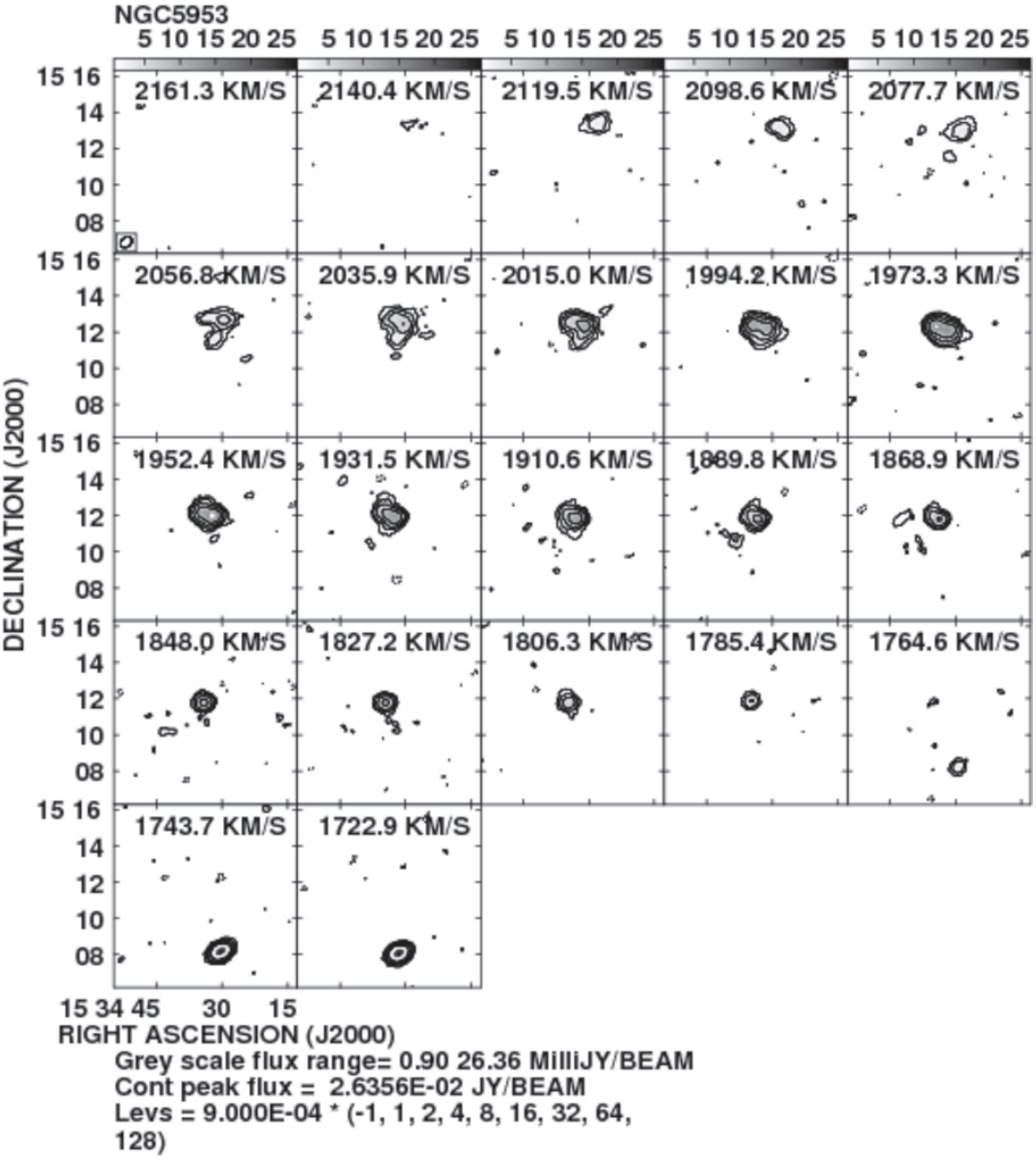

Grey scale flux range= 0.90 26.36 MilliJY/BEAM
Cont peak flux = 2.6356E-02 JY/BEAM
Levs = 9.000E-04 * (-1, 1, 2, 4, 8, 16, 32, 64,
128)

Fig. A.2 (Continued)

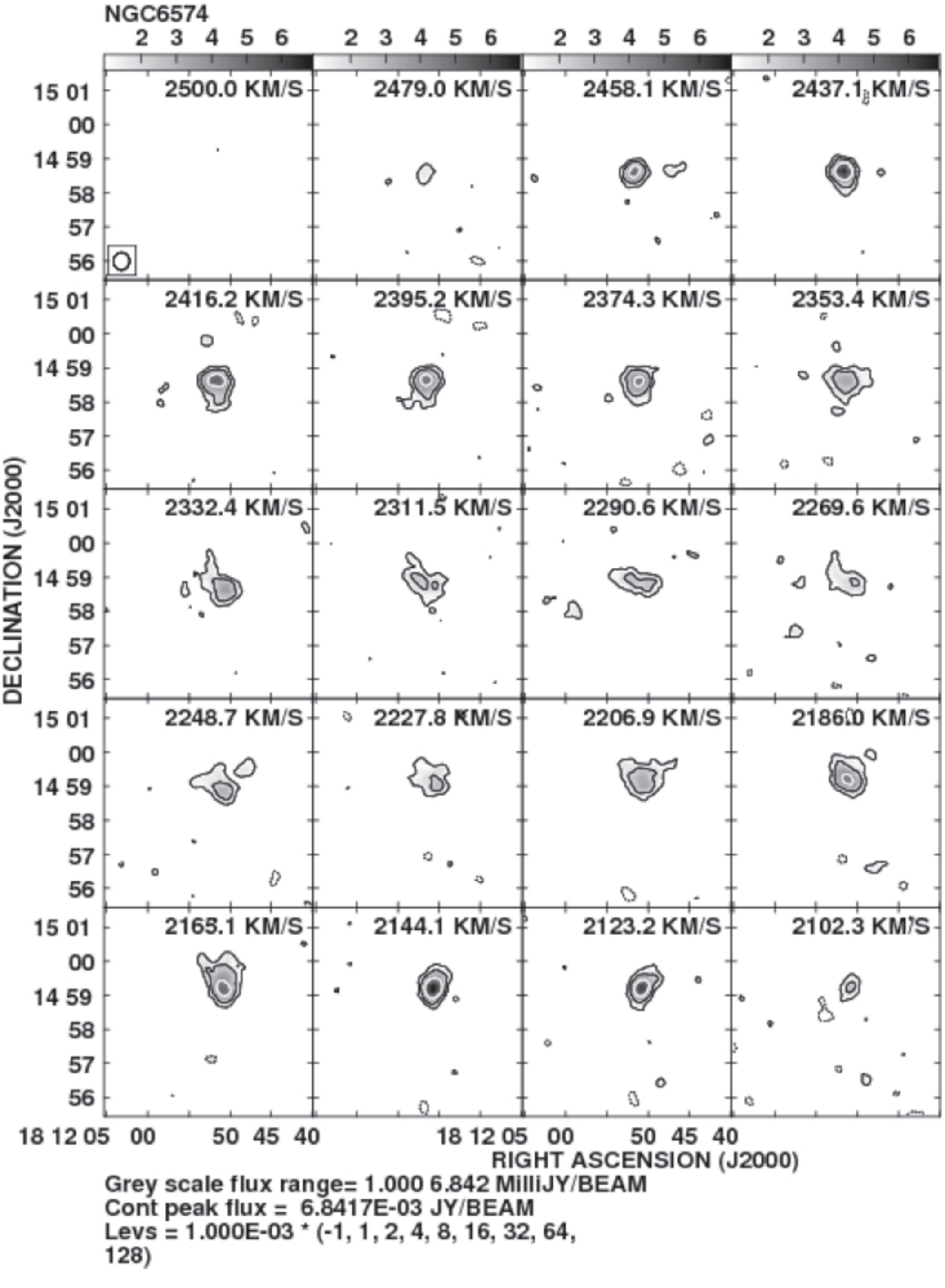

Fig. A.2 (Continued)

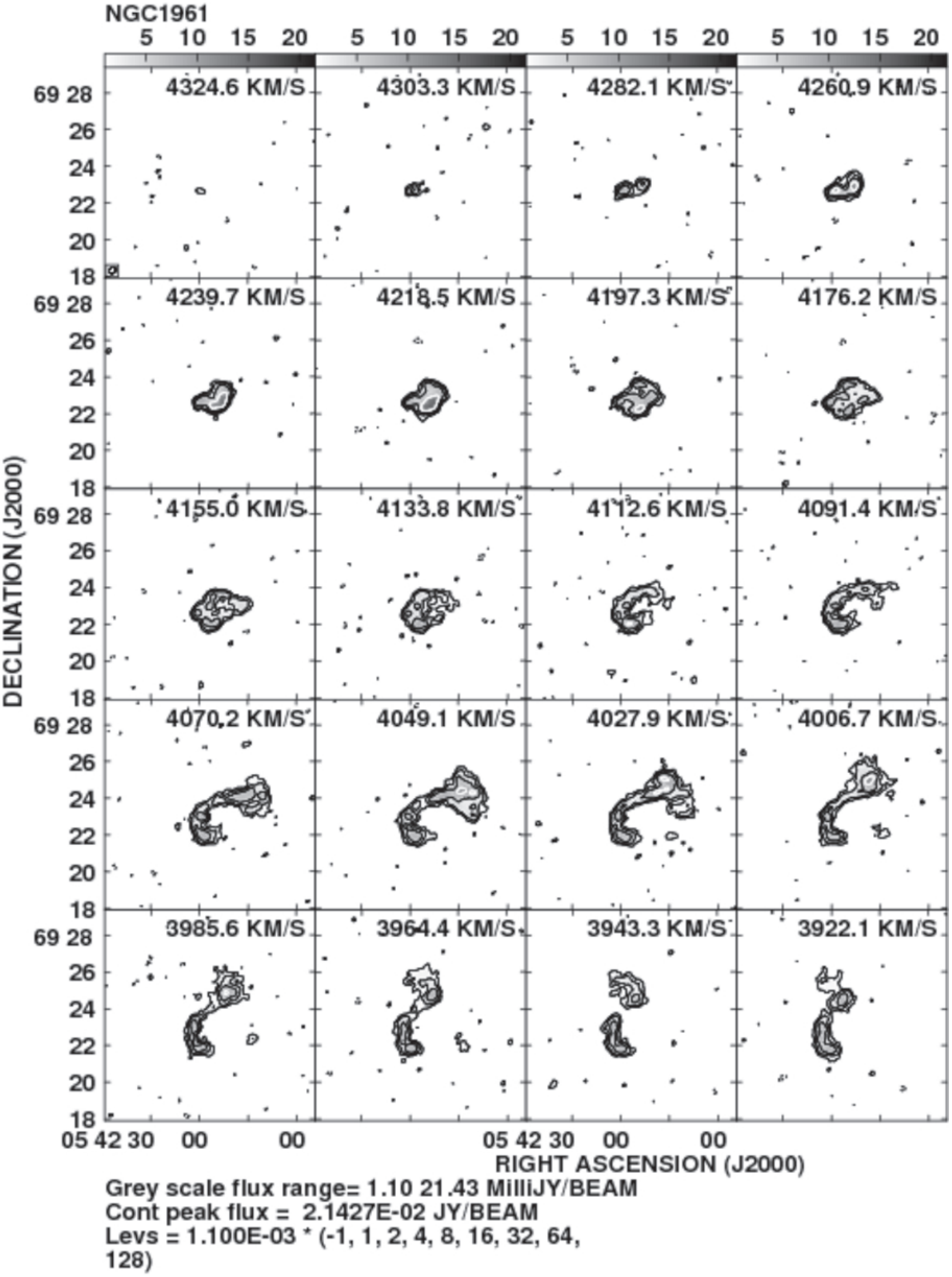

Fig. A.2 (Continued)

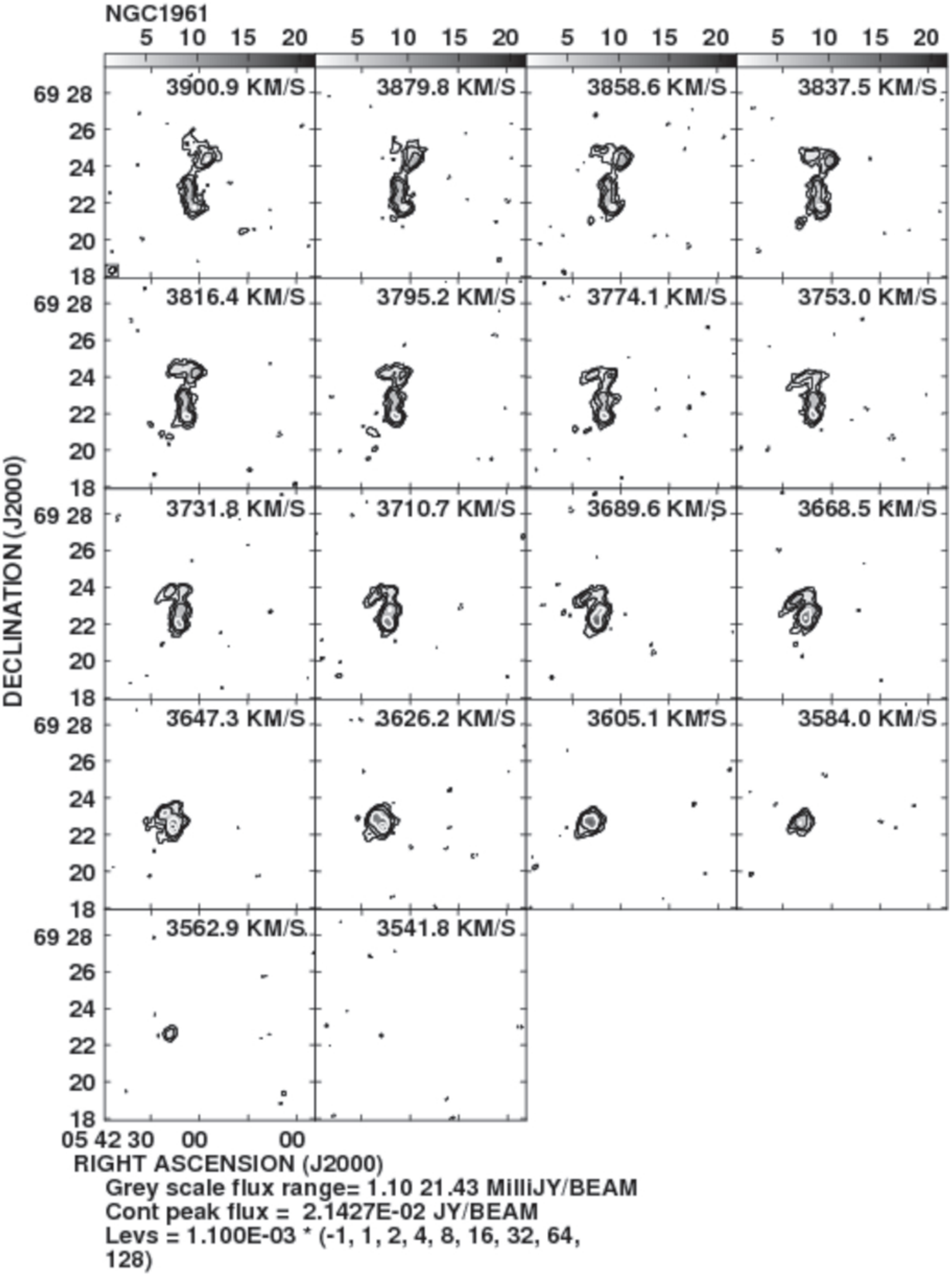

Fig. A.2 (Continued)

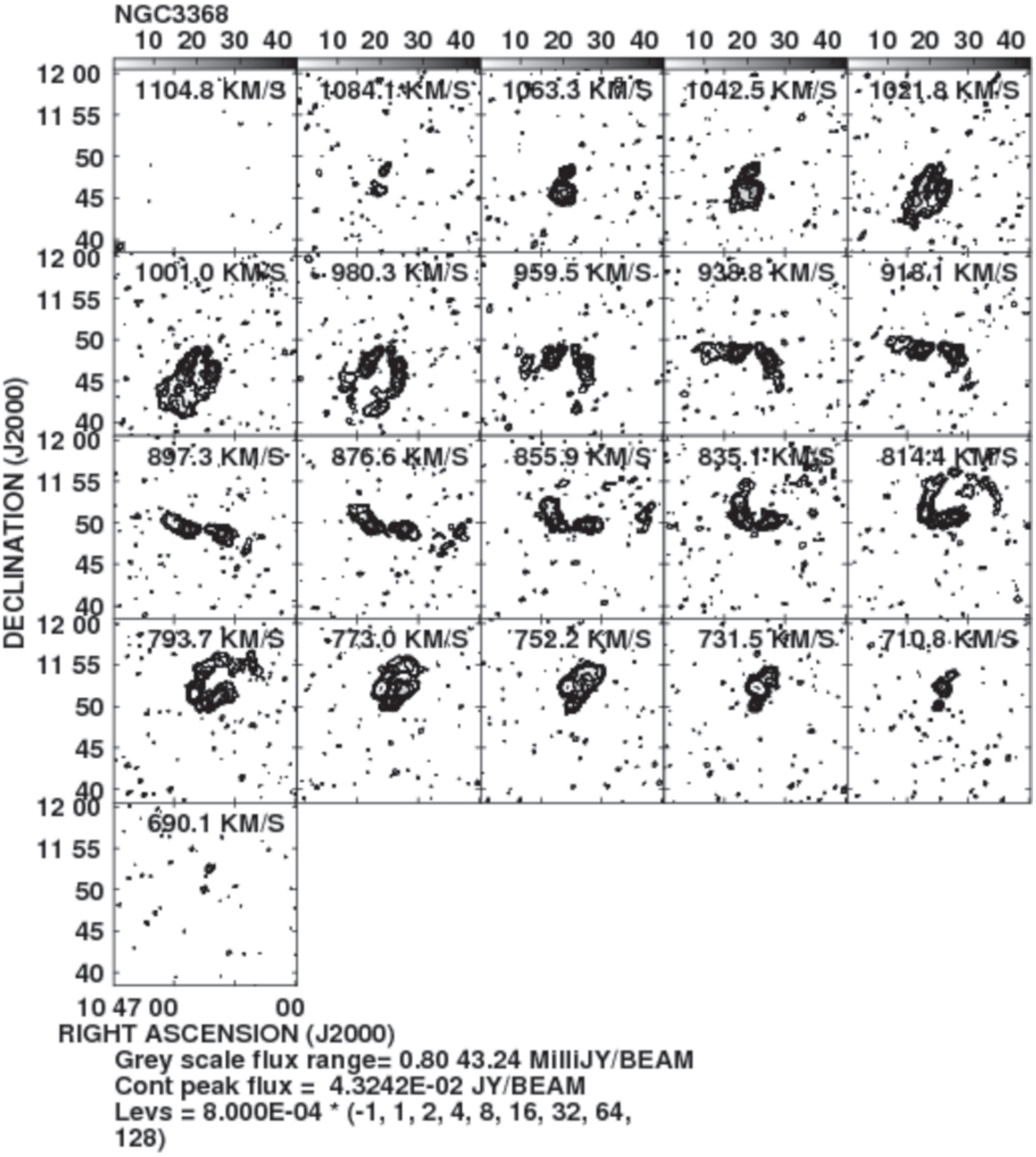

Fig. A.2 (Continued)

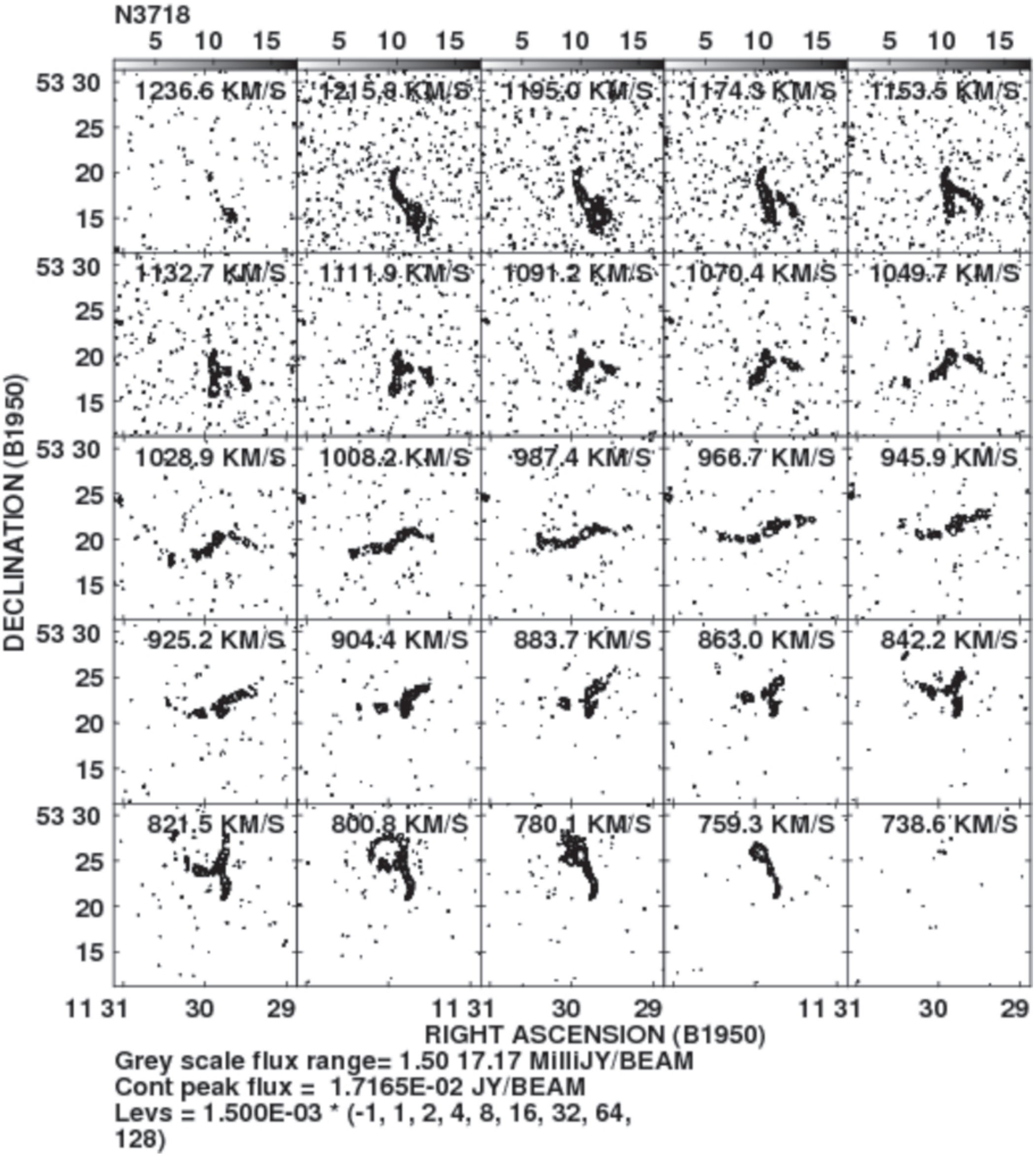

Fig. A.2 (Continued)

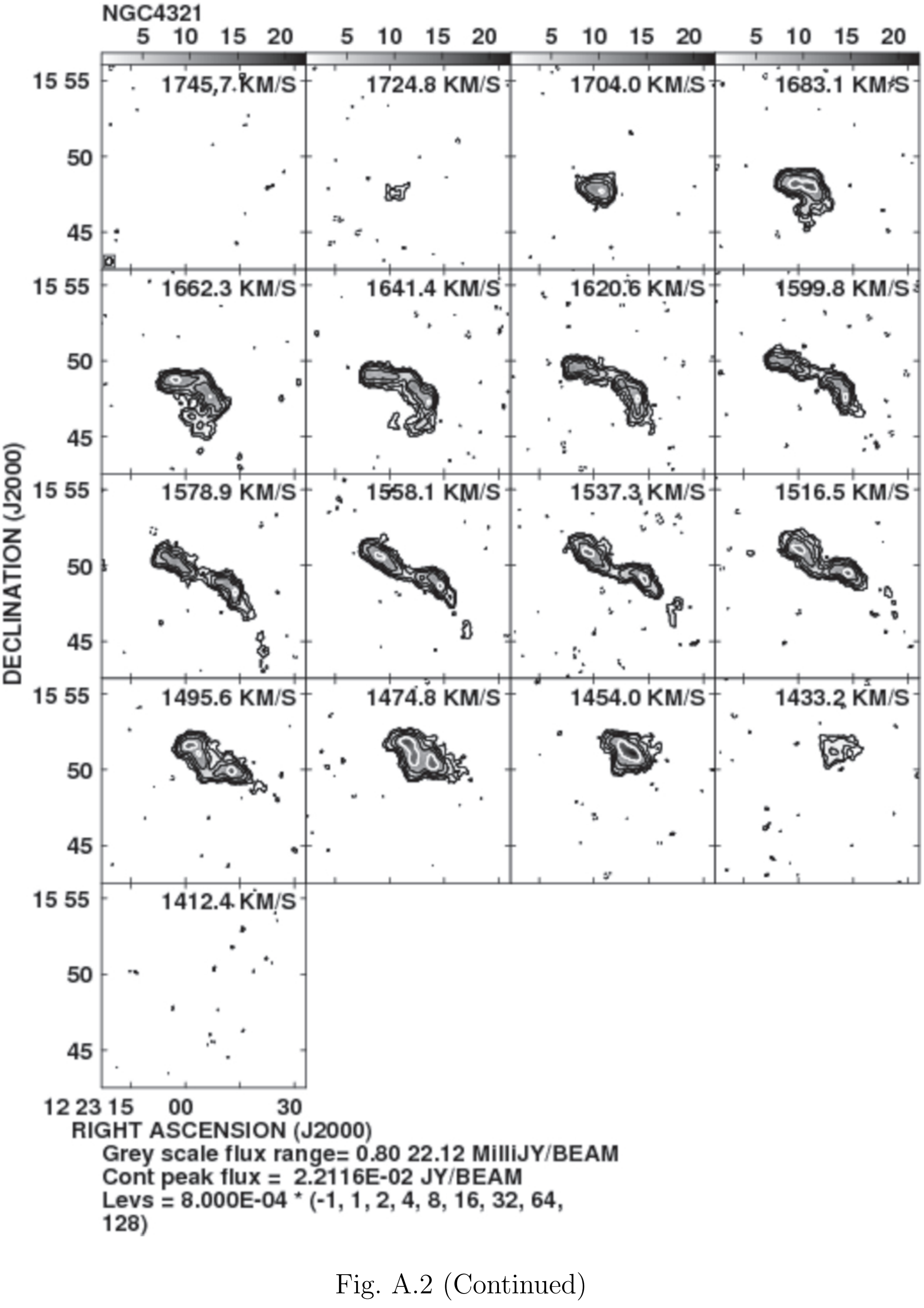

Fig. A.2 (Continued)

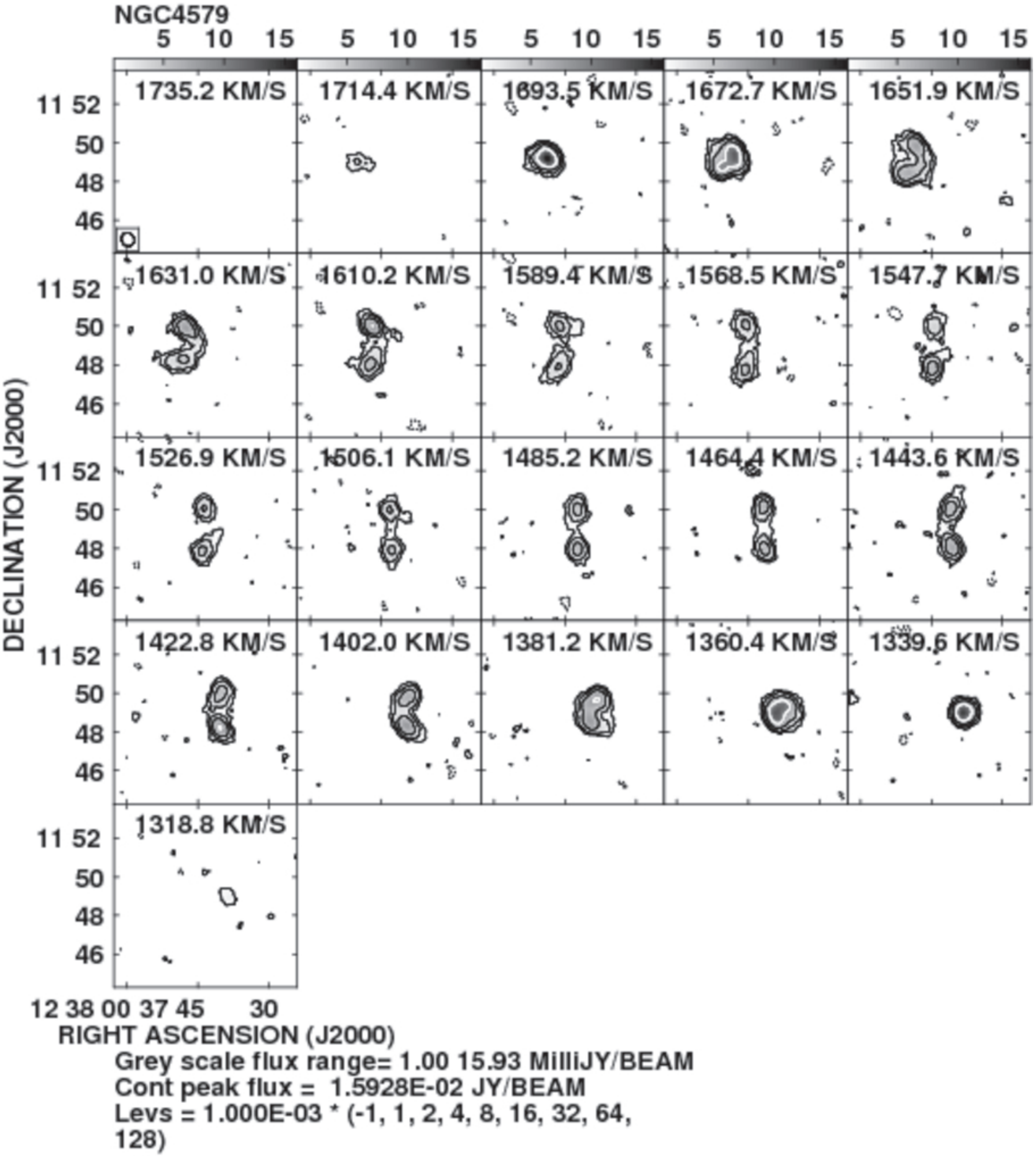

Fig. A.2 (Continued)

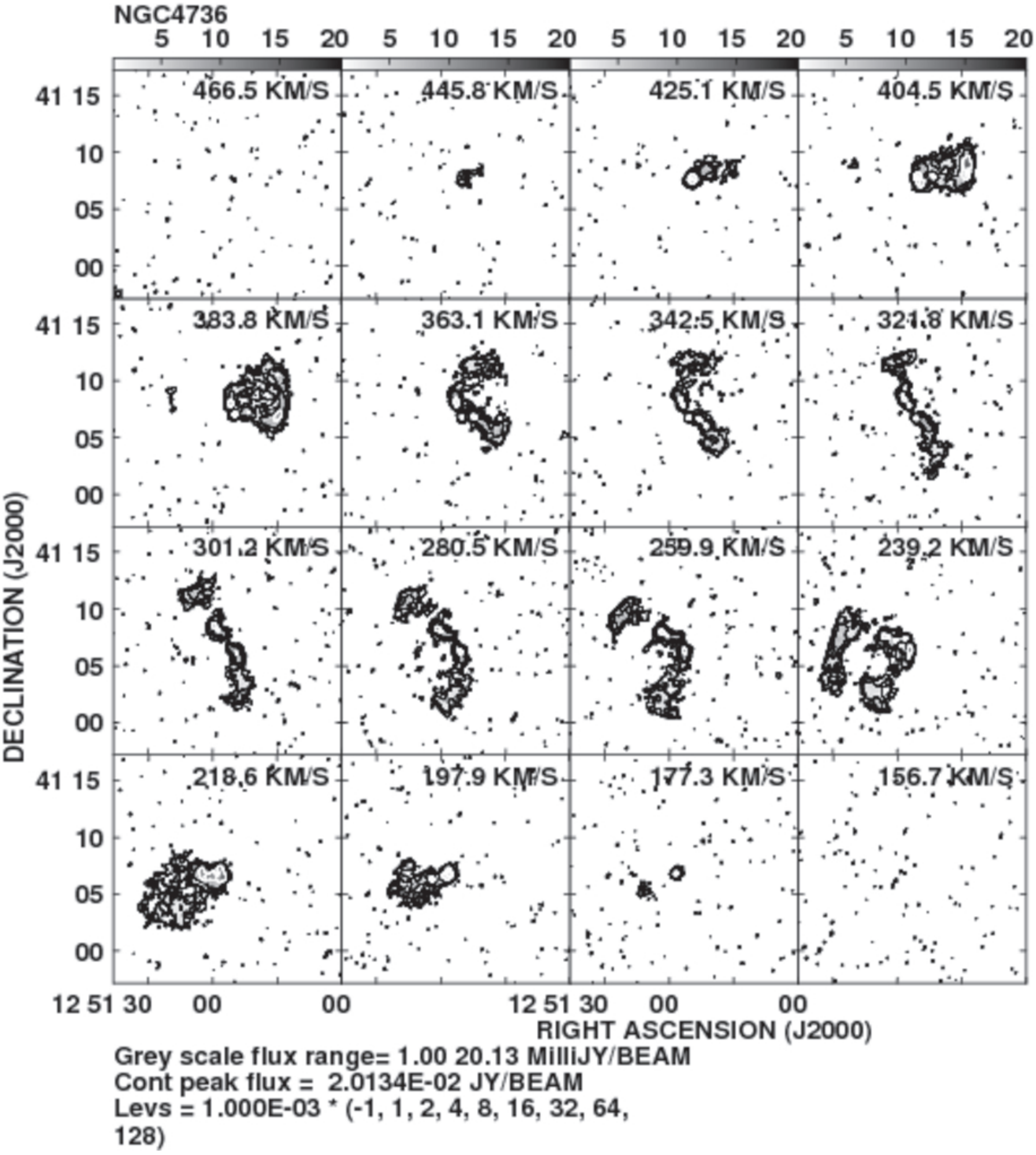

Fig. A.2 (Continued)

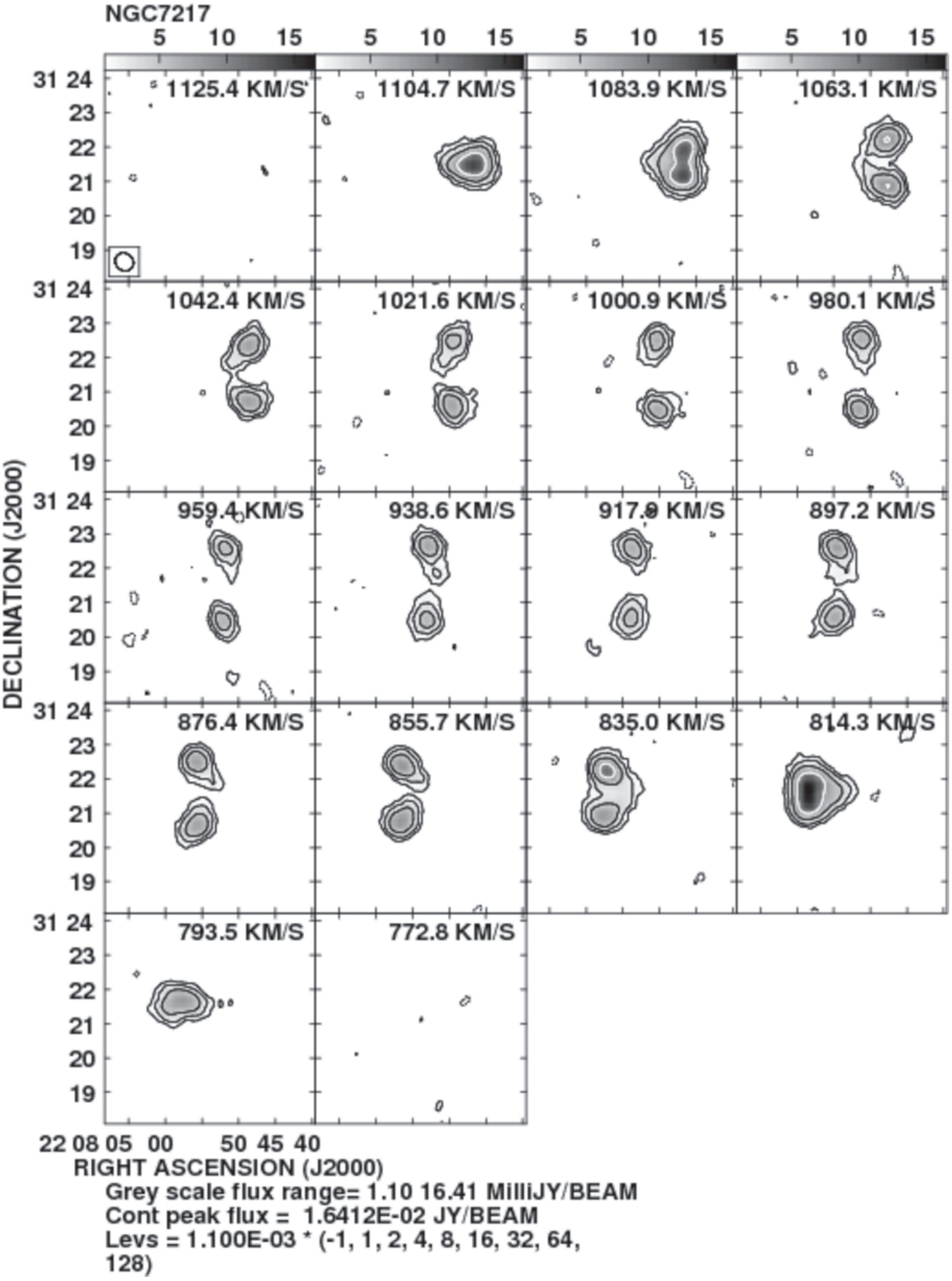

Fig. A.2 (Continued)

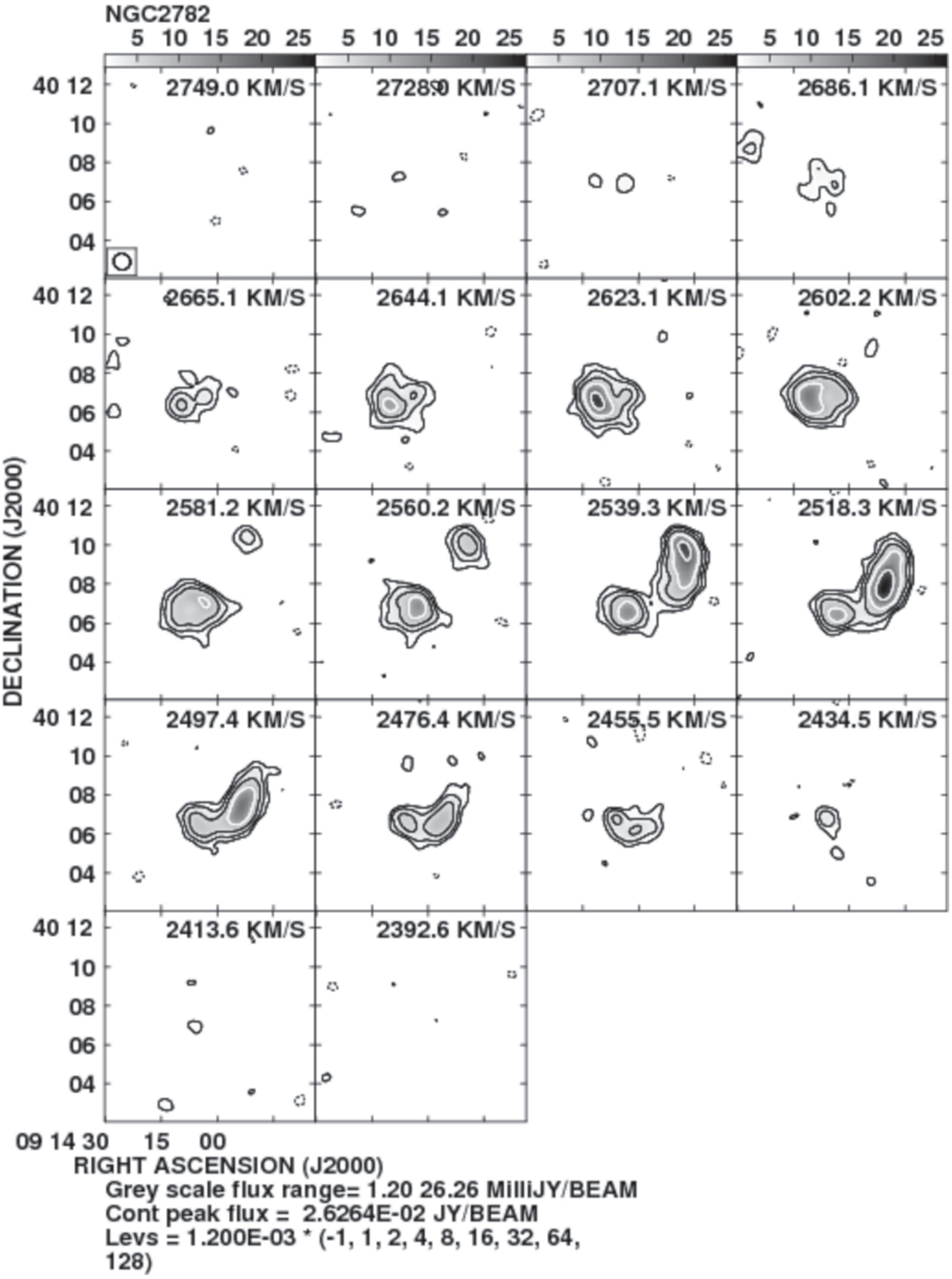

Fig. A.2 (Continued)

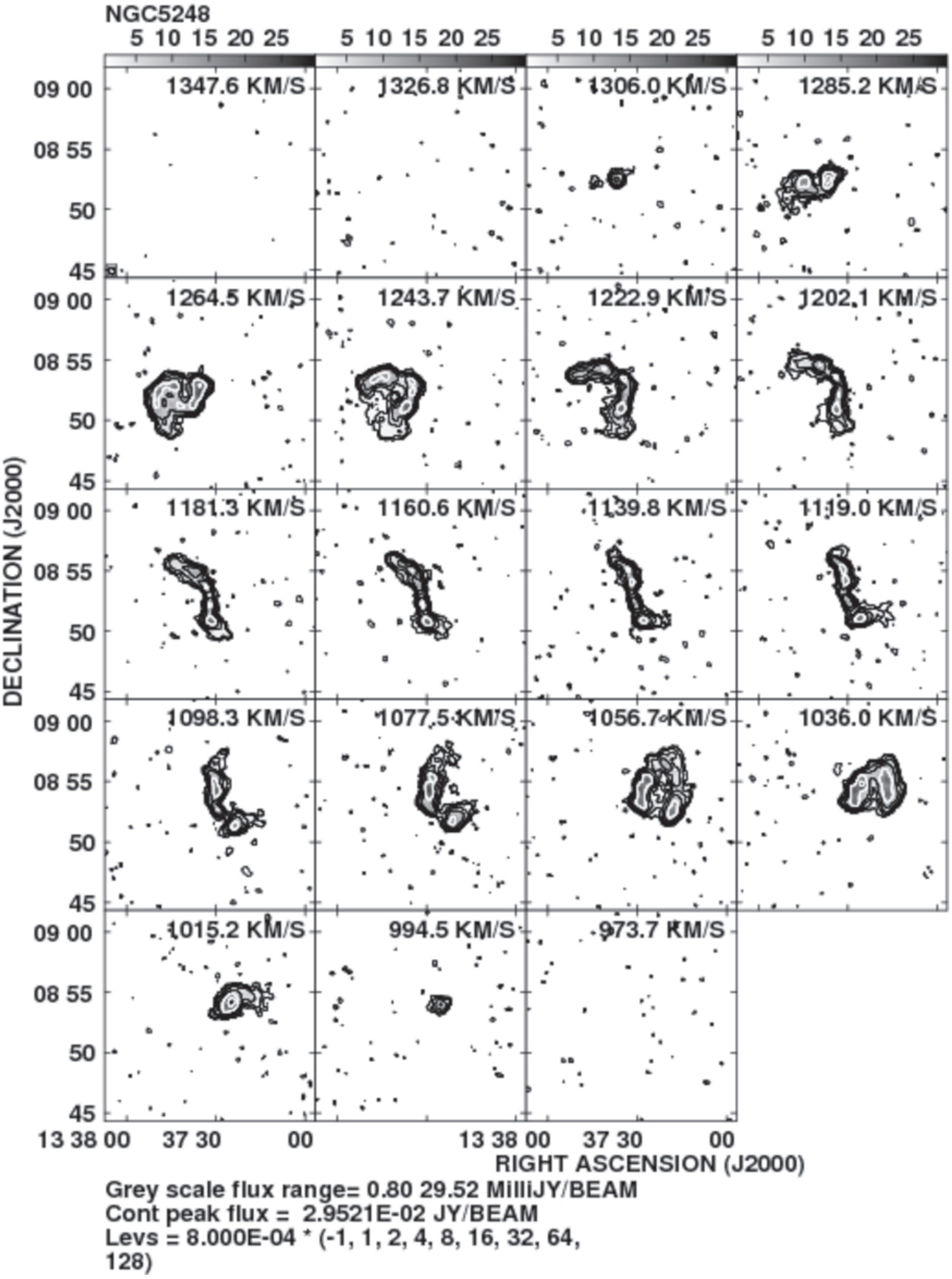

Fig. A.2 (Continued)

Bibliography

Aaronson, M. 1977, Ph.D. Thesis, Harvard University

Athanassoula, E. 1992, MNRAS, 259, 345

Athanassoula, E. 2000, Stars, Gas and Dust in Galaxies: Exploring the Links, 221, 243

Athanassoula, E. 2003, MNRAS, 341, 1179

Bailin, J., et al. 2005, ApJ, 627, L17

Baldwin, J. A., Phillips, M. M., & Terlevich, R. 1981, PASP, 93, 5

Barnaby, D., & Thronson, H. A., Jr. 1992, AJ, 103, 41

Barnes, J. E., & Hernquist, L. E. 1991, ApJ, 370, L65

Barnes, E. I., & Sellwood, J. A. 2003, AJ, 125, 1164

Beck, R. 2004, Ap&SS, 289, 293

Beck, R., Ehle, M., Shoutenkov, V., Shukurov, A., & Sokoloff, D. 1999, Nature, 397, 324

Begeman, K. G. 1989, A&A, 223, 47

Bender, R., Burstein, D., & Faber, S. M. 1992, ApJ, 399, 462

Berentzen, I., Heller, C. H., Shlosman, I., & Fricke, K. J. 1998, MNRAS, 300, 49

Bettoni, D., Galletta, G., & García-Burillo, S. 2003, A&A, 405, 5

Binney, J., & Tremaine, S. 2008, Galactic Dynamics: Second Edition, by James Binney and Scott Tremaine. ISBN 978-0-691-13026-2 (HB). Published by Princeton University Press, Princeton, NJ USA, 2008.,

Blitz, L. 1996, CO: Twenty-Five Years of Millimeter-Wave Spectroscopy, 170, 11

Boone, F., et al. 2007, A&A, 471, 113

Bournaud, F., & Combes, F. 2002, A&A, 392, 83

Boyle, B. J., Jones, L. R., & Shanks, T. 1991, MNRAS, 251, 482

Brandt, J. C. 1960, ApJ, 131, 293

Braun, R., Walterbos, R. A. M., & Kennicutt, R. C., Jr. 1992, Nature, 360, 442

Bullock, J. S., Dekel, A., Kolatt, T. S., Kravtsov, A. V., Klypin, A. A., Porciani, C., & Primack, J. R. 2001, ApJ, 555, 240

Buta, R., & Combes, F. 1996, Fundamentals of Cosmic Physics, 17, 95

Canzian, B. 1993, ApJ, 414, 487

Canzian, B., & Allen, R. J. 1997, ApJ, 479, 723

Cavaliere, A., & Padovani, P. 1989, ApJ, 340, L5

Cayatte, V., van Gorkom, J. H., Balkowski, C., & Kotanyi, C. 1990, AJ, 100, 604

Cayatte, V., Kotanyi, C., Balkowski, C., & van Gorkom, J. H. 1994, AJ, 107, 1003

Chatzichristou, E. T. 2002, ApJ, 581, 161

Collin, S., Boisson, C., Mouchet, M., Dumont, A.-M., Coupé, S., Porquet, D., & Rokaki, E. 2002, A&A, 388, 771

Combes, F. 2001, Advanced Lectures on the Starburst-AGN , 223

Combes, F. 2003, in Active Galactic Nuclei: from Central Engine to Host Galaxy, (Astronomical Society of the Pacific), Conference Series, Vol. 290, p. 411.

Combes, F., et al. 2004, A&A, 414, 857

Conselice, C. J., Bershady, M. A., Dickinson, M., & Papovich, C. 2003, AJ, 126, 1183

Contopoulos, G., & Grosbol, P. 1989, A&A Rev., 1, 261

Dahari, O. 1984, AJ, 89, 966

Dumas, G. 2007 , PhD Thesis, Astrophysics Research Institute Centre de Recherche Astrophysique de Lyon - Observatoire de Lyon

Dumas, G., Mundell, C. G., Emsellem, E., & Nagar, N. M. 2007, MNRAS, 379, 1249

Efron, Bradley 1979, The Annals of Statistics 7 (1), 1-26.

Emsellem, E., Greusard, D., Combes, F., Friedli, D., Leon, S., Pécontal, E., & Wozniak, H. 2001, A&A, 368, 52

Emsellem, E., Fathi, K., Wozniak, H., Ferruit, P., Mundell, C. G., & Schinnerer, E. 2006, MNRAS, 365, 367

Englmaier, P., & Shlosman, I. 2000, ApJ, 528, 677

Englmaier, P., & Shlosman, I. 2004, ApJ, 617, L115

Eskridge, P. B., et al. 2002, ApJS, 143, 73

Faber, S. M., Wegner, G., Burstein, D., Davies, R. L., Dressler, A., Lynden-Bell, D., & Terlevich, R. J. 1989, ApJS, 69, 763

Fabian, A. C. 1979, Royal Society of London Proceedings Series A, 366, 449

Fathi, K. 2004, PhD thesis, Rijksuniversiteit Groningen

Ferrarese, L., Pogge, R. W., Peterson, B. M., Merritt, D., Wandel, A., & Joseph, C. L. 2001, ApJ, 555, L79

Ferrarese, L., et al. 2006, ApJ, 644, L21

Forbes, D. A. 1992, A&AS, 92, 583

Franx, M., van Gorkom, J. H., & de Zeeuw, T. 1994, ApJ, 436, 642

Friedli, D., & Martinet, L. 1993, A&A, 277, 27

Fuentes-Williams, T., & Stocke, J. T. 1988, AJ, 96, 1235

Garcia-Burillo, S., Combes, F., & Gerin, M. 1993, A&A, 274, 148

García-Burillo, S., Sempere, M. J., Combes, F., Hunt, L. K., & Neri, R. 2000, A&A, 363, 869

García-Burillo, S., et al. 2003, ASP Conf. Ser. 290: Active Galactic Nuclei: From Central Engine to Host Galaxy, 290, 423

García-Burillo, S., et al. 2003, A&A, 407, 485

García-Burillo, S., Combes, F., Schinnerer, E., Boone, F., & Hunt, L. K. 2005, A&A, 441, 1011

García-Burillo et al. 2008, A&A, submitted

Gebhardt, K., et al. 2000, ApJ, 539, L13

Genzel, R., Pichon, C., Eckart, A., Gerhard, O. E., & Ott, T. 2000, MNRAS, 317, 348

Ghez, A. M., Salim, S., Hornstein, S. D., Tanner, A., Lu, J. R., Morris, M., Becklin, E. E., & Duchêne, G. 2005, ApJ, 620, 744

Greene, J., Lim, J., & Ho, P. T. P. 2004, ApJS, 153, 93

Greisen, E. W., 2003, Information Handling in Astronomy - Historical Vistas, 109

Groves, B., Kewley, L., Kauffmann, G., & Heckman, T. 2006, New Astronomy Review, 50, 743

Guth, A. H. 1981, Phys. Rev. D, 23, 347

Haan, S., Schinnerer, E., Mundell, C. G., García-Burillo, S., & Combes, F. 2008, AJ, 135, 232

Haehnelt, M. G., & Rees, M. J. 1993, MNRAS, 263, 168

Häring, N., & Rix, H.-W. 2004, ApJ, 604, L89

Heckman, T. M., Balick, B., & Sullivan, W. T., III 1978, ApJ, 224, 745

Helfer, T., et al., 2002, ApJS, 145, 259

Helfer, T. T., Thornley, M. D., Regan, M. W., Wong, T., Sheth, K., Vogel, S. N., Blitz, L., & Bock, D. C.-J. 2003, ApJS, 145, 259

Hills, J. G. 1975, Nature, 254, 295

Ho, L. C., Filippenko, A. V., & Sargent, W. L. W. 1997, ApJ, 487, 579

Ho, L. C., Filippenko, A. V., & Sargent, W. L. W.1997b, ApJS, 112, 315

Ho, L. C. 1999, ApJ, 516, 672

Ho, L. C. 2008, ArXiv e-prints, 803, arXiv:0803.2268

Hu, W., & Dodelson, S. 2002, ARA&A, 40, 171

Huchra, J., & Burg, R. 1992, ApJ, 393, 90

Hunt, L. K., Malkan, M. A., Moriondo, G., & Salvati, M. 1999, ApJ, 510, 637

Hunt, L. K., & Malkan, M. A. 1999, ApJ, 516, 660

Hunt, L. K., & Malkan, M. A. 2004, ApJ, 616, 707

Hunt, L. K., et al. 2008, A&A, 482, 133

van der Hulst, J. M., Terlouw, J. P., Begeman, K. G., Zwitser, W., & Roelfsema, P. R. 1992, Astronomical Data Analysis Software and Systems I, 25, 131

Jogee et al., 2002, ApJ, 575, 156

Jogee, S. 2004, in LNP Volume on AGN Physics on All Scales,Chapter 6

Jogee, S., Scoville, N., & Kenney, J. D. P. 2005, ApJ, 630, 837

Junqueira, S., & Combes, F. 1996, A&A, 312, 703

Karachentsev, I. D., Karachentseva, V. E., & Huchtmeier, W. K. 2006, A&A, 451, 817

Kauffmann, G., & Haehnelt, M. 2000, MNRAS, 311, 576

Kauffmann, G., et al. 2003, MNRAS, 346, 1055

Keel, W. C., Kennicutt, R. C., Jr., Hummel, E., & van der Hulst, J. M. 1985, AJ, 90, 708

Keel, W. C. 1996, AJ, 111, 696

Kewley, L. J., Dopita, M. A., Sutherland, R. S., Heisler, C. A., & Trevena, J. 2001, ApJ, 556, 121

Kewley, L. J., Groves, B., Kauffmann, G., & Heckman, T. 2006, MNRAS, 372, 961

Kim, D.-C., Sanders, D. B., Veilleux, S., Mazzarella, J. M., & Soifer, B. T. 1995, ApJS, 98, 129

Kim, W.-T., & Ostriker, E. C. 2002, ApJ, 570, 132

Knapen, J. H., de Jong, R. S., Stedman, S., & Bramich, D. M. 2003, MNRAS, 346, 333

Knapen, J. H., Whyte, L. F., de Blok, W. J. G., & van der Hulst, J. M. 2004, A&A, 423, 481

Kormendy, J., & Kennicutt, R. C., Jr. 2004, ARA&A, 42, 603

Krajnović, D., Cappellari, M., de Zeeuw, P. T., & Copin, Y. 2006, MNRAS, 366, 787

Krips, M., et al. 2005, A&A, 442, 479

Krips, M., et al. 2007, A&A, 464, 553

Krips, M., et al. 2007, A&A, 468, L63

van der Kruit, P. C., & Allen, R. J. 1978, ARA&A, 16, 103

van der Kruit, P. C., & Searle, L. 1982, A&A, 110, 61 van der Kruit, P. C., & Searle, L. 1982, A&A, 110, 79

Laurikainen, E., & Salo, H. 1995, A&A, 293, 683

Lin, C. C., & Shu, F. H. 1966, Proceedings of the National Academy of Science, 55, 229

Lindblad, B. 1959, Handbuch der Physik, 53, 21

Lindt-Krieg, E., Eckart, A., Neri, R., Krips, M., Pott, J.-U., García-Burillo, S., & Combes, F. 2008, A&A, 479, 377

Loeb, A., & Barkana, R. 2001, ARA&A, 39, 19

Lynden-Bell, D., & Kalnajs, A. J. 1972, MNRAS, 157, 1

Lynden-Bell, D. 1979, MNRAS, 187, 101

Maciejewski, W., & Sparke, L. S. 2000, MNRAS, 313, 745

Maciejewski, W. 2002, Ap&SS, 281, 325

Maciejewski, W. 2004, MNRAS, 354, 883

Maciejewski, W. 2004, MNRAS, 354, 892

MacKenty, J. W. 1989, ApJ, 343, 125

Magorrian, J., et al. 1998, AJ, 115, 2285

Márquez, I., Masegosa, J., Moles, M., Varela, J., Bettoni, D., & Galletta, G. 2003, Ap&SS, 284, 711

Martini, P., & Pogge, R. W. 1999, AJ, 118, 2646

Martini, P., Regan, M. W., Mulchaey, J. S., & Pogge, R. W. 2003, ApJ, 589, 774

Martini, P. 2004, The Interplay Among Black Holes, Stars and ISM in Galactic Nuclei, 222, 235

Miller, C. J., Nichol, R. C., Gómez, P. L., Hopkins, A. M., & Bernardi, M. 2003, ApJ, 597, 142

Mirabel, I. F., & Wilson, A. S. 1984, ApJ, 277, 92

Moiseev, A. V., Valdés, J. R., & Chavushyan, V. H. 2004, A&A, 421, 433

Mulchaey, J. S., Regan, M. W., & Kundu, A. 1997, ApJS, 110, 299

Mundell, C. G., Pedlar, A., Axon, D. J., Meaburn, J., & Unger, S. W. 1995, MNRAS, 277, 641

Mundell, C. G. and Pedlar, A. & Shone, D. L. & Robinson, A. 1999, MNRAS, 304, 481

Mundell et al., 2006, proceedings of The Fate of Gas in Galaxies, astro-ph/0610196

Mundell, C. G., et al. 2007, New Astronomy Review, 51, 34

Netzer, H., & Shields, J. C. 2007, ArXiv e-prints, 705, arXiv:0705.2192

Norman, C., & Scoville, N. 1988, ApJ, 332, 124

Ostriker, E. C., & Binney, J. J. 1989, MNRAS, 237, 785

Paturel, G., Petit, C., Prugniel, P., Theureau, G., Rousseau, J., Brouty, M., Dubois, P., & Cambrésy, L. 2003, A&A, 412, 45

Peterson, B. M. 2001, Advanced Lectures on the Starburst-AGN , 3

Pott, J.-U., Hartwich, M., Eckart, A., Leon, S., Krips, M., & Straubmeier, C. 2004, A&A, 415, 27

Quillen, A. C., Frogel, J. A., & Gonzalez, R. A. 1994, ApJ, 437, 162

Quillen, A. C., Frogel, J. A., Kenney, J. D. P., Pogge, R. W., & Depoy, D. L. 1995, ApJ, 441, 549

Quinn, T., & Binney, J. 1992, MNRAS, 255, 729

Rafanelli, P., Violato, M., & Baruffolo, A. 1995, AJ, 109, 1546

Rautiainen, P., et al., 2008, arXiv/0806.0471

Regan, M. W., Thornley, M. D., Helfer, T. T., Sheth, K., Wong, T., Vogel, S. N., Blitz, L., & Bock, D. C.-J. 2001, ApJ, 561, 218

Rees, M. J. 1984, ARA&A, 22, 471

Rubin, V. C., Burstein, D., Ford, W. K., Jr., & Thonnard, N. 1985, ApJ, 289, 81

Sakai, S., et al. 2000, ApJ, 529, 698

Sánchez-Salcedo, F. J. 2006, MNRAS, 365, 555

Sandage, A. 1990, JRASC, 84, 70

Schinnerer, E., Eckart, A., Tacconi, L. J., Genzel, R., & Downes, D. 2000, ApJ, 533, 850

Schmitt, H. R. 2001, AJ, 122, 2243

Schoenmakers, R. H. M., Franx, M., & de Zeeuw, P. T. 1997, MNRAS, 292, 349

Schoenmakers, R. H. M. 1999, PhD thesis, Rijksuniversiteit Groningen

Schwarz, M. P. 1984, MNRAS, 209, 93

Schwarz, U. J. 1985, A&A, 142, 273

Sellwood, J. A., & Wilkinson, A. 1993, Reports of Progress in Physics, 56, 173

Shakura, N. I., & Syunyaev, R. A. 1973, A&A, 24, 337

Shen, J., & Sellwood, J. A. 2004, ApJ, 604, 614

Shlosman, I., Frank, J., & Begelman, M. C. 1989, Nature, 338, 45

Shlosman, I., Begelman, M. C., & Frank, J. 1990, Nature, 345, 679

Shostak, G. S., van der Kruit, P. C., Hummel, E., Shaver, P. A., & van der Hulst, J. M. 1982, A&A, 115, 293

Shu, F. H., Tremaine, S., Adams, F. C., & Ruden, S. P. 1990, ApJ, 358, 495

Simões Lopes, R. D., Storchi-Bergmann, T., de Fátima Saraiva, M., & Martini, P. 2007, ApJ, 655, 718

Simkin, S. M., Su, H.-J., van Gorkom, J., & Hibbard, J. 1987, Science, 235, 1367

Smith, B. J. 1991, ApJ, 378, 39

Smith, B. J. 1994, AJ, 107, 1695

Sofue, Y., Honma, M., & Arimoto, N. 1995, A&A, 296, 33

Sofue, Y., & Rubin, V. 2001, ARA&A, 39, 137

Solomon, P. M., & Barrett, J. W. 1991, Dynamics of Galaxies and Their Molecular Cloud Distributions, 146, 235

Sparke, L. S., & Sellwood, J. A. 1987, MNRAS, 225, 653

Spekkens, K., & Sellwood, J. A. 2007, ApJ, 664, 204

Springel, V. 2005, MNRAS, 364, 1105

Storchi-Bergmann, T., González Delgado, R. M., Schmitt, H. R., Cid Fernandes, R., & Heckman, T. 2001, ApJ, 559, 147 Edition: 8th ed., Publisher: Garching: European Southern Observatory (ESO), 1998, Series: ESO Scientific Report Series vol no: 18

Thompson, A. R., Moran, J. M., & Swenson, G. W., Jr. 2001, Interferometry and synthesis in radio astronomy, Jr. 2nd ed. New York : Wiley, c2001.xxiii, 692 p. : ill. ; ISBN : 0471254924

Toomre, A. 1964, ApJ, 139, 1217

Trachternach, C., de Blok, W.J.G., Walter, F., Brinks, E., Kennicutt, R.C., Jr. 2008, AJ, submitted

Tremaine, S. 1989, Dynamics of Astrophysical Discs, 231

Tully, R. B., & Fisher, J. R. 1977, A&A, 54, 661

Ulrich, M.-H., Maraschi, L., & Urry, C. M. 1997, ARA&A, 35, 445

Verley, S., et al. 2007, ArXiv e-prints, 706, arXiv:0706.2555

Vilenkin, A., & Shellard, E. P. S. 1994, Cambridge Monographs on Mathematical Physics, Cambridge: Cambridge University Press, —c1994 ISBN 0521391539.

Virani, S. N., De Robertis, M. M., & VanDalfsen, M. L. 2000, AJ, 120, 1739

Vollmer, B., Marcelin, M., Amram, P., Balkowski, C., Cayatte, V., & Garrido, O. 2000, A&A, 364, 532

Vollmer, B., Cayatte, V., Balkowski, C., & Duschl, W. J. 2001, ApJ, 561, 708

Wada, K., & Koda, J. 2004, MNRAS, 349, 270

Wada, K. 2004, Coevolution of Black Holes and Galaxies, 186

Wainscoat, R. J., Freeman, K. C., & Hyland, A. R. 1989, ApJ, 337, 163

Walter, F., Brinks, E., de Blok, W.J.G., Bigiel, F., Kennicutt, R.C., Jr., Thornley, M.D. 2008, AJ, accepted

Warner, P. J., Wright, M. C. H., & Baldwin, J. E. 1973, MNRAS, 163, 163

Wong, T., Blitz, L., & Bosma, A. 2004, ApJ, 605, 183

Young, J. S., & Scoville, N. Z. 1991, ARA&A, 29, 581

Zhang, X., Wright, M., & Alexander, P. 1993, ApJ, 418, 100

Zhang, X. 1996, ApJ, 457, 125

Zhang, X., & Buta, R. J. 2007, AJ, 133, 2584

Acknowledgments

This thesis could not have been written without the support of many people and I would like to thank all of them.
First and foremost, I would like to thank my advisor Eva Schinnerer for giving me the opportunity to work on this interesting project. Her patience to discuss all questions and to help solving problems of every kind enabled me, who started as a total newcomer in this field, to complete the study presented here. She always found the time for a careful proofreading of all manuscripts during the last three years and has constantly challenged me to expand my point of view and see the bigger picture. My special thanks go to Hans-Walter Rix who has not only agreed on supervising this thesis as my official second advisor, but also contributed many fruitful discussions.

I want to express my gratitude to all members of the NUGA project, especially to Françoise Combes and Santiago García-Burillo, for their support throughout the work on my PhD thesis and all the inspiring discussions on galaxy evolution and related topics. In particular I am very much in debt to Eric Emsellem who introduced me to many of the scientific and modeling concepts necessary for this work. His detailed knowledge of galaxy dynamics and ongoing willingness to discuss and help solving problems was critical to develop successfully the modeling tool PyPot, and thus, to derive the results for this work. I also want to thank him for receiving me as a guest for two weeks at the Observatoire de Lyon where we started to write the simulation code for NGC 6951. I very much appreciated the friendly atmosphere in the entire Lyon group, especially I want to thank Gaëlle Dumas, not only for helping me to survive in France with my very basic french vocabulary, but also for her many contributions in modeling velocity fields. I would like to thank Carole Mundell for introducing me to the VHIKINGS project and her inspiring suggestions and comments on this thesis. I benefited greatly from discussions with Fabian Walter, Adam Leroy, Dominik Riechers, and Frank Bigiel. I want to thank Vernesa Smolčić for showing me all the subtle tricks how to tame AIPS. My thanks go also to Susanne Koltes-Al-Zoubi for all the organization work and Ulrich Hiller, Frank Richter, and Marco Piroth for their very efficient help with all things computer-related. In addition I thank the German DFG for their financial support during my study.

I would also like to thank all the people that are not directly involved with my work, but that have supported me otherwise and made sure I had a life outside the institute as well. At first I would like to thank my office mates during the last three years who have been supportive in every way: Michael, Marie-Helene, Markus, Jan, Martin, and Felix.

Steve, thanks for the countless banana cakes and for teaching me all the french words that one would never hear in France. Hope you will manage not to get lost again somewhere. I thank Jelte for his words of infinite wisdom and his sophisticated humour, Frithjof for showing me how to play piano at a level that I will never reach, Matt and Dave for all the great dinners, drinks and inspiring discussions on astronomy as well as on unrelated topics, Sophie for showing me the best of college life in Paris, Jakob for introducing me to all the Drum'n'Bass locations in the Rhein-Neckar Delta, Ingo and Constantino for not letting me alone at Untere Strasse when all others had left, and all the team-mates of the almost weekly basketball match.

My thanks also go to my flatmates, the ABB group, and all other friends who made my life in Heidelberg and Mannheim so enjoyable. In particular, I would like to thank Kai, Christian, Christine, Peter, Sebastian, Christiane, Björn, Christophe, Frank, and Tobias. Thank you for the great times!

Finally, I wish to thank my family for their great support and for not giving up on me since day one.